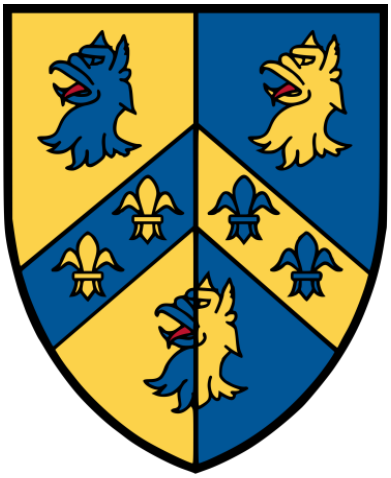
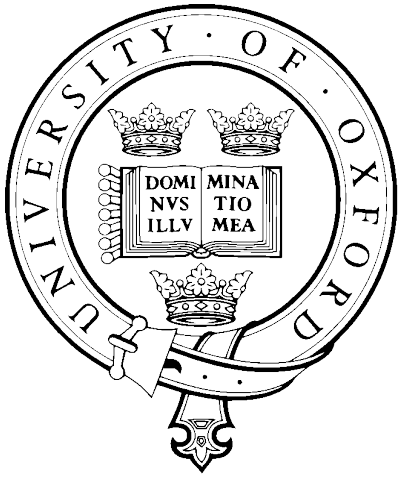
Quantitative Structural and Compositional Characterisation of Bimetallic Fuel-Cell Catalyst Nanoparticles Using STEM





A thesis submitted for the degree of

Doctor of Philosophy

Katherine E. MacArthur

Trinity College, University of Oxford

Hilary 2015

ABSTRACT

Platinum-based catalysts for hydrogen fuel-cell applications have progressed greatly with the addition of a second element in either a mixed-alloy or core-shell structure. Not only do they contain a reduced amount of the more expensive platinum metal but they have been shown to demonstrate a significant improvement in catalytic activity.[1,2] Further improvement of these systems can only be made by careful investigation of such catalyst nanoparticles on an atomic scale. These nanoparticles provide a significant characterisation challenge due to their minute size and beam sensitivity.

A new method of quantifying the annular dark-field (ADF) scanning transmission electron microscope (STEM) signal on an absolute scale has been developed to address this problem. Experimental images are scaled to a fraction of the incident beam intensity from a detector map. The integrated intensity of each individual atomic column is multiplied by the pixel area to yield a more robust imaging parameter: a scattering cross section, σ.

Using this cross section approach and simulated reference data, I show it is possible to count the number of atoms in individual columns. With some prior knowledge of the sample, this makes it possible to reconstruct the 3-dimensional structures of pure platinum nanoparticles. Such an approach has subsequently been extended to bimetallic particles where the elements are close in atomic number, using the platinum-iridium system as an example.

In the same way that the cross section can be calculated from ADF image intensity, it is possible to calculate an energy dispersive x-ray (EDX) partial scattering cross section, beneficial especially because of the simplicity of its implementation. In sufficiently thin samples such that the number of x-ray counts is linearly proportional to sample thickness, we can determine element-specific atom counts. Finally, it is possible to combine EDX and ADF cross sections to provide us with quantitative structural and compositional information.

LIST OF PUBLICATIONS

Some of the work contained in this thesis has been published elsewhere in peer reviewed journals and conference proceedings. A list of these publications is given here.

Peer Reviewed Journal Articles

- *Quantitative EDX analysis of catalyst nanoparticle using a partial scattering cross section approach.* K.E. MacArthur, T. Slater, S.J. Haigh, D. Ozkaya, P.D. Nellist, & S Lozano-Perez. *Microscopy and Microanalysis,* (2015). Accepted.

- *Optimal ADF STEM imaging parameters for tilt-robust image quantification.* K.E. MacArthur, A.J. D'Alfonso, D. Ozkaya, L.J. Allen, & P.D. Nellist. *Ultramicroscopy,* (2015). **156**, 1-8.

  doi:10.1016/j.ultramic.2015.04.010

- *Dose limited reliability of quantitative annular dark field scanning transmission electron microscopy for nano-particle atom-counting.* A. De Backer, G.T. Martinez, K.E. MacArthur, L. Jones, A. Béché, P.D. Nellist, & S. Van Aert. *Ultramicroscopy*, (2015). **151**, 56-61.

  doi:10.1016/j.ultramic.2014.11.028

- *Rapid estimation of catalyst nanoparticle morphology and atomic-coordination by high-resolution Z-contrast electron microscopy.* L. Jones, K.E. MacArthur, V.T. Fauske, A.T.J. van Helvoort, & P.D. Nellist. *Nano Letters*, (2014). **14** (11), 6336–41.

  doi:10.1021/nl502762m

- *Probe integrated scattering cross sections in the analysis of atomic resolution HAADF STEM images.* H. E, K.E. Macarthur, T.J. Pennycook,

E. Okunishi, A.J. D'Alfonso, N.R. Lugg, L.J. Allen, P.D. Nellist, *Ultramicroscopy*, (2013). **133**, 109–19.

doi:10.1016/j.ultramic.2013.07.002

Conference Proceedings

- *IT-2-O-2221 Channeling Effects on the Accuracy of HAADF STEM Quantification of Bimetallic Catalyst Nanoparticles.* K.E. MacArthur, S. Lozano-Perez, D. Ozkaya, P.D. Nellist. *18th International Microscopy Congress 2014.*

- *MS-1-P-2222 Quantification of PtIr Catalyst Nanoparticles using ADF STEM.* K.E. MacArthur, L.B. Jones, S. Lozano-Perez, D. Ozkaya, P.D. Nellist. *18th International Microscopy Congress 2014.*

- *How flat is your detector? Non-uniform annular detector sensitivity in STEM quantification.* K.E. MacArthur, L.B. Jones, & P.D. Nellist. *Journal of Physics: Conference Series* (2014). **522** (1), 012018.

  doi:10.1088/1742-6596/522/1/012018

- *Structural quantification of nanoparticles by HAADF STEM.* K.E. MacArthur, L.B. Jones, S Lozano-Perez, D. Ozkaya & P.D. Nellist. *Journal of Physics: Conference Series* (2014). **522** (1), 012061.

  doi:10.1088/1742-6596/522/1/012061

ACKNOWLEDGEMENTS

This thesis is really a tribute to the hugely supportive and friendly environment which Oxford has provided me with during my time here. I would firstly like to express my gratitude to my supervisors Peter Nellist, Sergio Lozano-Perez and Dogan Ozkaya, for their knowledge, support and confidence in my abilities. Such a trio of support has meant that I've never lack for momentum in propelling the project forward.

I consider myself immensely lucky for the range of collaborators far and wide who have provided invaluable microscope time and scientific discussions. My thanks in particular go to Eiji Okunishi, Armand Béché and Tim Pennycook for their microscope driving skills which has yielded a good portion of my earlydata whilst facilities were not available in Oxford. Les Allen and Adrian D'Alfonso in Melbourne helped me greatly with the simulation work and their precise knowledge of channelling and electron optics.

To all the members of the Atom workshops I am appreciative of the relaxed environment which these workshops have provided for my first scientific presentations and the in depth scientific discussions which followed. I am especially grateful to Sandra Van Aert's group in Antwerp, including Gerado Martinez and Annick De Backer, for their attention detail an alternate approach to ADF STEM quantification. Collaborating with them has provided invaluable discussion yielding and broadening of my theoretical knowledge, yielding fruitful new directions to take the research.

Sarah Haigh and Thomas Slater from Manchester University have provided me invaluable time on their Titan, which has provided a large portion of the EDX data for this thesis.

For financial support, I acknowledge EPSRC and Johnson Matthey for funding my DPhil and Trinity College for aiding with conference travel funding.

I would like to thank my friends and colleagues during my time in Oxford who have be a constant source of support and scientific discussions; Neil Young, Ron Doole, Fay Chicken, Rebecca Nichols, Adam Papworth, Juan Lozano, Peng Wang, Jack Severs, Hao Yang, George Theodossiou, Aleksey Shemliov, Gareth Hughes, Gabriella Chapman, Greg Cook, and especially Lewys Jones. I am grateful to Emma Walker, Matthew Sullivan, Stuart Dingle whom I coerced into reading and helping me edit this thesis.

I would like to thank my family who never fail to keep me grounded. My sister Alice MacArthur I would like to thank in particular who meticulous typed out a whole paper whilst I suffered with a broken hand. Finally, I would like to acknowledge my husband James who has helped me overcome many a crisis of confidence. He has listened to me complain about microscopes misbehaving or delivered me late night dinners at the microscope when things were working too well that I didn't want to leave.

CONTENTS

1. Introduction 1

1.1. Outline 2

2. Heterogeneous Catalysts 5

2.1. Platinum Group Metals 7

2.1.1. PGMs for Hydrogen Fuel-Cells 8

2.1.2. Surface Adsorption and Active Sites 11

2.1.3. Size Effects 13

2.2. Catalyst Design 14

2.2.1. Core-shell Geometry 14

2.2.2. Pt-X Alloy 15

2.3. Methods of Characterisation 17

2.3.1. Optical Spectroscopy 18

2.3.2. Electrochemical Techniques 19

2.3.3. X-ray Photon Spectroscopy (XPS) 19

2.3.4. X-ray Characterisation (XRD, SAXS, EXAFS) 20

2.4. Electron Microscopy 21

2.4.1. Scanning Electron Microscopy 21

2.4.2. Transmission Electron Microscopy 22

2.4.3. In-Situ Electron Microscopy 27

2.5. Conclusions 27

3. Scanning Transmission Electron Microscopy 29

3.1. Variety of Signals 31

3.1.1. Bright-Field STEM 32

3.1.2. High Angle Annular Dark-Field and Z-Contrast 33

3.1.3. Damage and Contamination 35

3.2. Aberration Correction 38

3.3. Three-Dimensional Information 40

3.3.1. Tomography 41

3.4. Composition Analysis 45

3.4.1. Electron Energy Loss Spectroscopy 46

3.4.2. Energy Dispersive X-ray Analysis 48

3.5. Quantification of ADF Images 50

3.5.1. Recent Advances in STEM Quantification 51

3.5.2. Detector Calibrations 55

3.5.3. Channelling 60

3.5.4. Image Simulation Techniques 61

3.6. Quantification of EDX 65

3.6.1. K-Factor 66

3.6.2. ζ-Factor 67

3.6.3. Accuracy Limitations 69

3.7. Conclusions 71

4. Methods for ADF Quantification 73

4.1. Sample Preparation 74

4.2. Image Intensity Normalisation 75

4.2.1. At the Microscope 75

4.2.2. Image Calibration 77

4.3. Measuring the Detector Collection Efficiency 80

4.4. Detector Angle Calibrations 84

4.4.1. Outer Cut-Off Angle 86

4.5. Simulation Optimisation and Accuracy 88

4.5.1. Details of Simulation Parameters 89

4.5.2. Comparison between different simulation codes 90

4.5.3. How Many Phonon Configurations to Use 93

4.5.4. Reciprocal Space Sampling 95

4.5.5. Conclusions 96

5. Scattering Cross Sections 98

5.1. Mathematical Framework 99

5.2. Simulation Methods 101

5.2.1. Tilting Simulations 102

5.3. Cross Sections vs. Peak Intensities 103

5.4. Microscope Imaging Parameters for Single Atoms 105

5.4.1. Defocus 105
5.4.2. Source Size and Coherence 106
5.4.3. Probe Convergence Angle 107
5.5. Single Atom Investigation 108
5.6. Applicability of Cross Sections to Imaging Crystals 112
5.6.1. Defocus in a Crystal 112
5.6.2. Integration Area and Probe Position 113
5.6.3. Probe Convergence Angle 114
5.6.4. Crystallographic Zone-Axis 115
5.6.5. Temperature and the Debye Waller Factor 116
5.6.6. Cross-Talk 118
5.7. Channelling and Tilt 121
5.7.1. Tilt Dependence of HAADF Cross Sections 122
5.7.2. The Tilt Dependence of ADF Cross Sections 123
5.7.3. The Origin of the Plateau 127
5.7.4. The Effect of Probe Convergence Angle 130
5.7.5. Tilt Variation with Thickness 131
5.7.6. Tilt in Bimetallic Systems 133
5.8. Conclusions 136
6. Single Particle Reconstruction Methodology 139
6.1. At the Microscope 140

6.2. Automated Integration Code ‘Absolute Integrator’ 141
6.2.1. Detector Calibration 141
6.2.2. Image Calibration 144
6.2.3. Peak Finding 144
6.2.4. Background Subtraction 146
6.2.5. Integration 148
6.3. Converting to Atom Counts 149
6.4. 3-Dimensional Reconstruction 150
6.5. Error Analysis 152
6.5.1. Pixel Width 153
6.5.2. Poisson Noise Statistics/Dose 154
6.5.3. Scan Noise 154
6.5.4. Background Subtraction 155
6.5.5. Convergence Angle 158
6.5.6. Detector Collection Angles 158
6.5.7. Summary 160
6.6. Reconstructed Nanoparticles 163
6.6.1. Pt Nanoparticles 163
6.6.2. Pt-Ir Nanoparticles 172
6.6.3. Comparison with Wulff Construction 180
6.6.1. Energy Relaxation 182

6.7. Conclusions 183

7. Energy Dispersive X-ray 185

7.1. EDX Partial Scattering Cross Sections 186

7.1.1. Comparison with ζ-Factors 187

7.2. Experimental Calibration 188

7.2.1. Comparison between microscopes 193

7.3. Background Subtraction 195

7.4. Converting to Atom Counts 196

7.5. Error Analysis 200

7.5.1. Counting Statistics 201

7.5.2. Probe Interaction Volume 202

7.5.3. Wedge Geometry 203

7.5.4. Probe Current 206

7.5.5. Integration Window and Background Subtraction 207

7.5.6. Channelling 207

7.5.7. Error Variation with Thickness 208

7.6. Pt-Pd Nanoparticles 209

7.7. Pt-Co Nanoparticles 215

7.8. Conclusions 218

8. Combining ADF and EDX Scattering Cross Sections 220

8.1. Initial Cross Section Analysis 220

8.2. EDX Composition Analysis 222

8.3. Comparison of ADF and EDX Quantification 224

8.4. Combining ADF and EDX Quantification 225

8.4.1. Thickness Profile 228

8.5. Conclusions 231

9. Conclusions and Future Work 232

9.1. Towards High Throughput and Statistics 236

9.2. Hybrid Method with ICL 237

9.3. Improving EDX Counts 242

9.3.1. EDX Analysis at 80kV Accelerating Voltage 243

9.4. Electron Energy Loss Spectroscopy 244

9.5. Combining ADF and EDX Cross Sections 245

10. References 246

11. Appendices 266

1. INTRODUCTION

As the world's energy demands are increasing and we look towards greener alternatives in order to reduce our carbon footprint, hydrogen fuel cells represent an encouraging prospect for small scale energy generation. In particular, fuel cells are a promising technology for use as a source of heat and electricity for buildings and as an alternative power source to combustion engines in the automotive industry. Fuel cells are often referred to as zero emission technology as the only reactant product is H_2O, although methanol fuel will also produce CO_2. The primary factor limiting their more wide scale use is the high cost of the platinum catalyst, required at both the anode and cathodes.

A great deal of research, time and money has been spent on improving these catalysts and designing novel geometry bimetallic particles with a significantly higher activity per gram of platinum loading. The premise behind such designs is to limit the Pt location to only the particle surface where it is required. However it is still not entirely clear what about these catalysts causes their improved activity. In order to improve our understanding of such catalysts we need to improve our ability to characterise them at the length scales at which the chemical reactions will be taking place, in particular their 3-dimensional shape and where the platinum is located at the particle surfaces.

The focus of this thesis is to characterise these bimetallic catalyst particles at the atomic scale. Quantification techniques of both annular dark-field (ADF) scanning transmission electron microscopy (STEM) and energy dispersive x-ray

(EDX) analysis have been developed and improved for a high resolution particle by particle analysis, with the particular aim of trying to quantify and extract 3-dimensional information. We will also look at separating out the composition and thickness contributions to the ADF STEM intensity.

1.1. Outline

Chapter 2 provides the background on platinum catalysts including the motivations towards novel geometries to reduce the platinum loading and lower their cost. The methods for analysis of catalysts are also discussed. In particular, we will look at the trade-off between averaging techniques, which give statistically representational, but not particle specific, information and high resolution electron microscopy which provides much more local particle by particle analysis. However, the high resolution particle specific information has an inherent limitation of poor statistics and the potential of not being representational of the whole sample.

Chapter 3 is a literature review focusing specifically on ADF STEM for the study of nanoparticles and its ability of acquiring multiple signals in parallel. The Z-contrast nature of the annular image lends itself particularly to the study of polymer exchange membrane fuel-cell (PEMFC) catalysts because the heavy metal nanoparticles stand out from the low Z carbon support. The more recent progressions in quantifying the ADF STEM signal for accurate atom counting as well as image simulation are also discussed. Finally, we introduce the methodologies for quantifying EDX microanalysis for accurate composition determination and the limitations involved therein.

In Chapter 4, I outline the methods used in this thesis for sample preparation and accurate calibration of the microscope, including a newly-discovered outer cut off limitation to the electron flux. The importance of optimised simulations and their comparison with different simulation codes in order to estimate which are the most trustworthy is also discussed.

Chapter 5 introduces the scattering cross section method for ADF STEM quantification. The scattering cross section of an atomic column is robust to a wide range of microscope imaging parameters, which allows greater flexibility for imaging such challenging samples as nanoparticles. The mathematical theory is combined with image simulation to test the limitations of this robustness for quantifying nanoparticles. Work towards experimental design to overcome the sample effects of channelling and mis-tilt is also discussed.

Chapter 6 looks at ADF quantification and atom counting of single element nanoparticles. With the addition of a few simple assumptions it is possible to use the atom counts to reconstruct 3-dimensional (3D) particle shapes from a single experimental STEM image. The coordination and surface facet ratio information can also be extracted from these 3D shapes, providing valuable atomic level catalytic information that can be compared with theoretical Wulff predicted structures.

Chapter 7 proposes a new method of EDX quantification using partial scattering cross sections. Such cross sections can be determined experimentally from pure element wedge samples. I use this approach to quantify the Pt surface enrichment of Pt(Pd) core-shell and de-alloyed PtCo nanoparticles.

In Chapter 8, I look at how the two scattering cross section quantification approaches (both ADF and EDX) can be combined to solve the 3D thickness profile of bimetallic particles. The potential for exploiting the top bottom effect to determine column by column ordering is also discussed.

Finally the conclusions and future work prospects are in Chapter 9.

2. HETEROGENEOUS CATALYSTS

A *catalyst* is, *'a substance which when present in small amounts increases the rate of a chemical reaction or process but which is chemically unchanged itself by the reaction'.*[3] Although not normally included in the overall stoichiometric reaction equation, catalysts are important for lowering activation energy barriers by providing an alternative reaction pathway for all or part of a reaction, thus allowing industrially vital reactions to proceed at much lower temperatures than they would otherwise be able. Catalysts can also provide selectivity or specificity to particular reactant products and are divided into two main types: heterogeneous or homogeneous, heterogeneous if the catalyst is a different phase to the reactants or the products and homogeneous if it is the same phase.

Heterogeneous catalyst surfaces are covered in sites, known as 'active sites',[4] where the reactant molecules are preferentially adsorbed. Although exact mechanisms are poorly understood, it is thought that this adsorbing to the surface weakens or breaks bonds in the reactant molecules, allowing them to form new bonds more readily and thereby accelerating the reaction rate. Therefore good catalysts have a larger number of active sites with easy access for all the reactant molecules. Nanoparticles lend themselves for use as catalysts due to their large surface area[5] per unit mass or cost and ease of transportation of reactants and products to and from the particles when on a 3-dimensional porous support.

Catalyst nanoparticles are normally dispersed on a porous and nominally inert substrate, often an oxide, the type and structure of which can produce widely varying activities and selectivities[6] indicating the presence of strong particle-support interactions.[7] This suggests that both the catalyst-support interface and the catalyst-reactant interface have a bearing on the final reaction mechanism.

'75% of all chemicals are produced with the aid of catalysts; in newly developed processes, the figure is over 90%'.[8] Despite their wide use we know very little of how they work. Therefore, a major aim of current research is in identifying and understanding structure-performance relationships. Historically catalysts were found by empirical methods and improved through a process of trial and error. Even small changes in the sample preparation route can produce a significant change in the catalytic response,[9] making their behaviour difficult to understand and subsequently predict. The well documented variety of the parameters which can affect the catalytic performance of nanoparticles include the seed crystal,[1] [10] particle size and shape,[11] local surface composition, chemical bonding, support material and particle-support interactions,[6] and surface structure. All these parameters will evolve and change during synthesis, use and subsequent catalyst regeneration[2].[12] One of the primary challenges in nanoparticle synthesis is therefore in trying to create a sample of mono-dispersed particles of uniform size and structure which will all exhibit as uniform a catalytic activity and selectivity[13] as possible throughout.

[1] A seed crystal is an initial small nanoparticle used as the starting point for nanoparticle synthesis. Reaction conditions are used to maximise nucleation to produce seed crystals before being changed to promote ripening and uniform growth for a mono-dispersed size range.

[2] Regeneration is where the catalyst is heated in a clean environment in an effort to burn off contaminants and dirt that have built up on the surface during use and are inhibiting or 'poisoning' catalytic activity.

In this chapter I will introduce the platinum group metals (PGM) as catalysts for hydrogen fuel cells. The catalysts need to be understood in terms of their surface structure and active sites and how this changes for small particles. I will also explore how the limitation of platinum's high cost is overcome through combining it with other elements and careful catalyst design. Finally, I look at the main methods used for characterising catalyst particles including electrochemistry and electron microscopy.

2.1. Platinum Group Metals

Platinum group metals (PGMs) is the name given to a small group of metals clustered together around Pt in the periodic table with similar physical and chemical properties. They are particularly prominent for their uses in the production of nitric acid,[8] the contact process,[8] three-way exhaust catalysts[14] and hydrogen fuel cells.[8] These six metals have high melting points making them structurally stable at high temperatures. As well as their extreme corrosion resistance, oxidation and reduction properties,[15] PGMs show continued use despite their high cost because there is no comparable alternative. Table 2.1 gives an estimate of their costs, with cobalt included for comparison.

Metal	Price ($/100g)[3]
Ru	1400
Rh	13000
Pd	5833
Os	7700
Ir	4200
Pt	13000
Co	27

Table 2.1 – Cost of the platinum group metals and cobalt per 100g in weight.

PGMs found their fame in 1909 when the idea of a supported platinum catalyst in the exhaust of a car was first introduced by Frenkel;[16] it was only a couple of years later that the first of these went into production in the Model T Ford. Today *'an increasing emphasis on greenhouse gas emissions combined with a need to meet NO_x and particulate emissions legislation, means that manufacturers are forced to design improved engines which are reduced in size or hybrids'*.[17] This will mean a reduction in the output temperatures; PGM catalysts of the future will need to be more active, work at lower temperatures and be able to remove pollutants as soon as the engine is switched on.[4]

2.1.1. PGMs for Hydrogen Fuel-Cells

PGM catalysts show great promise in the proton-exchange membrane fuel-cell (PEM-FC) (see Figure 2.1), which is being promoted as a clean energy alternative to the combustion engine for the automotive industry, negating the

[3] Values taken from http://www.chemicool.com on 30/04/2014
[4] Previously, exhaust emission tests waited until the engine had been running for a few minutes and the car had warmed up before the exhaust gases were tested.

need for catalytic converters. First demonstrated in 1839 by Sir William Grove,[18] Pt supported on carbon is still the catalyst of choice due to its stability under the corrosive environment.[19] The porous carbonaceous support is designed to maximise the surface area of platinum available to the reactant and product gases, as well as acting as electrodes for completing the electrochemical cell.

The principle of the PEM-FC is that hydrogen gas is oxidised at the anode, separating the H^+ ion, or proton, from its electron.

$$H_2 \rightarrow 2H^+ + 2e^- \qquad 2.1$$

The proton is able to migrate through the polymer membrane separating the anode and cathode, whilst the electron must travel through the carbon support and around an external circuit. At the positive cathode, oxygen from the air is reduced and reacts with the proton, to produce H_2O.

$$\frac{1}{2}O_2 + 2H^+ + 2e^- \rightarrow H_2O \qquad 2.2$$

Platinum-carbon catalysts are necessary for both the anodic and the cathodic reactions to proceed at the low operating temperatures. The efficiency of PEM-FCs is severely limited by the kinetically lethargic oxygen reduction reaction at the cathode. The catalyst is especially important to prevent the formation of the other energetically favourable species from oxygen reduction, hydrogen peroxide, H_2O_2,[20] which can dissolve the polymer membrane, resulting in total failure of the fuel-cell.

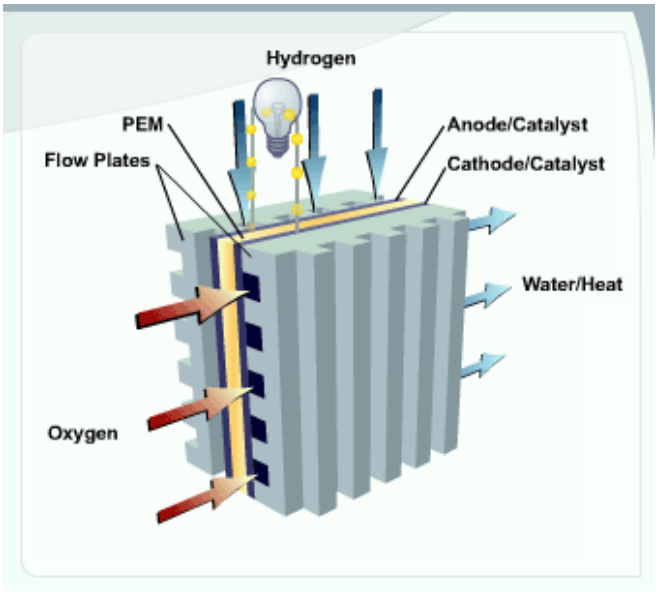


Figure 2.1 – Schematic of a PEM fuel cell taken from the website of the United States Department of Energy.[21] Only protons and not electrons can diffuse through the polymer or proton exchange membrane. Several of these cells will need to be stacked together to produce a significant power output.

The total content of PGMs in these fuels cells has decreased by more than 80% since 2005.[21] However, the current aim of PGM research is to meet the United States Department of Energy target of reducing the platinum loading further still to below 0.125g/kW by 2017, in order for PEM-FCs to represent a realistic alternative to the internal combustion engine. One way to achieve this is to increase the catalytic activity, the rate of reaction per unit area of surface,[22] thereby increasing the power output of the fuel-cell or indeed reducing the amount of catalyst needed. Another way is to minimise the platinum loading by reducing nanoparticle size or by creating alloy particles so the amount of platinum per nanoparticle is reduced.

2.1.2. Surface Adsorption and Active Sites

Different surface planes and facets have a differing number of 'dangling bonds' which will affect how the surface atoms attract the reactant molecules. With nanoparticle catalysts this is likely to mean that certain facets are more catalytically active than others. Understanding the surface adsorption of reactant species is therefore critical to being able to understand the reaction mechanism, and also the activity and selectivity of the catalyst nanoparticles.[23][24] An intermediate binding energy with reactant molecules is the most advantageous for catalysis. If the species bind too weakly, the adsorption will not sufficiently weaken other bonds in the molecules; bind too strongly and the molecules will not proceed with other steps in the reaction, they will just remain adsorbed to the catalyst.[25]

Early studies by Lang[26] using a combination of chemisorption and low energy electron diffraction (LEED) techniques showed that the high energy, larger Miller Index, planes contain remarkably thermally stable (111) or (100) terraces of constant width linked by steps of monatomic height. Later confirmed by Gambardella[27] using scanning tunnelling microscopy (STM), oxygen was only seen to adsorb to these step sites; indeed they seem vital to dissociation of the O_2 molecule. Hydrogen was also seen to preferentially adsorb to the tops of these steps, not adsorbing to close-packed surfaces until temperatures above 1000K. Work by Feibelman which combined scanning probe techniques with DFT (density functional theory) calculations confirms the importance of these steps and kinks for O_2 dissociation on Pt(111).[28] A similar relationship has also been demonstrated for the selective reduction of NO to N_2.[29]

Problematically, PGM catalysts are prone to 'poisoning'.[30] This is where a species unrelated to the reaction bonds strongly to an adsorption site, thereby reducing the number of available active-sites on the catalytic surface and causing a drop in activity.[31] For PEM fuel cells these poisoning species (e.g. SO_2, COS, H_2S) are present in the air, so mostly affect the site of oxygen reduction at the cathode. Additionally CO is a by-product in the reforming of hydrocarbons to H_2 gas and so is also present at the anode,[19] it has been shown to preferentially adsorb to close-packed (111) Pt surfaces.[28,32] Yates Jr. noted that *'step sites exhibit special chemisorptions and catalytic properties'* and more specifically in his research steps acted as trap sites for migrating CO molecules.[23] This explains why CO is the most prominent poisoning species for Pt catalysts; the CO molecules are competing for the same active sites as the reactant H_2 and O_2 molecules.

Pt-Sn, Pt-Ir, and Pt-Co catalysts have demonstrated improved tolerance to CO poisoning[31] as the onset potential of CO oxidation is lower, whereas Pt-Pd catalysts have demonstrated greater susceptibility to SO_2 poisoning.[33]

A problem for nanoparticles produced by colloidal methods is the difficulty in removing the surface ligands used during manufacture to carefully control particle size, as these will, most likely, restrict the access of reactants to the surface. Recent work by Lopez-Sanchez et al.[34] has shown that some of the stabilizing ligands can be removed by solvent extraction without significant increases to the particle size. Zhou et al.[12] have discovered water soluble ligands that can then be 'washed' off in a warm water bath; however this is unlikely to be directly applicable to other catalyst systems.

2.1.3. Size Effects

The surface nature of heterogeneous catalysis means that any metal atoms not exposed to the surface are most likely not contributing towards the catalyst activity, making it essentially wasted material. The first avenue for catalyst improvement is to decrease the size of the PGM particles in order to increase their surface area to volume ratio, and thereby decreasing the mass of expensive metal needed for the same activity.

The process however is not quite that straightforward; in terms of energetics the ratio of surface atoms to bulk atoms increases significantly at smaller particle sizes. Whereas in a bulk material these surface atoms would have been considered negligible in energetics calculations, at the nanometre scale they have a larger impact to both the structure and properties of the material. This causes a large variety of properties to become dependent on nanoparticle size and differ significantly from that of the bulk material.[35] For example, a range of complex structures made from twinned subunits have been seen for those FCC (face-centred cubic) metals prone to twinning, such as gold, which are energetically favourable because they minimise surface energy.[10,36,37] These multiply twinned structures are due to the 20 percent difference in {001} and {111} surface energies[38] and are therefore not as readily seen in PGM-based nanoparticles, where the difference in surface energies is significantly smaller.[39]

Small particles have also been seen to exhibit a drop off in the melting temperature below a particle diameter of 20nm.[40] Considering the possible locally induced heating provided by an electron beam, melting and structural rearrangement studies have been carried out in high voltage microscopes.[41,42] This instability can be reduced with a surface carbon covering or surfactants.[43]

Whilst improving beam stability this would not be representative of real catalysts samples as surface coverings are detrimental to catalytic properties.

All this means that varying particle size is not a straightforward process to provide increased catalytic surface area. Instead we need to be more clever with catalyst design which is where bimetallic particles come into play.

2.2. Catalyst Design

In order to achieve the significant improvement in activity in order to meet the DOE targets it is essential to design catalysts which use Pt more efficiently. This research includes the designing of bimetallic particles or particles with larger area of the more catalytically active surface facets than occurs in a spherical particle.[44] The two main bimetallic catalyst designs, mixed alloy and core-shell geometries, work on the premise of decreasing the amount of Pt within the nanoparticle by alloying with a less expensive metallic element. Another reason for bimetallic particles is to try to minimise the effect of poisoning of PGM catalysts by the adsorption of certain unwanted species.[45,46] In this work I will focus on three bimetallic catalysts: Pt(Pd) with core-shell geometry, Pt-Ir as mixed alloy particles and Pt-Co in the de-alloyed form with surface Pt enrichment.

2.2.1. Core-shell Geometry

The principle behind core-shell particles is to maintain catalyst surface area for reduced precious metal weight by limiting the Pt use to only the nanoparticle

surface, encapsulating a less expensive core metal. These are normally produced by growing a core seed crystal and then changing reaction conditions in the solution to deposit a layer of the Pt on the outside. Core-shell particles with base-metal core and a PGM shell have seen some success with the Pt-Sn system.[31]

Pt(Ru) particles have demonstrated significant specificity improvements[47] whilst core-shell particles of Pt(Pd) have been shown to demonstrate a 20-fold increase in Pt mass-specific activity as well as increased stability of Pt against oxidation.[33][34] It is estimated that the effect on the electronic structure of the Pt surface due to the proximity of the core metal is what produces this improvement in activity.[50]

Unfortunately the activity gains seem to come at the cost of particle stability, particularly at small particle sizes where the core-shell interface area is reduced, meaning we often witness increased amounts of alloying at the boundary.[51]

2.2.2. Pt-X Alloy

An alloy particle is formed by co-precipitation of the two elements producing a randomly distributed mixture throughout the particle. The mixed alloy nanoparticles are thought to produce improvements in the catalytic activity due to the compressive strain effect introduced by alloying with elements of smaller atomic radius.[52,53]

The greatest improvement in catalytic activity has been seen for subsequently de-alloyed or acid leeched nanoparticles, where in an acidic solution the less

inert alloying element reacts preferentially to the platinum resulting in a platinum enriched surface. Whilst essentially a poor version of the core-shell geometry discussed above, the activity improvement from strain effects also remains[54–56] (see Figure 2.2) whilst also providing near surface effects from the sub-surface alloy.[57]

Ordered alloy cores seem to demonstrate a further increase in catalytic activity over those particles with disordered cores, over 300% in platinum mass specific activity increase for the Pt-Co system.[58] Although the origin of this additional increase is unclear. Ordered Pt-Fe particles with a Pt-enriched core show an increased stability over a 1000 cycles in comparison to particles with the core-shell type structure.[59] A similar stability and increase in ORR (oxygen reduction reaction) has been seen for de-alloyed Pt-Cu[60] and Pt-Ni[61] particles.

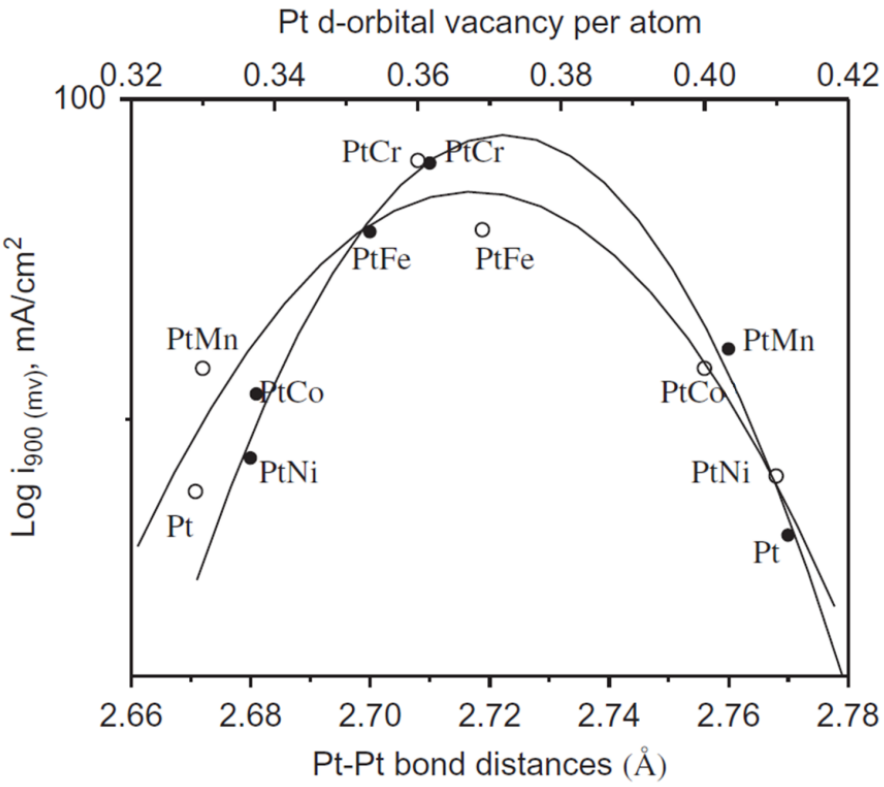


Figure 2.2 – Correlation of oxygen electrode performance of a Pt and Pt alloy electrocatalysts in PEMFCs with Pt-Pt bond distance (•) and Pt d-orbital vacancy (○), obtained from in situ X-ray absorption spectroscopy. Republished with permission from the Electrochemical Society.[2]

2.3. Methods of Characterisation

A vital component to understanding catalyst particles is to be able to fully characterise their atomic scale structure and relate this back to their catalytic properties. The characterisation techniques for catalysts fall under two main categories:

→ Averaging techniques, which provide information about the whole system, including the support, giving an average conclusion for a statistically large number of particles. These include:

- Optical spectroscopy

- Cyclic-voltammetry (CV)
- X-ray photon spectroscopy (XPS)
- Small angle X-ray spectroscopy (SAXS)
- Extended X-ray absorption fine structure (EXAFS)[15]

→ Higher resolution localised techniques, which give much more in-depth information about the structure of individual particles. These include:

- Atom probe
- Scanning tunnelling microscopy (STM)
- Scanning electron microscopy (SEM)
- Transmission electron microscopy (TEM)
- Scanning transmission electron microscopy (STEM)

The averaging techniques provide a good statistical representation over the whole sample; however they may not necessarily yield information on the particular species or particle size which is providing the catalytic activity. Zhou et al. demonstrated this with their oxide supported gold catalyst system in which the active species for their reaction were shown to be small atomic bi-layer structures accounting for only 10% of the gold mass used in the sample.[12] The high resolution techniques can yield much more particle specific information; however, here there is a danger for poor statistics and the data not being representative of the real particle structure distributions within the sample.

2.3.1. Optical Spectroscopy

Optical spectroscopy, including UV-vis, Raman and infra-red, involves measurement of the elastic/inelastic scattering of a particular incident

wavelength of light. UV-vis spectroscopy can provide information on the electronic structure, which is particularly important for oxide supports or measuring the degree of oxidation within the metallic nanoparticles themselves. Raman spectroscopy is well known as a technique to discriminate between multiple molecular structures whilst infra-red spectroscopy provides important information on identifying surface species.[12]

2.3.2. Electrochemical Techniques

One regularly used and relatively simple method to measure the activity of fuel-cell catalysts is CV. This is an electrochemical test where the half-cell is constructed with the catalyst particles adsorbed to the surface of the working electrode; a voltage sweep is carried out to measure its current-voltage characteristics.[62] The reverse current sweep can be used to establish how reversible any changes are. This is a particularly important technique for PEM-FCs as it gives information relevant to their final application.

2.3.3. X-ray Photon Spectroscopy (XPS)

XPS is a surface sensitive technique useful for analysing the first 10Å depth into a catalyst sample surface. A soft X-ray probe is scanned over the sample and characteristic X-rays are detected with respect to probe position and with a great deal of statistical accuracy that allows detection limits down to 0.01 percent. This theoretically makes it an excellent technique to determine the amount of platinum at a particle surface, or for analysing any contamination or poisoning species also present on the system.

Unfortunately for nanoparticles below 5nm in size the percentage of the atoms which are sufficiently close to the surface for detection becomes too great to be able to determine such surface information accurately.

2.3.4. X-ray Characterisation (XRD, SAXS, EXAFS)

Powdered X-ray diffraction (XRD) is a rapid and non-destructive method of analysing the crystal structures present in a sample. A powdered sample contains every possible crystal orientation, to produce an averaged diffraction pattern of all the different phases present. It is frequently used to estimate the average crystallite size; however as it is a crystallography technique it provides no information about any amorphous regions within the sample, or coagulations of particles or twinning.

SAXS can be used to determine information about size and shape of nanoparticles.[12]

EXAFS[63] provides information on local atomic structure and bonding within the material.[64] The degree of ordering in multiple element particles is frequently determined by examining the ratio of Pt-Pt bonds versus Pt-X bonds. This is a process which can equally be applied to estimate core-shell coverage, if the core-size is accurately known. The technique is suited to in-situ studies, by constructing an electrochemical cell in the beam line, making it possible to measure the effect of cycling on the particle ordering.

2.4. Electron Microscopy

For higher resolution and localised information we look towards electron microscopy, where the very small wavelength makes it capable of resolution at the nanoparticle length scale and below. Fast electrons accelerated by a given potential V have a wavelength λ given by the relativistic equation:

$$\lambda = \frac{h}{\left[2m_e eV\left(\frac{1+eV}{2m_e c^2}\right)\right]^{\frac{1}{2}}} \qquad 2.1.$$

Where *h* is Planck's constant, *e* is the charge on an electron and $m_e c^2$ is its rest energy.

2.4.1. Scanning Electron Microscopy

SEM is frequently limited to bulk materials where the resolution is limited due to a large interaction volume from multiple scattering events and beam spreading effects within the specimen. A typical resolution for an ideal sample in a 20kV SEM is 1.5-3.5nm depending on the electron source type.[5]

The resolution of these microscopes has increased by using them at lower voltages, down to 1kV, demonstrating sub-nanometre resolution. The low voltage significantly decreases the interaction volume allowing not only Pt particle distribution to be imaged but the morphology of the carbon support as well.[65] The topographical information obtainable from the secondary electron (SE) signal, due to the low energy electrons only being able to escape from within a couple of nanometres of the sample surface, combines with the

[5] http://mee-inc.com/sem.html

microscope's large depth of field to provide valuable 3-dimensional information, particularly relevant for understanding the support structure.

Recently, a number of STEMs have had an SE detector fitted, allowing simultaneous high resolution and topographical information to be detected. SE signals have been detected of Pt particles on a γ-alumina support[66] and Au-Pd particles on TiO_2.[63]

2.4.2. Transmission Electron Microscopy

TEM imaging has been widely used to investigate catalyst systems[67] since the technique's invention in 1939.[68] Conventionally the contrast is achieved by using either a bright-field (BF) or dark-field (DF) contrast mechanism; this refers to the intensity of regions of vacuum in an experimental image achieved by putting an aperture in the diffraction plane. DF imaging, achieved by imaging only with a diffracted beam, is advantageous over BF imaging in that it enables us to differentiate particles from their low scattering support.[69]

Understanding atomic structure, including the precise positioning of atomic columns, is a very important aspect in understanding materials properties. High resolution TEM (HRTEM) has been an important tool for this, particularly when determining non-crystallographically symmetric structures.[29][42][43] In HRTEM the contrast is achieved by a slight defocusing of the image to cause coherent interference of the diffracted beams forming a phase contrast image. The amount and type of contrast is dependent on the oscillating contrast transfer function of the microscope; causing contrast inversions with thickness and lateral delocalisation[72] of the information in the image. This can make HRTEM

images almost impossible to interpret without the aid of extensive image simulation, such as multislice simulation,[73] carried out for a range of sample thicknesses and defoci.[25][45]

HRTEM image interpretation is complicated by its coherent nature making the contrast difficult to directly interpret. The contrast of the small metallic particles is strongly dependent upon the orientation of both the particle and the crystalline substrate;[70] therefore any misalignment could affect the information interpreted from the images. Secondly, there are often contrast inversions with sample thickness[71] which means the internal structure of a larger particle can become confused by atomic columns which switch between being bright (with the vacuum dark) or dark (with the vacuum bright) within the same image. With supported particles the information from the support and the nanoparticles will overlap producing Moiré type fringes which do not necessarily represent lattice information. Fuel cell nanoparticles are supported on a conducting and nominally amorphous carbon support, which should minimise this problem; however there will always be areas with graphitic fringes which complicates the image interpretation (see Figure 2.3).

HRTEM of metallic nanoparticles on geometrically simple supports makes differentiating between the support and the nanoparticle easier, due to the precise knowledge of where the support ends and nanoparticles begin.[74] Known as ‘model catalysts’ the support shape is well defined, for example MgO smoke produces atomically sharp cubes.[75] The problem with this approach is it takes the catalysts one step further from the real industrial application which we are trying to understand. This is especially important because particle-support

interactions are known to have an effect on both the nanoparticle structure and their resulting activity/selectivity.[76]

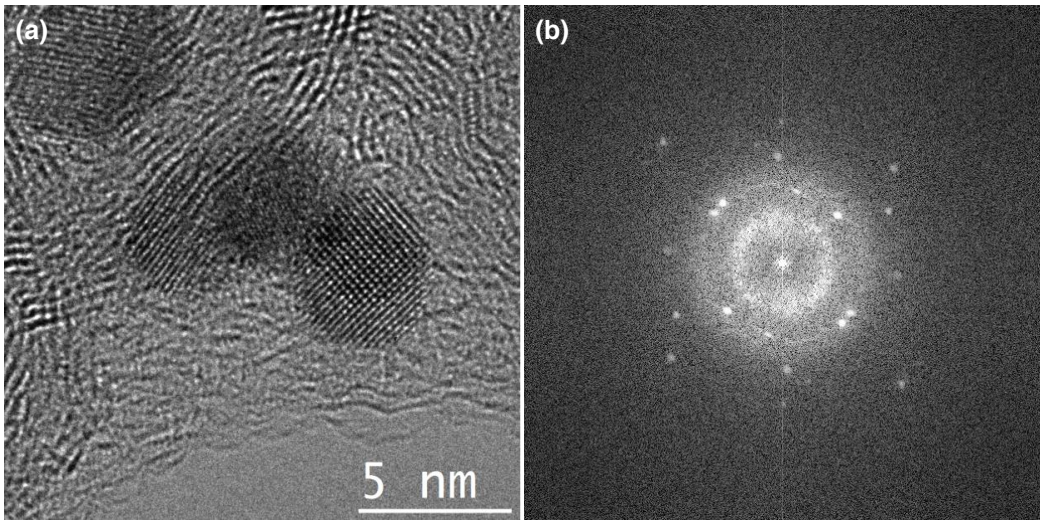


Figure 2.3 – Phase contrast HRTEM image of carbon support Pt(Pd) core-shell nanoparticles taken using a Jeol-ARM S/TEM (a) with the corresponding FFT (b). Lattice fringe information is present for the particles on or close to a low order zone-axis. However, this overlaps with the graphitic planes information from the carbon-black support, making it difficult to interpret. The image also provides no compositional information about the core-shell structure. Image taken by E. Okunishi.

Certain methods of filtering can be used to simplify the images, but should always be used with caution. For example, Bragg filtering can make column spots extend beyond where they were in the original particle due to enforcing the periodicity, which confuses the interpretation of particle structure. A specialised technique for improving HRTEM image resolution known as exit wave reconstruction uses a Weiner filter and a focal series of images to reconstruct the exit wave function of the sample (see Figure 2.4). Gontard et al.[47][48] demonstrated, on nanoparticles, the basic method for this reconstruction. This is a time consuming process which requires a clean damage-resistant sample for 20-30 images. The greater stability the sample has the better, because the

resolution is proportional to the square-root of the number of images combined to create the final reconstruction. Exit wave reconstruction should be carried out with care to make sure the reconstructed image does not contain processing artefacts absent from the original object.

TEM image acquisition is normally carried out using a charge-coupled device (CCD) camera. Careful error correction for the noise and the response of the CCD[79] should always be carried out prior to analysis.

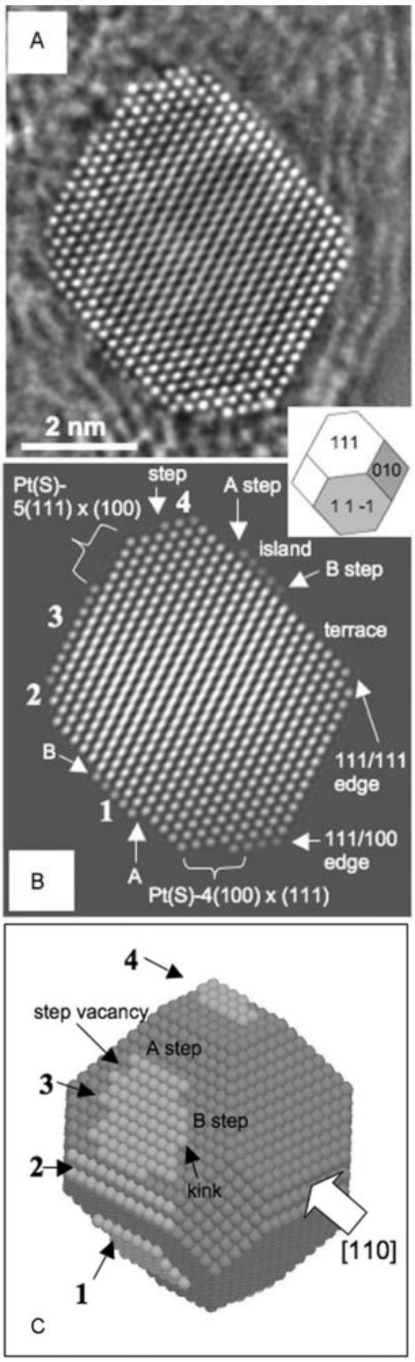


Figure 2.4 – a) A restored phase of an exit wave reconstruction of a 6nm Pt particle, obtained by applying spherical aberration correction and through-focus series of 20 images.[14] b) The best-fitting simulated phase. c) Three-dimensional atomic model used to calculate b). The inset shows the crystallographic details of the particle. In b) and c) the numbers correspond to the same surface features in each image. Published with permissions of the Wiley Co.

2.4.3. In-Situ Electron Microscopy

In-situ electron microscopy on catalysts is an expanding area of research, working towards bridging the gap between analysis conditions in a vacuum and the final operating pressures and temperatures for real catalytic reactions.[7,22] There are two main approaches, using either an in-situ cell in the sample holder or a specialised microscope referred to as an environmental TEM or E-TEM. Watching these dynamic processes in the real time requires either high temporal resolution or lethargic reaction kinetics. This is why most in-situ investigations are using TEM rather than a STEM to accelerate the image acquisition rate. Unfortunately this does severely restrict the extraction of compositional information from such data sets.

In-situ work has also been used to improve our understanding of the aging and degeneration of catalyst systems during use.[80] One vital point of debate for all in-situ work is trying to understand what effect the electron beam has on the dynamical processes being observed. Because of these restrictions and the focus of this project on bimetallic catalysts, in-situ microscopy will not be used.

2.5. Conclusions

In this chapter I have introduced PGMs as heterogeneous catalysts, and their major uses in catalytic converters and hydrogen fuel cells. There is a benefit of using small nanoparticles for increased surface area. However quantum confinement and size effects need to be understood and taken into account, because nanoparticle properties can vary considerably with particle size and shape. Novel geometries such as core-shell and de-alloyed particles have

shown considerable improvements to catalytic activity whilst also reducing the amount of the Pt loading.

The more traditional electrochemical and bulk averaging methods for characterising these catalysts are limited by the fact that they represent a statistical average of the whole sample. In contrast, electron microscopy has the potential to provide more local information which may lead to a greater understanding of the fundamental chemistry going on. HRTEM and in-situ microscopy are more specialised techniques which have been used to analyse catalysts but are more complex to interpret and are limited in terms of what compositional information can also be extracted. In contrast ADF STEM discussed in the next chapter allows for a multi-signal approach where several signals can be acquired in parallel.

3. SCANNING TRANSMISSION ELECTRON MICROSCOPY

Although some of the advantages of electron microscopy have been discussed in the previous chapter it is important that scanning transmission electron microscopy (STEM) is introduced in further detail as it is the key technique for this project. Whilst it does have the inherent problem of many other high resolution techniques that the particularly small area investigated may not be representational of the whole sample, it provides the local atomic scale information which is essential to really understanding catalysts at the length scale where reactions take place. In this chapter, I will introduce the key advantages and limitations of STEM for materials characterisation. I will also discuss some of the more recent advances and developments in the field of quantification, in both imaging and composition, to begin using the machine for accurate structural and compositional characterisation.

STEM is a process where pre-specimen lenses focus the beam into a small probe that is scanned in a raster pattern across the sample (see Figure 3.1). This is similar to SEM except that here one uses an electron transparent TEM thin foil, which significantly improves resolution because the thin specimen means beam-spreading scattering events are reduced. No post specimen lenses are necessary so a variety of, and indeed multiple, detectors can be used depending on the information sought.

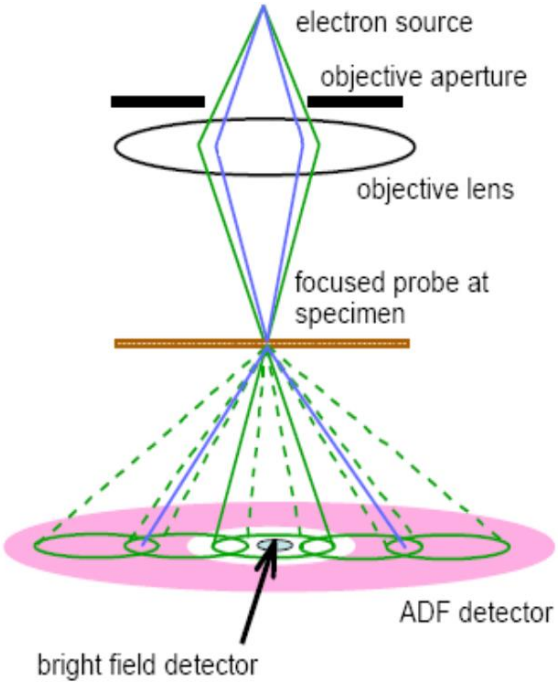


Figure 3.1 – Schematic of image formation in a STEM, showing the on-axis small bright-field detector and the larger annular dark-field detector, pink.

Since the technique's infancy,[81] high angle annular dark field (HAADF) STEM has been utilised for the study of catalysts due to the strong dependence of signal intensity on atomic number. This so called 'Z-contrast' has enabled differentiation of single heavy atoms from a lighter, even crystalline support well before atomic resolution was possible; as first demonstrated by Crewe[81] and later by Nellist and Pennycook[82] among others.

The incoherent image formation mechanism can be described by a convolution of the probe intensity profile, $P(\boldsymbol{r_0} - \boldsymbol{r})$, with a discrete object function sharply peaked at the projected atomic sites, $O(\boldsymbol{r})$ (see equation 3.1).[83] Where $\boldsymbol{r}$ is a two-dimensional position vector in the sample illuminated by the STEM probe located at $\boldsymbol{r_0}$.

$$I(\boldsymbol{r_0}) = \int P(\boldsymbol{r_0} - \boldsymbol{r}) O(\boldsymbol{r}) d^2\boldsymbol{r} \qquad 3.1.$$

The contrast of annular dark-field (ADF) images, so called for the annular detector used to collect the signal, can be manipulated by changing the range of detection angles collected.[39][57] This is normally carried out by using post specimen lenses to change an apparent camera length within the microscope column.

The maximum theoretical point resolution of un-corrected STEM images is controlled by the probe diameter, d; (equation 3.2), where C_s is the spherical aberration of the objective lens λ is the wavelength of the electrons used to form the probe. This is smaller than in TEM (where the pre-factor is ~0.66), suggesting that STEM imaging can surpass the information limit of conventional TEM.[85]

$$d \approx 0.43 C_s^{\frac{1}{4}} \lambda^{\frac{3}{4}} \qquad 3.2.$$

3.1. Variety of Signals

One of the major advantages of STEM is the ability to detect several signals in parallel whilst the probe is scanning. There are a variety of signals emitted by the sample due to excitation from the high energy electron probe (see Figure 3.2). Collecting several signals in parallel allows an even greater insight into the structure of a material without having to change any microscope settings. The use of several signals in parallel is particularly beneficial for beam sensitive samples which suffer from beam damage such that a subsequent image will probably not present the same sample structure, especially at atomic resolution.

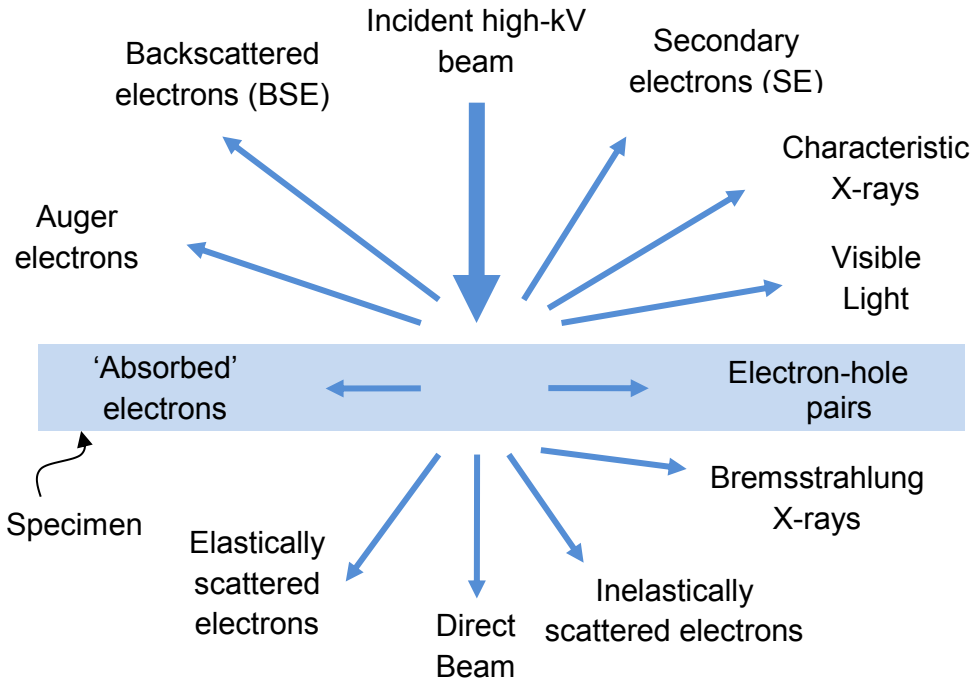


Figure 3.2 – Signals generated when a high-energy beam of electrons interacts with a thin specimen. The directions shown for each signal do not always represent the physical direction of the signal but indicate, in a relative manner, where the signal is the strongest or where it is detected. Image redrawn from Williams and Carter.[86]

3.1.1. Bright-Field STEM

A small on-axis detector with an outer collection angle typically less than 5mrad produces a bright-field STEM image. The origin of the image contrast is interference between overlapping Bragg disks (see Figure 3.1). Due to the theory of reciprocity bright-field STEM, with a convergent illumination and small on-axis detector, is analogous to bright-field HRTEM, with a small point source and a large detector collecting the resultant divergent beams. It also results in the same contrast inversions with defocus and thickness and the difficulties associated with image interpretation of a coherent signal.

Recently the idea of producing a more incoherent bright-field image by using an annular detector, referred to as annular bright-field (ABF) has been developed.

The theory is that ABF is more sensitive to lighter elements like oxygen or lithium.[87–89] Although origin of the image contrast is still a matter of debate so whether or not quantitative intensity information can be extracted is uncertain.

3.1.2. High Angle Annular Dark-Field and Z-Contrast

Using an annular detector to only collect the beams scattered to the higher scattering angles, typically larger than 80mrad, produces a coherency loss in the signal detected, resulting in a completely different image formation from HRTEM. Originally, Howie proposed[90] the cause of this coherency loss was due to thermal diffuse scattering (TDS) at larger detector angles becoming the more dominant scattering mechanism over elastic or Bragg scattering. However, it was later demonstrated[91] that a TDS model does not correctly explain the image formation because TDS calculations often neglect partial coherence along an atomic column and therefore only predicts an image intensity proportional to the number of atoms, *n*, within the column. Jesson and Pennycook[91] demonstrated that coherency involving scattering between atoms in different columns is not lost due to the high detector scattering angles, rather the integration over the large annular detector, and therefore a large range of scattering angles, is the cause of the coherency loss. This means that dynamical elastic diffraction for electrons scattered into the detector has no effect as it only redistributes intensity elsewhere in the detector, which is still integrated into the total collected signal.[30]

ADF STEM produces an image with atomic number sensitivity or Z-contrast following power law relationship Z^{α}, where α is between 1 and 2. This Z-contrast

results in heavy metal nanoparticles shining up brightly over the low atomic number carbon support (Figure 3.3). Research by Wang et al.[92] has shown that the value of α approaches 2, nearing the Z^2 relationship of Rutherford scattering, at larger inner detector collection angles (see Figure 3.4). This is, however, at a loss in the signal-to-noise ratio (SNR) of the images as the number of electrons, scattered out to such high angles, decreases rapidly.

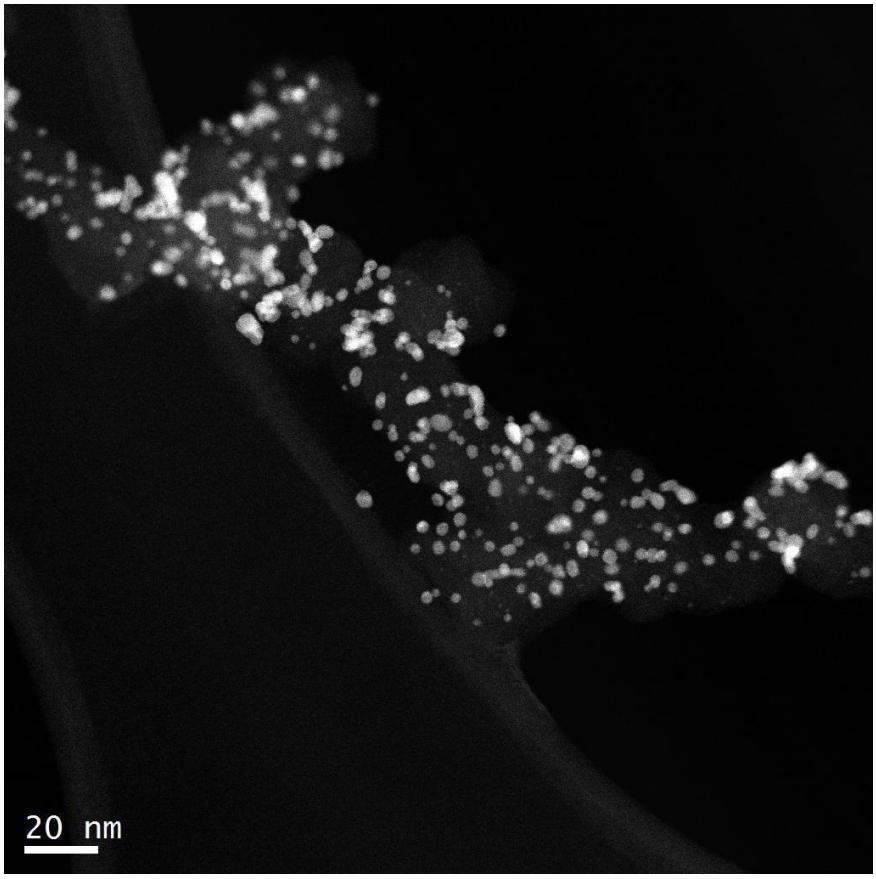


Figure 3.3 – Example low magnification image of Pt(Pd) core-shell catalyst nanoparticles on a carbon black support. Image was taken on a Jeol ARM.

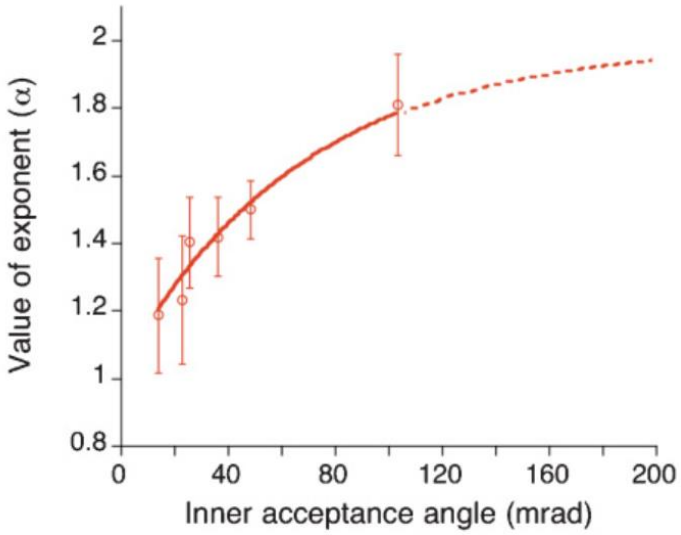


Figure 3.4 – Plot showing the value of the exponent α as a function of inner acceptance angle by assuming STEM intensity is proportional to Z^{α}. The dashed line represents extrapolation of the curve fitted to the data points. Reprinted with permission from [92] copyright (2011) by the American Physical Society.

3.1.3. Damage and Contamination

With all methods of characterisation we must consider if and how the technique itself might affect the structure of the material being investigated. This is particularly important when investigating nanoparticles, as the high surface area to volume ratio causes higher surface energy[93] and greater atomic mobility during imaging. The higher surface energy is thought to be responsible for the high catalytic activity witnessed in nanoparticles which is not present in the bulk material.[94]

In STEM, the main damage mechanisms for electron microscopy are:[5]

- Knock on damage due to atomic displacements caused by collision with the electron beam
- Radiolysis due to inter-band transitions from inelastic scattering resulting in bonding damage.

In catalyst nanoparticles this damage manifests itself in the following ways:

- Exit-surface sputtering; atoms provided with enough energy to be knocked away by the beam as it exits the sample.
- Surface mobility
- Drilling holes with a focused probe
- Beam induced heating

All these can cause distortion of the sample during imaging and analysis. Knock on damage and exit-surface sputtering often decrease with atomic number so should not affect the heavy nanoparticles as badly but could occur in the carbon support, destabilising the nanoparticle and making it rotate under the beam. In STEM one becomes more prone to drilling holes into the sample, particularly if the probe is left stationary for too long, which can occur during microanalysis, between image acquisitions and during tuning.

Egerton[95] has described the notion of damage limited resolution for different accelerating voltages (see Figure 3.5). For beam sensitive samples increasing the accelerating voltage and therefore decreasing the wavelength of the electron beam increases the rate of damage and so does not necessarily improve the imaging resolution.

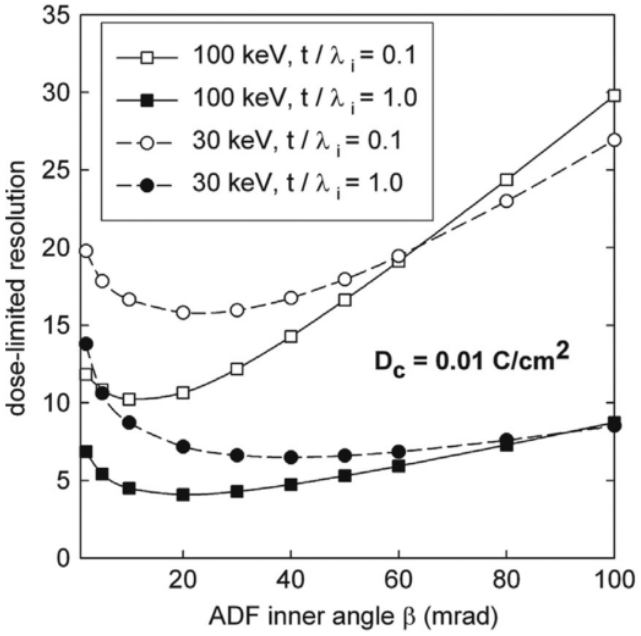


Figure 3.5 – Dose limited resolution (nm) for ADF STEM as a function of inner angle β of the detector, for accelerating voltages of 30kV and 100kv. t/λ is the sample thickness normalised by the total inelastic scattering mean free path. Republished with permissions from Elsevier BV.[95]

Contamination is a separate issue where mobile remnant hydrocarbons are cracked by the electron beam and deposited producing an amorphous layer of carbon covering the sample. This results in an increasing sample thickness the longer it is exposed to the electron beam, reducing image contrast and making quantification difficult. Recent work[96] has shown that contamination could well come from the carbon grids used to support the sample in addition to the sample itself (see Figure 3.6). Plasma cleaning reduces the contamination but there is obvious damage on the carbon film therefore vacuum baking is a safer approach.[96] This emphasises the need for cleanliness in order to maximise the accuracy of our quantification.

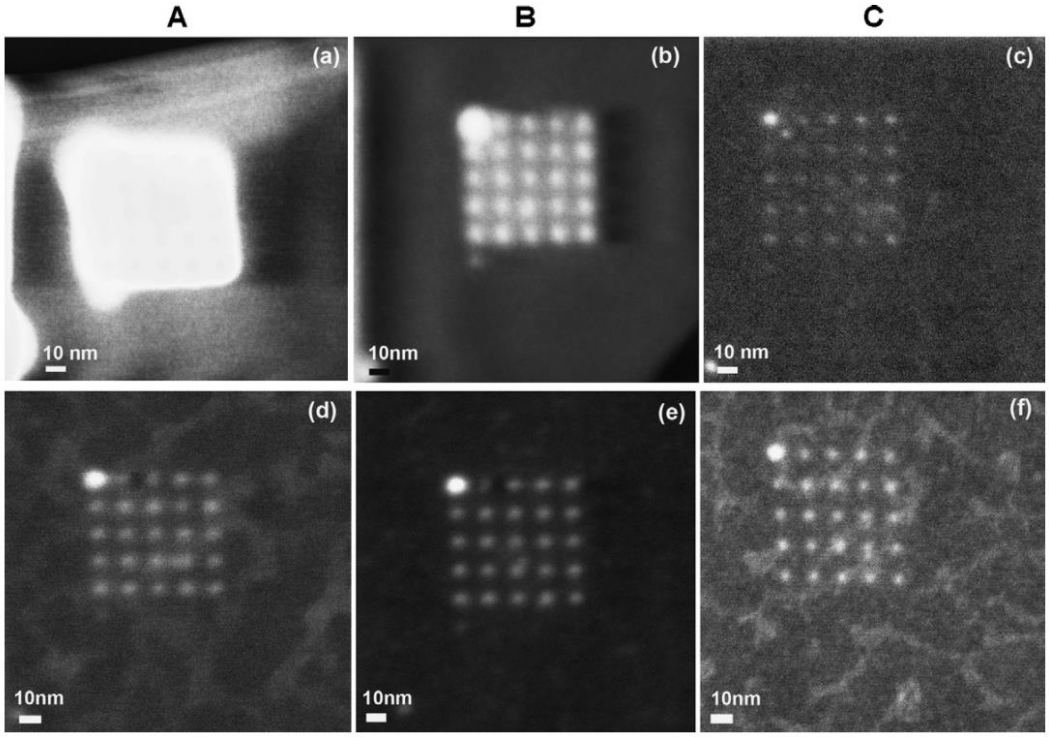


Figure 3.6 - STEM experiment of carbon films from supplier A, B and C before (a–c) and after (d–f) plasma cleaning. The STEM probe was positioned at each point of a 5 × 5 matrix for 2 s. The bright dots are where contamination has built up at the probe position. Republished with permission from Pergamon Press.[96]

3.2. Aberration Correction

Unlike optical lenses, electromagnetic lenses contain inherent aberrations that are unavoidable.[97] This idea was first proposed by Scherzer in 1936.[98] In early instrumentation (TEMs) resolution was improved by using higher accelerating voltages[68] in order to minimise the sample interaction volume, a process which inevitably had its own limitations due to high damage rates. The aberrations can be written as a Taylor series as a function of the probe convergence angle, α. This means that reduction of one aberration will only improve resolution until the point where the next coefficient in the series becomes the resolution limiting aberration.

When aberration correction is discussed it normally refers to correction of the positive spherical aberration often referred to as C_s, or C_3. This is where the rays furthest from the optic axis are over focused by the lens field (Figure 3.7). Initially this was combatted by using a so called high resolution or narrow gap pole piece with a much smaller C_s of 0.7mm. With these lenses STEM images of silicon (111) 1.92Å spacings were obtained by Xu using a 100kV uncorrected microscope.[99] However, the narrow gap produces large restrictions on specimen holders, including tilt ranges and in-situ cells, and limits the possible additional detectors for microanalysis, including EDX or Auger electrons.

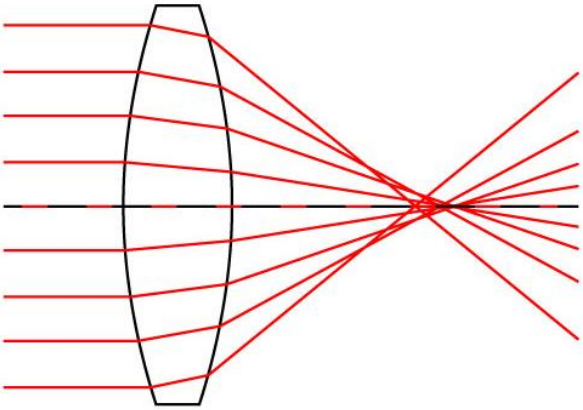


Figure 3.7 – Ray diagram demonstrating a lens with positive spherical aberration where electrons entering the lens further away from the optic axis are focused more strongly than those closer.

In the field of STEM the effect of aberration correction is even more significant despite being originally designed for TEMs. This is because in addition to the reduction in probe size there is an increase in the current density within this corrected probe (see Figure 3.8), causing an enhanced SNR during imaging and significant improvement in counts for microanalysis.

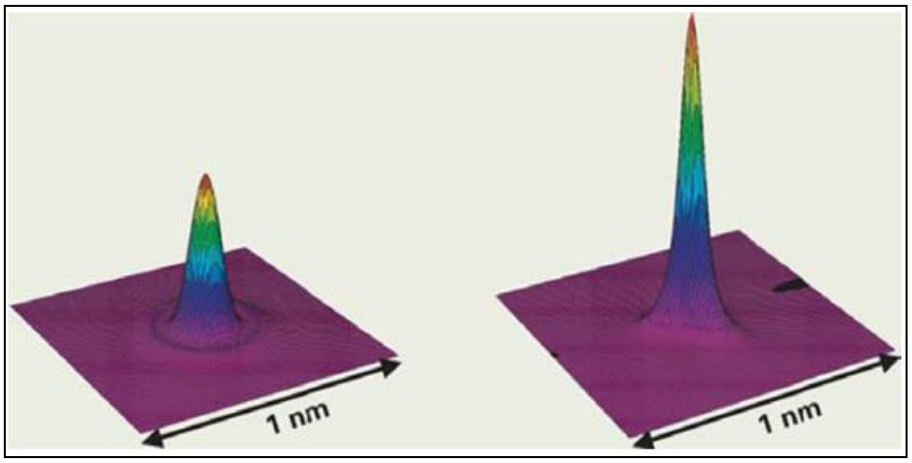


Figure 3.8 – The simulated intensity distributions of an electron probe of Lehigh University's JEOL 2200FS (S)TEM before (left) and after (right) C_s correction. Reprinted from reference.[100]

The principle behind C_s correctors is to produce a device with an associated negative C_s without introducing any other parasitic aberrations of their own, through using a series of non-round lenses. There are two types of commercially available correctors, both of which have been shown to demonstrate significant resolution improvement for HAADF STEM;[101] the hexapole corrector[102,103] and the quadrupole-octupole corrector.[101,104] In an uncorrected machine the best achievable point resolution is only 2Å, which is not small enough to isolate single atomic columns. In a corrected STEM point resolutions of 78pm are possible.

3.3. Three-Dimensional Information

A fundamental problem of (S)TEM is that images are a 2-dimensional (2D) projection of a 3-dimensional (3D) structure.[105] For catalyst samples in particular the surface structure, and therefore the 3D structure, is critical to understanding their activity and selectivity. Direct comparison with simulated

images is a powerful method for esmtimating 3D structures from experimental images; however, it requires a process of simulating a range of particle structures at range of tilts in order to achieve a direct comparison, which is painstaking and slow.[24]

3.3.1. Tomography

Electron tomography is a long established labour intensive technique developed from X-ray tomography[106] to combat the 2D representation issue. A 3D structure is reconstructed from a tilt series of images using one of a variety of possible reconstruction algorithms. It is important that the image intensities are a monotonic function of mass as the sample is tilted. In a lot of cases imaging of crystalline materials causes problems if the image series is obtained in bright-field mode due to Bragg reflected intensities destroying the monotonic relationship. The two most prevalent methods of reconstruction are the simultaneous iterative reconstruction technique (SIRT) and the weight back projection technique (WBP). SIRT begins as a back projection method based on '*filling'* a 3D Fourier space using a sufficiently large number of Fourier slices; once full an inverse transform reveals the full 3D structure in real space.[107] After the first reconstruction is complete it is forward projected in the same directions as the experimental tilt series of images. The difference images between each forward projection and the original image are combined into a difference reconstruction, which is added back onto the first 3D construction. Several iterations of this should then converge closer to the original object. The WBP takes into account the fact that the high frequencies are over sampled in reciprocal space in comparison to the lower frequency components, which is

why a weighting is incorporated to the back projection. The main requirement is for the micrographs to be *'true projections of the structure',*[108] and as such use of HRTEM is not desirable because Fresnel fringes and diffraction contrast are a significant problem.

Tomography was initially developed for biological samples, incorporating as much prior knowledge about symmetry of the object in order to minimise the computation.[91][93] An early demonstration of 3D characterisation of catalysts was carried out in The Netherlands by Koster et al.,[110] where it was used to study silver nanoparticles on a zeolite support but is regularly used to determine the location of particles on their supports.[111–115] In order to extract more quantitative information about surface structure and location of nanoparticles on the support it is important to segment each image into different materials through thresholding. This process requires automation of the thresholding process because carrying out the threshold adjustment based on visual inspection is likely to give different results each time.[115] Once the 3D shape has been reconstructed important information such as surface area, volume and thickness distributions can be measured for particles.[116]

The main limitation with tomography is trying to minimise artefacts from the reconstruction algorithm, in particular the 'missing wedge' problem, originating from the fact that the maximum tilt range achievable even with specialised holders is only up to ±70°, leaving a missing range of 40° where no experimental images can be acquired. The missing wedge results in a smearing or elongation in the wedge direction.[117] This can be reduced to a cone by taking series of tilt images around a perpendicular tilt axis. Another problem is the dose inflicted on the sample not just from acquiring several images, but also during both the tilting

and re-centring processes. A recent reconstruction technique called compressed sensing electron tomography (CS-ET) has been proposed based on utilising images in which only a limited number of pixels contain non-zero values. It has been shown to demonstrate improved reconstruction for fewer images,[118] which may provide the opportunity of reduced dose tomography.

3.3.1.1. Discrete Tomography

Discrete tomography is a technique where the number of projection images can be significantly decreased to less than 10 projections, even in the presence of noise or defects, through the use of 'prior knowledge'. The first reconstruction algorithm for discrete tomography is DART (discrete algebraic reconstruction technique) proposed by Batenburg and Sijbers.[119,120] This is based on modelling the reconstruction problem as a large system of linear equations where each material contributing to the object has a characteristic, approximately constant, grey level in the reconstruction.

Atomic resolution discrete tomography uses the following prior knowledge:[121]

- Atoms in the sample all lie on atomic lattice sites.
- There are no vacancies.
- The particle is spherical where the number and heights of edges should be minimised.

This is primarily carried out by defining each crystallographic point as a boxed region and then only one atom may lie within each box.

Van Aert et al. were the first group to publish atomic resolution discrete tomography data on their embedded silver nanoparticle[121] (Figure 3.9) and also the core of core-shell semi-conductor nanocrystals.[122] In their research they found that two or three quantified HAADF STEM images down crystallographic orientations (for example [100], [010] and [110]) was sufficient information to reconstruct the particle, provided you restrict the atoms to a particular, in this case FCC, crystalline structure. The method made use of their quantitative STEM method[123] by quantifying each image to estimate the number of atoms before carrying out a reconstruction. It is, however, important to note that both of the example particles used to demonstrate this method had been embedded in another material, thereby limiting the surface mobility and improving the dose tolerance for such reconstructions to be carried out.

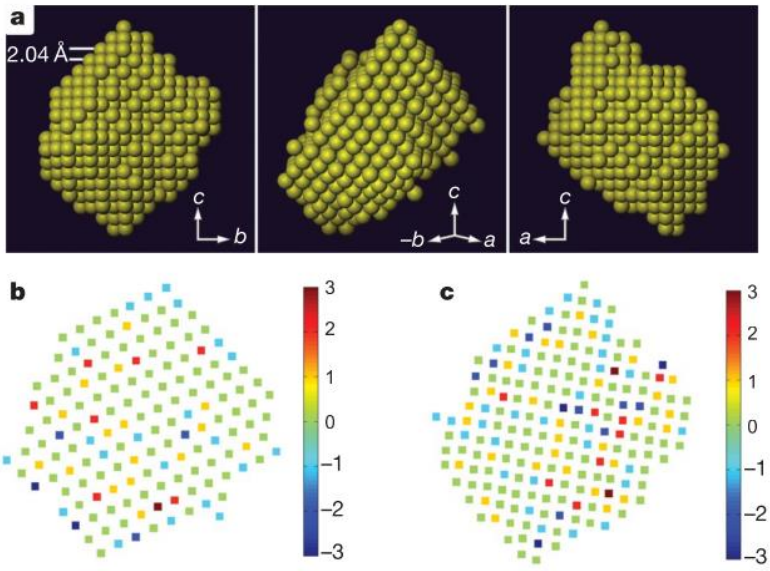


Figure 3.9 – (a) The computed 3D reconstruction of the Ag nanocluster viewed along three different directions. (b), (c), Difference between the computed atom counts for the reconstructed particle and the atom counts determined by the experiment in {110} (b) and {100} (c) zone-axis orientations. Reprinted by permission from Macmillan Publishers Ltd: Nature,[121] copyright (2011)

Achieving an atomic resolution 3D reconstruction is problematic for several reasons. Firstly, alignment of images to a common-axis with atomic scale precision is technically challenging.[124] Secondly, the conventional approach for aligning the images either relies on fiducial markers or cross-correlation between neighbouring atoms. Scott et al.[124] believe these approaches do not achieve atomic scale alignment accuracy which can be achieved through their centre of mass approach.

3.4. Composition Analysis

Due to the complications already discussed with analysing and quantifying either STEM or TEM images it is often useful to detect compositional information from the microscope, to gain additional insight into what is going on inside the material. Elemental analysis of catalyst particles began as early as 1983.[125] The advantage of using microanalysis in the electron microscope is the ability to achieve compositional information at the same length scale as the electron micrographs; a combination of both techniques together provides invaluable local micro-structural and compositional information of a sample. Here we will focus on the two analysis techniques which can be carried out within a TEM/STEM machine known as energy dispersive X-rays (EDX) and electron energy loss spectroscopy (EELS). Microanalysis is a region where STEM demonstrates advantages over TEM due to the focused probe providing localised information and the ability to collect ADF and microanalysis signals simultaneously.

Aberration correction has produced a significant advancement for microanalysis; particularly in the realms of 2D elemental mapping due to the significant increase in current density within the finer corrected probe (see Figure 3.8, page 40). This advancement does have its draw backs; for mapping in particular, one must be aware of the damage being caused by the long acquisition times in order to improve total counts.[126] For samples prone to beam damage this high current density is a problem. From the experience obtained during research for this thesis it has been found that this damage can be minimised by sequential fast scanning, where several fast acquisitions of a line scan or map are combined, to reduce the dwell time per pixel per scan while still maintaining the total live time necessary for high counts. Ideally sub-pixel scanning is also used so the beam is never stationary over the sample. It is unclear why such an approach yields lower damage unless the lower dose rate per pixel allows sufficient time for the charge or heat to dissipate away from the analysis region into the remainder of the sample. For signals like EELS, increasing the signal by increasing the number of sequential aquisitions also results in an increase of the contributions from shot noise.

3.4.1. Electron Energy Loss Spectroscopy

In EELS, the electrons from the primary beam which have lost energy through an interaction with electrons in the sample are separated by a magnetic field and can be plotted as an energy loss spectrum. They can then be used to map and/or quantify the distribution of different elements in the sample. The spectrum can be separated into two distinct regions; low loss and core loss. The former is the energy region where the electrons have induced plasmon oscillations and

single electron excitations, and is often used to estimate sample thickness and band-gaps in semi-conductors amongst other things.[127,128] The core loss region usually gives the compositional information in the form of ionization edges. These edges appear as a step jump in intensity above the uniformly decaying background at a specific minimum energy needed to expel an inner shell electron, making them element specific. If the fine structure of the edge is taken into account, more information can sometimes be gathered about the elemental oxidation state and bonding within the sample.[64,129]

The EELS drift tube entrance aperture lies on-axis in the electron column which means it replaces the bright-field detector. Therefore, only ADF images can be acquired simultaneously with EELS images.

Energy loss signals in the core loss region of the spectrum (>100eV) are sufficiently localised that the spatial resolution is limited only by the probe size,[130] making atomic resolution mapping possible. Cosgriff et al.[131] discuss that EELS has lower resolution than ADF STEM due to the delocalisation of the EELS interaction.

EELS normally provides higher spatial resolution than EDX due to the entrance aperture which limits contributions from electrons scattered to high angles resulting in a smaller effective interaction volume, where as X-rays suffer from the problem of fluorescence which can happen outside the interaction volume. The energy resolution is also significantly better (~1eV) than most EDX detectors (120-140eV). However the EELS count rate can be considerably lower for heavier elements[132] which have a much higher energy loss. Background subtraction, normally modelled as exponential decay, is non-trivial for heavy

metal absorption edges like Pt, often described as having maxima which are 'severely delayed'.[133]

3.4.2. Energy Dispersive X-ray Analysis

EDX analysis relies on the excitation and ejection of an inner shell electron within an atom in the sample. An outer shell electron fills the subsequent hole whilst emitting an X-ray of characteristic energy. Even without aberration correction Prestvik carried out some of the earliest investigations with STEM-EDX analysis of bimetallic nanoparticles where individual Pt-Re particles sized 0.5-2.5nm were imaged and the percentage Pt was plotted against particle size.[134]

EDX mapping has been used to demonstrate the localisation of sulphur on the nanoparticles in 'poisoned' catalysts.[126] In more recent years EDX of 5nm core-shell nanoparticles mapping has been able to differentiate the layered structure very effectively[132] however the atomic columns aren't resolved due to the trade-off between resolution and counts. Deepak et al.[132] did use multivariate statistical analysis[135] to improve their quantification, mining their data cube for independently varying parameters.

Atomic resolution EDX has recently been demonstrated on strontium-titanate, mapping both the strontium and titanium sub-lattices (see Figure 3.10).[136] This has only started to become possible through the development of the new generation of EDX detectors. These are ultrasensitive silicon drift detectors (SDDs) with much greater collection efficiency and often an improved solid angle of collection (up to 1.3 srad, whereas previous generation detectors only reach

up to 0.3srad solid angle); for example the FEI ChemiSTEM™. They give a significantly higher count rate allowing high resolution maps to be achieved at a more reasonable timescale. Tran et al. are among the first to apply these new detectors to nanoparticles,[137] allowing them to map their Cu-Au nanoparticles ranging 1-10nm in diameter. No comment or attempt is made towards quantification of the alloy ratio apart from establishing their particles as random alloys.

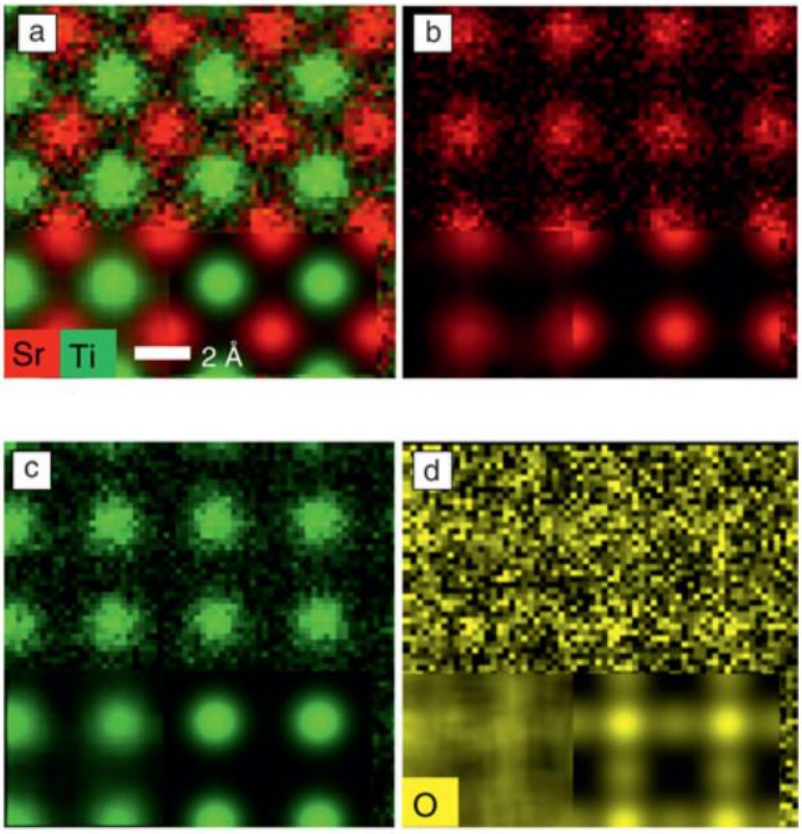


Figure 3.10 – Images demonstrating atomic resolution EDX mapping of Strontium Titanate. a)Composite Sr/Ti chemical map with an averaged map obtained from several such maps, inset at bottom left, and the simulation to the right of that; the top half of the map is the raw data from a single scan. b) The Sr(K- plus L-shell) contribution to a). c) The Ti K-shell contribution to a). d) O K-shell map with average and simulations inset as before. Republished with permissions from the Materials Research Society.[136]

3.5. Quantification of ADF Images

ADF STEM images are easy to interpret qualitatively due to the Z-contrast nature of the technique and the absence of any contrast inversions with thickness. The information they can provide when images are treated as data sets and analysed quantitatively is only just beginning to be explored.

In this section, I will examine previous and more current approaches to quantifying the intensity of ADF STEM images and some of the factors affecting their accuracy. In particular, asymmetries in the physical detector hardware and different image simulation approaches will be discussed.

The earliest attempts on quantification were by Retsky and Isaacson in the 1970s,[138,139] comparing the integrated intensity of heavy metal atoms, or small clusters, to those values calculated from first principle quantum mechanics. Work on small metallic clusters has often assumed the integrated HAADF intensity of a cluster scales linearly with the number of atoms it contains.[140,141] Therefore if the intensity of a single atom is known, dividing the total intensity of a cluster by this value yields the cluster size in atoms. The theory of this relative intensity approach relies on using a significantly large detector inner collection angle such that coherent effects can be neglected. However, it is overly simplistic to assume linearity and neglecting coherency effects in calculations is likely to cause significant errors for on-axis crystalline particles. Although it is an acceptable approximation for amorphous and off axis clusters where it can be assumed that no channelling is occurring.

Often what people mean by ‘quantification’ is a comparison with simulated images. Anderson et al.[142] scaled their simulated images to fit with experimental

data rather than acquire them on an absolute scale. Darji and Howie[133] have also discussed a necessity of correcting experimental data; in this case for additional scattering from a crystalline substrate, as they believed this was the origin of their mismatch between experiment and simulation.

3.5.1. Recent Advances in STEM Quantification

Whilst there have been a few quantification methods in the past, it is only more recently that is has been applied to directly analyse ADF intensity for extracting materials structure information.

A combination of sequential high resolution STEM images and multislice simulation has been successfully implemented by Ortalan et al.[143] on Ir-Rh clusters by using intensity ratios to predict possible combinations of Ir and Rh in each column. This procedure, however, was only possible due to the small size of the clusters investigated (containing a maximum of 3 atoms per column); at larger particle sizes with an exponential increase in the number of possible combinations this approach quickly becomes unrealistic.

LeBeau and Stemmer are generally acknowledged as the originators of a resurgence of interest in detector calibrations and recording images on an absolute intensity scale in 2008 (see Figure 3.11).[144] Their method relies on a full characterisation of microscope imaging parameters and detector response in order to achieve direct comparison with simulations,[145] although defocus has been fitted empirically from selecting the simulated image which fits most closely.

From a detector efficiency map like the one presented in Figure 3.11(b), the average pixel intensity in the active region can be considered to represent one hundred percent of the total electron beam, whilst the average intensity of the background region represents no-beam (also known as the black-level). Normalising experimental images using these maps results in images being scaled as a fraction of the incident beam which has been scattered out to the detector.

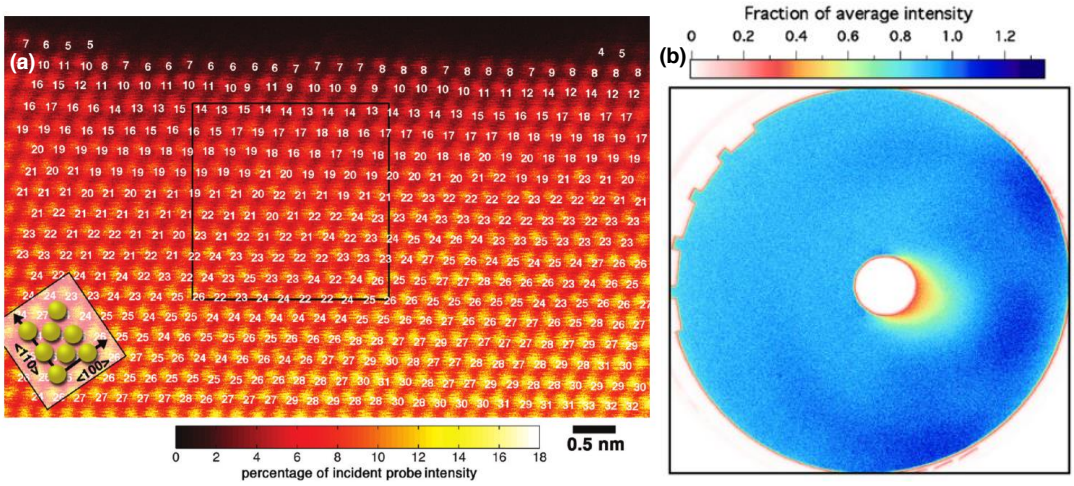


Figure 3.11 – a) One of the first ADF STEM images normalised to the incident beam. The sample is a gold wedge and the white numbers represent the assigned atom counts based on direct comparison with simulation. b) The associated detector efficiency map in units of fraction of the average intensity of the active region. Reprinted with permission from [146]. Copyright (2010) American Chemical Society.

An alternative technique to direct comparison with simulation is one based on statistical parameter estimation theory,[147] pioneered by Van Aert et al.[123] The theory relies on the inherently quantised nature of a histogram of integrated intensities from an experimental image. For a single element scenario, for example the silver particle in Figure 3.12, the integrated intensities should naturally be quantised in the histogram due to the fact that each column contains

an integer number of atoms. These discrete values become somewhat smeared by Poisson noise and other random errors; however, it should still be possible to decompose the histogram of all the integrated intensities into a series of Gaussian components, through statistical estimation and a maximum likelihood criterion. The critical component of this algorithm is a 'cost function' to minimise the total number of Gaussians incorporated, otherwise the best solution would be an infinite number of Gaussians. The Integrated Classification Likelihood (ICL) criterion is used for this purpose and provides a local minimum at the optimum number of components (Figure 3.12c). This method has also been used in combination with discrete tomography techniques to produce a 3-dimensional reconstruction of nanoparticles, as discussed in section 3.3.1.1 on page 43.[148]

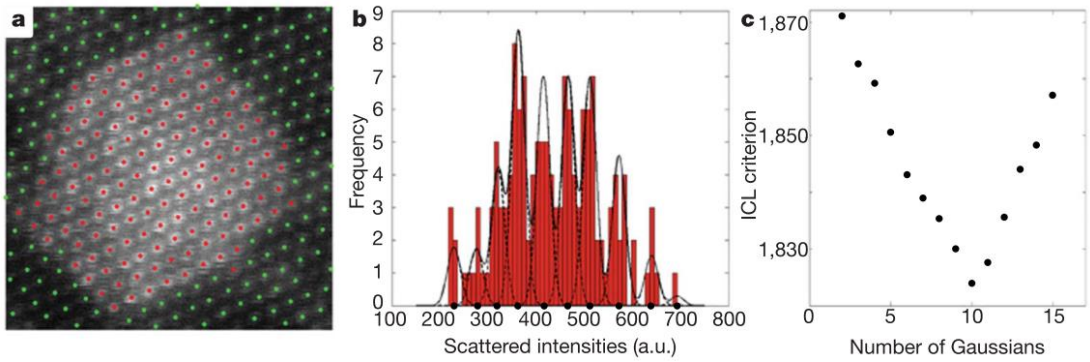


Figure 3.12 – a) Image of a silver nanoparticle embedded in an aluminium matrix, the dots represent the estimated position of the atomic columns with those assigned as silver marked in red. b) Histogram of the scattered intensities of the Ag columns. The black solid curve shows the estimated mixture model; the individual components are shown as dashed curves. c) The Integrated Classification Likelihood criterion evaluated as a function of the number of Gaussians in a mixture model. The minimum at 10 components represents the optimum number of components. Reprinted by permission from Macmillan Publishers Ltd: Nature,[121] copyright (2011).

The main advantage of ICL is that it doesn't require fitting to calibrated images. A systematic error or scaling can easily be incorporated, or alternatively it can be used as an independent method of atom counting. The limitations of the ICL approach have also been covered by Van Aert[149] and de Backer.[150] In particular the field of view and therefore the number of observations per Gaussian component greatly affects the ability of the ICL criterion to estimate the correct number of components. This is critical for investigations of nanomaterials where their finite size severely limits the number of observations available per component, but could potentially be overcome by combining several images for incorporation into the histogram.[151]

Katz-Boon et al.[152] used comparison with image simulations on non-atomic resolution of single element nanoparticles. They converted intensity profiles into thickness profiles to establish the 3D outer shape; aiming for speed of processing and simplicity over atomic resolution information. They also discuss their technique limitations, including the reliance on prior knowledge of specimen composition and crystal structure, making it unsuitable for my materials system where the elemental ratio is one of the parameters to be investigated.

The challenge facing quantification of bimetallic systems is how to incorporate additional information or assumptions in order to separate out the thickness and composition contributions to the ADF STEM signal. Hernández-Maldonado et al.[153] demonstrated a quantification approach relying on carefully controlled standards where the average intensity of a unit cell is used to calibrate the sample thickness, before estimating composition of individual atomic columns using a linear interpolation. Rosenauer et al. use a section of sample with known composition to interpolate the thickness where composition is unknown.[154,155]

This technique is rather limited to the semiconductor multilayer systems for which it was designed, where areas of known composition are present in the same image.

3.5.2. Detector Calibrations

Commercially available ADF detectors consist of a scintillator, a glass light pipe and a photomultiplier tube (PMT). The scintillator is normally either a powder Y_2SiO_5 doped with Ce, a single crystal made of yttrium aluminium garnet (YAG) or, more commonly, yttrium aluminium perovskite (YAP). Electrons hitting the scintillator are converted into a photon cascade. The photons are directed to a PMT through the light pipe and converted into an electrical signal. A constant voltage (DC offset) may be added by a preamplifier, controlling the 'brightness' in the final image. The output is digitized by an analogue to digital converter providing the varying 'contrast' in the final image.

When aiming for a truly quantitative comparison with simulations it is important to map and understand the detector efficiency, as most simulation software packages normally assume a perfect detector, modelled by a uniform efficiency mask.

3.5.2.1. Detector Mapping

In order to calibrate the STEM image intensity to fractions of the incident beam it is essential to map the exact efficiency of the detector being used in the microscope. There are two possible methods for mapping the efficiency of an

ADF detector. The first and more common method relies on using a confocal arrangement, referred to as STEM 'alignment' mode. The post specimen lenses are adjusted to translate an image of the probe at the specimen plane onto the detector plane (see Figure 3.13c). This produces a fine convergent beam which can be scanned over the detector; recording the detector output with respect to probe position provides a map of the detector efficiency (see Figure 3.11b). The gain and DC offset of the map are optimised from the detector map such that the maximum range of signal is achieved without saturating the detector or clipping any of the black level in the vacuum.[144]

The second method relies on forming a small parallel pencil beam illumination; scanning this beam across the front focal-plane of the objective lens produces a tilting of the beam through angle space (see Figure 3.13b). This approach has been widely used on VG machines; it is necessary because they are dedicated STEMs rather than (S)TEMs and so do not possess the post specimen lenses for the confocal method. The earliest published map can be found by Singhal et al.,[141] demonstrating their limited range of scanning motion such that the field of view is too small to investigate the whole detector.

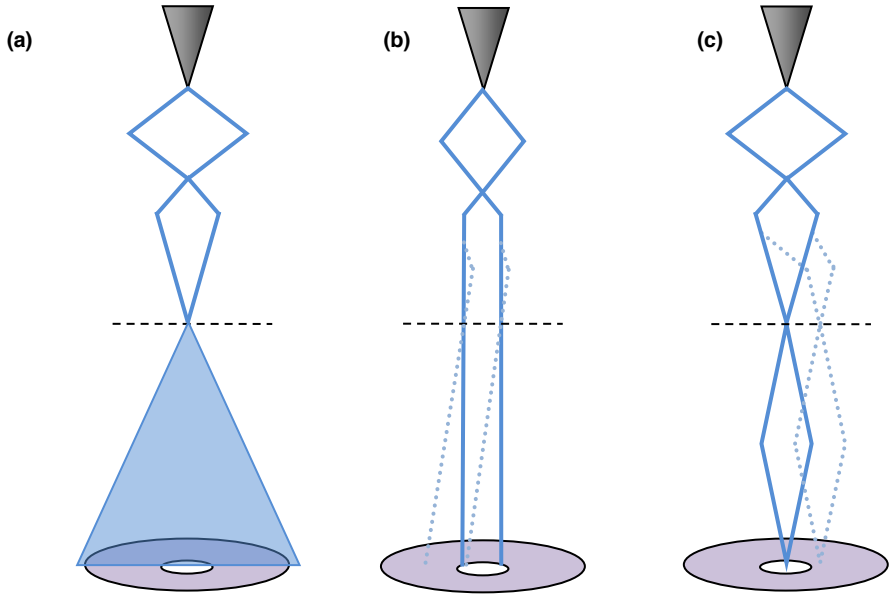


Figure 3.13 – (a) Ray diagram of a STEM with the electron flux seen by the detector due to scattering from the sample. (b) Swung pencil beam lens arrangement for mapping the detector in angle space. (c) Scanning confocal geometry where the image of the probe at the specimen plane is transferred to the detector plane.

The pencil beam method of detector scanning provides a more realistic map in angle space where the beam is travelling tilted from the specimen plane. This is more comparable to the experimental set up and diffuse electron flux 'seen' by the detector and post specimen lenses (Figure 3.13a). This is because of how the beam passes through the post specimen optics. The convergence angle of a typical STEM probe is around 20mrad, whereas the angle of scattering out to the detector can be up to 10x that. These scattered electrons will interact with post specimen lenses at a very large tilted angle, making it beneficial to map the detector in angle space, as in the pencil beam method. Mapping through angle space provides us with information about the detector collection efficiency and how the beam interacts with the post specimen lenses before it reaches the detector, whereas in the confocal method the beam will pass vertically through

all the post specimen optics, making it interact differently compared to the scattered electrons.

The confocal method, however, appears to be more widely used, with the pencil beam being limited to dedicated STEMs. There is also a limitation with how far the scanning coils are able to reach through the pencil beam arrangement, see the UltraSTEM map in Table 4.1, on page 83.

Once the detector efficiency is mapped it is important to be aware of the linearity of the detector response.[144,156] In particular, altering the detector contrast does not produce a linear variation[157] in the detector signal, which is why contrast and brightness settings should be kept constant between detector mapping and experimental images.

We must also be aware of how linearly the detected signal varies with the number of incident electrons. Care should be taken to not rely too heavily on this linearity alone. During experimental image aquisition the detector will see a diffuse electron flux at a much lower intensity, whereas during detector mapping the whole beam is scanned over it in a fine probe. To combat this it is prudent to drop the probe current by a known amount during the detector mapping, and subsequently incorporate a ratio of the probe currents into the quantification method. This method also helps to minimise damage to the detector and makes a greater contrast range available in the final experimental image, which is particularly useful for nanoparticle imaging or other low dimensional materials.

3.5.2.2. Flux Weighting

Working from the premise that real detectors are asymmetric in their collection efficiency[158,159] there needs to be a way to compensate for this to improve matching with simulations. Rosenauer et al.[156] use a 2D profile estimate of their detector asymmetry to simulated images with an asymmetric detector; however this approach is only possible with certain simulation packages. The flux weighting method developed by Martinez et al.[160] aims to improve the detector normalisation by accommodating for this asymmetry in the experimental images rather than adjusting the simulations.

The flux distribution hitting the ADF detector can be described by a power law variation with scattering angle.[160] Determining the exponent value of this power law can be done using a camera length series or azimuthally averaging a position averaged convergent beam electron diffraction (PACBED) pattern.[161,162] The detector map can be calibrated in angle space by knowing the inner angle used experimentally. The active area of the detector is selected and used as a binary mask, which corresponds to the detector response; using the knowledge of the flux cut-off the active region can be separated into the regions illuminated and not illuminated (see Figure 3.14b). The azimuthally averaged flux can be calculated within the masked region (see Figure 3.14c), which is multiplied pixel wise with the detector map resulting in Figure 3.14d. The average counts in the active region can now be determined from this new map and used to calculate a detector gain which takes into account the flux cut off and detector asymmetry.

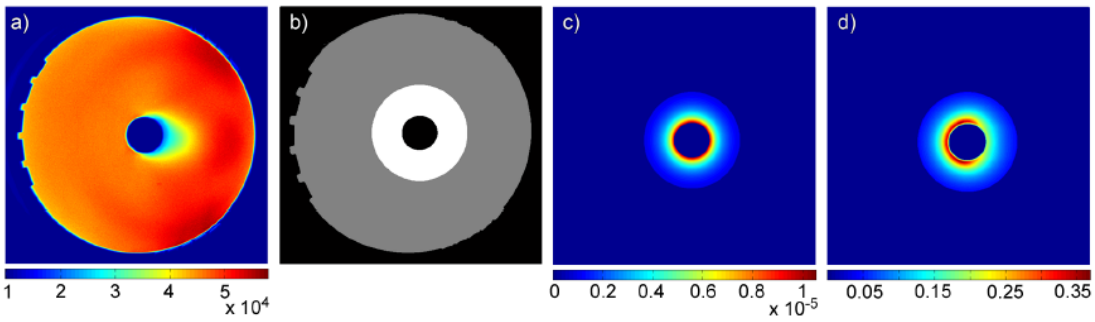


Figure 3.14 – Scattered electron flux weighted method. a) Map of ADF detector. b) ADF detector active area used as a binary mask (white region). The grey region corresponds to the area of detector that is inactive for this camera-length. c) Modelled scattered electron flux using power-law function obtained from PACBED or CL series reaching the active area of the detector, defined by the binary mask. d) Scattered electron flux weighted by the ADF detector inhomogeneous response.

3.5.3. Channelling

For direct interpretation of images and accurate quantification, on a column by column basis, cleanly resolved atomic resolution images are required. This necessitates viewing the sample down a low order zone-axis.[163] When atoms are aligned in this way, parallel to the incident electron probe, they provide a small lensing and therefore focusing effect on the beam[164] (see Figure 3.2). The subsequent atoms in the atomic column then experience a more focused probe than the first atom and so on, resulting in scattering to the detector that initially increases faster than linearly with respect to the number of atoms (see Figure 5.17, on page 124). Therefore the contribution of the second atom in a column to the total scattering cross section or integrated intensity of the column is larger than the contribution of the first, and so on. Along a longer column, oscillations in intensity are seen[165] and the process is often referred to as channelling. TDS simultaneously leads to a reduction in the electron intensity along a column which is often referred to as absorption. Channelling has considerable implications for ADF STEM. Heavier atoms provide a stronger

lensing effect than lighter atoms, which means that in columns containing a mixture of atom types the specific sequence of the atoms in the column will affect the resulting intensity scattered out to the detector.[166]

In certain circumstances channelling can be exploited to expose subtle sample changes; for example it has been used advantageously to map the height of dopant atoms within an atomic column based on their contribution to the image intensity.[162,167–169]

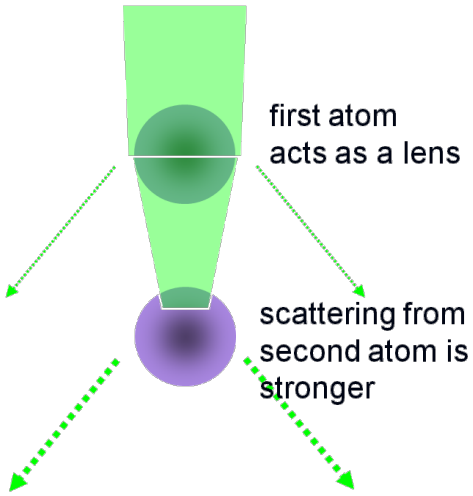


Figure 3.15 – Schematic of how a column of atoms focuses the STEM probe producing a stronger scattering and therefore a higher intensity than the atoms would produce individually.

3.5.4. Image Simulation Techniques

The nature of transmission microscopy means that for a thin sample it can be thought of as viewing a 2D projection of a 3D object. However, due to dynamical scattering effects careful simulation should be carried out for correct image interpretation, particularly when quantitative information is sought. Channelling

results in a non-linear variation of the intensity or cross section with sample thickness necessitating the simulation of images for accurate quantification.

There are two main approaches to image simulations, Bloch wave and multislice, both of which are solutions to the Schrodinger equation and are equivalent given the right conditions,[170] although there are a variety of ways to implement them, as discussed below.

3.5.4.1. Bloch Waves

The Bloch wave method[171,172] first proposed by Bethe in 1928 describes a wave-function of multiply scattered electrons by 3D Bloch waves. For HAADF intensity[171] the integrated convergent beam diffraction intensity needs to be evaluated over the annular detector for each probe. The Bloch wave approach is hugely computationally intensive for anything that is not a perfect crystal with a small unit cell where boundary conditions can be applied. This is because it involves inverting large matrices, which was reduced somewhat by Watanabe et al.[173] but not completely solved, making this method unfavourable for construction of large batches of simulation libraries.

3.5.4.2. Multislice

Multislice calculation is an invaluable tool for HRTEM and STEM as it provides a reduced computational time when looking at defects.[174] A crystal is sliced perpendicular to the beam direction, such that each slice is thin enough (typically 2-5Å) to allow being approximated as a weak phase object. An atomic potential is then used to describe each slice. The phase change due to electrons

interacting with this atomic potential is calculated and it is assumed the waves propagate freely through space before being incident on the next slice.

3.5.4.3. Absorptive Potential

Once the wave function in the crystal has been described by either Bloch waves or multislice[175] the interaction with the electron beam needs to be understood. For STEM imaging we need to understand the scattering at higher angles. The atoms in the sample are not stationary at any reasonable imaging temperature which results in a dampening of the Bragg scattering. The more dominating scattering at these high angles is more diffuse due to atomic vibrations and is referred to as thermal diffuse scattering or TDS. Absorptive potential (AP) derives its name from its origins in HRTEM image simulations,[176] where any TDS electrons are scattered to such high angles that they do not reach the detector and as such are considered to be absorbed by the sample. AP is the least computationally intensive and therefore fastest simulation method, first modified by Pennycook and Jesson for STEM simulations.[83] The absorption potential of each slice $V'(\boldsymbol{R})$ directs the electron density in the elastic part of the wave function into the inelastic channel.[176] TDS makes an important contribution to adsorption, particularly for elements of high atomic number.[176]

The primary problem with this method lies in the fact that once the wave function has been moved from the elastic channel to the inelastic channel it is essentially lost to the calculation. This means that any subsequent scattering of inelastically scattered electrons is not considered. The elastic wave can be propagated to the detector and added to the inelastic part. This can cause accuracy problems if

they are not combined correctly (see Section 4.5.2, page 90). During comparison between simulation codes it has become clear that the elastic and inelastic signals are not recombined correctly, making it not ideal for simulations at lower detector collection angles.

3.5.4.4. Frozen-Phonon

The frozen-phonon (FP) model was first proposed by Loane et al.[175] as a semi-classical approach for modelling the thermally diffuse scattering (TDS) from a crystal. It was modified for the simulation of ADF STEM by Earl Kirkland.[177] This was done by estimating that each electron will 'see' a different lattice with the atomic positions deviating by small random amounts from the perfect crystallographic configuration due to thermal vibration. Each electron will only see a frozen lattice because the interaction time is significantly shorter than the vibrating speed of the atoms. The final image intensity is produced by averaging over several configurations of atomic thermal displacements. The FP approach can only be applied with the multislice method for wave functions.

The quantum excitation of phonons (QEP)[178] model provides overall results numerically equivalent to the FP approach but provides different physical insights and allows both elastic and inelastic phonon scattering to be separated at a cost of requiring more computational power. The time independent Schrodinger equation is solved parametrically for displacements of crystal atoms. A Monte-Carlo integration is computed to obtain the elastic and total electron intensities, the inelastic is simply the difference between the two, in the same detector plane.

3.6. Quantification of EDX

Silicon drift detectors (SDDs)[179,180] have opened up a new era in microanalysis at the nanometre and even sub-nanometre scales. The improved detector design allows for larger devices and therefore increased solid angles for X-ray collection. They are also often windowless which allows them to be located closer to the sample thereby increasing the solid angle. Paired with their improved detection efficiency SDDs provide a significant improvement in X-ray count rates such that atomic resolution maps[136,181–183] and X-ray tomography[184] are both now possible. In addition, aberration correction in STEM[101,104] allows larger probe forming apertures to produce increased beam currents in much smaller probes.[100] The combined result provides huge improvements in X-ray counts leading to the potential for improved quantitative analysis.

EDX analysis provides element specific information which, if quantified, can be converted to accurate composition values. The EDX signal has significantly worse SNR than ADF but the elemental information is more readily separable. Quantification must take into account both X-ray absorption and subsequent re-fluorescence. This requires knowledge of, or estimation of, local thickness and density (although this can be neglected for thin specimens such as nanoparticles). The detector geometry and detection efficiency must also be included in quantification calculations, including both the solid collection angle and the take-off angle.

3.6.1. K-Factor

The original ratio approach to EDX quantification in TEM thin films was first proposed by Cliff and Lorimer nearly forty years ago.[185] The Cliff-Lorimer or k-factor relates the atomic fraction, C, of constituent elements to the measured X-ray intensities, I.

$$\frac{C_A}{C_B} = k_{AB}\frac{I_A}{I_B} \qquad 4.1.$$

In the technique's infancy a ratio approach was essential due to the mechanical and electrical instabilities present in the early analytical electron microscopes and therefore the low X-ray counts detected. Electron microscope capabilities are now considerably improved, especially the beam current stability. Despite this the k-factor approach remains the primary method for EDX quantification due to its incorporation into the majority of the commercial analysis software. Most EDX software often allows a quantification option, however this is a rather 'black box' approach meaning it does not necessarily make clear what exact method of quantification is being used. They rarely provide parameters for the user to vary and optimise; including peak selection, background subtraction and integration region.

K-factors are dependent on accelerating voltage and the TEM EDS system. They can be calculated from first principle quantum mechanics; these theoretical k-factors have a minimum estimated error of around 10%[186] but could contain a significant systematic error of up to 20%.[187] The only way to reduce such an error is to calculate an experimental k-factor using multiple samples with accurately known composition and thickness. A standards approach to EDX

quantification involves selecting known samples with very similar density and thickness at a range of compositions to create a calibration curve and therefore an experimental k-factor (~±1% error is achievable). Unfortunately this is time consuming and there is an inherent difficulty in manufacturing such samples where the composition is homogenous on the nanoscale and corresponds to the macroscopic chemical composition determined by other methods.

3.6.2. ζ-Factor

A more recent alternative to the k-factor approach is the ζ(zeta)-factor method first proposed in 1996 by Watanabe et al.[188] Designed for thin film specimens it makes use of pure element standards which are rather more readily available than the alloy alternatives. Modified ten years later by Watanabe and Williams[187] to include a normalisation by dose, ζ_x is the factor connecting I_x , the raw X-ray counts, to ρt, the total density multiplied by sample thickness. C_x is the weight fraction of x, with a similar relationship holding independently for other elements in the system.

The primary advantage of this approach over the more traditional k-factor is its applicability to use of pure element standards. It assumes that the characteristic X-ray intensity from element A, I_A, is proportional to the mass-thickness of the sample. This holds well as long as X-ray absorption and fluorescence are negligible, which is the case for thin specimens; for thicker specimens an absorption correction could be incorporated.[100]

$$\rho t = \zeta_x \frac{I_x}{C_x D_e} \qquad 4.2.$$

$$D_e = N_e i_p \tau \quad 4.3.$$

D_e is the total number of electrons seen by the sample during acquisitions defined in terms of N_e, the number of electrons in a unit electric charge (or $1/e$), the probe current, i_p, and the acquisition time, τ .The ζ-factor, therefore, is independent of acquisition time, beam current, composition and mass-thickness providing it with units of kg.electron/(m^2.photon). However, there is still a dependence on the illumination area such that careful knowledge of the probe size and the magnification will need to be taken into account.

It is vital to know the beam current at the time of analysis by a direct measurement (e.g. Faraday cup) in order to calculate the dose. In a binary system with $C_A+C_B=1$ the compositions can then be written as:

$$C_A = \frac{\zeta_A I_A}{\zeta_A I_A + \zeta_B I_B} \quad 4.4.$$

$$C_B = \frac{\zeta_B I_B}{\zeta_A I_A + \zeta_B I_B} \quad 4.5.$$

$$\rho t = \zeta_A I_A + \zeta_B I_B \quad 4.6.$$

Whilst this method may seem less trivial as it requires thickness calibration and current measurements it does have the significant advantage that pure element thin films can be used as standards,[189] which are often more routinely available. This method can prove more accurate than the k-factor method and is an absolute value rather than a ratio based on other elements within the system. It can also be used as a method of instrumentation comparison, to evaluate which microscopes have better analytical capabilities.

3.6.3. Accuracy Limitations

The key problem with STEM EDX of nanoparticles[33,190,191] is the limited count rate because of the small number of atoms excited. For example, in early maps produced by Lyman et al.[33] in 1987 the number of counts from a background area pixel was 7 whilst the maximum number of counts from a Pd pixel was only 36. The problem with EDX is finding the balance between high beam currents for improved analytical resolution which increases the probe diameter, or keeping the probe diameter small for improved spatial resolution but which results in poor counting statistics. E et al.[192] confirmed that the limiting factor for EDX of nanoparticles will be in achieving high enough counts of characteristic X-rays (Figure 3.16) with such a beam sensitive sample. A low number of counts produces poor statistics, making quantification estimates significantly less reliable.

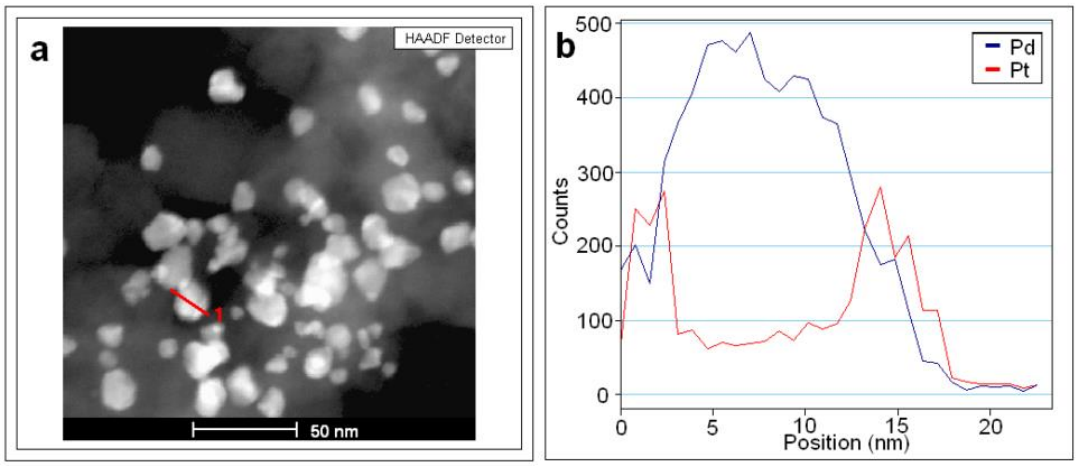


Figure 3.16 - a) HAADF image of a cluster of nanoparticles, b) EDX line profile taken across and nanoparticle, showing clear core-shell structure. Reproduced from E et al.[192]

Another fundamental limitation for accurate STEM EDX quantification is absorption of X-ray photons before they are able to escape the sample. This absorption rate varies between elements, so results in an error in the quantification results. Work by Watanabe and Williams[187] has demonstrated the effect both the sample thickness and X-ray line selection have on EDX quantification. Figure 3.17 shows the critical thickness for 5% absorption for the K, L and M lines. For the very small sample thicknesses of nanoparticles any K or L lines will provide sufficient quantification accuracy; however the M-lines may still provide small absorption errors and should therefore be avoided where possible. For elements with an atomic number lower than 30, quantification should only be carried out with the K-lines as the L-lines also begin to drop below the safe limit. Often the degree of absorption occurring within the sample can be estimated through the K-line to L-line height ratios because the L-lines begin to be absorbed much sooner, thereby changing the peak height ratios.

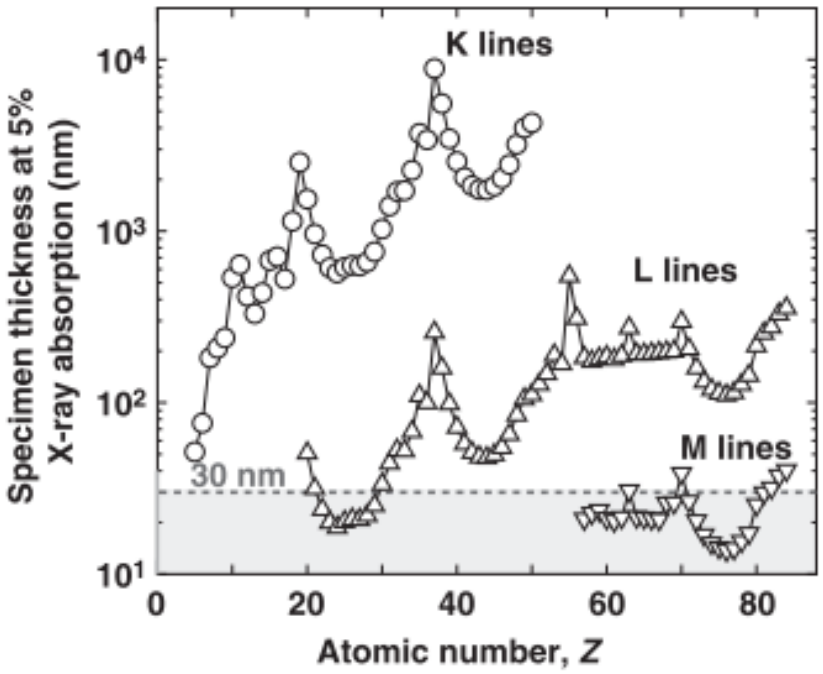


Figure 3.17 – The critical specimen thickness at 5% X-ray absorption in pure element thin films. The shadow area indicates specimen thickness range below 30nm. The critical thicknesses at the 5% absorption for all the K-lines and most of the L-lines above Zn (Z=30) are higher than the 30nm. Copyright © 2006 Wiley Co. Republished with permissions from Watanabe and Williams. [187]

3.7. Conclusions

ADF STEM is a powerful tool for understanding materials at the atomic scale, particularly due to the Z-contrast nature of the ADF images and the potential of acquiring several different signals in parallel. In this chapter, I have discussed the key advances in characterisation of nanoparticles and the technique developments which have led to them.

Aberration correction brings higher beam currents in smaller probes which drastically improves the potential for EDX high resolution analysis and quantification. Combining this with the new generation of improved SDDs there is now real potential for improved quantification.

ADF STEM quantification has progressed from the assumption of intensity scaling linearly with the numbers of atoms a cluster contains. More recently there has been a great deal of comparison with simulations for atom counting and composition investigation of on-axis samples. The first attempt at calculating scattering cross sections from ADF STEM intensity was back in the 1970s with much worse resolution. Now with aberration correction we have the potential for calculating the cross section of individual atomic columns.

4. METHODS FOR ADF QUANTIFICATION

In this chapter, I will outline the methodologies used for sample preparation and the microscope calibrations. As previous quantification analysis has shown, accurate calibration is essential. Although this becomes less critical when using scattering cross sections, certain parameters like the detector collection angles and the uniformity of its response will still affect the recorded intensity and therefore the quantification results.

From this point on I will use the scattering cross section for our quantification method and comparison with image simulation rather than peaks or integrated intensities. It is a more robust measure for such a comparison and is a fundamental basis of this thesis. The mathematical definition of cross sections can be found in Section 5.1 on page 99, where the measure is discussed and analysed in more detail.

In the second half of this chapter I will look at the accuracy of the simulation software itself. Any quantification results are critically dependent on the accuracy of the simulations used for comparison. It is therefore important to optimise simulations to ensure complete convergence and to make sure no artefacts are being introduced. Additionally, it is important to compare simulation codes, ensuring that matching simulation input parameters result in matching scattering cross section outputs.

4.1. Sample Preparation

A selection of industrially relevant fuel cell catalysts were prepared using wet chemistry methods by Johnson Matthey and supplied on a carbon black support. The elements were deposited on a support in a salt form and then calcined until coagulated into a nanoparticle distribution. The samples cover the range of novel catalyst geometries discussed.

- Pure Pt - 40wt% Pt on Ketgen.[6]
- Pt/Ir mixed alloy – Approximately 16.7% Pt with average particle size of 2.6nm.
- Pt/Co – Approximately 75% Pt before acid leaching. Both leached and un-leached particles were examined.
- Pt(Pd) core-shell – 2monolayer Pt on core of Pd with core size approximately 6nm.

For the alloy particles both elements were co-deposited onto the carbon support and treated to form alloy particles on the carbon. Acid leaching is applied afterwards to remove some of the surface Co and provide Pt enrichment. For the core-shell geometry Pd nanoparticles were deposited and their surface functionalised with hydrogen which the Pt atoms supplied in the form of another salt then attach to.

Taking into account the wet chemistry processing route used to synthesis the nanoparticles, a critical factor in the sample preparation for electron microscopy is to minimise the amount of contaminates present before putting the sample into the microscope. As such the grids (copper 300 mesh with an amorphous

[6] A highly conductive brand name carbon black support.

holey carbon film) were all vacuum baked at 80°C for two hours, prior to deposition of the catalyst as they are known to be covered with solvents from the manufacturing process.[96]

All samples were received on a carbon black support ground into a powder. Further dry grinding was carried out by placing a small amount of powder between two glass slides. The copper grid was then dusted over the surface of one of these slides. Finally, the grids with samples were again vacuum baked at 80°C for a further half an hour before loading into the microscope. Each grid sample was kept a maximum of four months before a new grid was made up as it was found that contamination got worse with time, due to solvents seeping out from the plastic in the storage boxes.

4.2. Image Intensity Normalisation

The image intensity normalisation method used within this thesis makes use of the flux weighting adaption, which is particularly important for asymmetric detectors (see Figure 4.2). The current was also dropped for detector mapping in order to reduce dependency on the detector linearity.

4.2.1. At the Microscope

Outlined here is a step by step method originally designed for the Oxford-JEOL 2200MCO but later used on the ARM using a confocal arrangement of the post specimen lenses by selecting ‘Alignment Mode’.

- Without scanning, move the sample so that the probe is going through a large hole.
- Switch on the TEM lenses below the sample (click 'Alignment' button in the ASID or STEM control panel).
- You want a much lower current on the detector so that you can use the same contrast and brightness settings as you do for sample imaging; this is because pixel brightness does not vary linearly with contrast.[157]
- For detector imaging we use the same spot size as that used for imaging but drop the probe forming aperture to the smallest available.
- Insert the detector (ASID/STEM control panel).
- In Digital Micrograph start scanning and decrease the magnification until you find the detector.
- Use PLA (and if not I-Shift in the TEM corrector could be used) to shift the detector image to the centre of the screen, gradually increasing the magnification.
- Make a note of your brightness and contrast settings, as these are not maintained when switching between the imaging and alignment modes.
- Image the detector using the same dwell time and image size that you use for the experimental images.
- Take several pictures at each dwell time you will use during your session.

4.2.1.1. Taking Current Readings

The method outlined here uses a specialised pico-ammeter to measure beam current. Measuring the current using the EELS drift tube is an equally valid approach which was applied on the ARM data taken in this thesis.

- Turn on the pico-ammeter (small separate console in microscope room).
- Switch to the lowest camera length setting to get the smallest beam (4cm).
- Raise the phosphor screen.
- Select ‘Dialogue’ – ‘Operation’ – next to Faraday cup select IN.
- Using PLA, move the beam into the cup shadow. With the ammeter running the beam can be moved around until a maximum current is measured to ensure the beam is completely within the Faraday cup.
- Blank the beam and take a zero reading on the pico-ammeter – pressing store will take 100 readings.
- Press recall and arrows to get average and standard deviation.
- Repeat this process with the beam un-blanked.
- This process should be carried out with the detector mapping beam and the beam used for imaging and you will need the current ratio later.

4.2.2. Image Calibration

The method of calibrating the image intensity is through detector normalisation; converting images to an absolute scale which is comparable to image simulations. Image normalisation uses the corresponding detector map for a particular experimental image with the same contrast and brightness settings. The equation to convert intensity to an absolute scale as a fraction of the incident beam is:

$$I_{frac} = \frac{(I_{raw} - I_{vac})}{(I_{det} - I_{vac})} \cdot \frac{i_D}{i_e} \qquad 4.1.$$

Where the I_{raw} is the raw image intensity and $\frac{i_D}{i_e}$ is the current ratio between mapping the detector and during experimental imaging. I_{vac} and I_{det} are the average intensity in the vaccum and the active region of the detector respectively. These can easily be determined by segmenting the histogram of a detector map (Figures 4.1 and 4.2).

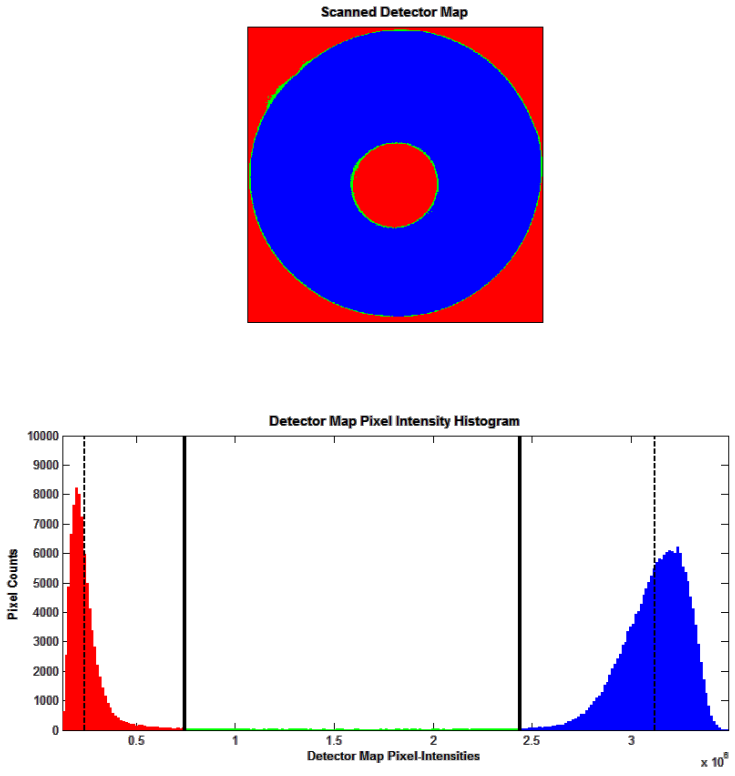


Figure 4.1 - Segmentation method for detector normalisation, demonstrated on the JEOL ADF detector from the OJ2200. Red indicates regions which are considered background and blue indicates regions which are considered part of the active region of the detector.

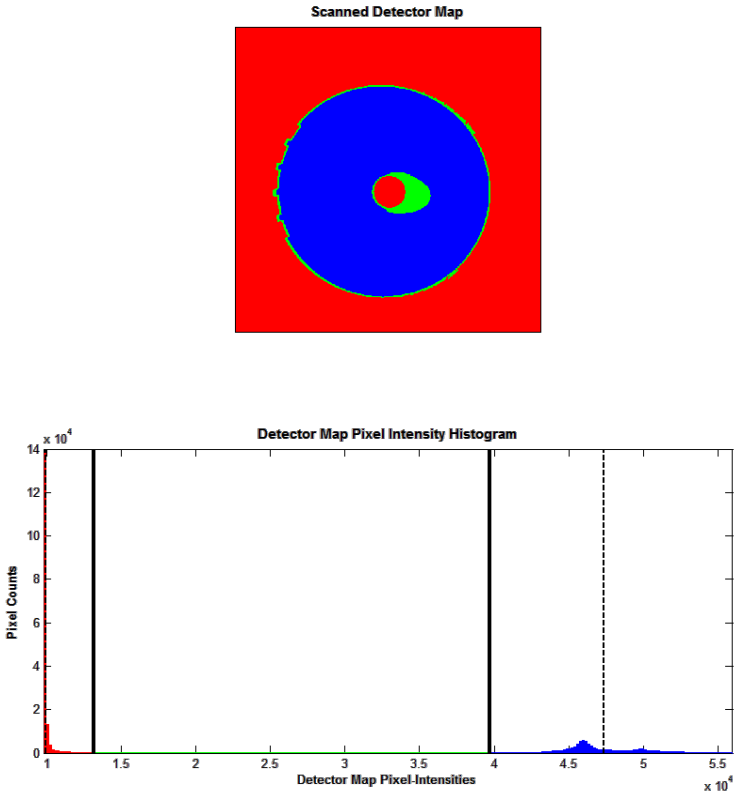


Figure 4.2 – Segmentation method for detector normalisation, demonstrated on the Fishionne 3000 detector. Red indicates regions which are considered background and blue indicates regions which are considered part of the active region of the detector. Anything highlighted in green are pixels of an intermediary value which cannot easily be assigned one way or the other.

During detector segmentation the average intensity in the blue region gives the detector sensitivity and the average intensity in the red region is the vacuum level. The green region, labelled as neither the background nor the active region, can be used to label parts of the detector support which demonstrate more counts than the remaining regions of vacuum or below average in the active region. Ideally this green area should be as small as possible.

The detector segmentation method holds only for considerably flat detectors (see Figure 4.1). Unfortunately certain detectors (Figure 4.2) demonstrate sufficient non-uniformity that it becomes difficult to separate out the active region

from the background through simple thresholding methods. As much of the data for this thesis comes from microscopes with a Fischione 3000 detector, a modification on the normal image normalisation needs to be applied. The flux weighting adaptation to this method has therefore been used for the data presented in this thesis.[160]

4.3. Measuring the Detector Collection Efficiency

Ideally, the efficiency of the active region of a detector would be uniform but this is rarely the case and instead an asymmetric detector map is often obtained. This can lead to a systematic error in the normalisation factor used and subsequently an error in the quantitative ADF images.[152,158] The most accurate comparison with simulation is achieved with uniform detectors.

From the range of microscopes used during this thesis it has been possible to map ADF detectors from all the main leading hardware manufacturers and draw a comparison to determine which will produce the most accurate quantification. All were mapped using a confocal method except for the Nion machine, which is a dedicated STEM so a pencil beam approach was used instead. Maps were taken by E. Okunishi on the ARM 200F, A. Beché on the Titan and T. Pennycook on the Nion UltraSTEM. In order to understand detector non-uniformity I define the following characteristics for comparison. The results for six different detectors are summarised in Table 4.1.

- Flatness from integrating concentric rings to see how the detector efficiency varies radially with scattering angle.

- Roundness from integrating thin slivers of the detector to how its efficiency varies azimuthally.
- Uniformity (or smoothness) evaluating the noise in terms of pixel by pixel variation across the detector map. This is taken from the full width quarter maximum of the histogram of pixel values in the active region.
- Ellipticity; how far the detector deviates from the ideal circular donut shape.

For detectors whose sensitivity varies with collection angle (radially) there will be a drop in collection-efficiency which will provide an error in quantitative measurements. The detector flatness has been well investigated in the literature[156,158] and can be overcome through flux weighting[160] or using a detector sensitivity profile in simulations.[156] Whilst both approaches have been shown to be equivalent, flux weighting is preferable as it can be used with any simulation software, whereas the sensitivity profile is only available with a few.

Detectors may also demonstrate varying sensitivity around the detector (azimuthally). In this case electron scattering over different directions may be recorded with varying efficiency, potentially leading to complicated and unwanted image artefacts.[158]

The primary cause of the ‘flatness’ and ‘roundness’ asymmetries is a shadow region which is present in many models of detector. This shadow results from the physical hole (drift-tube) in the detector (see Figure 4.3) which allows the bright-field or EELS signals to pass through its centre. The signal is read out to the side of the detector and regions on the far side of the drift-tube often exhibit a suppressed efficiency.

Thirdly, an otherwise perfect detector may still have a random non-uniform sensitivity-texture due to the quality of finish of the scintillator. Lastly, a detector can exhibit a degree of ellipticity. This can be due to the detector being physically tilted within the column, a result of manufacturing error, or (more likely) in systems with post-specimen aberration correction, a result of geometric distortions arising from these lower optics. Any such ellipticity will have a significant effect on the measurement of inner angle – itself a critical measurement for any comparison with simulation. For completeness the approximate outer angle (expressed as a multiple of the inner angle) is shown also. In general, a large outer angle is favourable for improved total electron-scattering collection-efficiency. Although, as discussed later for most ADF or HAADF conditions the outer regions of the detector are unlikely to be illuminated.

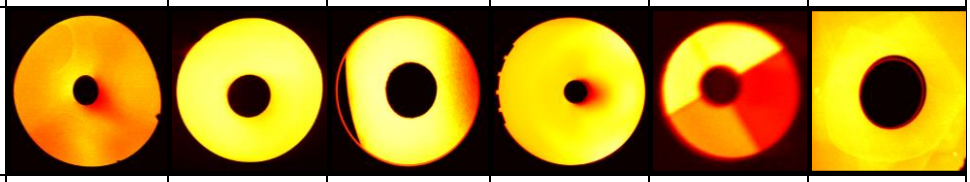
Manufacturer	Jeol			Fischione	FEI	Nion
	DC ARM 200F	DC 2200F	SC 2100 UDF	DC Titan[3]	DC Titan[3]	UltraSTEM 100
Detector Map						
Outer Angle	5.47 x	3.09 x	2.89 x	**5.91 x**	2.90 x	3.50 x
Non-flatness	8.93 %	**6.79 %**	24.90 %	10.39 %	9.19 %	14.49 %
Non-roundness	4.50 %	4.66 %	9.13 %	4.10 %	17.38 %	**2.39 %**
Non-smoothness	27.5 % *	**9.2 %**	13.7 %	14.7 %	28.4 %	23.5 % *
Ellipticity	19.59 %	4.77 %	8.94 %	**0.49 %**	4.31 %	13.30 %
Average	15.1 %	**6.4 %**	14.2 %	7.4 %	13.9 %	13.4 %

Table 4.1 – Scaled sensitivity images of the six detectors studied, grouped by manufacturer. DC and SC referred to whether or the microscope was double or single corrected respectively. For each type of non-uniformity, the percentage deviation from perfection is shown. For each performance metric the most uniform detector is highlighted in green. Lastly an average score is tabulated in order to be able to rank them.

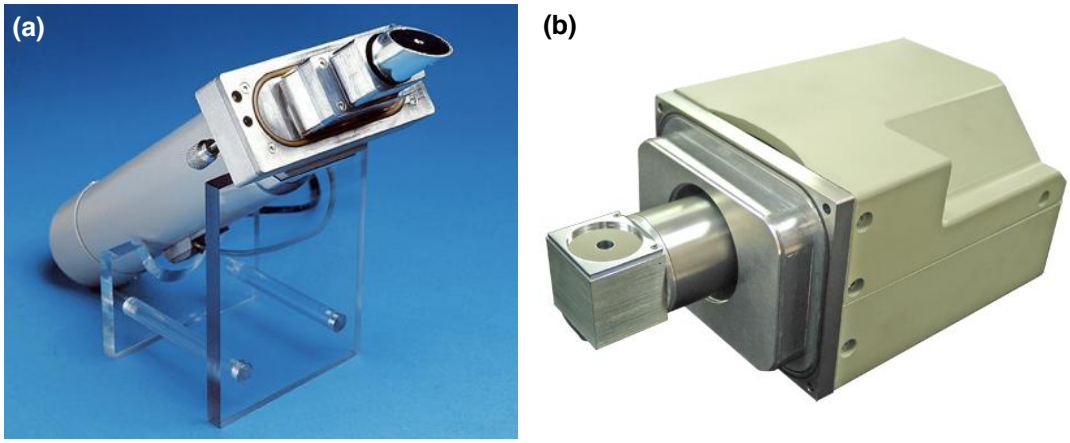


Figure 4.3 – Example hardware construction of an ADF STEM detector. The Fischione 3000 is fitted as the main ADF detectors to most FEI Titan machines, left[7]. The Gatan 806 detector, right[8].

[7] http://www.gatan.com/analysis/806.php
[8] http://www.axt.com.au/model-3000-annular-dark-field-adf-detector/

4.4. Detector Angle Calibrations

Scattering cross sections are hugely dependent on the detector collection angles used to simulate the library values because this affects the detector size and therefore the angular range over which the detector is integrating. The traditional method for calculating the inner angle, β, is to insert the detector over the convergent beam electron diffraction pattern or CBED of a known sample (see Figure 4.4). By knowing the characteristic diffraction spots of the material, $SrTiO_3$ in this case, it is possible to calibrate the CBED in angle space using equation 4.2.

$$\lambda = d_{hkl}\theta \qquad 4.2.$$

λ is the wavelength, d_{hkl} is the plane spacing of a particular (hkl) plane and θ is the scattering angle. In this thesis a key modification has been incorporated for accurate determination of β for the active region of the detector. Figure 4.5 shows a combined detector map, created by a simple summation of the two detector map images, with a second detector that is shadowed by the first; the dark region in this image is the drift tube of the first detector which will still contribute to the shadow on the CBED but is inactive in terms of measuring counts. Using this figure the calculated shadow detector inner angles can be multiplied by a scaling factor to account for this dead region, resulting in a larger final calculated β. For the Oxford ARM this ratio was calculated to be 1.45, showing that all real collection angles are 45% larger than that calculated by the CBED shadow method alone.

A calibrated CBED pattern such as Figure 4.4 can also be used to calibrate the probe convergence angle, which is simply the radius of each of the diffraction

disks. As will be discussed in Chapter 5 this is much less critical for the scattering cross section approach to quantification.

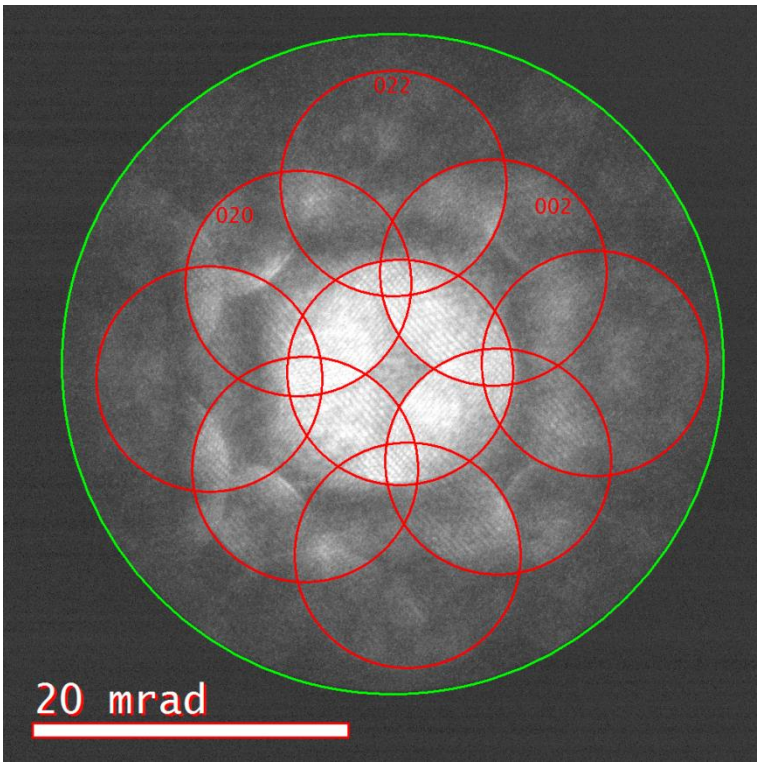


Figure 4.4 – Convergent beam electron diffraction pattern of <100> $SrTiO_3$ with the ADF detector inserted and therefore cutting off the outer region of the pattern, green circle. The diffraction spots are outlined and labelled in red.

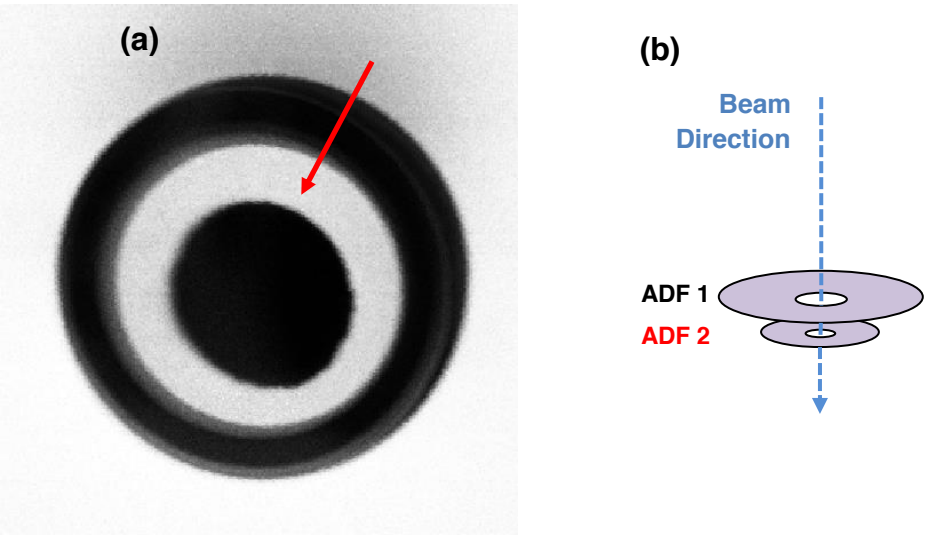


Figure 4.5 – Combined detector map (a) of ADF1 and a second detector, ADF2, which is situated behind the first. Such a map highlights the difference between the angle predicted from measuring the detector shadow and the angle for the active region of collection. A schematic of how the detectors are set up in the microscope (b).

4.4.1. Outer Cut-Off Angle

After the detector inner angle is calibrated using the shadow over a CBED, the simplest method for evaluating the outer angle is by using the inner to outer angle ratio of the physical hardware. However, since the investigations of electron flux distributions by Martinez et al.[160] and in this thesis (see Figure 4.6), it has become clear that there is an outer limit or cut-off in the electron optics to the scattered electrons which reach the detector plane.

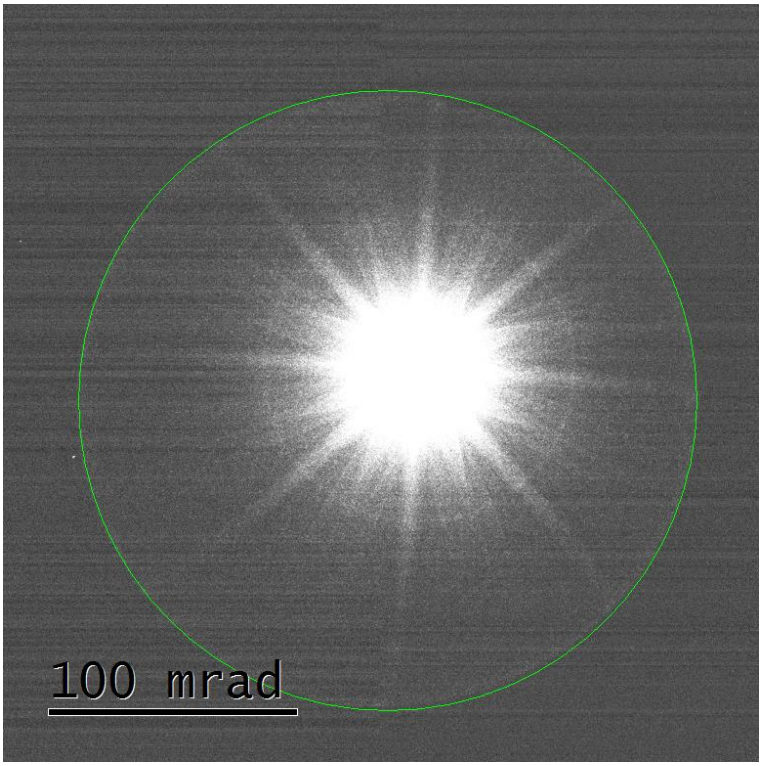


Figure 4.6 – Electron flux from $SrTiO_3$ from the probe-corrected ARM in Oxford. The green circle shows there a sharp cut-off to an otherwise smooth decay of the electron flux with scattering angle.

Investigations have shown the cut-off scattering angle to be independent of camera length, in terms of the angle at which scattering is cut off. Therefore a candidate for the origin of this cut-off is the internal bore diameter of the objective lens. The flux cut-off makes understanding the detector asymmetry more critical at shorter camera lengths as only the central ring of the detector will be illuminated, which is where the detector demonstrates greater asymmetry. The flatter more uniform outer region may see no illumination at all. For example, a typical cut off angle is around 160mrad. For the Fischione 3000 detector (see Figure 4.2) the inner to outer angle ratio is 5.47 so a 58mrad detector angle would expect an outer angle of 317mrad if the collection was limited by the detector geometry. However, because of the scattering cut-off, at

this camera length only the central half of the ADF detector will actually be illuminated.

4.5. Simulation Optimisation and Accuracy

In STEM quantification it is vital to remember that one is often dependent on direct comparison with theoretical simulations, especially as the ADF intensity varies non-linearly with thickness. The accuracy of these simulations is therefore critical to the final quantification results. This is where statistical techniques, like those demonstrated by Van Aert et al.,[123] have an advantage. The decomposition of the histogram of cross sections into a series of Gaussian components is an independent measure of atom counting within the specimen that can later be compared with simulations. The problem with direct comparison with simulation is the danger of introducing a systematic error due to comparison with inaccurate simulations. As such the method for image simulation has been investigated and carefully optimised to ensure complete and trustworthy convergence. The parameters used for the key elements in this thesis are covered in Table 4.2 and the different microscopes parameters corresponding to the experimental data are outlined in Appendix A.

Element	Co	Pd	Ir	Pt
Atomic Number	27	46	77	78
Crystal Structure	HCP	FCC	FCC	FCC
Lattice Parameter (pm)	a=250.71 c=406.95	389.07	383.9	392.42
Debye Waller Factor (300K) (Å^2)	0.062907	0.076816	0.036792	0.069739

Table 4.2 – Summary of the main elements investigated in this thesis; including their atomic number, crystal structure and Debye Waller Factor for a temperature of 300K from the Gao and Peng temperature parameterisation.[193]

4.5.1. Details of Simulation Parameters

Unless otherwise stated the simulations for this thesis were carried out using the QEP method[178] provided through the μSTEM software developed at the University of Melbourne.[9] The software is optimized to provide fast parallel calculations on a graphical processing unit (GPU). The simulations in this chapter are presented for a Pt crystal viewed down a <110> zone axis. They use an accelerating voltage of 300kV and although they do not substantially affect the cross section calculation, a C_s of 4.06μm and C_5 of -1.25mm were also used, corresponding to the settings of the FEI Titan^3 instrument in Antwerp (see Appendix A on page 266). Unless otherwise stated detector angles of 35-190mrad and a probe convergence angle of 20.2mrad have been used. Calculations were performed on a 1.7 x 1.7 nm^2 super-cell, sampled on a 1024 x 1024 mesh. This results in a sampling equivalent to a maximum scattering angle of 376 mrad (approximately twice the outer detector angle), when bandwidth

[9] http://tcmp.ph.unimelb.edu.au/mustem/muSTEM.html

limiting is incorporated to prevent aliasing. The probe step size in the final output images is 0.01667nm. The thermal mean-square displacement of the atoms were calculated using the Gao and Peng parameterisation[193] and a temperature of 300 K, which for Pt is $4.835 \times 10^{-4} nm^2$. An average was taken over 15 atomic configurations generated using these thermal displacement values

4.5.2. Comparison between different simulation codes

During this research a number of discrepancies between simulation packages were brought to light. Absorptive potential (AP) codes demonstrated the largest variation in the calculated cross sections between simulation packages due to the variation in whether or not and how the elastic contributions were re-incorporated into the final image. With access to several different simulation codes within the Oxford group and through collaborations it seemed prudent to compare the outputs of these codes with exactly the same simulation parameters. The parameters used are outlined in Appendix B, covering three different temperatures, two different sets of collection angles, and a single atom versus a crystal. The low angle ADF or LAADF simulations have a scattering angle of 35-190mrad and the high angle ADF or HAADF have a scattering angle of 90-190mrad. The temperature was defined by the DWF input using the temperature parameterisation published by Gao and Peng.[193] The simulation codes compared are the image simulation software from HREM research,[10] the

[10] www.hremresearch.com

μSTEM[11] (both QEP and AP codes), the STEMsim[12] frozen phonon (FP) code, QSTEM,[13] and Dr Probe.[14]

The first simulation was of a single atom of Pt in the centre of a 5Å square box (see Figure 4.7). The cross section of a single atom should have no temperature dependence because there is no channelling, so each simulation curve should be horizontal; this holds true for all but the HREM HAADF (90-190mrad) and the μSTEM-AP LAADF (35-190mrad). μSTEM-AP as the only absorptive potential code, is expected to deviate further from the others. Such deviation is likely to be more pronounced at smaller collection angles where there is a much larger contribution from elastic scattering which may or may not have been reincorporated correctly. However, QSTEM also seems to deviate further from the other codes.

The second simulation comparison was a 10 atom thick crystal of Pt viewed down the <110> zone-axis (see Figure 4.8). Here the AP code seems to produce more comparable results to the other codes, although it deviates with increasing temperature. The HREM and QSTEM codes seem to deviate from the remainder of the data. This suggests the safest codes to use are STEMsim and μSTEM-QEP which have demonstrated very good agreement over all the simulations. Additionally the STEMsim code has been shown to demonstrate good agreement with experimental data when atom counts have been independently verified through statistical methods.[149] The Dr Probe code shows

[11] http://tcmp.ph.unimelb.edu.au/mustem/
[12] http://www.ifp.uni-bremen.de/electron-microscopy/software/stemsim/
[13] http://elim.physik.uni-ulm.de/?page_id=834
[14] http://www.er-c.org/barthel/drprobe/

remarkably good agreement with STEMsim and μSTEM-QEP except for the low angle crystal simulation where considerable deviation is seen.

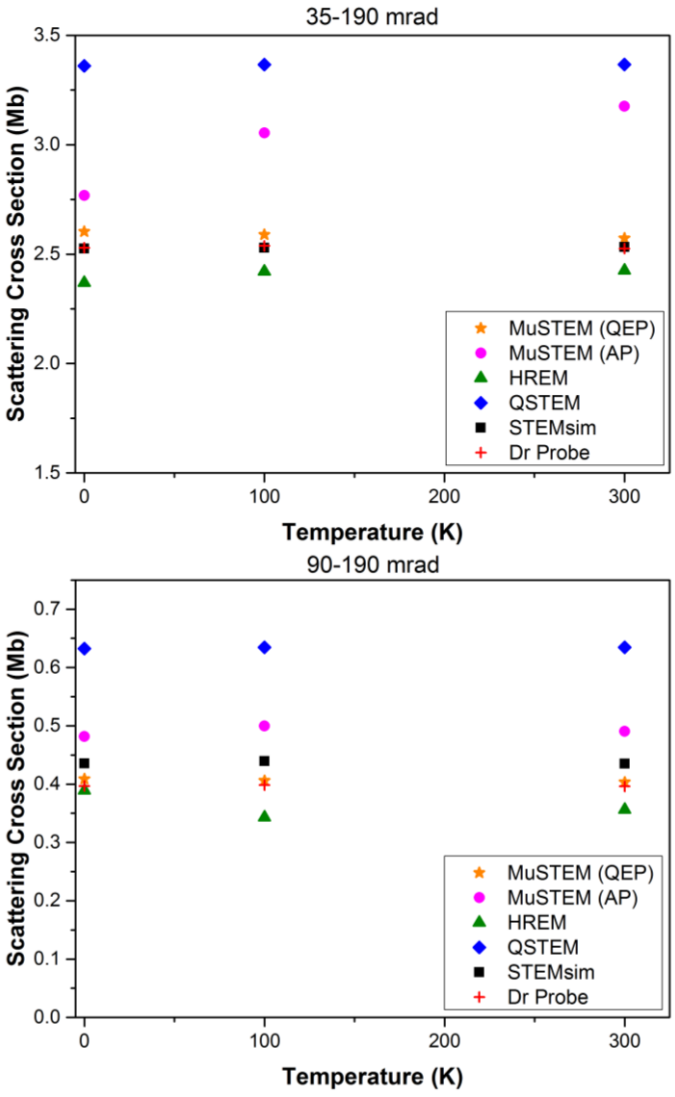


Figure 4.7 – A comparison of how the scattering cross section of one Pt atom varies with temperature. Results are shown for a selection of different simulation codes.

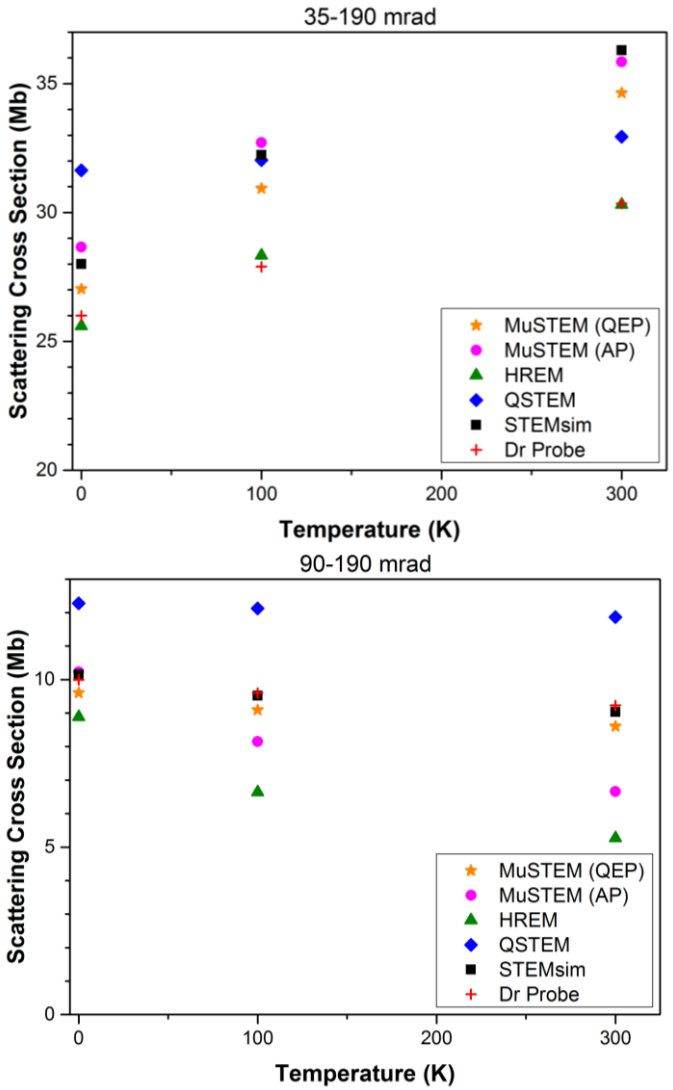


Figure 4.8 – Comparison of the cross section of a column of 10 Pt atoms in a crystal, viewed along the <110> zone-axis, simulated from different simulation codes.

4.5.3. How Many Phonon Configurations to Use

During FP or QEP simulations, the number of phonon passes or configurations would ideally be infinite or as large as possible as this is more realistic when considering what a real sample will 'see'. Large numbers of phonon passes, however, quickly becomes computationally intensive. In particular the μSTEM simulation code parallelised for use on a GPU has an upper limit to the number of atomic displacements which can be stored. This restriction is governed by the

number of cores available on the GPU. Therefore the effect of the number of frozen phonon passes on the calculated scattering cross section was investigated (Figure 4.9). The number of phonon configurations affects the calculated cross section very little. What it does affect is the range of values between different simulation runs (starting from a different random number generator) and therefore the error in the calculated cross section, if this is not taken into account.

For larger thicknesses of specimen, the number of frozen phonon configurations used in the simulations becomes less critical (see Figure 4.10). This is because a certain amount of averaging happens with the small displacements down an atomic column, meaning less averaging is necessary to smooth out the cross sections between several different simulation runs.

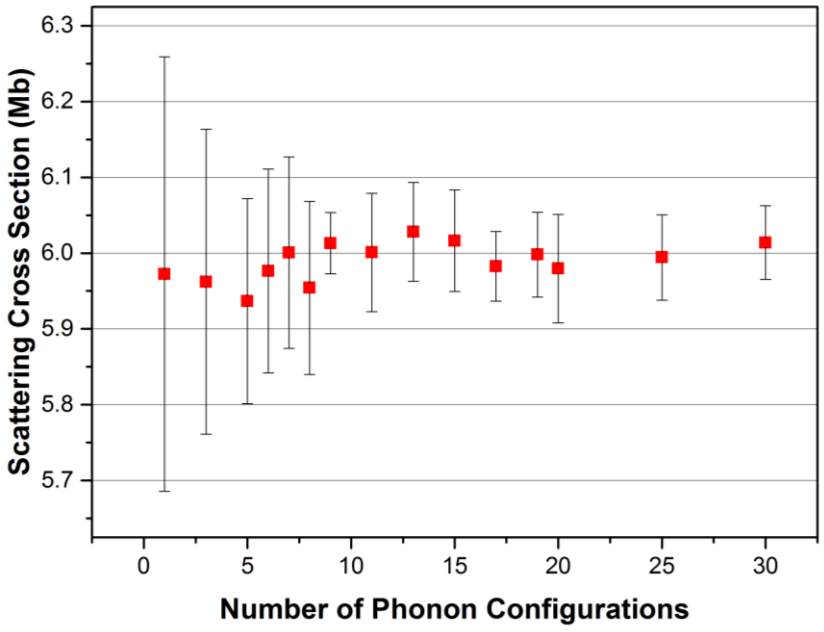


Figure 4.9 – The scatter cross section of a 2 atom thick crystal of Pt <110> crystal with increasing number of phonon configurations, using 35-190mrad detector collection angles and 300kV electrons. The error bar is taken from the standard deviation over 12 measurements.

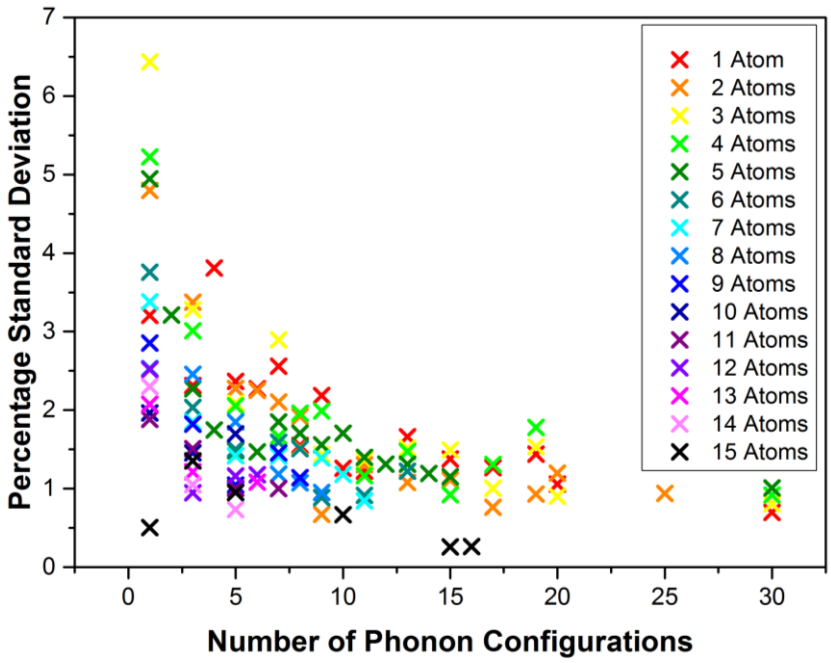


Figure 4.10 – Shows the effect of the number of frozen phonon configurations on the error in image simulations with increasing sample thickness. The sample is Pt <110> with 35-190mrad detector collection angles. The percentage standard deviation of the scattering cross section was calculated from 12 measurements with different random number starting positions.

4.5.4. Reciprocal Space Sampling

The reciprocal mesh used in a simulation governs the maximum achievable real-space sampling and is based on the following relation:

$$\delta_{min} = 2\Delta r = 2.\frac{a}{n} \qquad 4.3.$$

Where δ_{min} is minimum wavelength (equivalent to the Nyquist frequency) which has real space sampling of two pixels size Δr. Pixel width is simply determined by the super cell width, a divided by the number of pixels across the diameter of the image, n. Converting from this to establish the maximum scattering angle being simulated is simply:

$$\theta_{max} = \frac{\lambda}{\delta_{min}} = \frac{a\lambda}{2n} \qquad 4.4.$$

In the case of band-width limiting, which is incorporated to prevent aliasing of the electron wave function, a θ_{max} two thirds of that predicted by the equation above is used. Simulation convergence occurs once the reciprocal space sampling is beyond twice the outer detector collection angle (Figure 4.11) required for the output image.

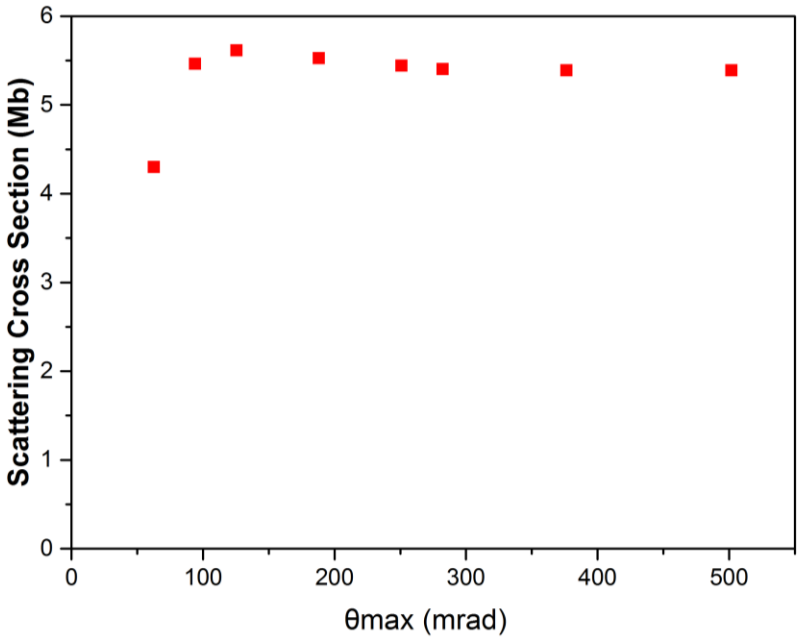


Figure 4.11 – The effect of reciprocal space sampling on the scattering cross section of a 3 atom thick column of Pt with detector collection angles of 50-190mrad. Convergence is reached for sampling out to an angle of 300mrad which is larger than 1.5x the detector collection outer angle, 190mrad is this case.

4.5.5. Conclusions

The μSTEM QEP code used for this thesis demonstrates good agreement with other available simulation software. For optimum convergence the reciprocal space sample should be at least 285mrad or 1.5x the outer detector collection

angle. Whilst the minimum number of phonon configurations needed for convergence changes with thickness, 15 seems be sufficient for up to 20 atoms thick.

5. SCATTERING CROSS SECTIONS

The idea of calculating scattering cross sections from STEM images was first proposed by Retsky et al.[138] in the 1970s, demonstrating excellent agreement between experiment and theoretical calculations. The concept of a scattering cross section is widely used through particle physics as a measure of the probability of scattering or absorption, and is used in areas including X-ray and neutron diffraction,[194] and electron energy loss spectroscopy.[195]

The motivation behind the scattering cross section approach is the search for a measure of intensity with greater robustness to microscope imaging parameters. In particular an improved robustness would allow greater flexibility for quantifying the ADF signal of more beam sensitive samples, in contrast to previous methodologies.[144,196]

In this chapter, I will outline the mathematical framework for the cross section approach to quantification. Afterwards it is important to understand the limitations of the technique. This is done through a simulation-based study using the μSTEM code to investigate how robust cross sections are to various microscope and sample imaging parameters. We begin by evaluating the robustness to the microscope parameters for investigating single atom species and apply this to the single atoms located on catalyst carbon supports. For single atom thickness the mathematics holds well and as probe does not change with sample thickness.

Dealing with crystals where the probe does not vary with sample thickness, I empirically show with simulations to what extent the scattering cross section is still a useful parameter. Finally I investigate sample limitations of tilt and channelling, also looking into the benefits of experiment design in order to minimise these effects on our quantification.

5.1. Mathematical Framework

A full derivation of ADF scattering cross sections equation (equation 5.5) from quantum mechanics was presented by E et al.[197] However we will start with the equation for incoherent image formation (equation 5.1). The approach assumes the detector, collecting the scattered electrons, is sufficiently large to produce incoherency and that the probe wave function does not change significantly within the thickness of the sample.

The formation of image intensity, $I(\boldsymbol{r_0})$, in ADF STEM can be described as a convolution between the crystal object function, $O(\boldsymbol{r})$, which is sharply peaked at the atom sites and a blurring function describing the intensity of the STEM probe, $P(\boldsymbol{r_0} - \boldsymbol{r})$ (equation 5.1). For the scattering cross sections we integrate over an atomic column which results in equation 5.2.

$$I(\boldsymbol{r_0}) = \int P(\boldsymbol{r_0} - \boldsymbol{r}) O(\boldsymbol{r}) d\boldsymbol{r} \tag{5.1.}$$

$$\int I(\boldsymbol{r_0}) d\boldsymbol{r_0} = \int\limits_{\substack{\boldsymbol{r_0} \\ atomic \\ column}} \int\limits_{\substack{\boldsymbol{r} \\ all \\ space}} P(\boldsymbol{r_0} - \boldsymbol{r}) O(\boldsymbol{r}) d\boldsymbol{r}\, d\boldsymbol{r_0} \tag{5.2.}$$

We can carry out the two integrations separately resulting in equation 5.3.

$$\int I(\boldsymbol{r_0})d\boldsymbol{r_0} = \int_{\boldsymbol{r_0}} P(\boldsymbol{r_0}-\boldsymbol{r}) \int_{\boldsymbol{r}} O(\boldsymbol{r})d\boldsymbol{r}\, d\boldsymbol{r_0} \qquad 5.3.$$

The detector normalisation method (discussed in section 4.2.1 on page 75) produces images with intensity presented as a fraction of the incident beam. Assuming the atomic columns are sufficiently well resolved, the total integration of the probe-function over the whole field of view is unity, resulting in equation 5.4.

$$\int I(\boldsymbol{r_0})d\boldsymbol{r_0} = \int O(\boldsymbol{r})d\boldsymbol{r} \qquad 5.4.$$

Real experimental images are quantised into discrete pixels of area, $A_{i,}$ allowing us to use a discrete summation (equation 5.5). The pixel area is also moved outside the summation sign as this is constant over a particular experimental image.

$$A\sum_i I_i = \int O(\boldsymbol{r})d\boldsymbol{r} = \sigma \qquad 5.5.$$

The resulting scattering cross section, σ, behaves like a real cross section in terms of the particle physics definition. It is a measure of the probability of an electron in the incident beam being scattered by the sample out to the ADF detector. It is only dependent on the object function and not the probe function, making it robust to the various astigmatisms and aberrations within the STEM probe. The origin of this robust nature is primarily due to the integration over an

atomic column; many of the detrimental parameters for peak intensities merely blur the probe or redistribute intensity within the integration region.

5.2. Simulation Methods

As in Chapter 4, the majority of the simulations use settings to match the Antwerp Titan^3 microscope operating at 300kV. The simulations were carried out using the QEP method[178] provided through the μSTEM software developed at the University of Melbourne.[15] This simulation also allows me to investigate separately the behaviour of the elastic and TDS scattering, which was important to understand tilt and channelling effects. Unless otherwise stated detector angles of 35-190mrad and a probe convergence angle of 20.2mrad have been used. Single unit cell simulations used an 8 x 8 tiling of a Pt unit cell viewed down the <110> direction sampled over a 2048 x 2048 reciprocal mesh.

Simulated images were used to calculate the scattering cross section of an atomic column as previously documented, by integrating over a Voronoi polygon. These values are represented in units of megabarn (Mb), which is 10^{-4} nm^2.

Some simulations carried out by H. E have been included here to explain the robust nature of scattering cross sections. These early simulations were carried out using the μSTEM absorptive potential code with a large enough detector collection inner angle such that elastic scattering contributions to the ADF signal become very small. These simulations were performed for a 200 kV instrument with ADF detector inner and outer angles of 90 mrad and 180 mrad, corresponding to that of the Oxford-JEOL 2200-MCO double aberration

[15] http://tcmp.ph.unimelb.edu.au/mustem/muSTEM.html

corrected microscope. Calculations were performed on a 3.112x3.112 nm^2 super-cell, sampled on a 512x512 mesh, which was found to be sufficient for convergence of the calculation for the thin specimens.

5.2.1. Tilting Simulations

The tilting simulations were performed on a 1.7 x 1.7 nm^2 super-cell, sampled on a 1024 x 1024 mesh. This results in a sampling equivalent to a maximum scattering angle of 376 mrad (approximately twice the outer detector angle), when bandwidth limiting is incorporated to prevent aliasing. The probe step size in the final output image is 0.01667nm. The thermal mean-square displacement of the atoms were calculated using the Gao and Peng parameterisation[193] and a temperature of 300K. An average was taken over 15 atomic configurations generated using these thermal displacement values. Source size was not included for the cross section calculations and has only been incorporated for the final published images when relating back to the predicted resolution for tilted images. The accepted method for an effective finite source size is to blur the images using a 2-dimensional Gaussian, here with a full width half maximum of 0.07nm.[198] The sample is a 7 atom thick crystal tilted towards the <001> direction away from a <110> crystallographic zone-axis. The same effect exists for other tilt axes or even an arbitrary tilt direction but for clarity only one is presented here.[163]

Where stated the probe convergence angle and the inner detector angle have been systematically varied to assess their effect on the channelling contribution to the total cross section in order to determine experimental conditions for

maximum robustness to sample tilts. The detector outer collection angle has been kept constant as we are more likely limited by the electron flux cut-off (see Section 4.4.1 on page 86) than the inner-to-outer radius ratio of the hardware itself.

5.3. Cross Sections vs. Peak Intensities

One of the primary advantages for using cross sections for comparison with simulations over contrast or peak intensities is that they have a more linear and monotonic response with thickness (see Figure 5.1). The peak intensity curve with thickness saturates at only 7 atoms thick. For scattering cross sections, this plateau is delayed until above 30 atoms in thickness allowing greater confidence for quantification at larger thicknesses. 30 atoms is an ample thickness for the investigation of catalyst nanoparticles. Peak intensities are also likely to be hugely dependent on the magnification, noise, and the pixel sampling relative to the maximum point of the 2D profile of each atomic column. It should be noted that the scattering cross sections discussed here are exactly the same mathematically as the Gaussian volumes utilised by Van Aert et al.[121,149,199]

The same Z-contrast variation seen in ADF STEM images also persists in the ADF scattering cross sections (see Figure 5.2). This allows the potential for quantitative compositional analysis.

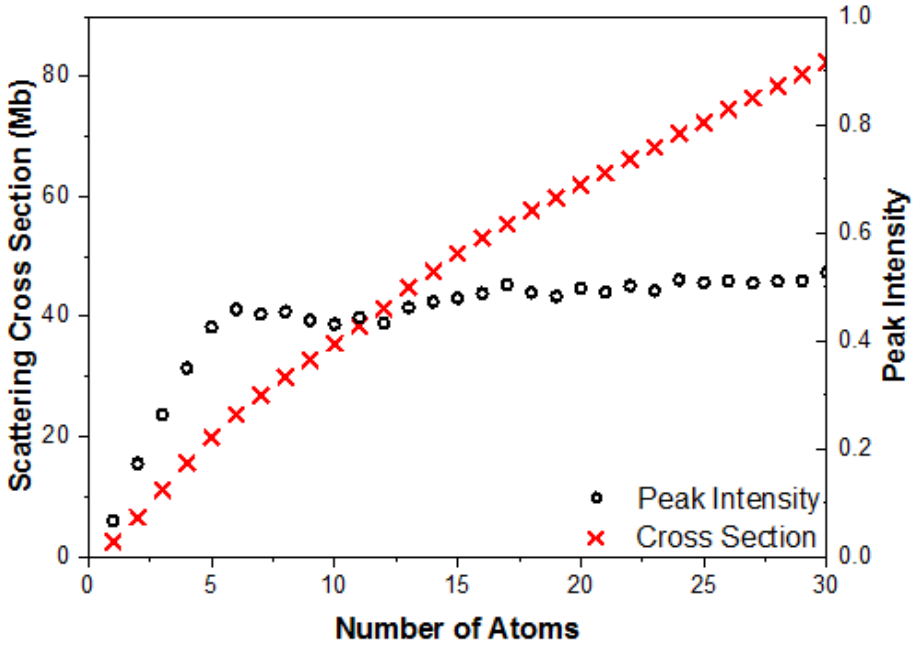


Figure 5.1 – A simulation thickness library for Pt showing the scattering cross section (Mb) or peak intensity (plotted as fraction of the incident beam intensity) variation with sample thickness. Simulations used 200kV electrons, zero aberrations, 22.48mrad convergence angle and 53.2-132.2mrad detector collection angles, corresponding to the Oxford ARM microscope settings. The peak intensity response is much less linear and the monotonic dependence is lost at about 7 atom thickness.

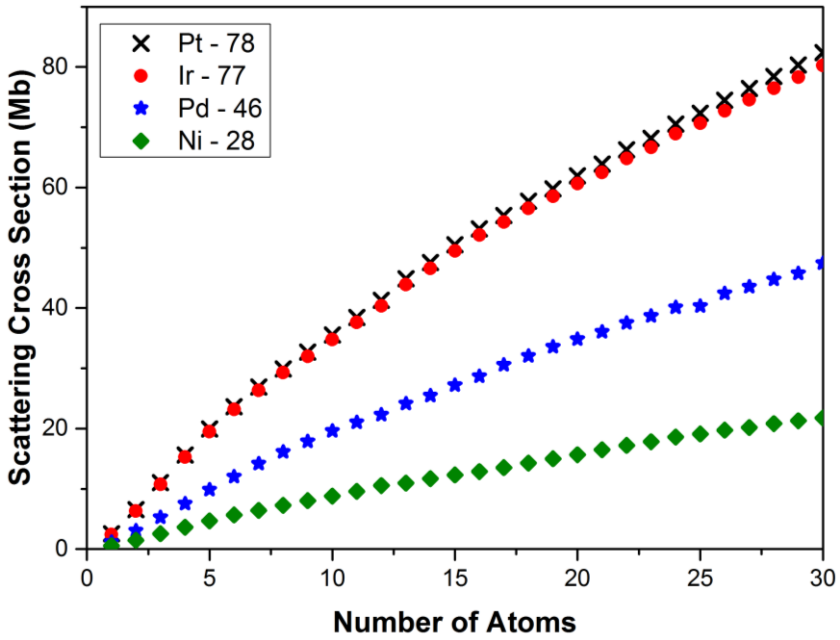


Figure 5.2- Simulation thickness libraries for Pt, Ir, Pd and Ni showing the clear Z-contrast behaviour witnessed in ADF STEM imaging. The simulations were carried on a single FCC unit cell viewed down a <110> zone axis, at 300kV with 35-190mrad detector collection angles and 20.2mrad probe convergence angle.

5.4. Microscope Imaging Parameters for Single Atoms

As demonstrated by the mathematical framework, scattering cross sections are largely independent of probe shape and structure provided the resolution and pixel sampling of the image is sufficient to resolve individual atomic columns. This provides a greater deal of flexibility over using the peak intensities or image contrast for comparison with simulations. Through image simulation we probe how robust scattering cross sections are to the key imaging parameters. We begin by investigating single atom species for which the mathematical assumptions completely hold.

5.4.1. Defocus

Focus is a parameter which is adjusted frequently during a microscope session in order to achieve optimum contrast. This is especially the case for real catalyst samples where, because of the 3-dimensionally varying carbon black support, z-height between neighbouring particles differs significantly. The process of looking for an on-axis particle suitable for imaging makes it difficult to accurately determine the defocus setting.

Simulations show that the scattering cross section for a single Pt atom imaged with a 200kV, aberration free probe of convergence angle 25mrad, with detector collection angles 90-190 mrad, is 0.48Mbarns (Mb). The peak image intensity drops off rapidly with increasing defocus of the probe (see Figure 5.3), whereas the cross section is relatively insensitive to focus, as long as the integration region is sufficient that it includes the whole atom. This is due to the integration

process incorporating all of the defuse beam, regardless of the probe shape or profile.

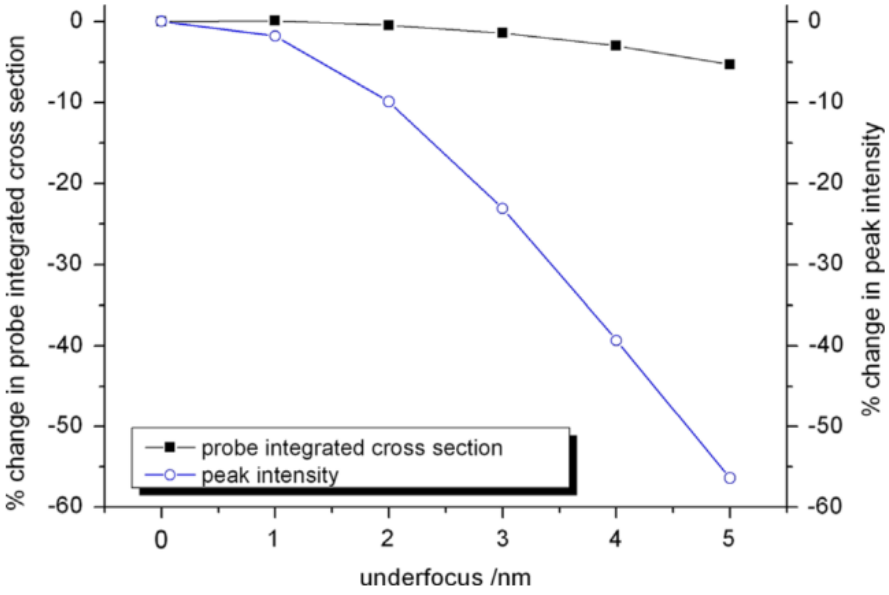


Figure 5.3 – The relative change in peak and cross section values as a function of defocus for a single Pd atom. While the cross section is reasonably insensitive, the peak value falls off very rapidly. Variations of the cross section for large defocuses are due to the broadened beam no longer being included in the area of the integration box.[197] *Figure courtesy of Haibo E.*

5.4.2. Source Size and Coherence

Source size is the hardest parameter to determine experimentally. In early work by Lebeau it was used as a free fitting parameter to help match the simulation and experiment.[144] In fact most simulation packages don't include contributions from the finite size of the electron source. The technique for applying source size effects relies on blurring the image with a 2D Gaussian proportional to the additional blurring produced from having a finite source rather than a point source.[200] For each point in the source we would achieve simulated images which are displaced with respect to each other by a small amount laterally.

Including source size means averaging over several of these displaced images, which is the same process as Gaussian blurring. This process only blurs the intensity in the image, resulting in a large variation of the peak intensity but zero variation in the cross section (see Figure 5.4).

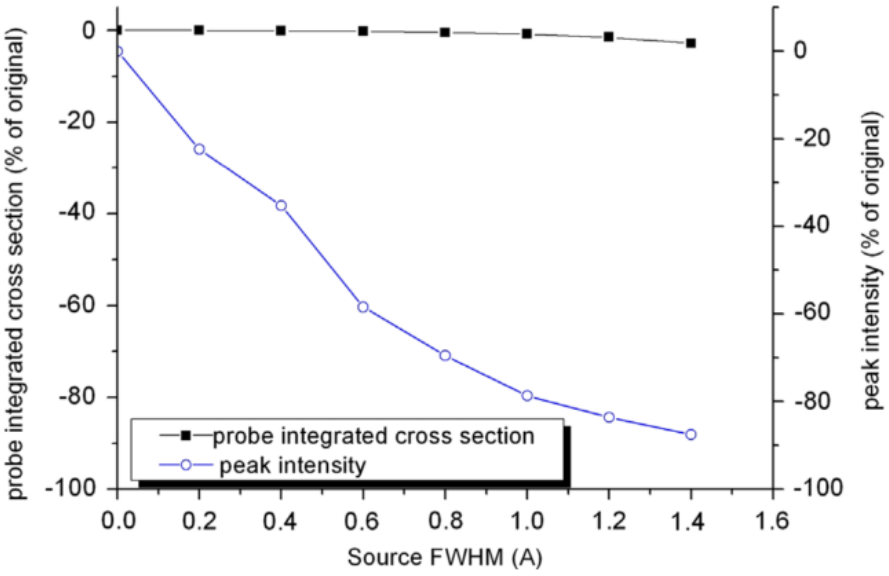


Figure 5.4 – The relative change of cross sections and column peak intensity with effective source size. The cross section is robust to a convolution with a Gaussian to account for the finite probe size, unlike the value of the peak intensity.[195] Figure courtesy of Haibo E.

5.4.3. Probe Convergence Angle

Accurately determining the probe convergence angle, controlled by the objective aperture size, requires calibrating from the CBED pattern of a known sample. It is a parameter known to widely affect the beam current and therefore the intensity of ADF images, although it should have a limited effect on the normalised intensity. Simulations on a single Pt atom demonstrate minimal variation with convergence angle (see Table 5.1).

Aperture size ($Å^{-1}$)	Convergence angle (mrad)	σ (Mb)	% change
0.8	20.1	0.477	0
0.9	22.6	0.486	1.7
1	25.1	0.483	1.2

Table 5.1 – The variation of cross section with respect to convergence angle. The objective aperture size, which controls the convergence angle of the probe, has very little effect on the cross section of a single Pt atom. Data courtesy of Haibo E.

5.5. Single Atom Investigation

In this thesis I have used the robust nature of cross sections to investigate single atom species. During imaging of catalysts there are always single atoms visible on the support, which can often be ignored. Work by Zhou et al.[12] has demonstrated the importance of understanding and investigating the entirety of a catalyst system, where they found that small atomic bi-layers were actually responsible for the catalytic activity in their reaction. This is hugely important from a commercial point of view as the catalytic activity was coming from only a small percentage of the precious metal weight, meaning the remainder of the weight was wasted in larger, unreactive particles.

From a quantification point of view it is important to begin comparing with simulation and experiment of single atom species. This is because the assumption that the probe shape does not change with sample thickness holds for very thin specimens; no channelling or tilt effects will occur and the background subtraction is much more trivial for single atoms. The problem with EDX analysis and EELS is achieving high enough numbers of counts,

particularly from single atoms, especially when they aren't bound like in the paper by Nicholls et al.[129]

These individual atoms can be found moving around on the carbon black support in Figure 5.5 although in a bimetallic system like Pt(Pd) we don't know which element these atoms are. Our initial experimental investigations gave scattering cross sections of the same order of magnitude as simulations. However, there was sufficient scatter in the data that distinction between elements or number of atoms was not possible.

Subsequent experiments were carried out at the SuperSTEM Facility (images recorded by T. Pennycook) on the Nion UltraSTEM-100 at both 100kV and 60kV accelerating voltages to see if this reduced atomic movement. The lower voltage significantly reduces atom movement (see Figure 5.6) but not enough for differentiation between the elements to be possible. These single atom investigations demonstrates a trade off for accuracy. Atoms near or on a nanoparticle surface have fewer degrees of freedom for movement so have a smaller error due to atomic motion; however background subtraction becomes more complicated. In comparison atoms further away, on the carbon black support, have simple background subtraction but move considerably more under the beam. If the atoms move with the scanning probe direction the beam will stay in contact with the atom longer, resulting in a larger cross section than would normally occur and vice versa if the atoms move away from the direction of the scanning probe. This results in significant variation of the cross sections calculated on the same atoms tracked through several sequential images (see Figure 5.7).

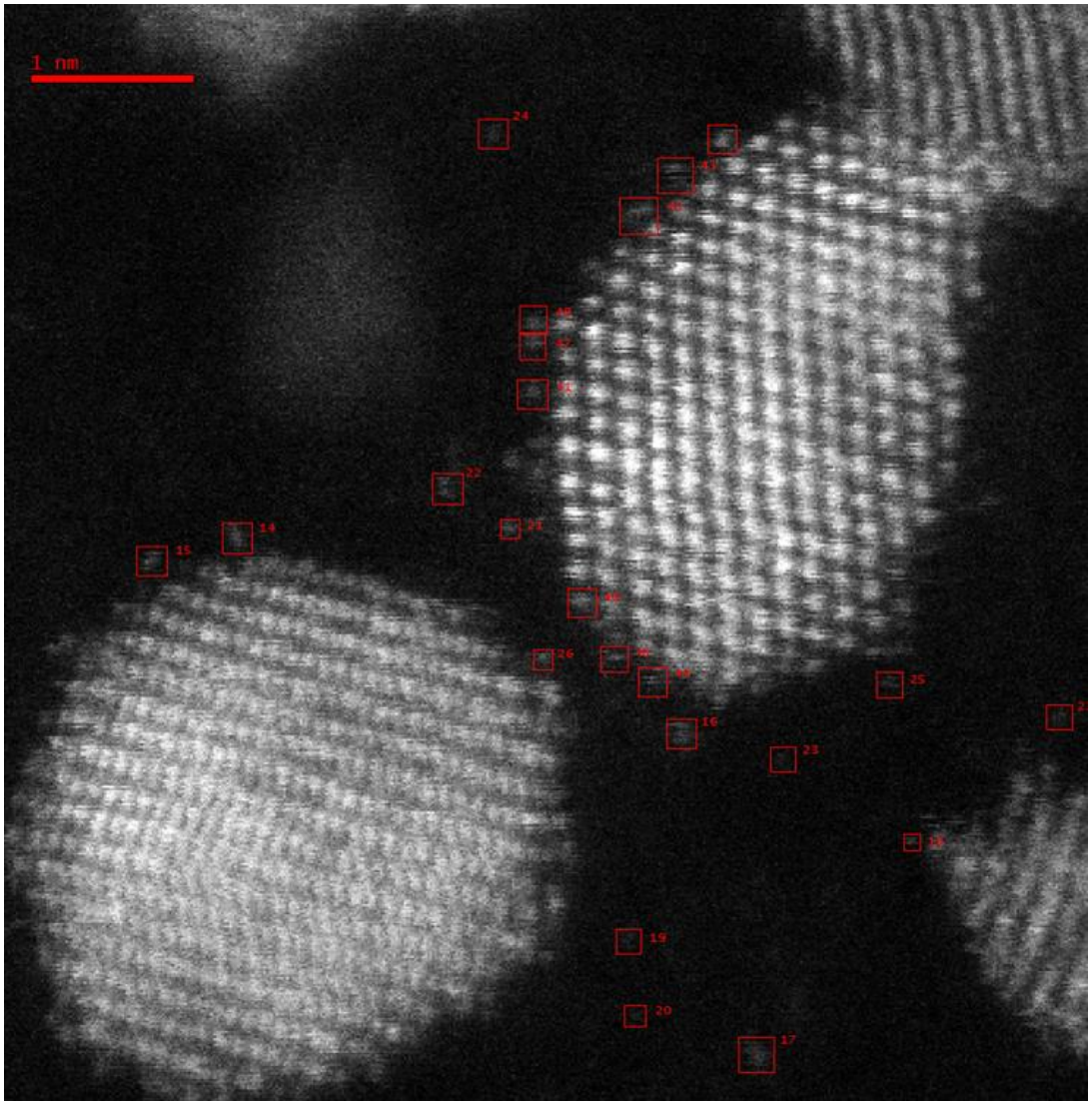


Figure 5.5 – Heterogeneous catalysts of Pt(Pd) on carbon black support, imaged at 200kV on the Oxford-JEOL 2200MCO. Single atoms can be clearly seen around the nanoparticle on the support; those boxed in red were used as part of the single atom investigation. Image acquired by Haibo E.

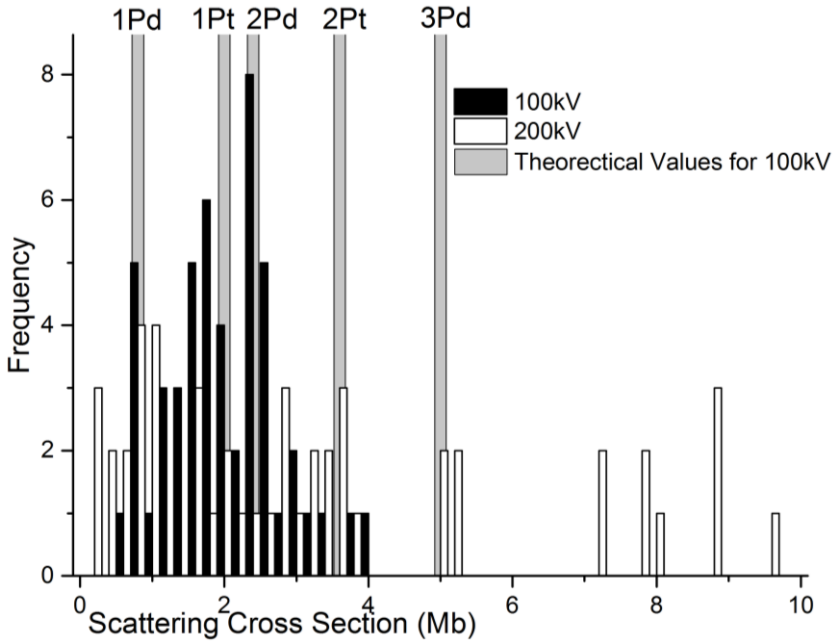


Figure 5.6 – Histogram representing the distribution of the scattering cross sections of single atom species measured from experimental images. Black bars show data from images taken at 200kV, on the Oxford-Jeol 2200MCO, and white bars show data from images taken at 100kV, on the Nion UltraSTEM-100. The grey bars represent the location of theoretical values calculated for 100kV accelerating voltage.

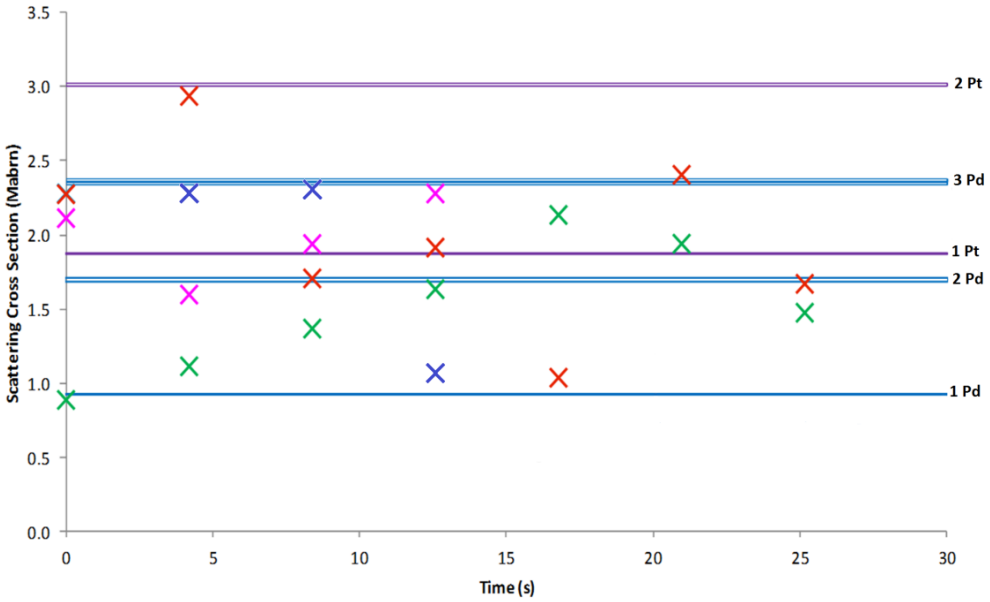


Figure 5.7 – Scatter plot showing the scattering cross section of single atoms over time. Each colour corresponds to one atom taken from sequential images on the Nion UltraSTEM-100 at 100kV. The horizontal lines mark the simulated values for the same operating conditions, of 1 Pd atom, 1 Pt atom etc.

5.6. Applicability of Cross Sections to Imaging Crystals

When expanding the cross section approach to the analysis of crystals one should keep in mind that the mathematical treatment, assuming the probe doesn't change with respect to specimen thickness, will begin to break down for thicker crystals. The scattering cross section of a crystal can still be defined in the same way as for single atom species; however, it will be greatly affected by channelling of the electron probe. For applications of cross sections to thicker samples their robustness was explored empirically.

5.6.1. Defocus in a Crystal

Changes in defocus will affect how the probe couples into the channelling states; however, this appears to have a limited effect on the scattering cross section of an atomic column (see Figure 5.8). The optimum focus for the peak intensity is in fact a few nanometres below the entrance surface of the crystal.[201] With increased defocus the peak intensity drops off rapidly by several tens of percent making it unreliable for simulation matching.

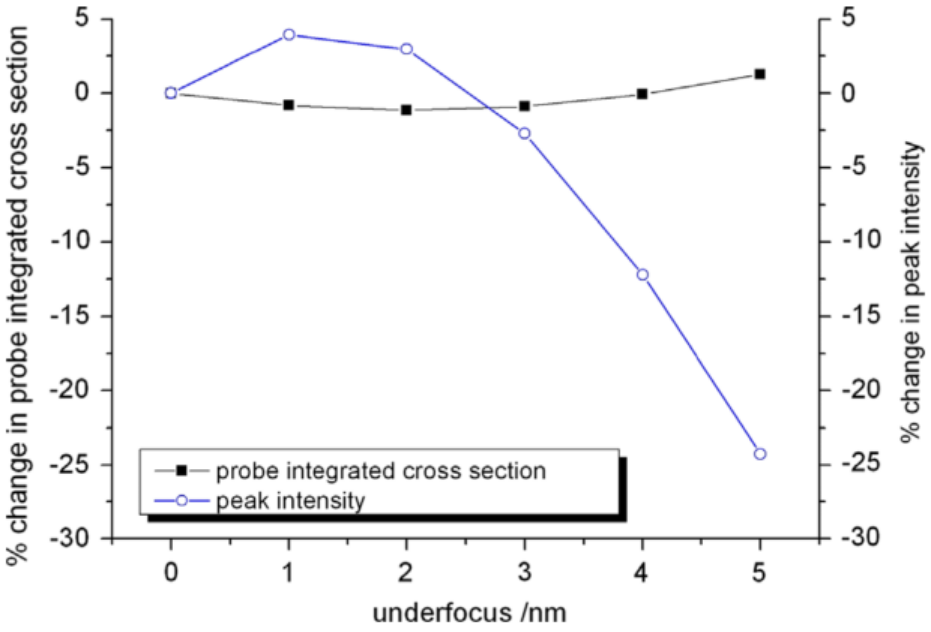


Figure 5.8 – The cross section and peak intensity of a single column in a crystal of Pd <100> of thickness 5nm, as a function of defocus. The cross section varies minimally with under-focus of the probe into the sample. However, the peak intensity shows significant deviation from the in focus value, both above and below the value. Figure courtesy of Haibo E.

5.6.2. Integration Area and Probe Position

One of the other inherent advantages of cross sections over just using peak positions is the effect of the probe position relative to the peak of the 2D Gaussian profile of an atomic column. If the pixel sampling of an image does not synchronise with the crystallographic spacing, there will be a variation in the peak intensity, even for a crystal of uniform thickness, due to where it intersects the Gaussian profile of each column. In the limitations of low magnification and poor pixel sampling this effect is reduced as pixels become closer in value to scattering cross sections.

Comparison of the effect of integration area size also shows that the point at which cross sections begin to saturate is much higher for integration radii approaching the Voronoi cell (see Figure 5.9). This is because the integrating

within the full Voronoi cell results in a value which contains all the scattering and channelling information from that column. For thicker crystals the intensity begins to leak outside of a smaller integration area when the probe broadens.

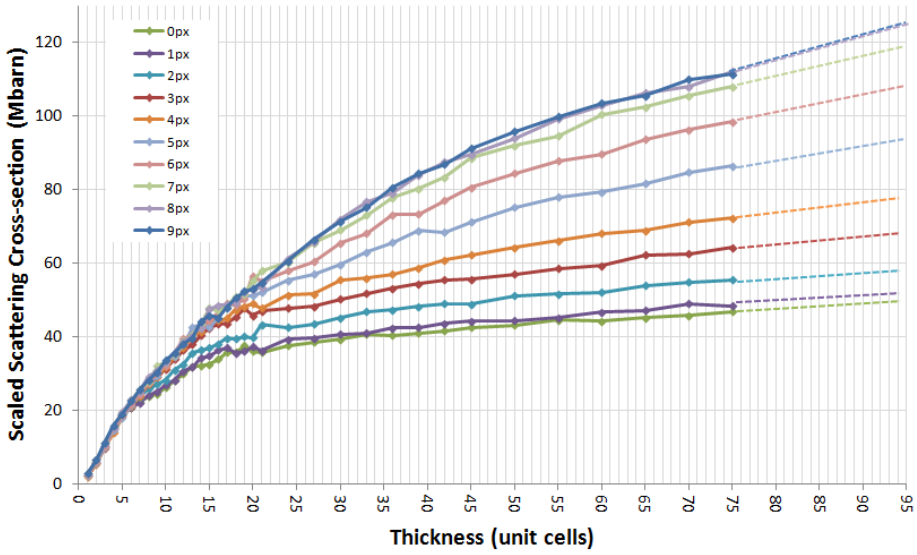


Figure 5.9 – Effect of integration region size on the cross section profile with thickness on a crystal of <110> Pt with a pixel width of 0.0166nm. A radius of 9 pixels is the full Voronoi cell size. For improved comparison the cross sections have been scale relative to the Voronoi cell. Smaller integration regions begin to plateau at smaller thicknesses. The dashed lines represent a polynomial fit to the data. Figure courtesy of Lewys Jones.

5.6.3. Probe Convergence Angle

There is an upper thickness limitation to the robustness to probe convergence angle for crystalline samples because changing the convergence angle affects how well the wave couples into the 1s Bloch wave states. Simulations show that it is still possible to accommodate small variations in the probe convergence angle for a 7 atom thick crystal (see Figure 5.10). Only the smallest (16mrad) convergence angle begins to show some variation from the remaining; therefore

as long as the convergence angle is known relatively large errors in the calibration measurement can be accommodated.

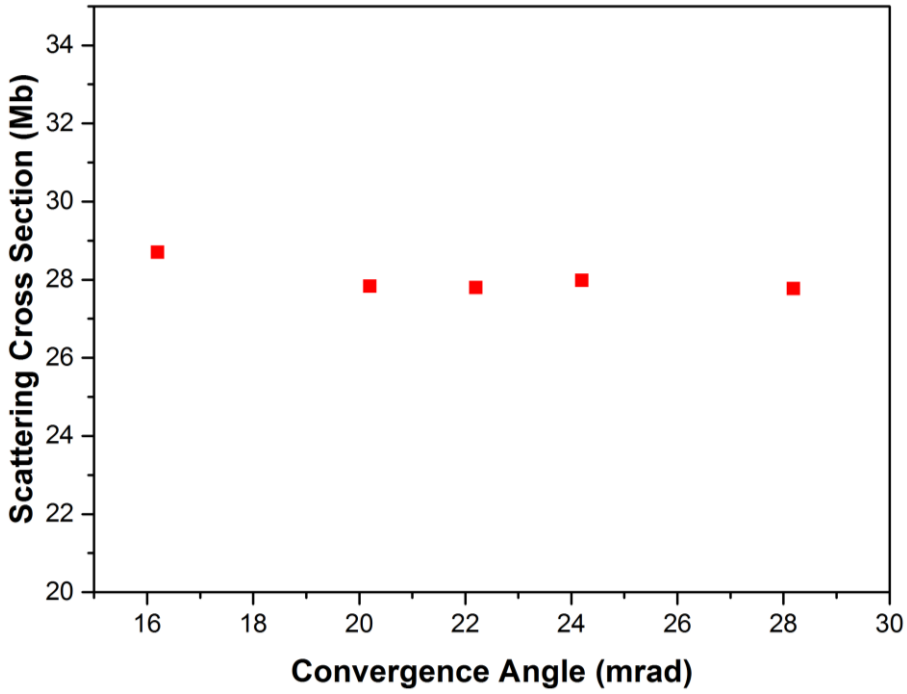


Figure 5.10 – The cross section of a single column in a crystal of Pt <110> of thickness 7 atoms, as a function of convergence angle.

5.6.4. Crystallographic Zone-Axis

Different crystallographic zone axes demonstrate different symmetries and atomic spacing with respect to the electron probe. The atomic separation changes parallel to the beam direction giving a 0.392nm separation for <100> and 0.277nm for <110>. This changes the lensing effect provided by the atoms and therefore the channelling. As Figure 5.11 shows, this results in a non-negligible dependence on the crystallographic zone-axis for thicker crystals but can be neglected below 10 atoms thickness. Simulation libraries should be prepared for the same zone-axis as the experimental image.

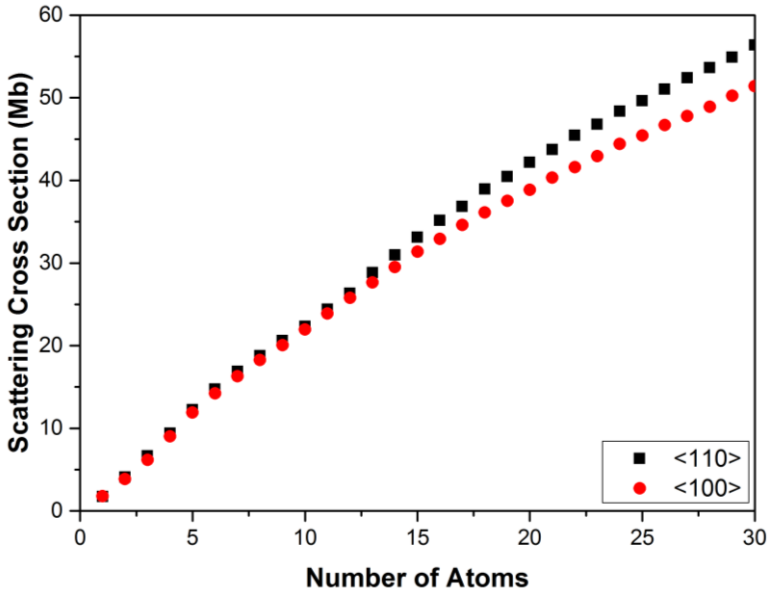


Figure 5.11 – Graph demonstrating the scattering cross section of a column of Pt Atoms viewed down the {100} and {110} crystallographic zone-axis.

5.6.5. Temperature and the Debye Waller Factor

The most common way to incorporate atomic vibrations or displacements and therefore temperature is with the Einstein model for phonons in particular by incorporating the mean square displacement (MSD) for each atom. MSDs are often tabulated as Debye-Waller Factors (DWF) of a material; typically these are calculated for bulk samples of pure element crystals. Temperature and therefore MSDs for an isolated atom should have no effect on the scattering cross section as we are simply integrating over the whole particle but can make a big difference in the quantification of crystals as it will affect the channelling. Figure 5.12 shows that temperature only has a small effect on the calculated cross section. For thicker crystals, the effect increases because the increased thermal motion attenuates the channelling of the beam as discussed in section 3.5.3 on page 60.

In this thesis I make use of the temperature parameterisation carried out by Gao and Peng.[193] However, there is no guarantee that these DWFs are directly applicable to nanomaterials as the collective phonon excitations could be very different.[202] In fact the well documented suppression of melting temperature for small nanoparticle sizes suggests that this may not be the case.[40] In the absence of an alternative this approach will still be used.

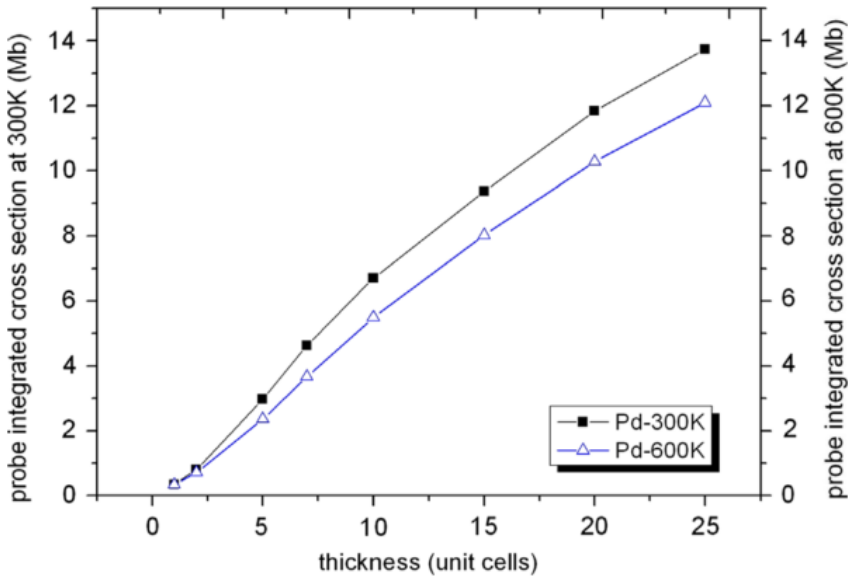


Figure 5.12 – Cross sections versus thickness for two different temperatures. Below thicknesses 2nm, a two-fold increase in the mean square displacement values, corresponding to an increase in temperature from 300K to 600K, has little effect on the calculated cross section. Image courtesy of Haibo E.

Knowledge of the correct DWF is critical for separating out atomic species. Figure 5.13 shows the cross section thickness profiles for Pt and Ir using their elemental DWFs determined by Gao and Peng.[193] The primary difference is that the Pt DWF was determined experimentally whilst the Ir DWF was determined from theoretical calculations alone, resulting in a significant difference. This variation is unrealistic due to their close proximity in atomic number; they are

also both FCC metals with the same bonding and no significant difference in electronic structure. Creating the Ir library with the Pt DWF results in the minimal variation expected between the two elements due to them having only one difference in atomic number. As such only experimentally determined DWFs will be used from Gao and Peng, Ir libraries will use the Pt DWF.

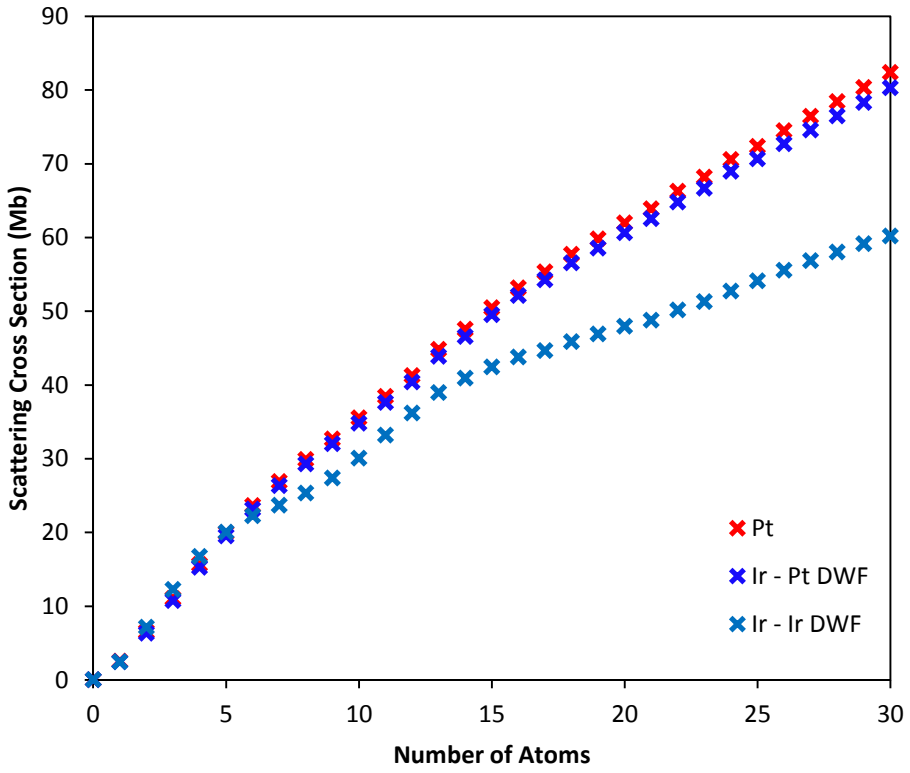


Figure 5.13 – Graph demonstrating the importance of using the correct DWF. The Ir DWF is calculated from the theory whereas the Pt DWF has been determined from careful experimental parameterisation. We would expect Pt and Ir to have very similar DWFs due to their proximity in atomic number. When the Ir library is created using the experimental Pt DWF the elemental curves lies on top of each other.

5.6.6. Cross-Talk

In thicker crystalline samples, so-called “cross-talk” between columns may occur as the probe de-channels or spreads geometrically towards neighbouring atomic columns, especially at larger convergence angles. The result is contributions to

the measured cross section from neighbouring columns which are a different composition and/or thickness; this thereby affects our ability to accurately assign intensity to individual columns. In this thesis this is likely to be of particular importance for bimetallic catalysts where the composition varies throughout the particles.

Simulations were carried out on pure crystals of Pt and Pd of varying thickness as well as corresponding ones for a fictional ‘ordered alloy’ of Pt and Pd, where pure Pt and Pd columns alternate in a <100> view. Up to thicknesses of 10nm the cross section is affected by neighbouring columns of a different species by up to 11% for Pt and 16% for Pd (see Figure 5.14). The Pt loses intensity to the Pd columns, whilst the Pd gains intensity from the Pt columns. For thinner crystals the cross section change in the ordered alloy is down to 5% for Pt and 10% for Pd. In a real system the variation in composition is unlikely to be this stark so the error could be further reduced.

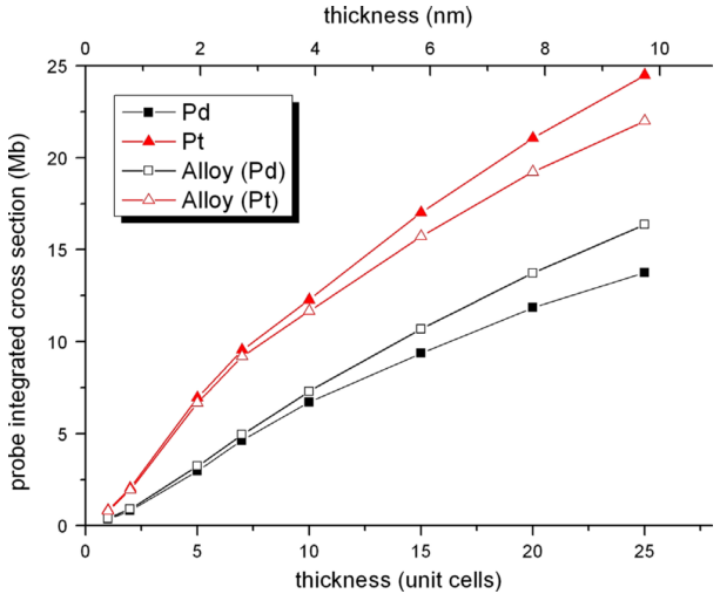


Figure 5.14 – The cross section of an ordered alloy of neighbouring Pd and Pt columns and also pure Pd and pure Pt. With neighbours of different atomic species, the heavier Pt loses intensity to the lighter columns of Pd.

For a more realistic example a cuboctohedral nanocrystal of Pd with a single monolayer shell of Pt was simulated along the <110> orientation. Comparison between the columns containing 3Pt and those containing Pt(2Pd)Pt demonstrates that the variation of cross section due to differences in the neighbouring columns within each group is 0.6%, and sufficiently small that differentiation between each column type is still possible (see Figure 5.15). This difference is not obvious from the original simulated image, demonstrating that the cross section approach does provide more information than can be determined from qualitative analysis alone.

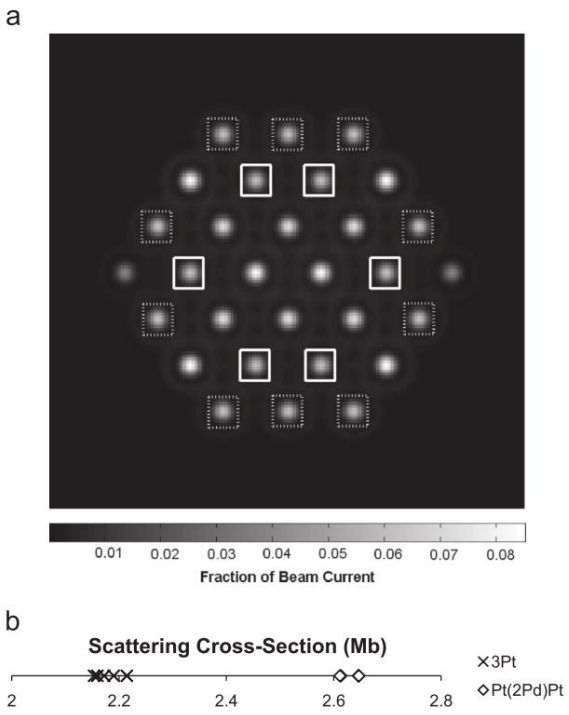


Figure 5.15 – (a) Simulation of a Pt(Pd) core-shell particle viewed down a <110> projection. Cross sections from two types of columns are shown: Pt(2Pd)Pt columns are indicated by the solid boxes in (a) and diamonds in (b); 3Pt are indicated by the dashed box in (a) and as x in (b). Differentiation between columns types by scattering cross section values is possible (b). There is, however, scatter of the cross section values depending on neighbouring configurations and discrete pixel sampling. There are 6 pixels per Angstrom and the cross section is taken with an integration circle of radius 5 pixels from the pixel with maximal intensity in the column.

5.7. Channelling and Tilt

As discussed in section 3.5.3 on page 60 channelling has considerable implications for ADF STEM. In particular, the reduction in channelling when a sample is tilted away from a low order zone-axis.[151,163,197] This occurs because the atoms become less well aligned, and may result in an error in the comparison with simulation if not taken into account.

For more beam sensitive samples, such as catalyst nanoparticles, which are liable to rotate under the beam especially during sequential images,[151] it is not usually possible to accurately tilt the sample to a low-order zone-axis.

Experimentally, smaller detector angles have been shown to demonstrate lower sensitivity to mis-tilt,[151] which has been backed up by a statistical analysis of accuracy in atom assignments.[203] In this section, I show that it is possible to optimise the experimental parameters in order to minimise quantification errors should small sample mis-tilts occur. At low detector angles we find that the cross section is robust to limited tilts, which we explain in terms of the balance between TDS (thermal diffuse scattering) and elastic scattering.

5.7.1. Tilt Dependence of HAADF Cross Sections

Firstly I simulated an isolated column of 10 Pd atoms with detector angles of 90-190mrad, so called HAADF imaging conditions. The relative change in both peak intensity and cross section with respect to tilt (see Figure 5.16) again demonstrates the improved robustness for cross sections. It also shows a phenomena which is seen experimentally of atomic columns 'lighting up' as they rotate onto a zone-axis. An isolated column, however, is unrealistic making it important to understand the effect on an extended crystal.

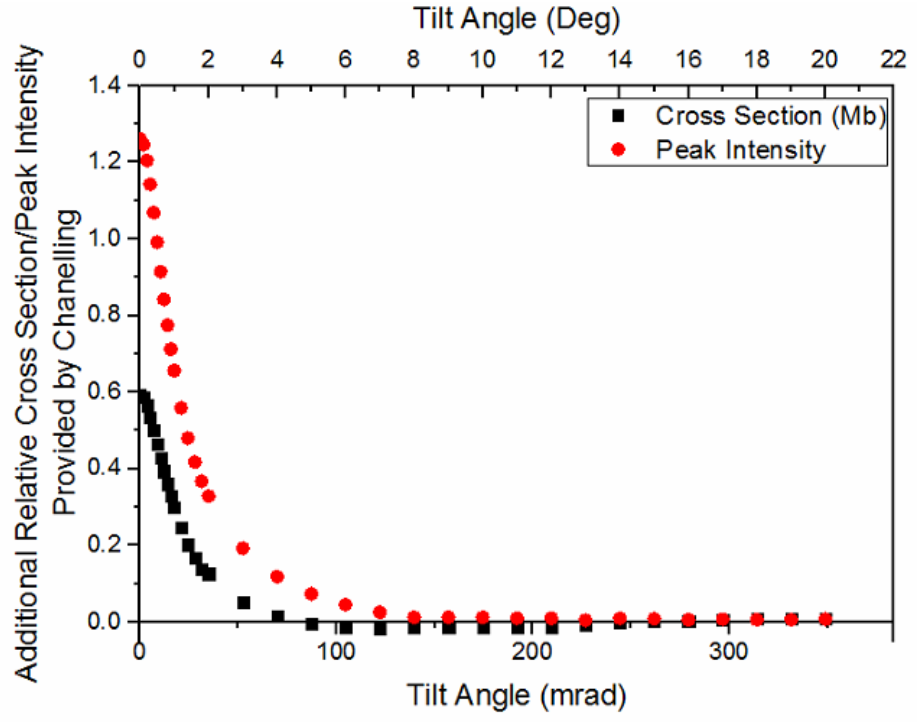


Figure 5.16 – The fractional increase of cross section and peak values relative to the sum of 10 individual atoms plotted as a function of tilt angle for a single isolated Pd column of 10 atoms, showing how the column 'lights up' when rotated parallel to the STEM probe. At larger tilts away from the axis it reaches a plateau which is equal to the sum of 10 individual cross sections and no channelling is present.[197]

5.7.2. The Tilt Dependence of ADF Cross Sections

It is possible to visualise the channelling effect by re-plotting Figure 5.1 onto a scale of the relative cross section normalised by that of one Pt atom. Channelling of the electron probe provides additional scattered intensity over that predicted by assuming a linear multiplication of the cross section for 1 atom, as shown in Figure 5.17. This additional scattering varies non-linearly with thickness, making comparison with careful simulation essential for accurate quantification. At small sample thicknesses, below the first channelling length, the channelling contribution increases with thickness. Beyond this small oscillations are seen in the curve corresponding to the intensity oscillations down an atomic column. At the larger thicknesses the contribution from channelling

begins to decrease again as absorption processes (mainly due to excitation of phonons, also known as thermal diffuse scattering) begin to dominate.

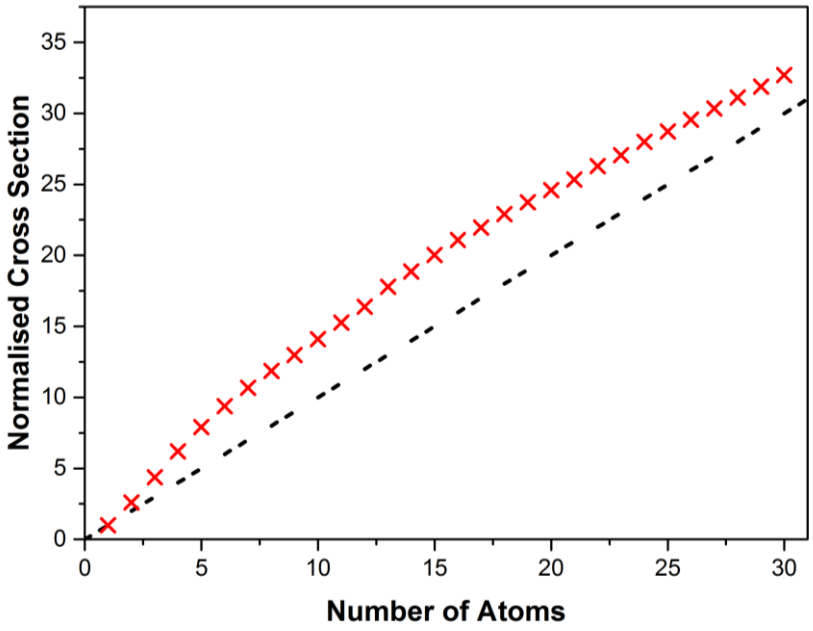


Figure 5.17 – Graph of cross section with increasing thickness of a single atomic-column of Pt normalised by the scattering from a single atom, for an inner detector angle of 35mrad. The dashed line has a gradient of one (linear model). The difference between the two lines is therefore the additional intensity provided by the atomic columns channelling the electron probe.

The additional intensity provided due to channelling is lost when a sample is tilted away from a low order zone-axis and the atoms become less well aligned to the beam direction. In Figure 5.18 I evaluate the effect of detector collection angle, or camera length, on this reduction in cross section with sample tilt. As seen in Figure 5.18a there is a larger scattering cross section at smaller collection angles. This provides an improvement in signal per unit dose[95] as well as signal to noise gains, but could potentially increase sensitivity to strain effects.[204] At larger inner collection angles the relative cross section drops off more rapidly with sample tilt (see Figure 5.18b) which would provide a greater

sensitivity to mis-tilt errors in quantification. At smaller detector collection angles we see a plateau begin to develop where the cross section is robust to small sample tilts.

By separating out how the intensity varies across a series of concentric rings (see Figure 5.18c) we see that for the larger inner collection angles (greater than 80mrad, often called HAADF) the scattering cross section drops of monotonically with sample tilt. At the smaller detector angle ranges the scattering cross section drops off more slowly, or even begins to increase initially with sample tilt for the smallest angles.

Optimising robustness to sample tilt requires careful experiment design in order to maximise the width of the plateau region for a particular sample. Here I have optimised the inner collection angle for a Pt nanoparticle sample. To optimise the inner detector angle collection I simulated a crystal of thickness 7 atoms, 1.94nm, viewed down the <110> zone-axis at a series of different tilts and detector angles. For single atom sensitivity in atom counting of a typically 15 atom thick nanoparticle our error from tilt needs to be less than 2%. Therefore, the optimum detector angle of 35mrad was selected from Figure 5.18b by extracting the largest possible sample tilt tolerable before this 2% deviation is reached, as shown in Figure 5.19; the peak in this curve is the optimum detector angle for robustness to sample tilt. The cross section decreases more quickly with respect to tilt for larger detector collection angles. At the smallest collection angles, the cross section increases but then drops off more quickly afterwards. Additionally, to maintain signal to noise ratio we must stay clear of the bright-field disk to keep the maximum signal to background ratio.

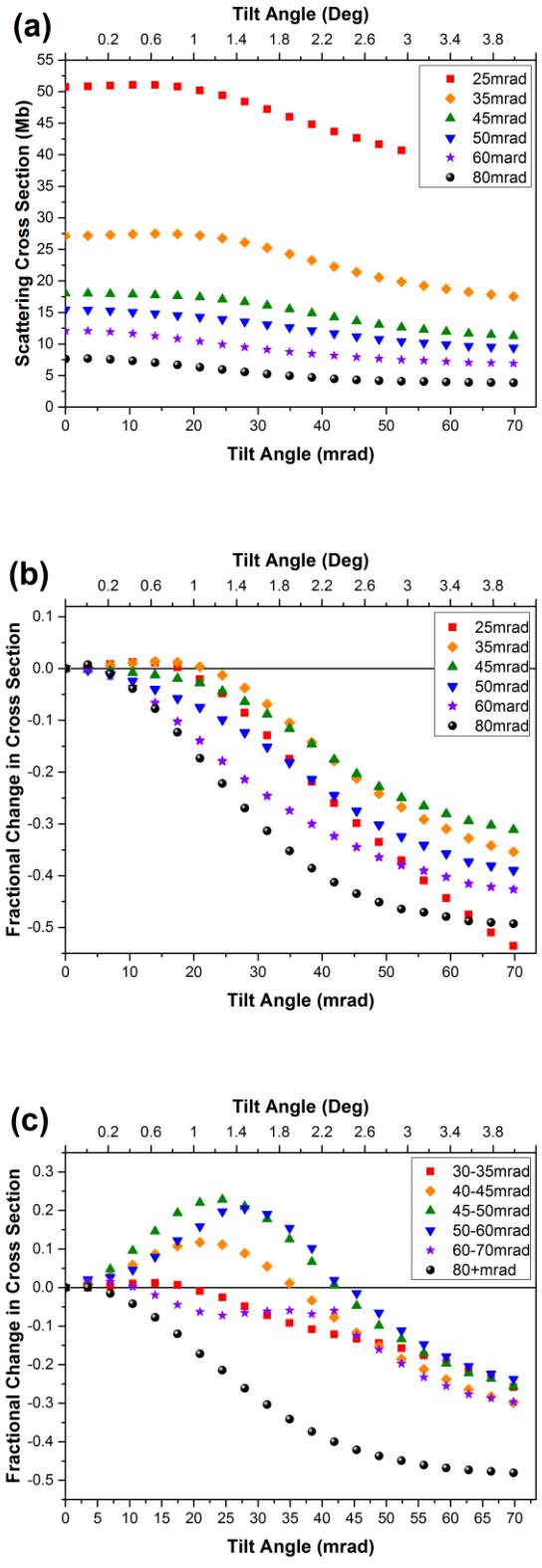


Figure 5.18 – (a) The dependence of column cross section on sample tilt for a range of detector inner radii with outer radius kept constant at 190mrad. (b) The data presented in (a) now re-plotted as the fractional change in cross section relative to zero tilt. (c) As for (b) but with narrower annuli of detection to show the detection angle dependence more clearly.

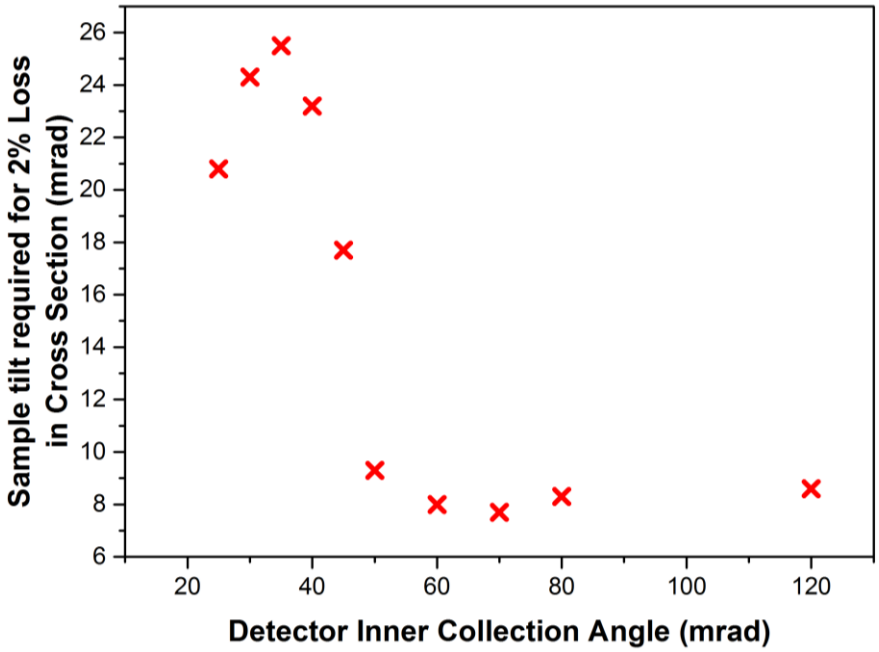


Figure 5.19 – Graph showing the angle at which angle 2 percent deviation in cross section, from the on-axis case, is exceeded for a given detector inner collection angle.

5.7.3. The Origin of the Plateau

The origin of the plateau at smaller detector collection angles can be investigated theoretically by separating out the elastically and inelastically scattered electrons and examining how they contribute to the ADF signal. The elastic signal initially increases with sample tilt (see Figure 5.20). The origin of this increase can be explained by understanding the Ewald sphere construction (see Figure 5.21) used to describe Bragg scattering, where scattering occurs most strongly for reciprocal lattice vectors which intersect with the Ewald sphere. For a tilted probe a large number of higher angle reflections intersect with the Ewald sphere, resulting in more scattering out to the detector. In conventional TEM SAD (transmission electron microscopy selected area diffraction) a Laue circle is observed at sample tilts away from a lower order zone-axis. We can imagine this Laue circle intersecting the ADF detector when a tilt of half the

detector angle, β/2, is reached resulting in this increase in cross section (see Figure 5.22). As you push the Laue circle further out for larger tilts it gets fainter due to the DWF, resulting in a subsequent decrease in the elastic contribution to the cross section.

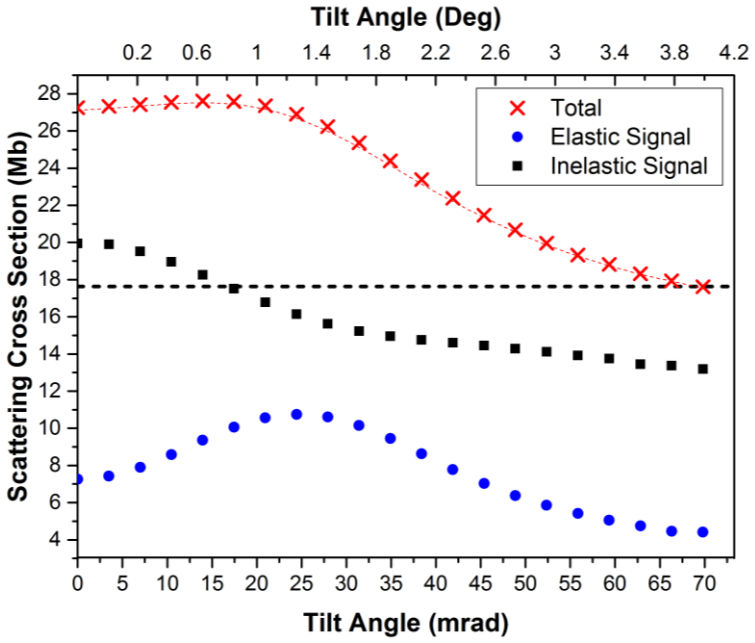


Figure 5.20 – Graph shows the scattering cross section of a 7 atom thick crystal of Pt separated into the elastic and TDS scattering components. At small tilts below the convergence angle of 20.2mrad there is a plateau region in the total cross section, where it is remarkably robust to tilt, due to balance between the elastic and TDS contributions to the signal. Towards large tilts we see the complete loss in channelling as the cross section value trends towards the linear model, dotted black line. The crosses and the dots for the total signal are taken from simulations for different tilt directions from a <110> zone-axis.

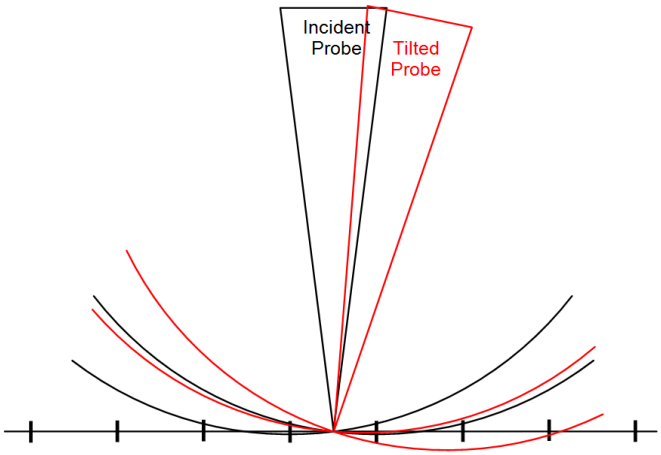


Figure 5.21 – Diagram of the Ewald Sphere construction for both and on-axis, black and a tilted probe, red. Due to the convergence of the STEM probe the Ewald construction is blurred out over a small range of angles. The tilted probe intersects with more reciprocal lattice spots (represented by short vertical lines) than the on-axis beam.

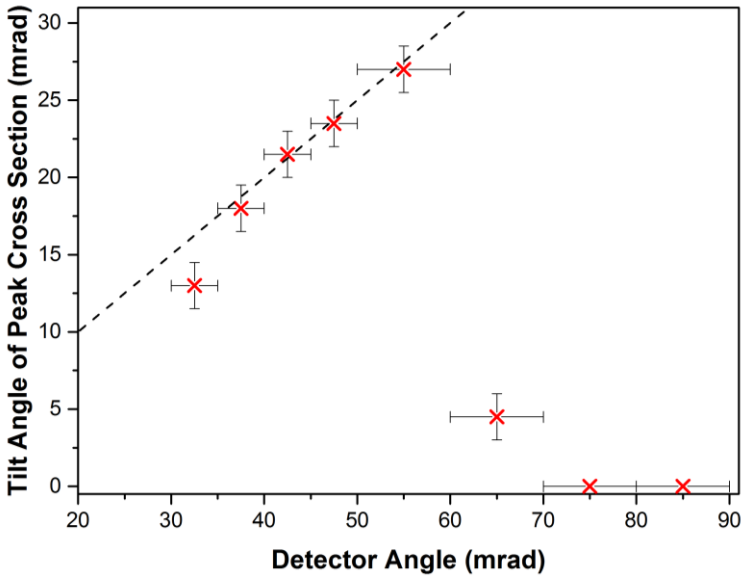


Figure 5.22 – Graph showing the location of the peak in cross section with tilt for given detector collection inner angles. The peak increases with collection angle due to the intersection of the Ewald sphere with more reciprocal lattice points. It drops off at larger inner collection angles where the angle is sufficiently large that there is no elastic contribution to the cross section.

The Ewald sphere construction does not apply to TDS, which therefore drops off monotonically with sample tilt, much in the same way as the HAADF image

intensities drop of monotonically with tilt. When tilting the atoms are less well aligned resulting in a reduction to their channelling ability and therefore a lower cross section. At sufficiently large detector collection angles the signal can be assumed to be entirely TDS,[156] and therefore the similarity to the tilt curves for large detector collection angles is expected.

There is therefore an optimum detector inner angle for which the initial increase in the elastic signal with sample tilt almost perfectly compensates for the loss in TDS, with the overall result of producing a tilt robust region where the cross section hardly varies. At larger sample mis-tilts, beyond 20mrad in this case, the cross section drops off rapidly trending towards the value predicted by a simple linearity assumption i.e. where a 7 atom thick crystal has the same cross section as 7 times one atom. Whilst it would be ideal to work in this linear regime it comes at a cost of both resolution and a large tilt dependence variation in the cross section.

5.7.4. The Effect of Probe Convergence Angle

Another microscope parameter which can be controlled is the probe convergence angle. Figure 5.23 shows that the plateau region scales with the convergence angle meaning that increasing the probe convergence angle can also be used to extend the plateau region. The angular range provided by the convergent electron probe causes a broadening in the range of reciprocal points intersected by the Ewald sphere, which provides the convergence angle dependence witnessed in our simulations. For the 28.2mrad convergence angle

in Figure 5.23 the plateau region begins to shrink again preventing further extension of the plateau beyond this point.

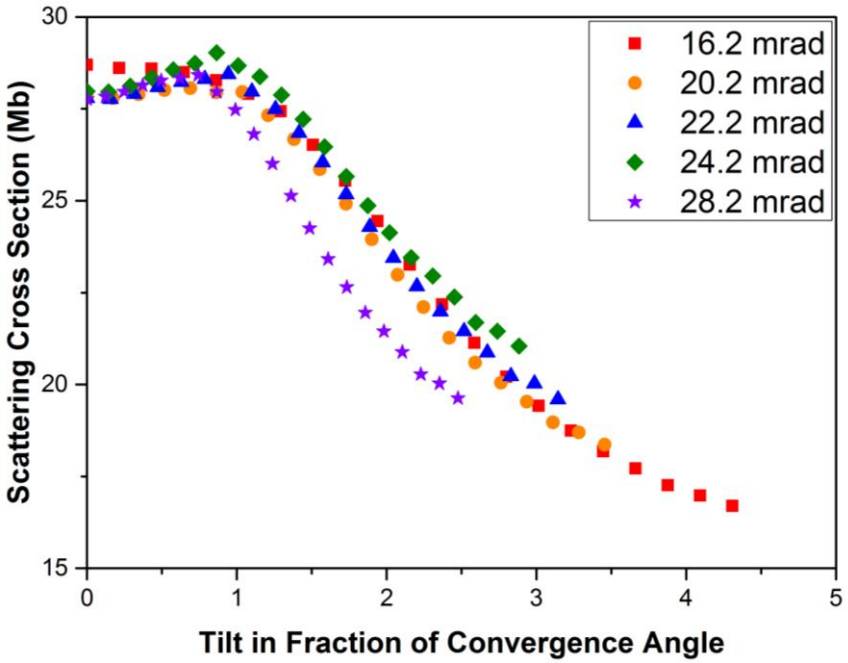


Figure 5.23 – A normalised graph demonstrating the dependence of the plateau region on the incident probe convergence angle for fixed detector collection angles of 35-190mrad. For each convergence angle the cross section remains roughly constant at small tilts but then drops off quickly after exceeding one convergence angle of tilt.

5.7.5. Tilt Variation with Thickness

Focusing on only three different detector collection angles allows us to explore how the decrease in cross section behaves for different sample thicknesses, as shown in Figure 5.24. It is important to note that the percentage decrease in cross section generally becomes larger in magnitude with increasing sample thickness. This can be explained through a combination of geometry, as the same sample tilt angle will produce a larger offset between the top and bottom atoms at larger sample thicknesses, and the effect that this larger offset has on

the channelling of the electron probe. As the plots are in percentage a uniform up-scaling to compensate for tilt would require the change in cross section to be constant with sample thickness (a horizontal line in Figure 5.24). However, single atom thickness will always demonstrate zero decrease in cross section with tilt. At larger thicknesses the curves flatten out which means for thicker samples a post-processing method of 'up-weighting' may be possible. Figure 5.24 demonstrates that a simple up-scaling is not possible; therefore we need to optimise experimental conditions for maximum robustness to tilt, although at larger thicknesses the curves flatten out which means for thicker samples a post processing method of 'up weighting' may be possible. The oscillations seen with thickness are due to the oscillations of the electron probe as it is channelling down an atomic column.[164] At a small tilt of 17.5mrad (1°, within the plateau region) the cross section only oscillates around a mean of zero, for the 35mrad detector (see Figure 5.24a). For the larger detector angles this variation is overlaid on a decrease in the cross section. Even at larger mis-tilts, beyond any plateau region (see Figure 5.24b), where we have a considerable decrease in the cross section, this still seems to be significantly reduced by using the smaller detector collection angle.

The example simulated images in Figure 5.24 are displayed on a common grey scale, demonstrating the significant increase in counts available for smaller detector angles. The images also show that when a sample is tilted sufficiently such that a decrease in cross section will occur, there is clear ellipticity of the atomic columns visible in the image. Therefore it is obvious to the user at the microscope if an image is unlikely to provide the basis for accurate quantification.

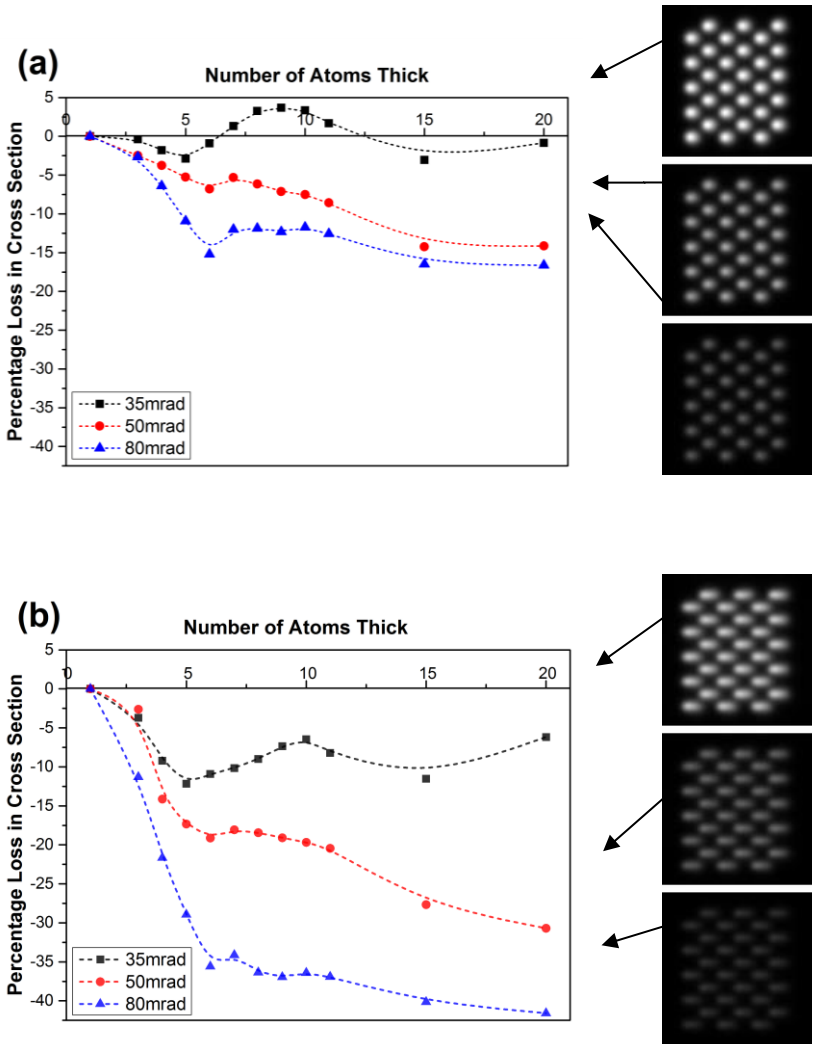


Figure 5.24 – The graphs shows the percentage decrease in cross section after (a) 1 degree tilt and (b) 2 degree tilt from a 110 viewing direction with increasing number of atoms. Examples of the simulation images from which the cross sections were calculated are displayed to the right of the graphs for 20 atoms thickness, present on the same grey scale.

5.7.6. Tilt in Bimetallic Systems

The ratio between elastic and TDS scattering changes for different elements. Therefore the conditions optimised to produce a plateau for one element may be less optimal for other elements (see Figure 5.25a). For lighter elements, like the nickel in Figure 5.25b shown here, we see a larger fraction of elastic signal or smaller relative fraction of the inelastic signal. This will result in the optimised

detector collection angle for tilt robustness being larger than the 35mrad angle for Pt, because the amount of elastic scattering increases at small detector angles.[156] The similarity between the Pd and Pt curves (see Figure 5.25a) demonstrates that, provided there isn't a larger variation than 40 in atomic number within one sample, it may be possible to simply optimise the tilt robustness to the average atomic number of the sample.

Finally I investigate the effect of bimetallic columns. We know from channelling theory that the location of an atom in an atomic column affects how much it contributes to the cross section. This is often referred to as a 'top-bottom effect' (see Figure 5.26). When tilting away from a crystal zone-axis, because we lose that channelling contribution to the cross section, the two atomic columns with the same composition and thickness (but different ordering) move much closer together in cross section value. At large tilts, where channelling is largely eliminated, ordering within an atomic column no longer affects its cross section value.

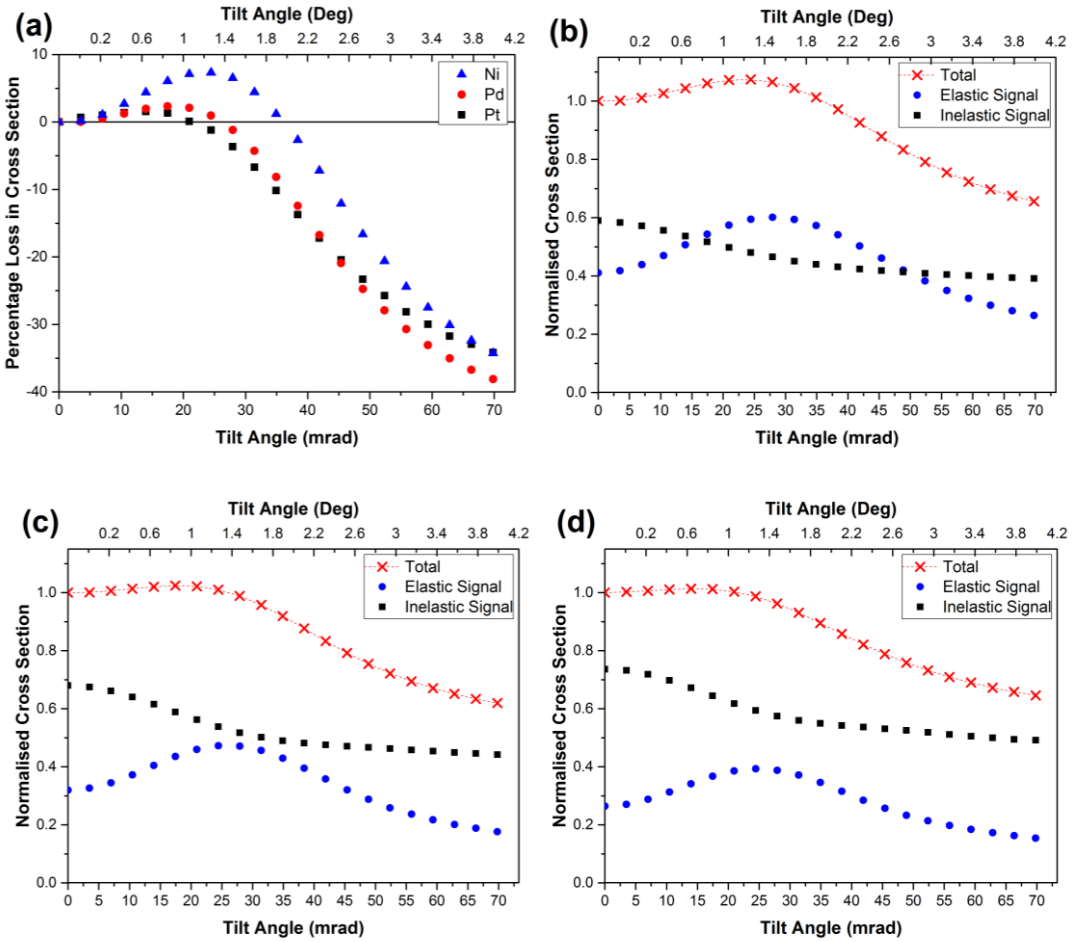


Figure 5.25 – Graph (a) demonstrates the effect of element on the tilt independent plateau. Fractional change in cross section for Ni (b), Pd (c), and Pt (d) has been separated into the elastic and inelastic components.

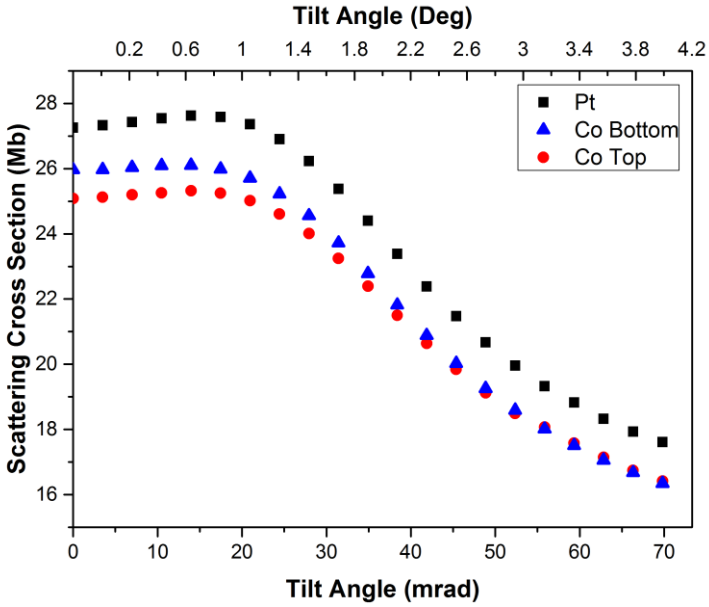


Figure 5.26 – Graph demonstrates the loss of top-bottom effect when tilting away from a 110 zone-axis of a 7 atom Pt crystal, with the top, red, or bottom, blue, atoms replaced with an atom of Co (ie 6 atoms of Pt plus one atom of Co). The red and blue points demonstrate top-bottom effects due to channelling when the crystal is on-axis but this separation reduces with increasing tilt. The detector collection angles for these simulations are 35-190mrad.

5.8. Conclusions

The scattering cross section is a robust measure for quantifying ADF STEM images. The process of integrating over well resolved atomic column provides a much more stable measure for comparison with simulations than using the peak or image contrast. The probe defocus, convergence angle and source coherence remain robust even in thicker crystals when the probe shape is likely to change through the sample thickness.

Channelling contributions to the scattering cross section of an atomic column provides additional intensity when the sample is on-axis but decreases with sample tilt as the atoms become less well aligned to the incident beam direction. This can cause an error in quantitative measurements, particularly with beam

sensitive samples where it is difficult to acquire an image of the sample exactly on-axis. The decrease in the scattering cross section at a given tilt does not scale uniformly with thickness making it impossible to compensate with a scaling factor across an image. I therefore recommend experiment design to minimise this error.

The dependence of cross section on sample mis-tilt can be diminished using a smaller detector collection angle. This is due to the balance between elastic and TDS contributions to the signal. The TDS signal drops off smoothly with tilt whereas the elastic signal initially increases with tilt due to the intersection with the Ewald sphere in reciprocal space. At smaller detector angles there is both a larger elastic contribution and a larger total scattered intensity which will provide signal to noise gains, assuming Poisson noise, which follows a $\sqrt{N}$ relationship. A larger probe convergence angle can also be used to increase the width of the mostly tilt-independent plateau as this broadens the Ewald sphere construction. With careful simulations it is possible to design a sample-specific set of experiment design guidelines to maximise this effect, whilst also gaining improvement in counts and therefore signal per unit dose on the sample. Care should be taken when using low angles if there is significant strain present as this could produce artefacts. However, in the case where tilt is the limiting factor on quantification accuracy this approach should be used.

This investigation has been carried out only looking at platinum; however we also know atomic number affects the degree of lensing which the atoms provide. Figure 5.25 shows that an inner angle optimised for Pt does not produce a plateau for lighter elements. However, I believe I have demonstrated the

general framework to understand the channelling nature of any material in order to obtain a sample-specific set of experiment design guidelines.

6. SINGLE PARTICLE RECONSTRUCTION METHODOLOGY

In this chapter, I discuss the method for analysis and quantification of nanoparticle images; from acquiring the image at the microscope through to the 3D reconstruction, and the assumptions involved therein. The automation discussed in this chapter is critical in the work towards high throughput analysis in order to reconstruct a statistically representational set of nanoparticles which could then be related back to some of the more bulk averaging characterisation techniques discussed in section 2.3 on page 17. Being un-representational of the whole catalyst system is one of the primary arguments against using electron microscopy and the key gap of information between this and other characterisation techniques. Working towards automation and being able to carry out this process on many particles will help to close this gap.

Once the methodology has been outlined and the main sources of error discussed I apply use of this technique to a selection of Pt nanoparticles and then Pt/Ir mixed alloy nanoparticles. The Pt/Ir mixed alloy sample has only a 16.7% Pt content which means the particles are typically larger in diameter for a comparable catalyst cost. The larger particle size results in increased stability under the beam and larger facets in the final reconstructed shape. Both samples are then compared with the structure predicted by a theoretical Wulff calculation, the truncated octahedron.

6.1. At the Microscope

The primary requirement of atomic resolution nanoparticle imaging is to select particles as close to on-axis as possible. As discussed in section 5.7 (page 121) it is important to be imaging at a detector angle within the plateau region where the scattering cross section is robust to small sample mis-tilt. Minimising overlap with neighbouring particles is essential for improved accuracy of the background subtraction procedure. The background or carbon support should be as thin as possible in order to minimise background contributions, although this should not be done at a cost of the particle stability. Ideally particles should be on the edge of the carbon black support overhanging a hole in the carbon film; however this often results in the whole carbon black support vibrating or moving under the electron beam, making such particles too unstable to image at atomic resolution. A compromise between background thickness and stability must therefore be found.

A detector map needs to be acquired with brightness and contrast settings that keep the detector within the linear regime and at the same values as those used to acquire the experimental image of the particles using the method outlined in Chapter 4. The potential advantages of a swung pencil beam, over that of using a confocal arrangement, have been discussed. However, the reproducibility of mapping with a pencil beam is not fully understood, providing a potential source of unknown systematic errors for a small accuracy improvement. As such the confocal method, with flux weighting, has been used for the duration of this thesis. It has been demonstrated to show good agreement with simulations and other established quantification techniques.[160]

Finally, an image of the electron flux needs to be recorded (see Figure 6.1a). It should be taken through a region of sample of comparable thickness to all the experimental images with a stationary probe and by replacing the ADF detector with a CCD. Only one electron flux map is needed for any given sample and microscope combination.

6.2. Automated Integration Code 'Absolute Integrator'

In order to be able to process large numbers of particles a MATLAB code was developed in collaboration with Lewys Jones[16] to automate the process of integrating over each atomic column within an image. 'Absolute Integrator' was used as the primary method for ADF data analysis within this thesis, in particular for the background interpolation and subtraction and the ability to analyse the hundreds of atomic columns in any experimental particle image, in a matter of minutes. The description of the code processes below has tried to stay as true to the ordering in which these processes happen within the code as possible.

6.2.1. Detector Calibration

The user is first asked to provide a detector map for the microscope which is imported and the centre found through a process of thresholding and then eroding the active region. The choice is then available to use the original thresholding method or the new flux weighting method for calibration.

[16] The latest version of the Absolute Integrator Code is available to download from www.lewysjones.com/software/

For the thresholding method two points on a histogram of the image pixels must be selected to define the active region and the background region (see Figure 4.1 on page 78 and Figure 4.2 on page 79). The average intensity from the vacuum is the 'black level' and the average intensity from the active region gives the detector counts. The difference between the two provides us with the detector sensitivity or 'gain'.

6.2.1.1. Analysis of the Electron Flux Exponent

The flux weighting method[160] requires importing of a 2-dimensional (2D) electron flux pattern taken on the CCD, from a region of comparable sample thickness. The 2D flux map is presented on a logarithmic scale (see Figure 6.1) in order to make the high angle scattering more visible without saturating the bright field disc. Next the centre is found through a threshold and erosion approach and the electron flux pattern plotted in radial coordinates (see Figure 6.1b). The user then manually selects the point best representing the average cut off value; if a variation in the value is seen e.g. due to a misalignment of the centre of the flux relative to the cut-off or the presence of an image corrector,[205] the average cut-off value is selected. The 2D flux map is then radially averaged to create a 1-dimensional flux profile (see Figure 6.1c). With the scale in this profile calibrated by knowing the convergence angle of the bright field disc, a power law is fitted between the inner detector angle and the manually selected outer cut-off.

Using the approach derived in [160] the power law fitted to this flux profile is used to modify the detector analysis described above such that we are left with values

for the ‘gain’ and ‘black-level’, which take into account the sample flux and the asymmetric nature of our detector. The experimental image can then be imported; each pixel in the image has the ‘black-level’ subtracted and is then divided by the ‘gain’, incorporating any current ratio as outlined in Chapter 4. Any remaining counts within the image are due to the sample (including both the particles and the support) and any small fluctuation remaining from Poisson noise.

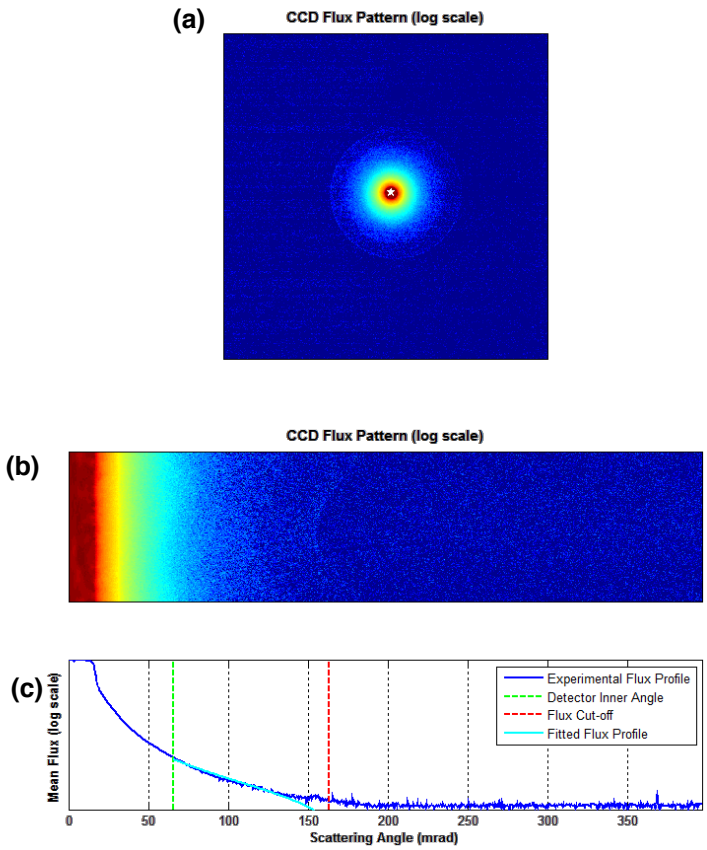


Figure 6.1 – 2-dimensional flux map presented on a logarithmic scale in Cartesian coordinates (a) and radial coordinates (b). The radially averaged flux profile (c) is used to fit an exponential curve between the inner detector collection angle and the cut off angle.

6.2.2. Image Calibration

Once the experimental image has been imported and normalised it is important to calibrate the magnification. The scattering cross section calculation includes multiplying through by pixel area, so it is dependent on the square of the pixel width, making accurate magnification calibration critical.

The 'Absolute Integrator' code, carries out the magnification calibration in Fourier space as the inverse relationship between an image and its Fourier transform (FT). The user selects two spots in the FT representing the same spacing type (Figure 6.2). The pixel width is then evaluated using the maths outlined in Appendix C on page 268.

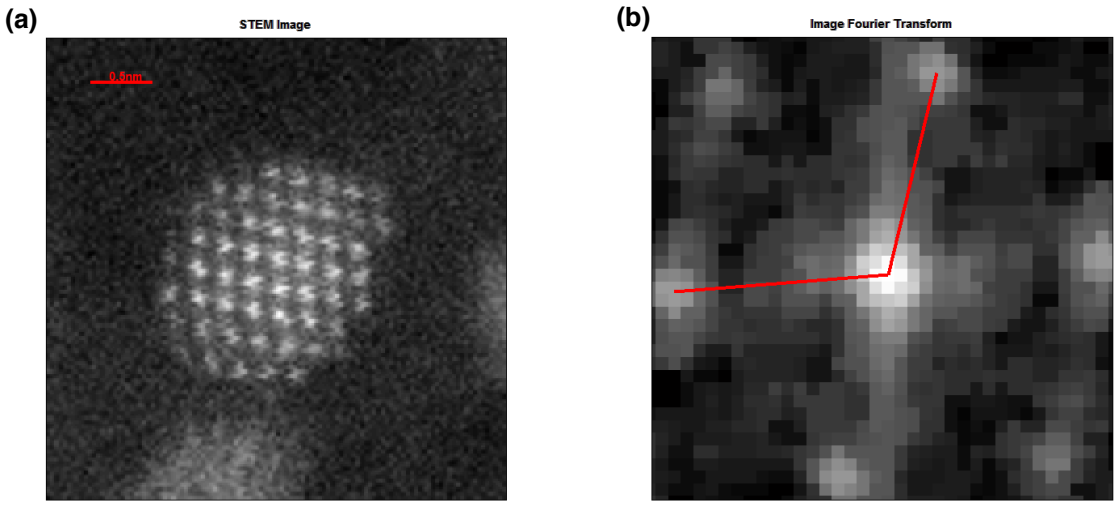


Figure 6.2 – Magnification calibration of an experimental image (a) using its Fourier transform (b). The selected points represented <111> type directions for a <110> oriented FCC crystal.

6.2.3. Peak Finding

The next step after calibrating the images (both the intensity and the magnification) is an accurate peak finding routine to establish the location of

each atomic column. An automated peak finding method is essential for high throughput analysis because manual selection is both time consuming but could also incorporate a user bias.

The method used in ‘Absolute Integrator’ designed by Lewys Jones uses a square region of interest (ROI) centred around each pixel in the image in turn. The width of this ROI should be around one atomic spacing to ensure that it contains the majority of any given atomic feature. Within the ROI a 2D Gaussian is fitted. Any Gaussians with height less than zero can be excluded as an ADF image contains bright peaks on a dark background. Any genuine features will have a width wider than one pixel but narrower than the region of interest. The offset distance from the centre of the ROI should also be as small as possible. These three restrictions are applied to the 2D Gaussians results. A binary image is then created by plotting an ROI around every pixel in the image in turn which fulfils all three requirements, resulting in an image with blobs, of a few pixels wide, demonstrating the location of genuine features. Erosion of these blobs yields the pixel coordinates of each atomic column.

The tuneable parameter of this method is the size of the ROI region which can be optimised in order to reduce the prior knowledge needed. Such an ROI is attempted centred around each pixel in the image in turn and the resulting number of features plotted against ROI size (see Figure 6.3). At ROIs smaller than the true feature spacing there will be an overestimate to the number of peaks in the image as background noise may be mistaken for genuine features. At ROIs larger than the feature spacing there will be an underestimate of the number of peaks as the atomic column widths become significantly smaller than the ROI region. In between these two extremes lies a stable plateau where there

is little change over the number of peaks identified. These are then the genuine peaks within the image.

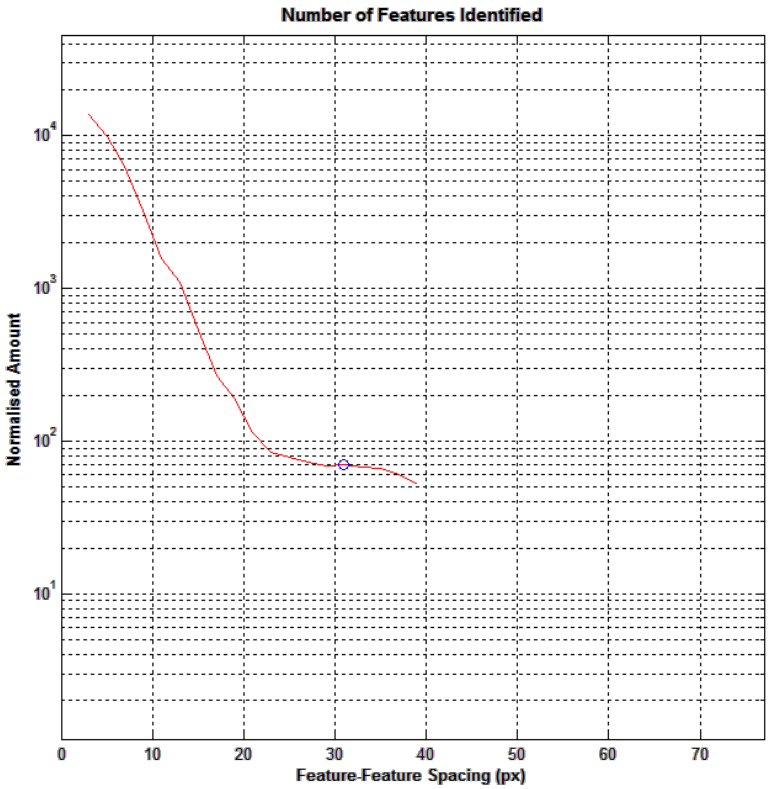


Figure 6.3 – Number of identified features as a function of ROI width used during the peak finding routine.

6.2.4. Background Subtraction

The three-dimensional carbon support provides a non-negligible spatially varying background in the experimental images which must be taken into account for accurate quantification.

The method used for background subtraction in this work designed by L. Jones mimics those used during fine art restoration. Once the peak finding routine is complete each peak is dilated by 1.5x the ROI size in order to form a mask,

which defines regions of the image containing sample and regions which can be considered to be only background. The intensity outside the mask is used to estimate the background intensity within the mask using a technique known as iterative Gaussian ‘in-painting’. The solution to the Laplacian is used to minimise steps at the mask boundary. The whole background image is then blurred with a 2D Gaussian the size of the feature spacing. After each blurring the known values for the background outside the mask are re-imposed. Iterations of this process are carried out until the change in background between iterations becomes very small (see Figure 6.4). This is a realistic method of background interpolation as the carbon black support in these samples varies relatively smoothly in thickness without large steps or abrupt changes. The background images for all the Pt particles investigated are included in Appendix D, page 270.

The option for a user defined addition to the mask is available for when a nearby particle is sufficiently close that it might cause leakage of higher intensity into the background estimation. This extra mask has been used at the bottom of Figure 6.4a.

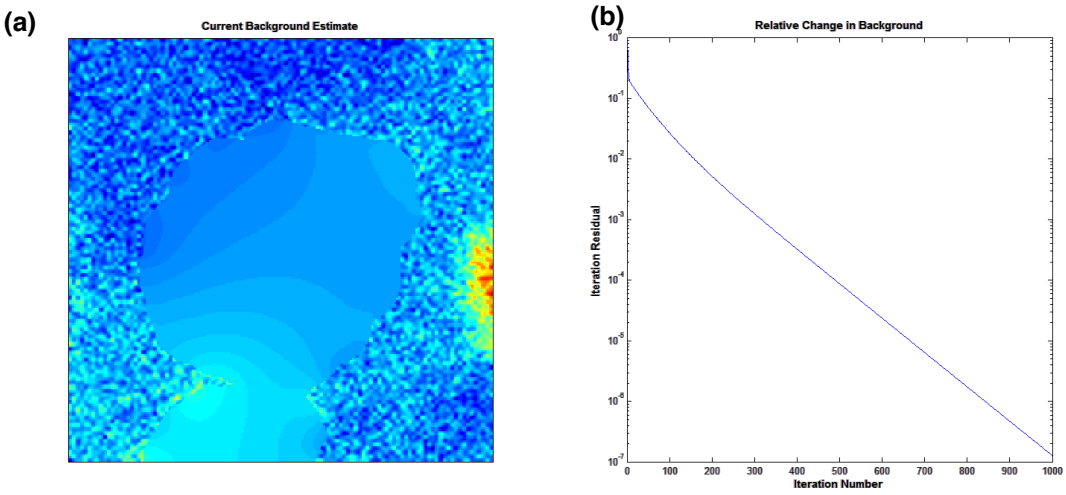


Figure 6.4 – The background subtraction image for the example particle which goes through a number of iterations (1000 in this case). (a) shows the final image used for background subtraction whilst (b) plots the relative change per iteration number presented on a logarithmic scale.

6.2.5. Integration

Once the background subtraction has been carried out all that remains is to integrate the intensity over each atomic column. Voronoi polygons are a fast method for segmenting images into integration regions (see Figure 6.5). Once the peak locations are known, each pixel within the image is assigned to the nearest peak. An upper integration limit (usually the ROI size) is applied to prevent bowing out into the vacuum at sample surfaces. In this way, no prior knowledge about any crystallography or defects is imposed in the final image by the image segmentation method.

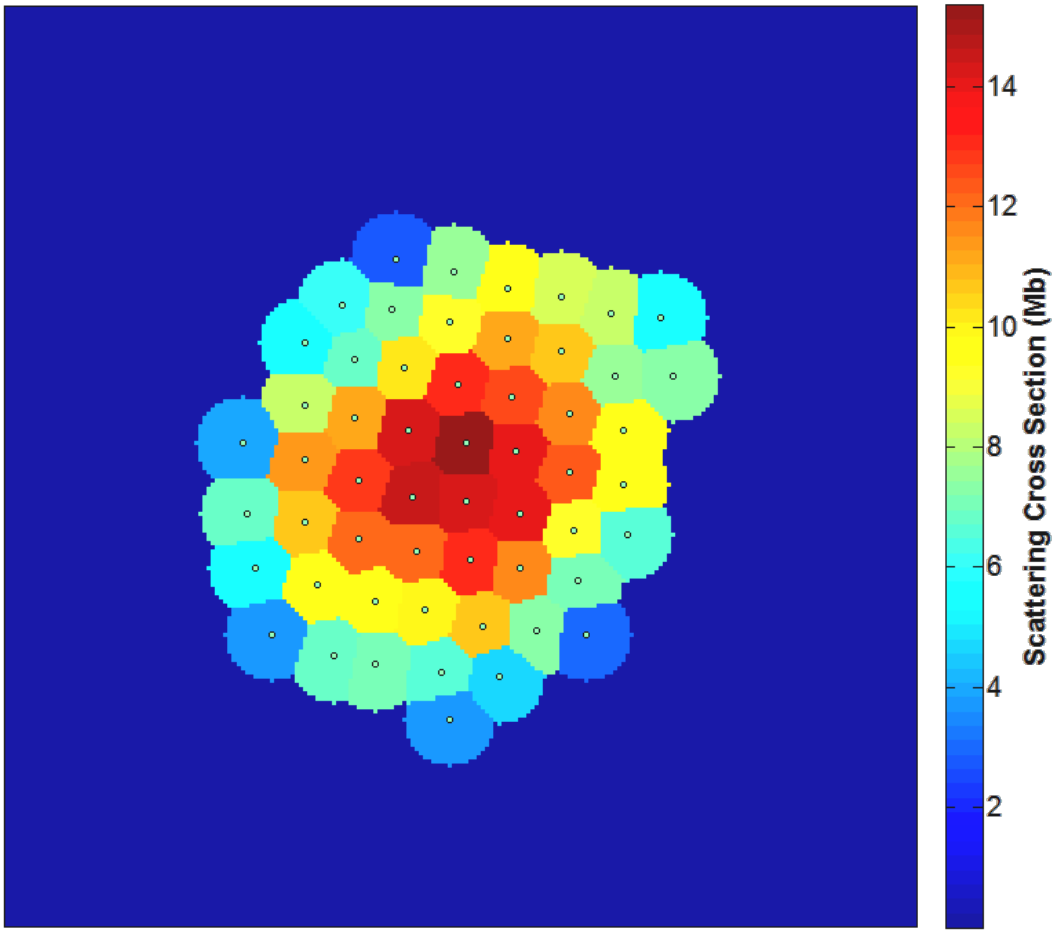


Figure 6.5 – Cross section map of the example Pt nanoparticle. Each distinct colour region around an atomic column is the Voronoi cell used for the integration.

6.3. Converting to Atom Counts

Finally the integrated intensity in each Voronoi cell is converted to the scattering cross section units of Megabarns (Mb). Each column is then simply assigned to the nearest number of whole atom counts (see Figure 6.6) based on direct comparison with a simulated library for the same crystallographic zone-axis (see Figure 5.11 on page 116). The crystal zone orientation affects the atom spacing in the beam direction which will in turn affect the degree of channelling they produce. For thicknesses of 12 atoms and below the zone-axis makes very little

difference to the atom assignments; however at larger thickness it is essential for improved accuracy.

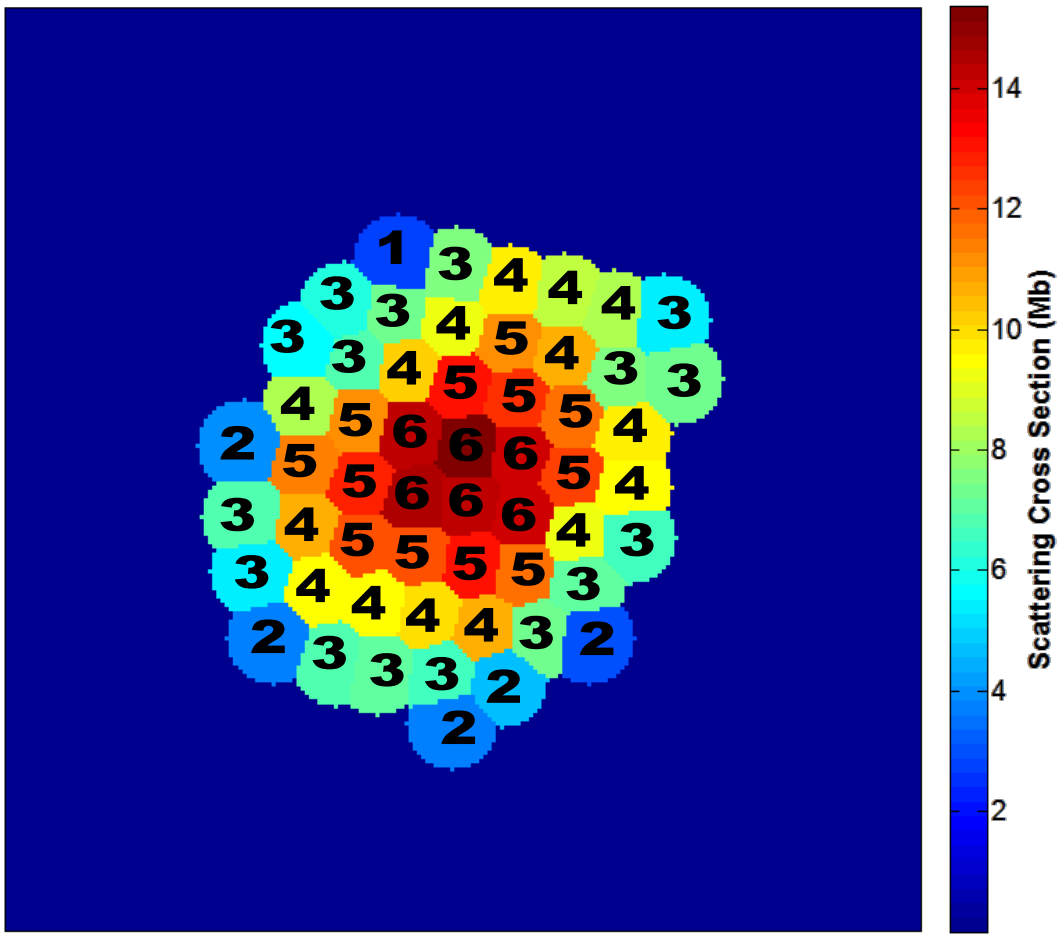


Figure 6.6 – Atom number assignments for the example Pt particle using the <110> simulation library.

6.4. 3-Dimensional Reconstruction

Armed with the peak positions and the number of atoms within each atomic column it becomes possible to reconstruct a plausible 3D structure (see Figure 6.7). Using the following assumptions:

- The particle is entirely FCC with all the atoms located on crystallographic sites.
- No voids or vacancies are present in the reconstructed volume.
- The particle is convex and aims to minimise surface steps and ad-atoms.

Voids or vacancies are statistically unlikely due to the small size of the particles being evaluated and any spontaneously developed vacancy will likely migrate out to the particle surface in order to minimise the total energy. Pure Pt particles are particularly known for being FCC single crystal in their structure, unlike other particles (for example Au nanoparticles), which have been seen to contain several twins and defects. Our assumptions here do neglect any particle-support interactions as the particle is assumed to be in vacuum. It is unknown whether or how the carbon support might affect the 3-dimensional structure of nanoparticles making it a wider problem beyond the scope of this thesis.

Using the Crystal Maker™ software a Pt nanocube crystal was created with FCC crystal structure based on knowledge of bulk Pt. It is then possible to reconstruct the 3D structure by 'cutting out' the particle shape from this nanocube. The 'cutting out' procedure is carried out by removing atomic columns until the cube has the same silhouette in the beam direction of the experimental image.

A crystal plane is selected from the centre of the particle and atoms are removed evenly from the top and bottom of the columns until they have the correct number of atom counts, whilst minimising the size of steps from column to column. This approach is repeated with the next crystal plane. When there is a choice between removing and atom from the top or the bottom of the column, the atom with the most nearest neighbours is kept. Each atomic plane is

analysed in turn working outwards to the edge until the whole particle is reconstructed.

In Figure 6.7 the reconstructed particle demonstrates a {111}:{100} surface ratio of 1.66; preference for {111} facets is expected due to difference in energy of these facets.[206] The validity of the reconstruction can be estimated by investigating the particle facets which are not parallel to the beam direction; looking at the degree of faceting which is non-parallel. Any facets parallel to the beam direction have been enforced due to the silhouette of the original ADF image so will be present regardless of the accuracy of the atom counting.

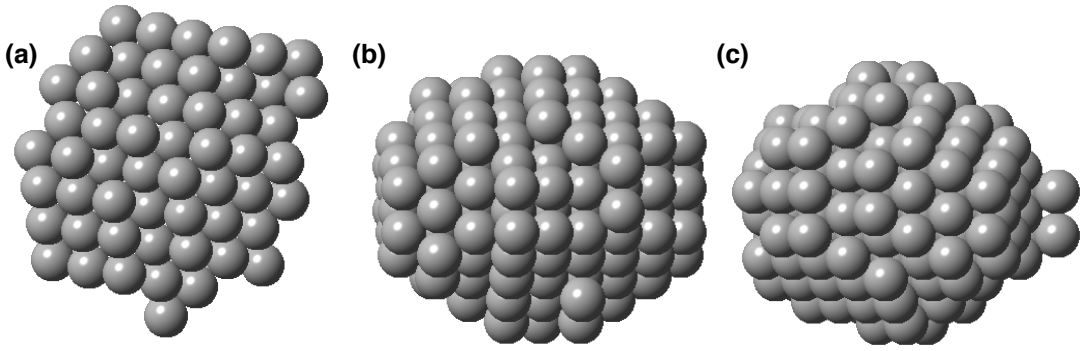


Figure 6.7 – 3-dimensional reconstructions of the example Pt particle; shown parallel to the beam direction (a) and perpendicular to the beam direction at two angles 90 degrees from each other (b) and (c).

6.5. Error Analysis

Whilst comparison with the Wulff construction could provide a qualitative estimate of how realistic the particle reconstructions are, a more thorough analysis of the sources of error is essential for a really quantitative understanding. Singhal et al.[141] predicted that their random errors were produced by the sample and systematic errors originated from asymmetries of

the detector and the size profile of the probe. Using this they tried to fully characterise their microscope in order to minimise systematic errors. The primary sources of error are discussed below and summarised in Table 6.1 with particular focus to those which are likely to provide the largest contribution.

Source of Error	Magnitude
Magnification	5.9%
$\sqrt{N}$ Counting statistics	negligible
Detector Angle	3.5%
Probe current	0.5%
Gun Emission Current	0.4%
Peak Finding	negligible
Convergence Angle	negligible

Table 6.1 – Summary of the main sources of error and their estimated magnitude (as relative errors).

6.5.1. Pixel Width

The error associated from mis-clicking the correct diffraction spots in the FT is ±1 pixel which is minimal, resulting in a relative error in the final pixel area of ±5.9%. This could be further improved by incorporating a Gaussian fitting sub-pixel refinement to the peak fitting.

A much more significant systematic error occurs for bimetallic particles where the lattice parameter is either unknown, or there is a significant degree of strain within the particles.[54] The lattice parameter for Pt is 0.392nm giving a $d_{(111)} =$.[54] The lattice parameter for Pt is 0.392nm giving a $d_{(111)} = 0.2263nm$, whereas the equivalent spacing in Co in 0.2507nm. Not knowing the lattice parameter in a Pt-Co alloy could produce a 20% systematic error in the pixel

area and therefore the cross section. In this case a pure standard should be used to calibrate the magnification separately and then the pixel size simply incorporated into the cross section calculation by entering it into the code manually.

6.5.2. Poisson Noise Statistics/Dose

There is a minimum dose necessary to provide high enough SNR in an ADF image such that the materials structure can be directly interpreted. Perhaps unsurprisingly this is also the case for accurate ADF quantification. In the cross section approach this dose dependent error can be estimated by assuming Poisson noise statistics and therefore a $\sqrt{N}$ error of the raw counts. Integrated raw counts for each atom column in particle 1 are of the order 1×10^{12} making the $\sqrt{N}$ error a negligible 1×10^{-4} %. Unlike in the EDX quantification the counting statistics are not accuracy limiting.

6.5.3. Scan Noise

All STEM images exhibit suffer from instabilities of the electron probe due to the serial acquisition nature of the technique. A typical STEM image will take tens of seconds to acquire. During which the low frequency distortions can perturb the image, locally changing the magnification. This will understandably affect quantification results as the integrated intensities will change with these distortions. An unstable probe will spend more or less time with certain columns of atoms resulting in a higher or lower scattering cross section than expected.

A further systematic study is needed to understand exactly how much image instabilities and scan noise will affect quantification results, and how much new non-rigid registration methods could be used to combat it.[207][208]

6.5.4. Background Subtraction

Background subtraction carried out in the manner discussed above must be done with care so as not to introduce errors or artefacts not present in the original particle. Errors include the mis-selection of a faint surface atom column leading to a much higher intensity at the edge of the mask. Extra intensity at the boundary bleeds into the background during the Gaussian blurring process resulting in the loss in intensity in the final background counts.

If no background subtraction is incorporated there could to be a systematic error in the atom counting equivalent to +1-2 atoms, although this is dependent on the thickness of the carbon support behind the particle. Figure 6.8 shows that difference in atom assignments with and without background subtraction can be up to 2 atoms. Figure 6.10 shows that the background subtracted from the original experimental image in Figure 6.9 appears to be roughly linearly ramping from left to right. This can be confirmed by calculating the vertically averaged mean and investigating the difference in atom counts resulting in a ±1 atom error in counting, which has been verified by statistical analysis by A. De Backer et al.[151]

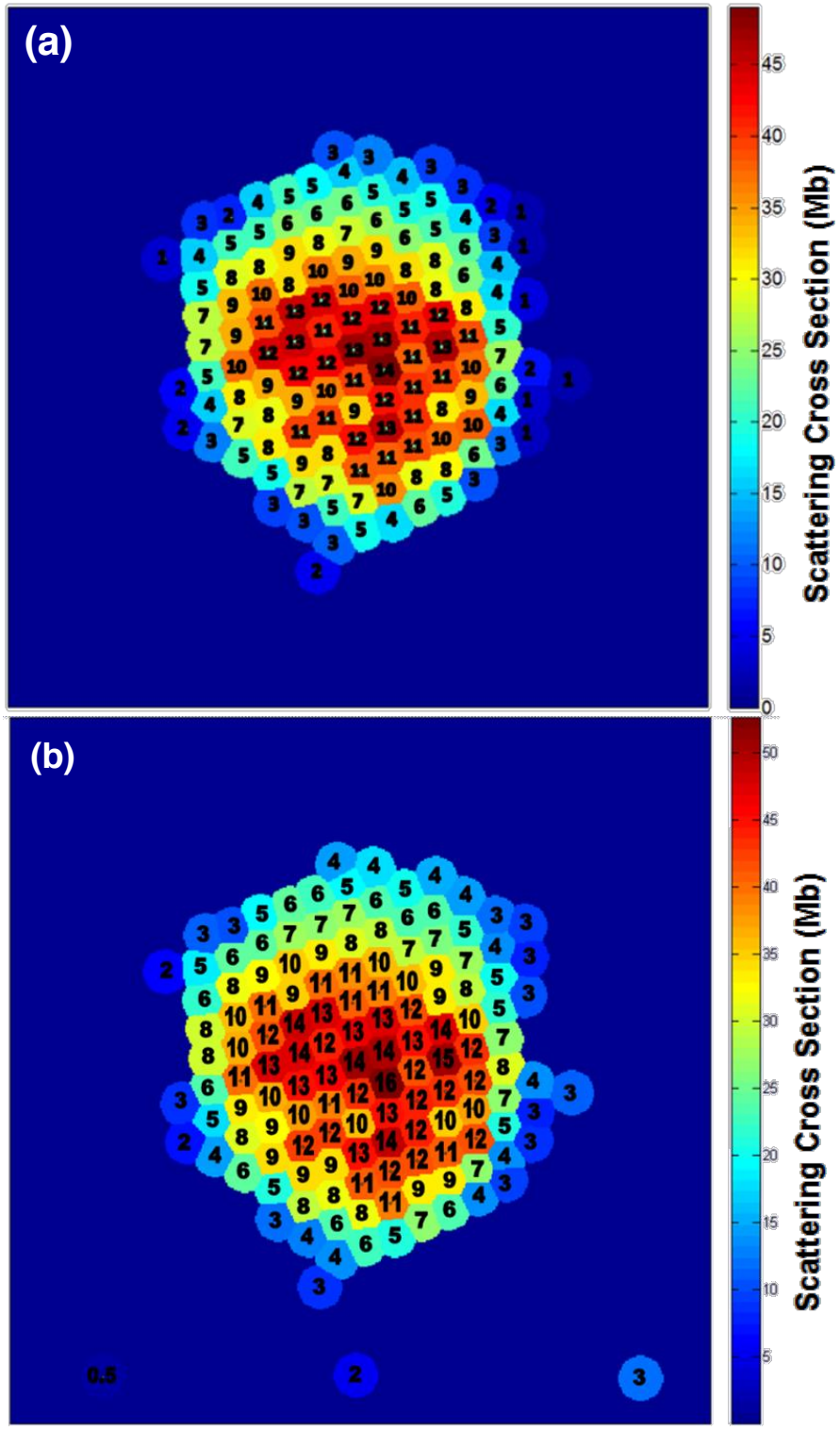


Figure 6.8 – Assignment of atom counts for a Pt/Ir nanoparticle with (a) and without (b) background subtraction. Along the bottom of (b) are three manually added points where no real atomic columns were present, showing the addition to atom counts possible from excluding the background contribution.

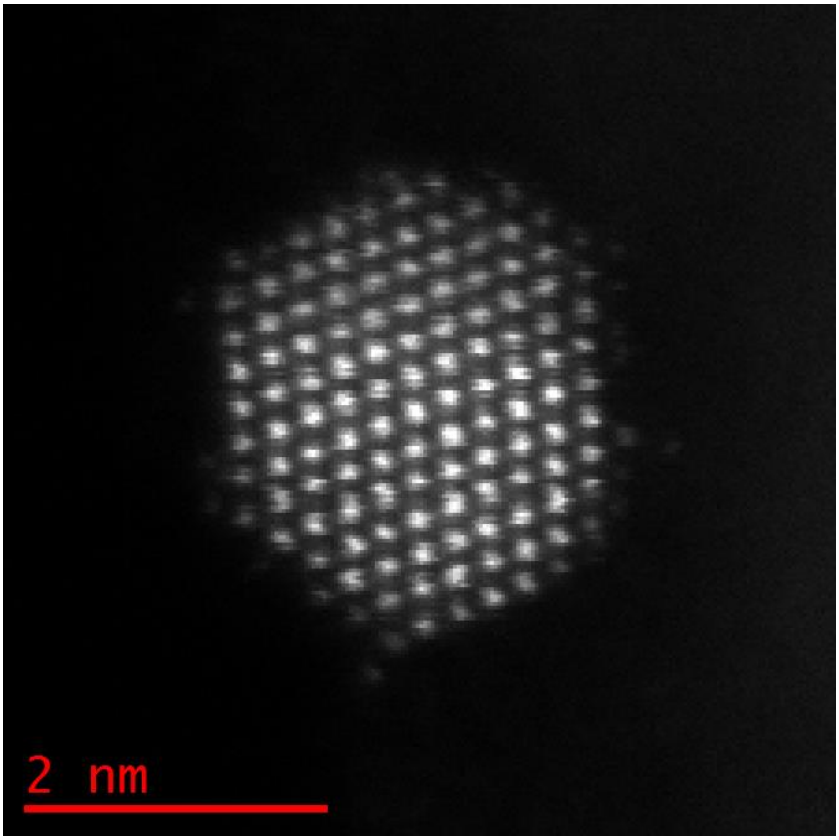


Figure 6.9 – Experimental image of a Pt/Ir alloy particle hanging off the edge of the carbon black. As such the background intensity is much higher on the right hand side of the image than the left hand side. Image taken by Armand Béché.

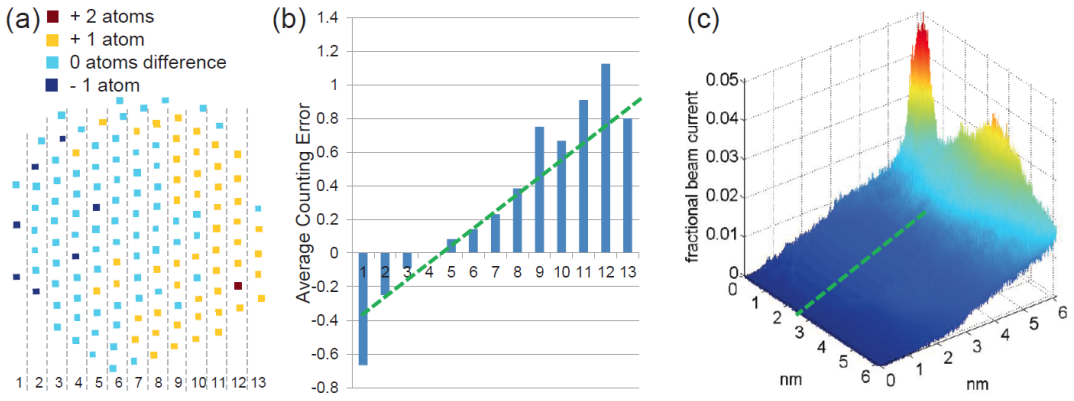


Figure 6.10 – Analysis of the contribution from the carbon support on atom counting of a PtIr nanoparticle. (a) The error observed when the carbon intensity is not considered. (b) Vertically averaged error. (c) The observed carbon contribution in the background-only image. Figure courtesy of Lewys Jones.

6.5.5. Convergence Angle

The accuracy of library simulations has already been discussed, in terms of making sure the simulations are realistic and have converged. However those simulations are only as accurate as the microscope parameters which are used to create them. In particular the detector collection angle and probe convergence angle need to be experimentally determined for the microscope using the CBED of a known sample.

From the simulation investigations carried out in Chapter 5 we know convergence angle has no affect for thin specimens. Indeed an error of ±10% can easily be accommodated for in the measurement without affecting the scattering cross sections. Therefore convergence angle is not a critical source of error. However, the convergence angle calibration is used to determine the detector collection angles as outlined in Section 4.4 on page 84. Therefore an error in the convergence angle measurement will translate across to the detector angle measurement error.

6.5.6. Detector Collection Angles

Scattering cross sections are hugely dependent on the detector collection angles used to simulate the library values because this affects the detector size and therefore the angular range of scattering which is being collected. Using the modified detector angle calibration method described in section 4.4 a significant accuracy improvement has been found in the angle calibration.

Examining the detector map more closely yields a slight asymmetry to the circular detector centre (see Figure 6.11) resulting in a relative error of 1.8% to

the measured inner detector angle, which translates to a 3.5% relative error in the scattering cross section assuming the outer detector angle (or outer cut off) remains constant.

However, if the main source of error in the detector calibration is thought to be in the calibration of the CBED then the outer and inner angles would vary by the same percentage. An increase in inner angle and therefore loss in cross section also produces an increase in outer angle and therefore a small increase in cross section. This results in a much lower estimated error in cross section of 0.9% (see Figure 6.12).

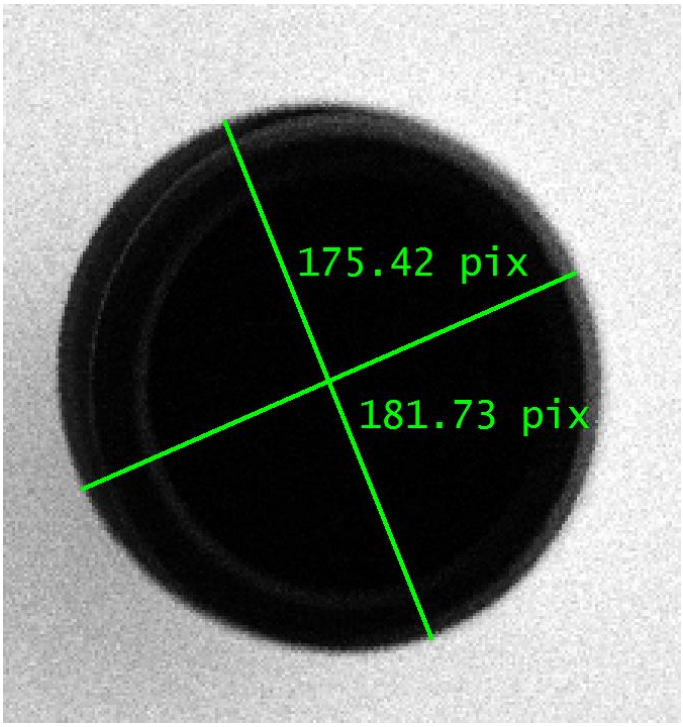


Figure 6.11 – Enlarged image of the ADF detector demonstrating a small amount of ellipticity of the central hole.

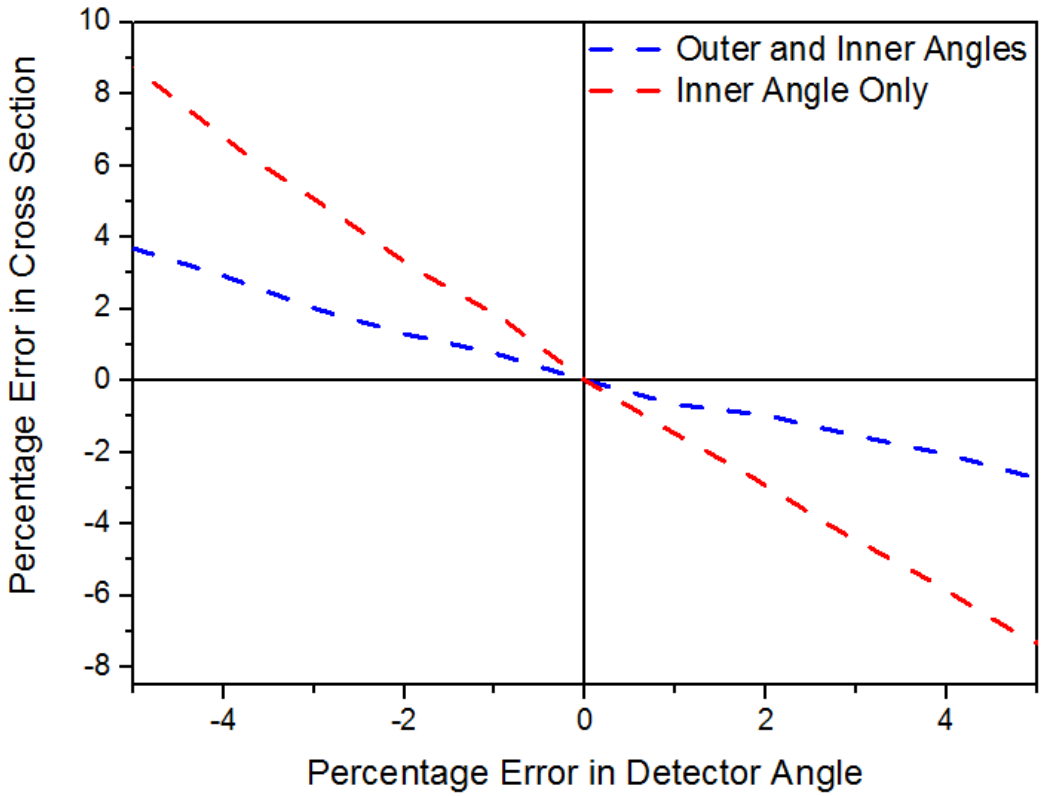


Figure 6.12 – A graph showing the percentage error in cross section resulting from a percentage error in detector angle. The result from assuming the inner and outer angles of the detector scale together is shown in blue and when the outer cut off is kept constant is in red.

6.5.7. Summary

Combining all the sources of error discussed above results in a total relative error of 6.89%. This error is thickness independent as all the contributing errors originate from the microscope calibrations. However, the library of scattering cross sections flattens out at larger sample thicknesses due to absorption beginning to take effect. This means the percentage difference between atom counts becomes smaller whilst the overall error remains constant, resulting in thickness limitations to the atom counting precision (see Figure 6.13).

In Figure 6.13 where the horizontal dashed black line (our experimental error) intersects with the three curves indicates the limits for ±0.5, 1 or 2 atoms

counting precision. Up to 6 atoms thickness better than ± 0.5 atoms precision can be achieved. Above 14 atoms thickness our counting precision becomes ± 1 atoms. Above 20 atoms the atom counting precision becomes ± 2 atoms or worse with increasing thickness. Changing the crystallographic zone-axis to <100> lowers these atom counting accuracy limits to one fewer atoms (see Figure 6.14). This is due to the smaller difference between atom counts in the simulation library resulting from reduced channelling due to increase atomic distances parallel to the beam direction.

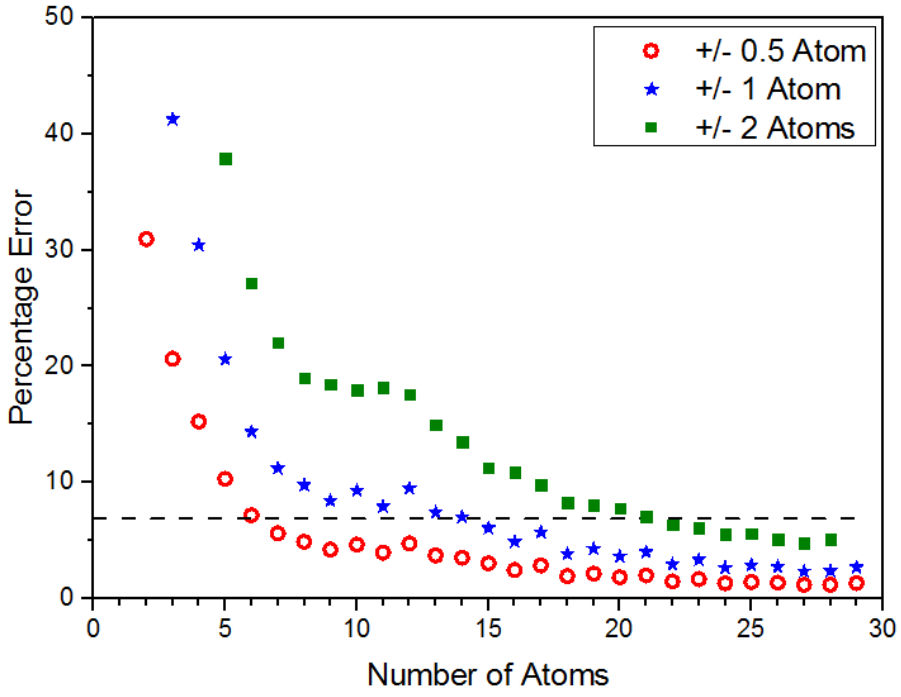


Figure 6.13 – Estimate of the atom counting error with increasing sample thickness for a <110> zone-axis crystal. The horizontal dashed black line indicates the calculated error in the experimental data. Where this line intersects with the curves indicates the various limits of atom counting accuracy.

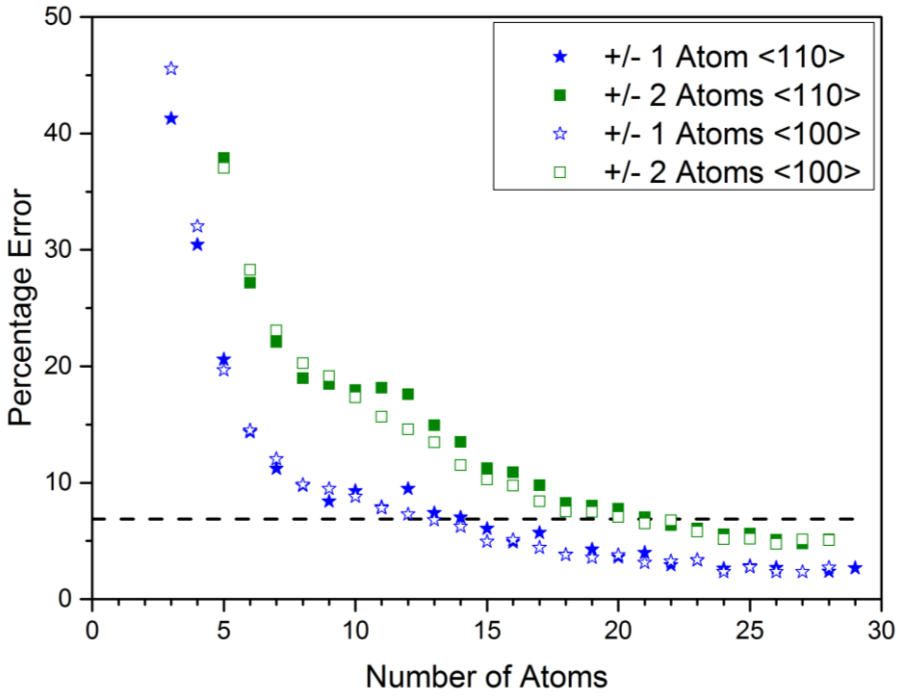


Figure 6.14 – Estimate of how the crystallographic zone-axis affects the atom counting accuracy. The horizontal dashed black line indicates the calculated error in the experimental data. Where this line intersects with the curves indicates the various limits of atom counting accuracy. Viewing down a <100> zone-axis reduces the limits of atom counting accuracy to one fewer atom counts than seen for the <110> direction.

Any instability in the extra high tension (EHT) used to produce the high voltage for the electron beam could also provide a source of error in detector calibration measurements. I have made use of Bragg's Law to calibrate the CBED pattern and used the manufacturer EHT. An error in the EHT would cause an error in the wavelength used in the calibration. A systematic error in the EHT would also relate to a systematic error in the simulation library. Such an error is estimated to be small in comparison to the other errors discussed but would be worth investigating further.

6.6. Reconstructed Nanoparticles

6.6.1. Pt Nanoparticles

Using the method outlined above it becomes possible to reconstruct several Pt nanoparticles from the sample of 20wt% Pt on Ketjen (carbon support). Figure 6.15 shows the particle size distribution of over 368 particles from this system taken from a combination of six lower magnification images similar to the one shown in Figure 6.16. Highlighted on this histogram are the analysed Pt structures presented below in order to give an idea of how representative these reconstructed particles are of the whole catalyst system. Four Pt particles of different sizes have been analysed and reconstructed (see Figures 6.17-6.20).

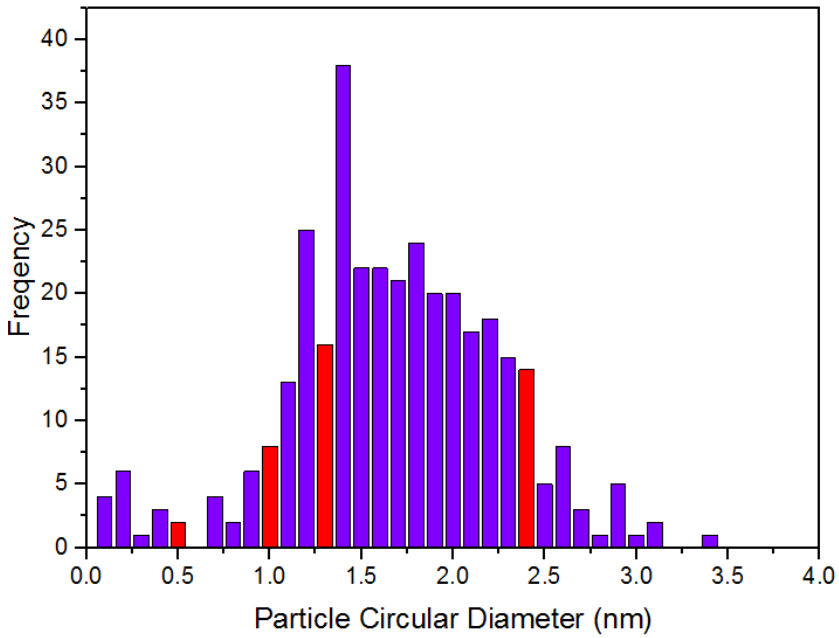


Figure 6.15 – Particle size distribution taken from several lower magnification images highlighted in red shows the average circular diameter of those particles selected for quantification and reconstruction.

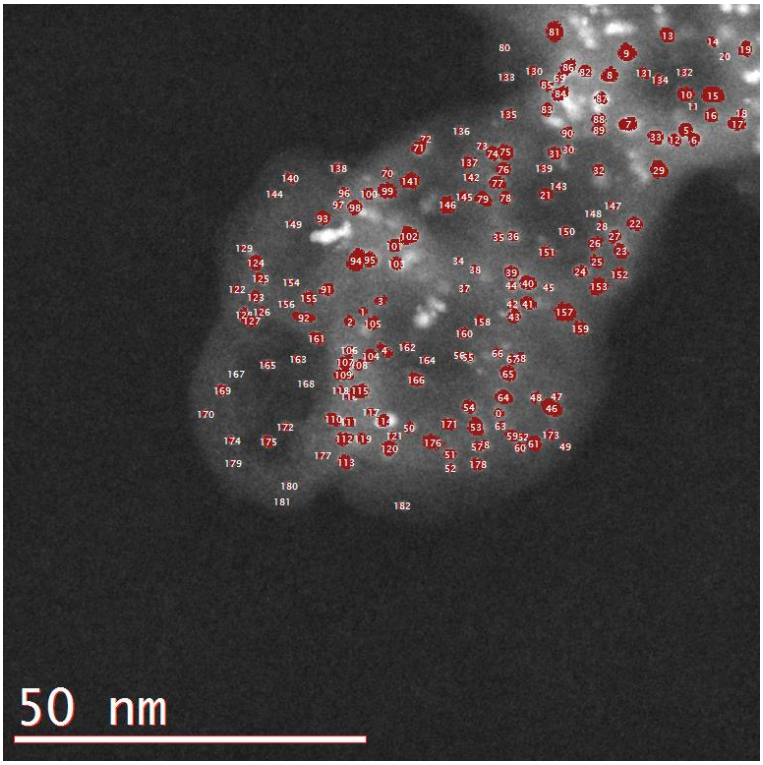


Figure 6.16 – Example low magnification image used for PSD where particles have been selected by median filtering and then thresholding the image. Each red spot corresponds to a selected and analysed particle.

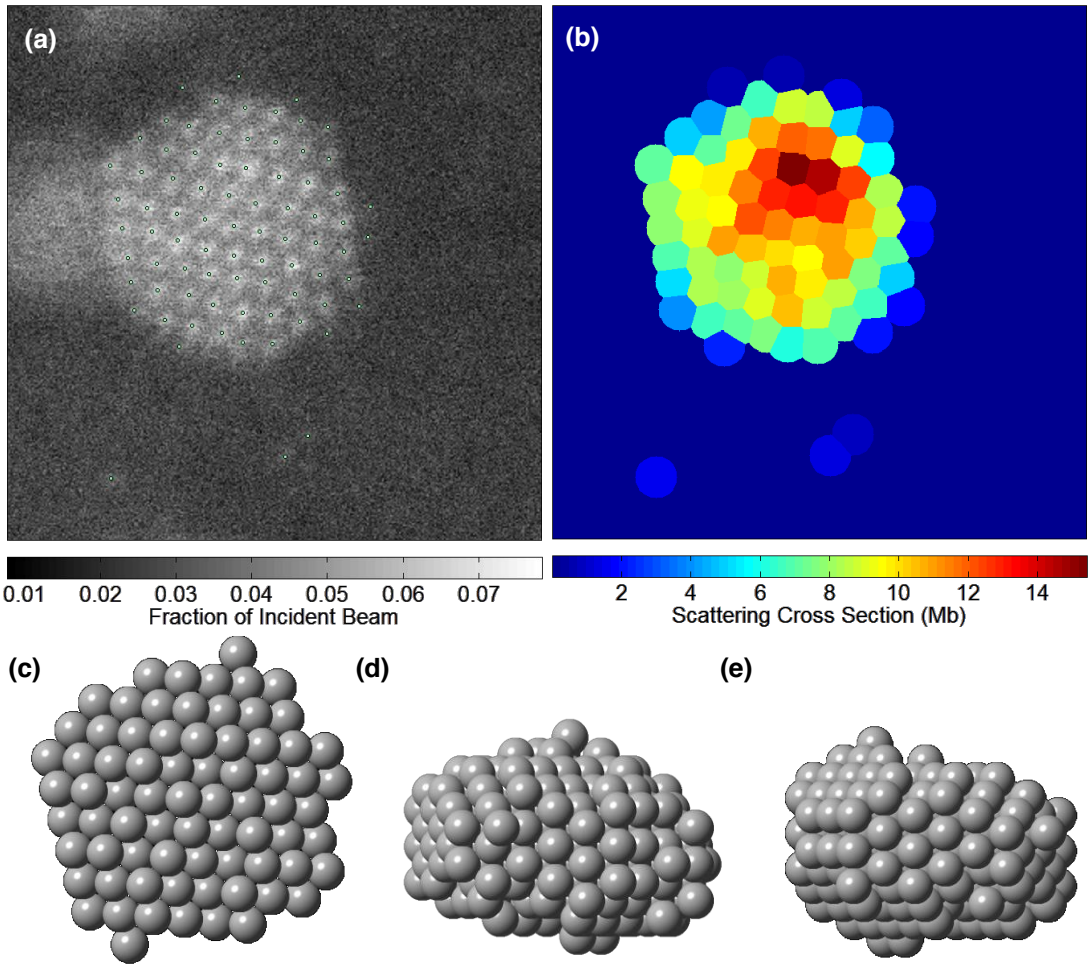


Figure 6.17 – Particle 2 - Normalised experimental ADF image (a) of a Pt particle, viewed down a <110> zone axis, with the calculated cross section map (b). The 3D reconstructed particle is shown parallel to the beam direction (c) and perpendicular to the beam direction at from two angles 90 degrees from each other (d) and (e).

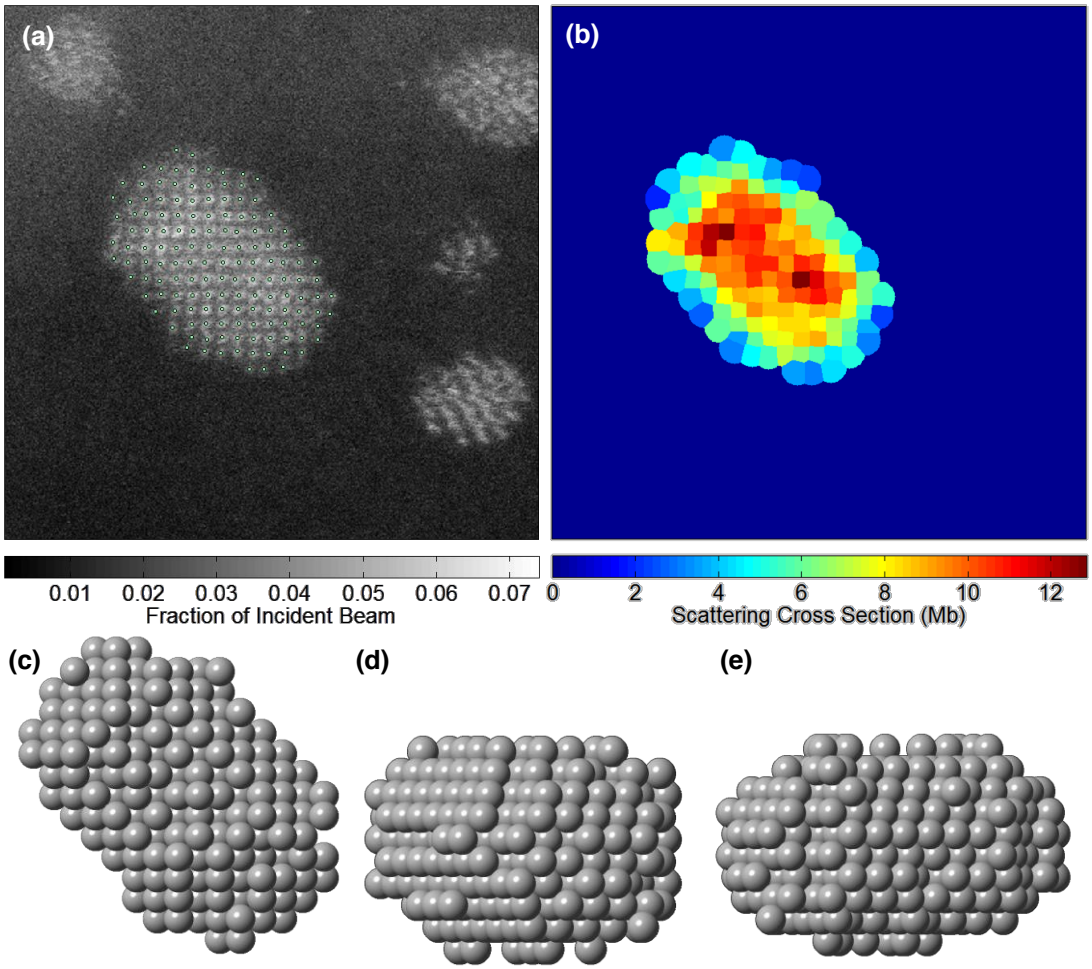


Figure 6.18 – Particle 3 - Normalised experimental ADF image (a) of a Pt particle, viewed down a <100> zone axis, with the calculated cross section map (b). The 3D reconstructed particle is shown parallel to the beam direction (c) and perpendicular to the beam direction at from two angles 90 degrees from each other (d) and (e).

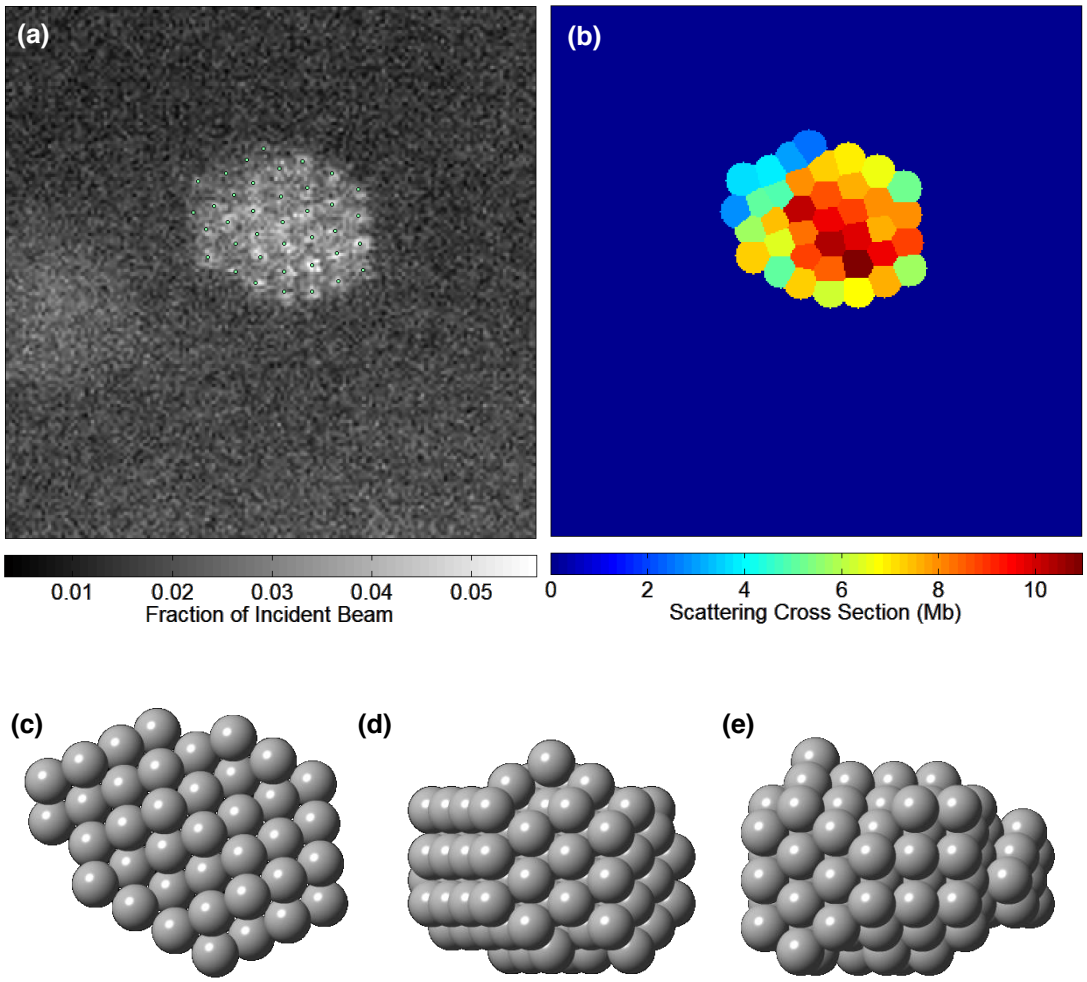


Figure 6.19 – Particle 4 - Normalised experimental ADF image (a) of a Pt particle, viewed down a <110> zone axis, with the calculated cross section map (b). The 3D reconstructed particle is shown parallel to the beam direction (c) and perpendicular to the beam direction at from two angles 90 degrees from each other (d) and (e).

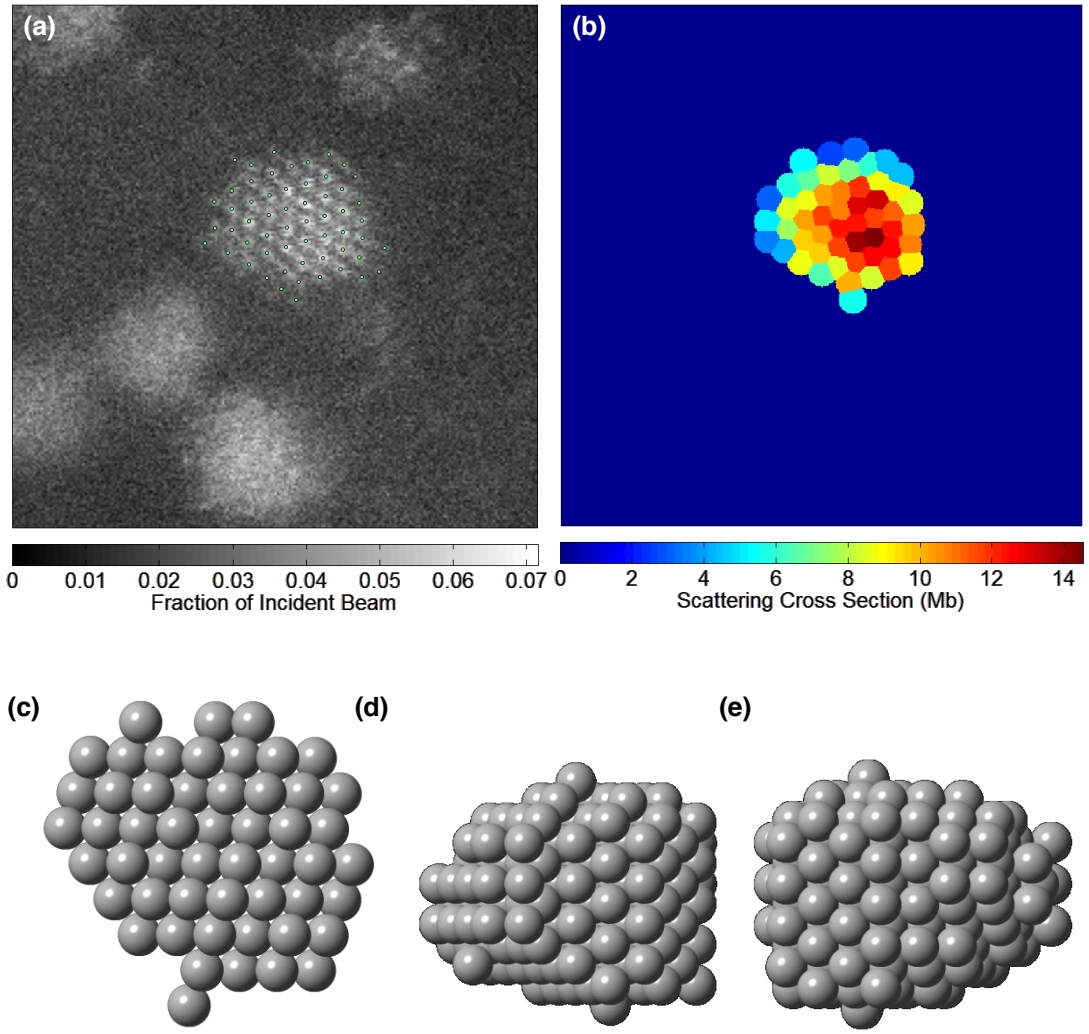


Figure 6.20 – Particle 5 - Normalised experimental ADF image (a) of a Pt particle, viewed down a <110> zone axis, with the calculated cross section map (b). The 3D reconstructed particle is shown parallel to the beam direction (c) and perpendicular to the beam direction at from two angles 90 degrees from each other (d) and (e).

From such particle reconstructions it is possible to extract a histogram of coordination numbers which can then be used to yield the ratio of surface areas (for example {111} to {100}), or the number of lower coordination atoms located at edges and corners can be evaluated (see Figure 6.29). Low coordination atoms have been hypothesised as the preferential location for oxygen adsorption.[209] The first reconstructed particle is roughly spherical with well-defined facets including ones non-parallel to the beam direction (see Figure 6.7).

The surface is relatively smooth with only six atoms of very low coordination which appear to be sat on top of otherwise smooth facets. Four of these ‘dangling atoms’ can be seen in the silhouette extracted from the ADF image which means they are a realistic despite being higher energy to maintain.

There are three factors to look at when examining the validity of the particle reconstructions: aspect ratio, surface roughness and the degree of faceting not parallel to the incident beam direction. In terms of aspect ratio we would largely expect the particles to be approximately spherical as with Particle 1 (see Figure 6.7). However, Particle 2 (see Figure 6.17) is thinner in the beam direction than its silhouette would suggest which may result from too low a thickness estimate from the atom counting, or an over estimate of the background intensity due to the out of focus particle directly behind it. Particle 3 (see Figure 6.18) demonstrates an elliptical silhouette in the ADF image suggesting that some of these particles are non-spherical. If the structure of Particle 2 was found alone without Particle 3 it would be reasonable to suspect elongation as an error in the atom counting when it is more likely to simply be an elliptical particle; this emphasises the need to analyse many particles in the sample.

Particles 1 to 3 all demonstrate well defined facets which are non-parallel to the beam direction. Particle 3 even demonstrates a facet perpendicular to the beam direction because of how it is aligned. This {100} facet is relatively flat although more rough than the less inclined {111} facets, and is evidence of the accuracy of the atom counting procedure.

Particles 4 and 5 are more misshapen and rough. Such roughness is also apparent in the ADF images so can be attributed to real structural information

rather than an error in the atom counting. They are also the smallest of the five particles analysed and appear less crystalline in the experimental images because their atomic peaks are less well defined. Blurred out peaks like this may be due to atomic movement during the course of the image acquisition suggesting them to be more molten or amorphous.

6.6.1.1. Particle Damage

The primary reason behind reconstructing the nanoparticle structures from a single experimental image is due to the high sensitivity of the particles under the electron beam. Figure 6.21 shows two sequential images of Particle 5 and the 3D structures extracted from them. The two particles contain 203 and 209 atoms. The slightly higher number of atom counts is within the error margins of our quantification method. This is encouraging especially from an imaging point of view because whilst some small structural rearrangement has occurred sputtering has been minimised. From an atom counting view point the particle outlines are roughly similar in both ADF images so similar numbers in the atom counting are expected. The peak finding results counted a higher number of atomic columns in the second image emphasising some degree of atomic scale reconstruction. In subsequent images taken of other particles there was sufficient particle rotation between images that further accurate quantification was not possible (see Figure 6.22).

In the top right of both images in Figure 6.21 there is a smaller cluster which demonstrates more dramatic rearrangements between sequential images than Particle 5. The larger particles have a lower surface energy to volume ratio so

seem to be able to withstand a larger dose. This is likely to improve the atom counting accuracy if atoms are less mobile.

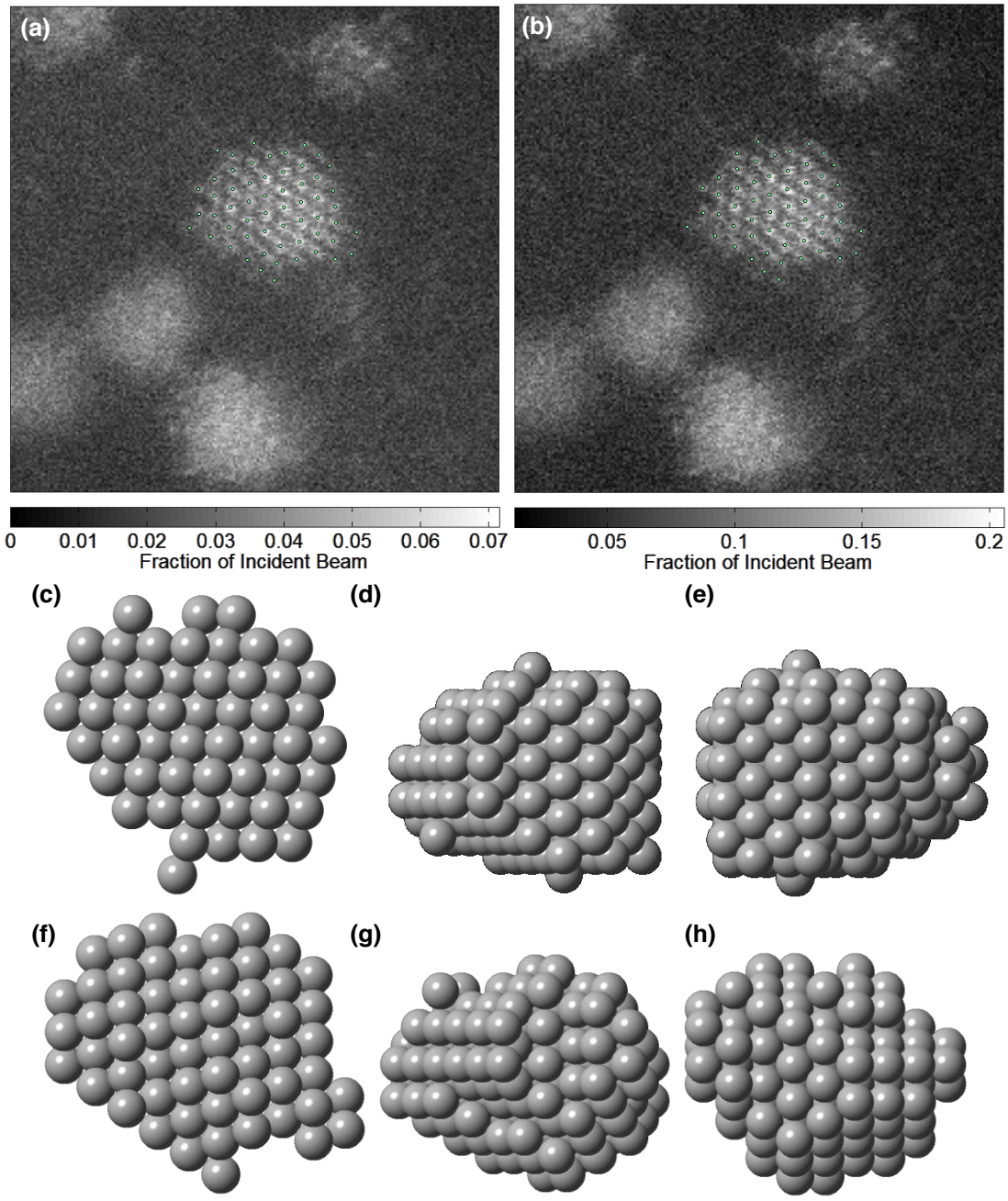


Figure 6.21 – Investigation of particle damage for Particle 5. Two sequential normalised experimental ADF images (a) and (b) with their 3D reconstructed shapes below. The projected shapes (c), (d) and (e) correspond to the particle in image (a) containing 203 atoms in total and the projected shapes (f), (g) and (h) correspond to the particle in image (b) containing 209 atoms.

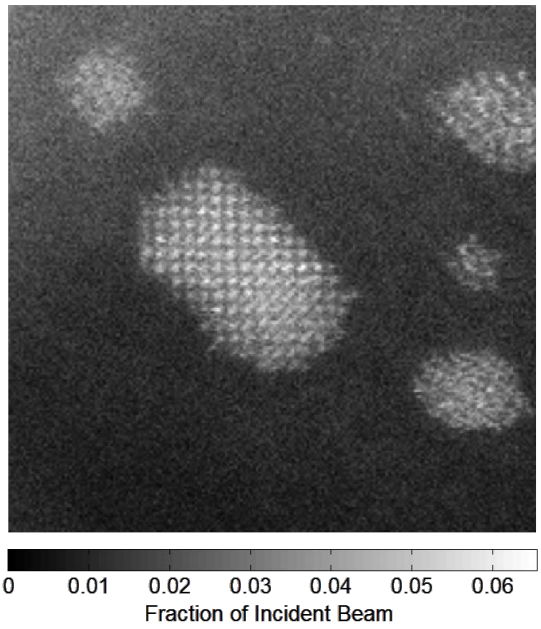


Figure 6.22 – Second ADF image of pure Pt Particle 3 which is far too tilted for accurate quantification.

6.6.2. Pt-Ir Nanoparticles

Platinum and iridium mixed alloy nanoparticles have demonstrated improved tolerance to CO poisoning, a by-product in the reforming of hydrocarbons to hydrogen gas.[19] These particles can have a larger average diameter than pure Pt particles due to lower cost of the Ir metal allowing them to be more stable under the beam leading to improved atom counting accuracy. Pt and Ir only differ by one atomic number which makes them virtually indistinguishable from each other using ADF cross sections alone (see Figure 6.23). In fact the crystallographic zone-axis has a greater effect on the calculated scattering cross section than the composition variation between Pt and Ir. For a 15 atom thick column the difference between a pure Pt or pure Ir column is only 1.95%. These are mixed alloy particles; therefore, it is unlikely that anything other than a few edge columns will contain only one element, making the difference error

substantially smaller than this 2%. Although this all makes them a non-ideal candidate for compositional analysis, it does mean that the composition can be ignored in order to carry out conversion to atom counts and particle reconstruction, using exactly the same method as developed for monometallic nanoparticles.

Whilst knowledge of the atom types would be the ideal end goal, knowing the atom locations in 3D can still provide a deal of insight into their properties. Based on the investigation on the effect of DWF (section 5.6.5, page 116) the libraries here have been constructed for both elements using only the experimentally determined Pt DWF as this is thought to be more accurate than using the Ir theoretical DWF. The library used for conversion to atom counts was a linear interpolation between the two single element libraries using the nominal composition of 16.7% Pt determined by bulk analysis.

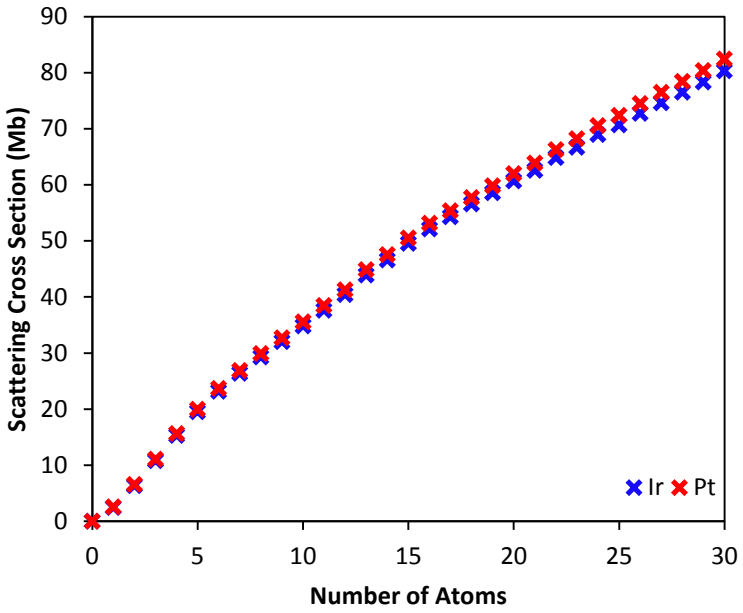


Figure 6.23 – Library of scattering cross sections for both pure Pt and pure Ir crystals viewed down a <110> zone-axis. The close proximity of both curves means they are indistinguishable from ADF image intensity alone.

6.6.2.1. 3-Dimensional Reconstructions

Four particles were selected to be as on-axis as possible and with sufficient resolution to allow accurate reconstruction of their 3D shape (Figures 6.24-6.27). 3D reconstruction was carried out using the same method as that derived for the pure Pt particles. In similarity with the Pt reconstructed particles most particles are elliptical rather than spherical, showing a reasonable number of surface steps to accommodate for this.

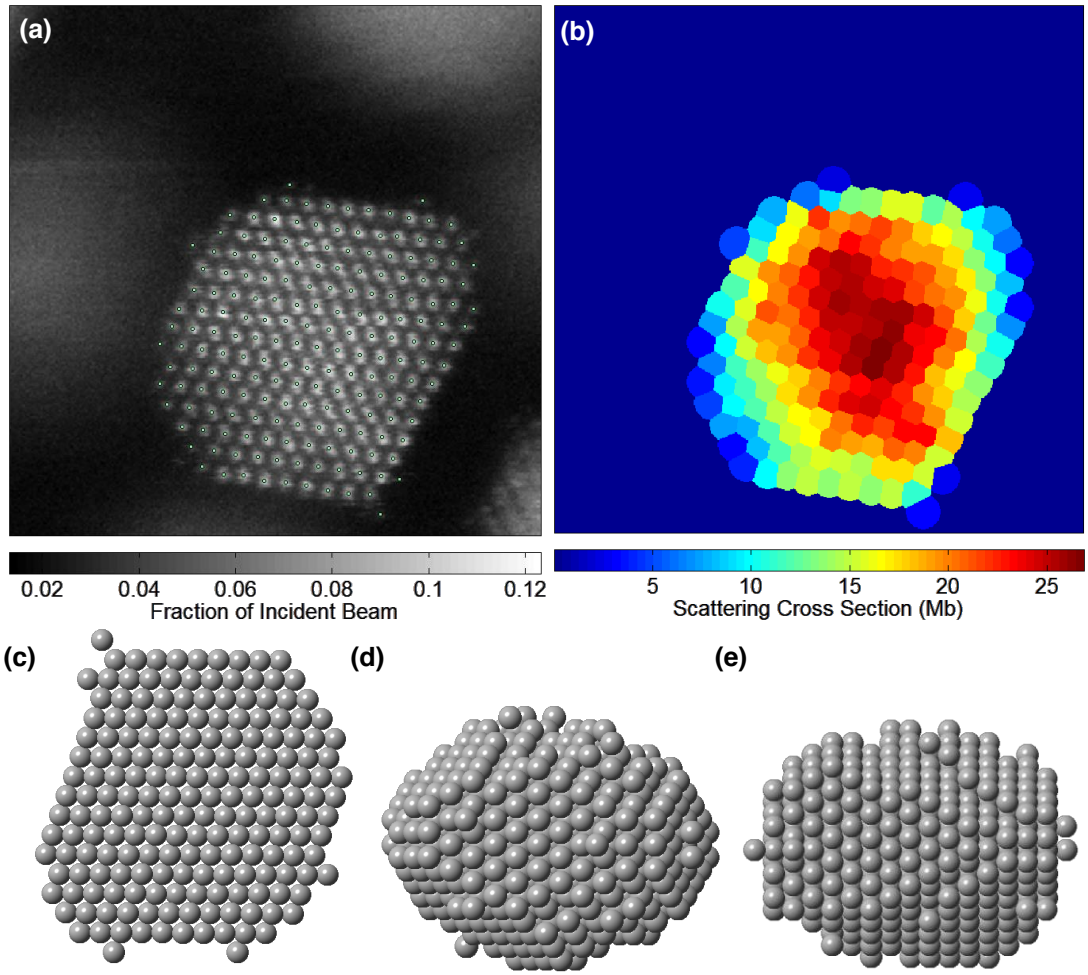


Figure 6.24 – Particle 1 - Normalised experimental ADF image (a) of a Pt/Ir particle with the calculated cross section map (b). The 3D reconstructed particle is shown parallel to the beam direction (c) and perpendicular to the beam direction at from two angles 90 degrees from each other (d) and (e). Experimental image taken by Armand Béché.

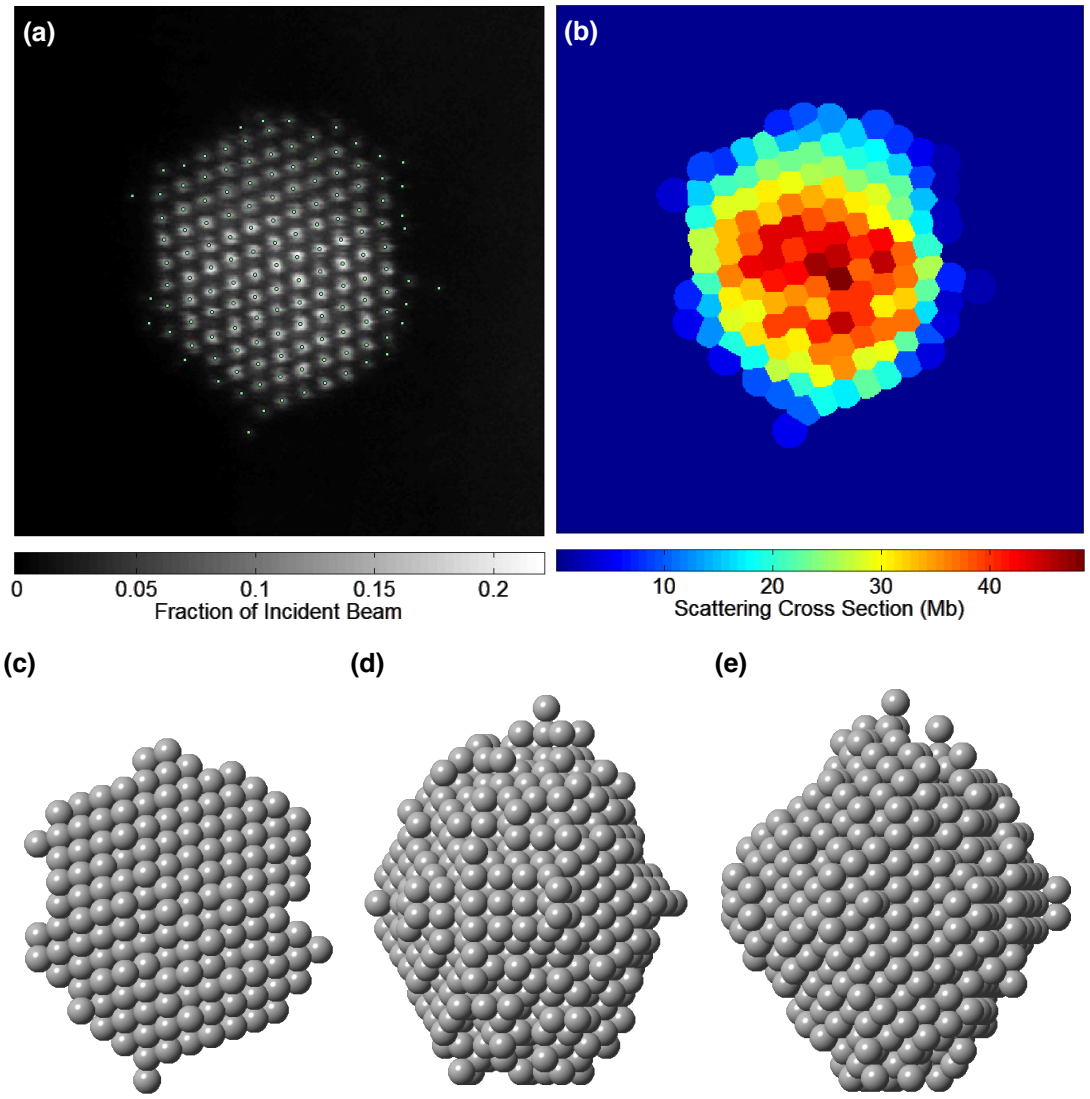


Figure 6.25 – Particle 2 - Normalised experimental ADF image (a) of a Pt/Ir particle with the calculated cross section map (b). The 3D reconstructed particle is shown parallel to the beam direction (c) and perpendicular to the beam direction at from two angles 90 degrees from each other (d) and (e). Experimental image taken by Armand Béché.

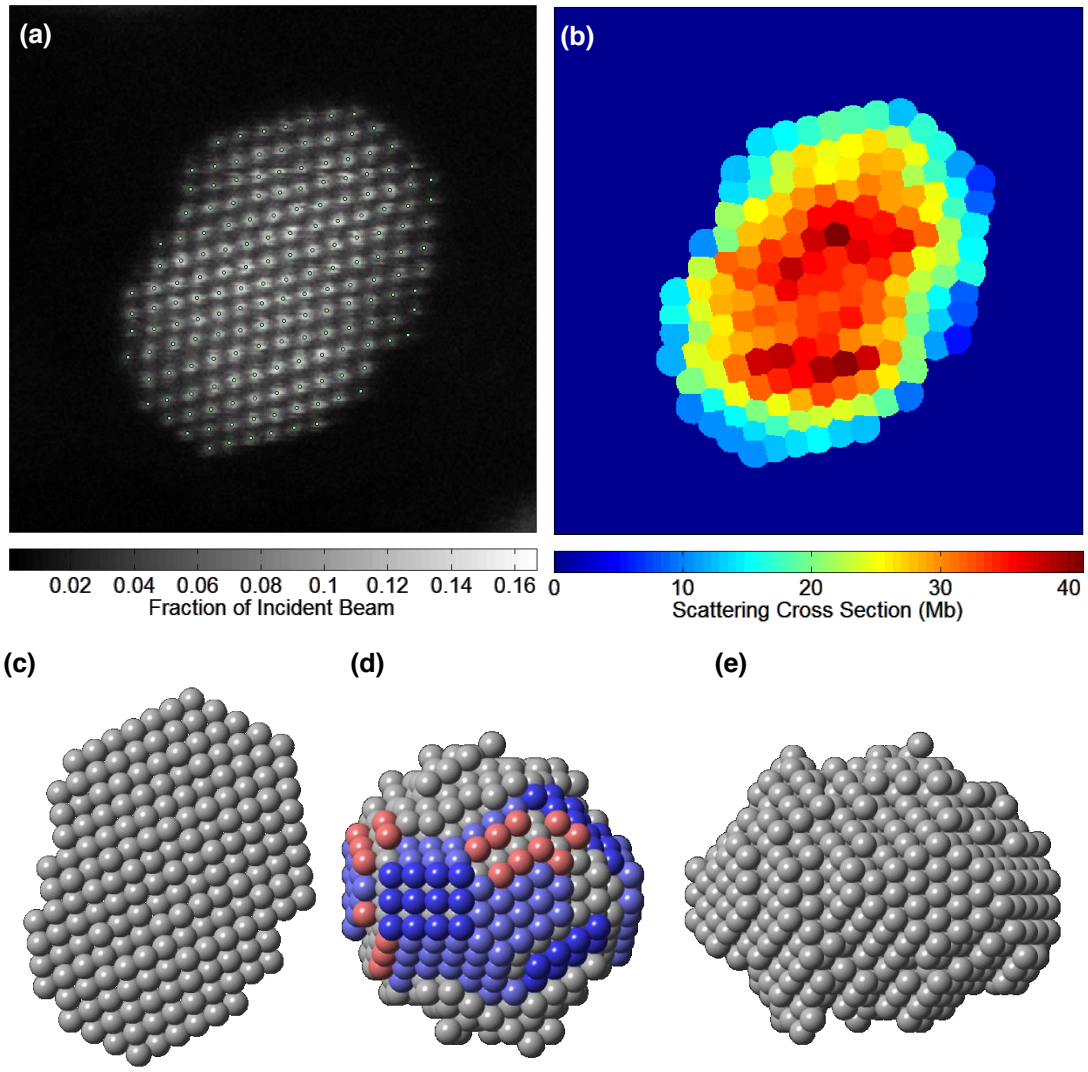


Figure 6.26 – Particle 3 - Normalised experimental ADF image (a) of a Pt/Ir particle with the calculated cross section map (b). The 3D reconstructed particle is shown parallel to the beam direction (c) and perpendicular to the beam direction at from two angles 90 degrees from each other (d) and (e). For ease of comparison with the Wulff construction the (d) projection has had the faces coloured in, {111} purple, {100} blue, {110} red. Experimental image taken by Armand Béché.

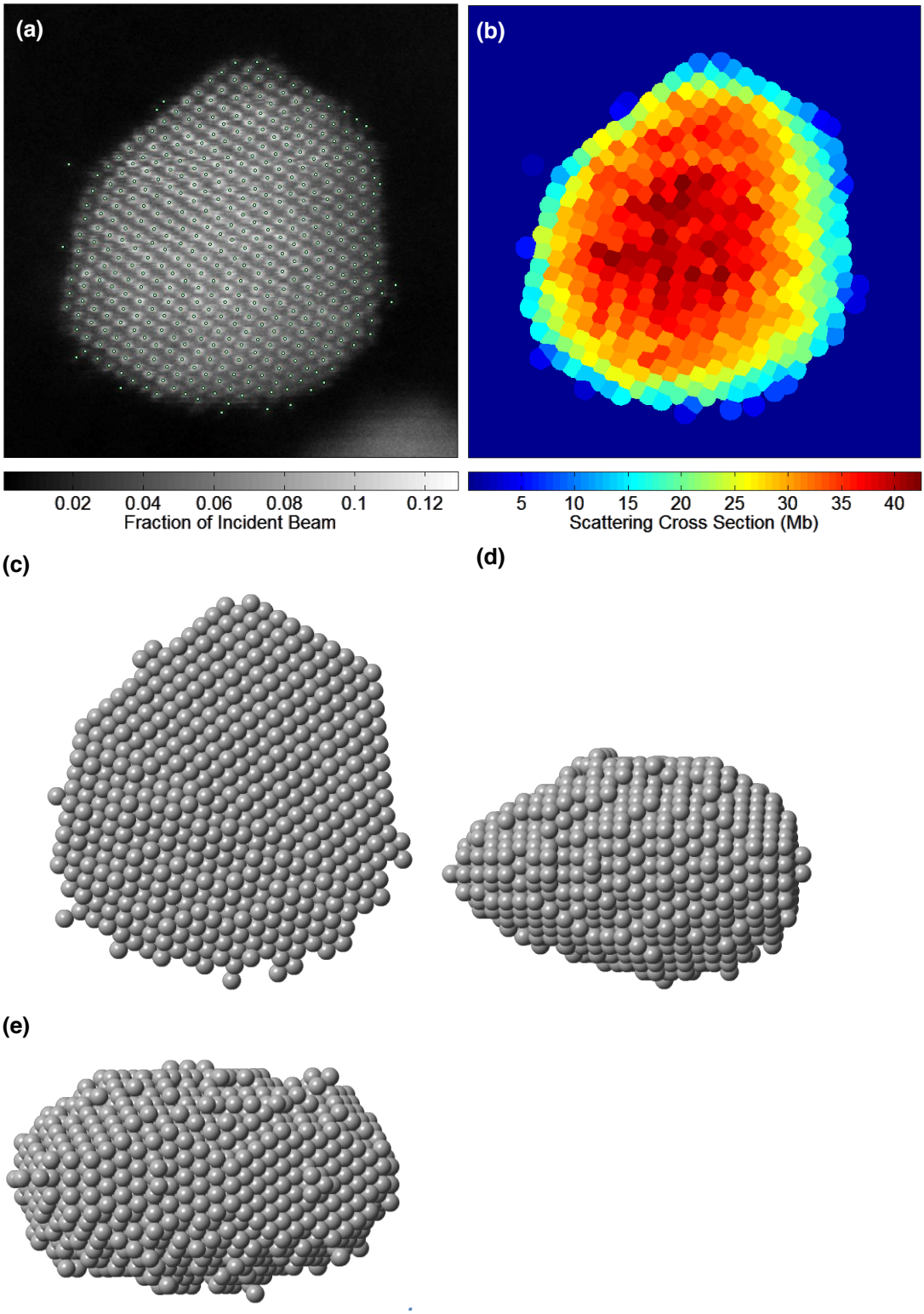


Figure 6.27 – Particle 4 - Normalised experimental ADF image (a) of a Pt/Ir particle with the calculated cross section map (b). The 3D reconstructed particle is shown parallel to the beam direction (c) and perpendicular to the beam direction at from two angles 90 degrees from each other (d) and (e). Experimental image taken by Armand Béché.

Particle 1 (see Figure 6.24) is largely bound by {111} surface facets with only very small areas of {100} facets with a {111}:{100} surface ratio of 2.9, resulting in an angular 3D shape that is also reflected in the ADF silhouette. The smooth facets all inclined to beam direction add confidence to the atom counting results. Particles 2 and 3 (see Figure 6.25 and 6.26) demonstrate elliptical shapes parallel and perpendicular to the beam direction thereby validating each other because of their different orientations. Particle 4 (see Figure 6.27) also seems rather squashed in the beam direction, although the source of this aspect ratio may be related to the twin boundary down the centre of the particle suggesting it was formed through the coalescence of two smaller particles.

When evaluating the likely accuracy of these reconstructions there is a considerable amount of roughness in the centre of Particle 2 with some large jumps in atom counts between neighbouring columns. This particle is the thickest particle analysed reaching up to a maximum of 15 atoms in thickness, where the atom counting accuracy becomes ±1 atom. To a lesser extent some roughness is witnessed in the thicker regions of Particle 3 as well. These reconstructions are snap shots in time; just as atom hopping is seen around the edge of the particles in sequential images it seems reasonable that the same degree of mobility may be exhibited by the surfaces not directly visible in the ADF image. Such atom mobility should provide uniformly distributed loose atoms over all the particle surfaces as in Particle 3 rather than the concentrated roughness demonstrated in the centre of Particle 2. For Particle 2, therefore, the roughness is more likely originating from the atom counting error at the larger thicknesses.

6.6.3. Comparison with Wulff Construction

A theoretical particle shape predicated by Wulff theory was constructed using Wulfmann[210] for both the pure Pt and the Pt/Ir alloy particle (see Figure 6.28). The Pt/Ir Wulff structure was created using a linear interpolation of the elemental surface facet energies for Pt and Ir[37] based on a nominal alloy composition of 16.7% Pt.

The equilibrium shape predicted by Wulff theory is based around a truncated octahedron primarily bound by {111} and {100} type surface facets, which are purple and blue respectively in Figure 6.28. The energy of the {110} surfaces are sufficiently large by comparison such that only a small sliver facet is seen in the large continuum Wulff models (red in Figure 6.28), which means they are very unlikely to be seen in real catalyst particles at much smaller length scales. The Pt/Ir Wulff construction predicts larger {110} facets but they are still unlikely to occur at the small length scales we are investigating.

In the experimental results, the Pt/Ir particles demonstrate larger and cleaner facets than the pure Pt nanoparticles, which may primarily be due to their increased size. They can be seen to qualitatively resemble the Wulff construction, even those particles which are not spherical in shape; in particular the atoms in Figure 6.26d on page 177 have been re-coloured to facilitate this comparison.

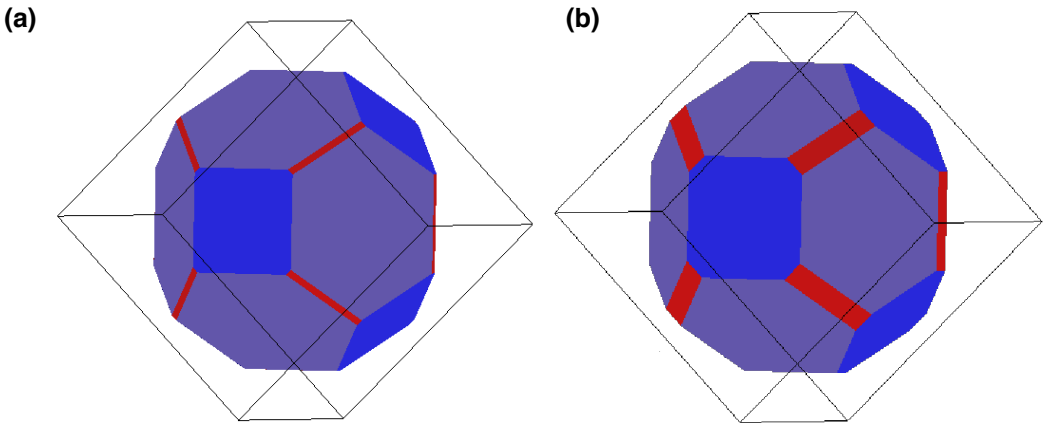


Figure 6.28 – The theoretical Wulff shape of a pure Pt nanoparticle (a) and a Pt/Ir nanoparticle (b) predicted by a linear combination of the pure element surface energies for Pt and Ir. The Wulff shape is predicted based on the ratio of the (111), purple, (110), red, and (100), blue, surface energies,[211] constructed using Wulffman.[210] [17] The (110) surfaces demonstrate very high surface energy so only appear as a very small sliver in the Wulff shape.

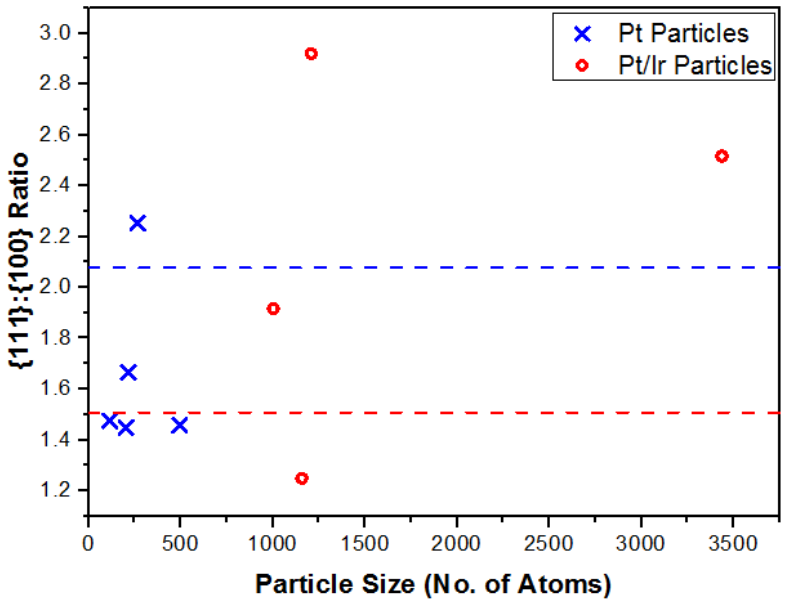


Figure 6.29 – Summary of the {111}:{100} surface ratios for the reconstructed particles plotted against particle size. The horizontal dotted lines represent the theoretical ratio predicted by Wulff for both the pure Pt particles (blue) and the Pt/Ir particles (red).

When examining the particle structures more quantitatively the Pt/Ir particles demonstrate a much higher {111}:{100} surface area ratio (Figure 6.29) which is

[17] http://www.ctcms.nist.gov/wulffman/

the opposite to that predicted by Wulff theory, although there is significant scatter to the results. One must assume therefore that Wulff plays a less key role than particle size at these length scales, or the Pt particles are roughened and damage more under the electron beam due to their small size. The particles with a much larger aspect ratio, in particular Pt/Ir Particle 3, seem to demonstrate a much smaller {111}:{100} ratio because a greater area of {100} facets are needed to bound such a non-spherical shape.

6.6.1. Energy Relaxation

In order to reduce the analysis time and improve the accuracy of the reconstructions ideally an automated reconstruction and energy relaxation should be carried out. In the reconstructions the particles are maintained as FCC such that no additional defects are incorporated during the relaxation, other than those already present in the experimental image (see Figure 6.27). For the initial investigations a Leonard-Jones potential was used with the modified coefficients for Pt metal.[205]

The Pt particle structures presented here have been used as inputs for molecular dynamic simulations, with the aim focused on moving away from describing nanoparticles as ‘perfect’ or ‘magic number’ clusters. In the real experimentally determined structures there are many more different types of electrochemical environments for the oxygen to adsorb to.

6.7. Conclusions

For the structural quantification of single element nanoparticles it is now possible to reconstruct their 3D structure from one experimental image. I have demonstrated single atom sensitivity (less than ± 1 atom) up to 14 atoms thickness. A counting precision of ± 2 atoms begins at 20 atoms and thicker. The Pt nanoparticles investigated were very small in size. This is often the case in order to reduce the total Pt loading; however this comes at a cost of the particle stability during imaging.

The Pt/Ir nanoparticles investigated here demonstrated greater stability under the electron beam and larger surface facets. However this may primarily be due to their larger size with an average diameter of 6.84nm in comparison to 1.3nm average diameter for the pure Pt nanoparticles analysed. The Pt/Ir nanoparticles only contain 16.7% Pt which means larger particle sizes are more economically viable. In the thickest particle investigated (15 atoms for the thickest column) we begin to reach beyond the limit of single atom counting precision, resulting in increased roughness only in the central region of the particle reconstruction.

The reconstructed particle structures are more rough and misshapen than theoretical calculations would predict. Due to the appearance of well-defined facets non-parallel to the electron beam it is unlikely to be as a result of errors in the atom counting, except for the thicker particles where the roughness is located specifically in the thick central region of the particle. The non-perfect structure of these particles may be in part due to the irradiation damage provided by the electron beam; a contribution which can never be wholly ignored. It may also simply be that real particles are not perfect and that investigating such

imperfections in their structure may yield a better understanding of catalytic mechanisms.

7. ENERGY DISPERSIVE X-RAY

Quantification of the ADF STEM intensity for two element systems requires separation of thickness and contributions to a column's scattering cross section. Several different thickness and composition combinations can result in the same or similar ADF cross sections. It is therefore necessary to draw additional information from other sources in order to reduce the problem complexity. The main advantage of EDX is that it is another signal which produces an incoherent image. In contrast to ADF STEM, the elemental signals are separable, so, assuming the sample is sufficiently thin such that we can neglect absorption and fluorescence effects, each X-ray signal can be treated and processed independently (assuming the characteristic peaks do not overlap in the spectrum). EDX provides us with an independent composition measure for combination with ADF cross sections.

The limitations of both k-factors and ζ-factors as methods for EDX quantification have previously been discussed in section 3.6 on page 65. In this chapter I introduce an improved method for quantification on an absolute scale using pure element standards. The main sources of error and their magnitude will also be discussed. Finally, this quantification will be applied to Pt(Pd) core-shell and Pt/Co alloy nanoparticles to determine local composition variations within the particles.

7.1. EDX Partial Scattering Cross Sections

In the same way that the scattering cross section, σ, can be calculated from ADF image intensity[138,197] and for ionisation edges in EELS,[212,213] it is possible to calculate an EDX partial scattering cross section using an approach that is in some respects similar to the ζ-factor method. The scattering cross section approach has been shown to simplify the quantification procedure in ADF STEM,[197,205] demonstrating robustness to a wide range of imaging parameters.[197] In EDX spectroscopy the advantage of a partial scattering cross section approach is again the simplicity of its implementation, in addition to its independence to illumination area which currently limits the ζ-factor approach. For sufficiently thin samples X-ray absorption and fluorescence can be neglected and assuming the crystal is not aligned along low-order zone axes, channelling can be ignored. In this situation the number of X-ray counts is linearly proportional to sample thickness so I can define an EDX partial scattering cross section, σ_x, for a single atom of any given element as:

$$\sigma_x = \frac{I_x}{D n_x t A} \qquad 7.1.$$

Where I_x are the characteristic X-ray counts for element x, $n_x t$ is the atom density per unit area, A defined in atoms/m^2 and A is the illuminated area. If you are undersampling so that the probe diameter is narrower than the pixel width A is defined by the probe area. This parameter is difficult to measure accurately and needs to include knowledge of beam spreading especially for thicker specimens. If you are oversampling such that the probe diameter is wider than the pixel width, or sub-pixel scanning is used, A is defined by the pixel area. Here I define the dose or fluence, D, as the number of electrons seen by the

sample per unit area in equation 7.2. This results in equation 7.3 for σ_x which is independent of magnification or pixel area and only dependent on the number of atoms being excited by the probe.

$$D = \frac{i\tau}{eA} \qquad 7.2.$$

$$\sigma_x = \frac{I_x e}{i\tau n_x t} \qquad 7.3.$$

Here, i is the probe current, τ is the total pixel dwell time and e is unit electronic charge. The EDX cross section is specific to a given microscope set up incorporating the solid-angle and collection efficiency of the EDX detector, as well as the microscope voltage, making it an appropriate method for measurement of system performance and comparison between different microscopes. It should be noted that these cross sections are also dependent on the specific X-ray peaks used for analysis, the background subtraction method, and the chosen energy window used for integration as well as the sample tilt when it affects the degree of shadowing from the holder.

7.1.1. Comparison with ζ-Factors

For comparison with the ζ-factor method it is important to note that the dose D_e definition in the Watanabe and Williams paper [187] is not defined per unit area. This makes it the total number of incident electrons on the sample and so is dependent on the size of the electron probe or the integration area. Also the definition of ρ is in kg/m^3 of the whole material for the ζ-factor rather than the number of atoms/m^3 for σ. The two methods are tricky to relate exactly because

of these differences in definition for density and dose, nevertheless they are inversely proportional according to the following equation.

$$\sigma_x = \frac{A_r}{N_A {D_e}^2 \zeta_x} \qquad 7.4.$$

Where the relative atomic mass, A_r, and Avogadro's constant, $\mathrm{N_A}$, are included to convert the density definition from kg/m^3 to atoms/m^3. Dose is D_e and so not per unit area.

7.2. Experimental Calibration

In order to evaluate the cross section of each element I need a sample of known thickness and density to help us estimate the number of atoms being excited by the electron probe. Early investigations worked on the assumption of spherical particles, assuming the particle thickness is equal to its circular radius perpendicular to the beam direction; however this appeared to overestimate the cross sections.

There are several approaches that can be used to manufacture a dedicated TEM standard sample. Needle-shaped samples have the advantage that their thickness can be measured experimentally by imaging at tilt angles 90° apart; however they offer a reduced range of thicknesses and require a dedicated tomography holder.[127] Wedge samples, on the other hand, can be easily fabricated with a focused ion beam (FIB) scanning electron microscope and have flexible thickness ranges[214] so have therefore been chosen for this work. The thickness determination in wedge samples relies on how accurately the wedge angle is known, which can be taken as the nominal value used during

FIB manufacturing or measured via theoretically calculated inelastic mean free paths.[215,216] Both methods of thickness measurement have associated uncertainties and these will be discussed.

Pure Co, Pt, and Pd standard wedge samples were created with nominal wedge angles of 1.5°, 0.5°, and 1° respectively by S. Lozano-Perez. The FIB lift-out method used to prepare them is described in [214]. All three samples are shown in Figure 7.2. An EDX line scan along such a wedge also provides information on how the number of X-ray counts varies with increasing sample thickness. Ideally the line profiles (see Figure 7.1) would be of the same length; however the Pt and Pd images have been taken at a higher magnification because X-ray absorption appears to occur sooner, at smaller sample thicknesses, in the heavier elements. This should not have a noticeable effect on the accuracy of the cross section calculation provided the sampling is sufficient to measure the gradient accurately. The line profiles, Co in particular, demonstrate step variation at low sample thickness due the polycrystalline nature of the wedges, because certain grains are closer to a low index zone-axis and therefore channel more than others, and has been witnessed for both EDX maps[217] and ADF images (see Section 5.7 page 121). In particular when a grain is tilted sufficiently far away from the crystal zone-axis channelling does not affect the X-ray yield. At larger thicknesses there is a greater chance of the probe exciting more than one grain in the beam direction; therefore this variation becomes smeared out. For this analysis an average over these step variations was used to extract the gradient. Small nanoparticles are liable to reconstruct and rotate under the electron beam during the course of EDX spectrum image acquisition. This results in the final elemental maps becoming maps which have been averaged

over range of different sample tilts, thus the use of an average gradient over the channelling variations in the wedge samples is justified.

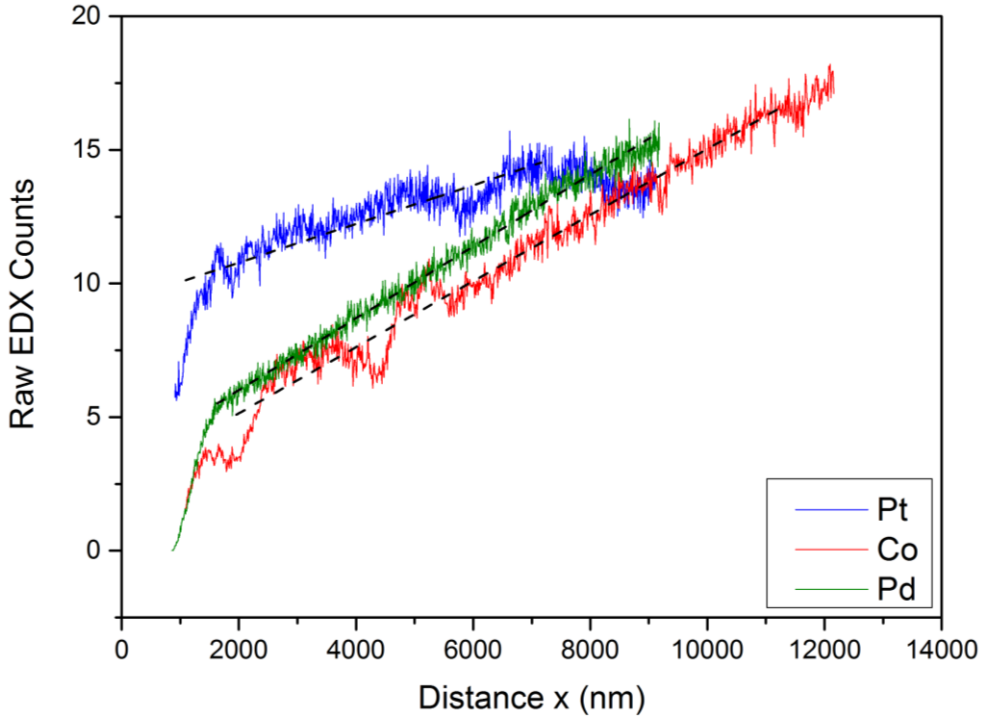


Figure 7.1 – Graph showing the line profiles extracted from wedge samples of both Co, red, and Pt, blue. The step increase in thickness at the left hand side of the profiles has been deleted for ease of interpretability. The linear equations (dotted black lines) were only fitted in the region of linearity of the X-ray counts.

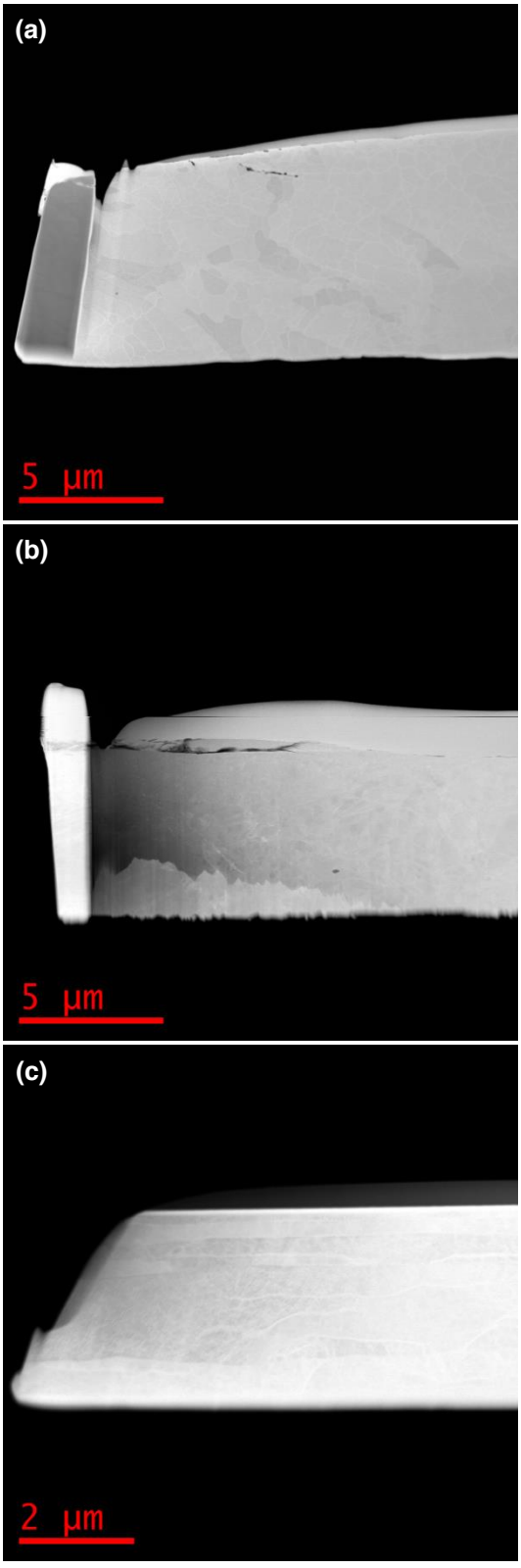


Figure 7.2 – Low magnification STEM image of the Pt, Co and Pd wedge samples taken on the Manchester Titan. The FIB beam direction runs from top to bottom on these images. The unusual contrast on the left hand-side of the image comes from a step increase in thickness to help strengthen the wedge tip.

Due to limitations of the sample preparation technique the wedge samples demonstrate a blunt or misshapen sample tip. It is therefore more accurate to take the relative change in intensity, or rather the gradient of a line scan $\frac{dI_x}{dn_x t}$, instead of simply $\frac{I_x}{n_x t}$. The partial scattering cross section varies with $n_x t$ such that equation 7.3 becomes:

$$\sigma_x = \frac{e}{i\tau} . \frac{dI_x}{dn_x t} \qquad 7.5.$$

By accurately knowing the geometry of the sample and angle of the wedge,[214] θ, the cross section, σ, can be calculated directly from the line profiles in Figure 7.1 using equation 7.6. The pixel dwell time, τ, comes from the EDX software. The probe current was read off from the phosphor screen on the Titan and using the GIF drift tube on the ARM.

$$\sigma_x = \frac{e}{i\tau n_x tan(\theta)} . \frac{dI_x}{dx} \qquad 7.6.$$

The EDX cross section for all three elements are presented in Table 7.1 and compared with the simulated ADF cross sections for equivalent microscope settings.[197] From comparison of σ for both the ADF and EDX signals it is clear that ADF detector collection is six orders of magnitude more efficient. This now quantifies the poor quality signal-to-noise ratio of the EDX maps in comparison to the other signals. Each electron-atom interaction therefore has a significantly higher probability of a scattering event occurring that deflects the electron out to the ADF detector than an ionisation event that leads to detection of an X-ray photon.

Exactly the same procedure can be used to extract partial scattering cross sections from EELS core loss signals and theoretically calculated EELS cross sections using the Hartree-Slater model have been included for comparison. We see these EELS cross sections lie between those of ADF and EDX in the kilobarn (kb) order of magnitude.[218] EELS collection efficiency is also several orders of magnitude better than EDX (which is expected, since most inelastically scattered electrons can be detected).

Increasing the detector solid angle will increase the EDX partial scattering cross section, as it provides an increase in the number of X-rays being collected by the detector. Whilst the cross section is independent of the dose used increasing the probe current will increase the rate of X-ray generation and so decrease the dwell time needed for the same number of X-ray counts.

Metal	ρ (atoms/nm^3)	EDX σ (b)	EELS σ (kb)	ADF σ (Mb)
Pt	66.41	5.42	0.323	1.12
Pd	67.95	7.41	-	0.515
Co	90.28	2.89	1.334	0.204

Table 7.1 – Density and calculated EDX, EELS and ADF cross sections for the Titan 80-200 ChemiSTEM operating at 200kV using a FEI low-background holder at α and β tilts of 0°. Note that the EELS cross sections were calculated using Hartree-Slater models (M edge, 100eV integration window for Pt and L edge, 40eV integration window for Co) for comparison purposes. Note that the units used for the cross sections differ by 10^6 (barn for EDX, kilobarn, for EELS, and megabarn for ADF).

7.2.1. Comparison between microscopes

The EDX quantification presented in this chapter was acquired using two microscopes; the Manchester Titan 80-200 ChemiSTEM, operating at 200kV, and the Oxford JeolARM cold FEG, operating at 200kV with a 100mm^2 side

entry detector. The Manchester data was carried out using an FEI low-background holder at α and β tilts of 0°. The Oxford data was acquired using a Be double tilt holder tilted 20° towards the detector for improved counts by preventing shadowing from the holder. Therefore a second set of line profiles (see Figure 7.3) and cross section determination was carried out.

The EDX partial scattering cross section is a measure for quantitative comparison of the X-ray collection efficiency between microscopes. Both the ADF and EDX cross sections for the two microscopes presented here are of the same order of magnitude (see Table 7.2), although the ARM seems to demonstrate higher scattering cross sections over all. The ADF cross sections could be improved by using a smaller detector collection angle; the Titan data was taken with a 70mrad inner angle whilst the ARM data was taken with the 53.2mrad angle. However this data does suggest the ARM to be a better machine for quantitative microanalysis measurements.

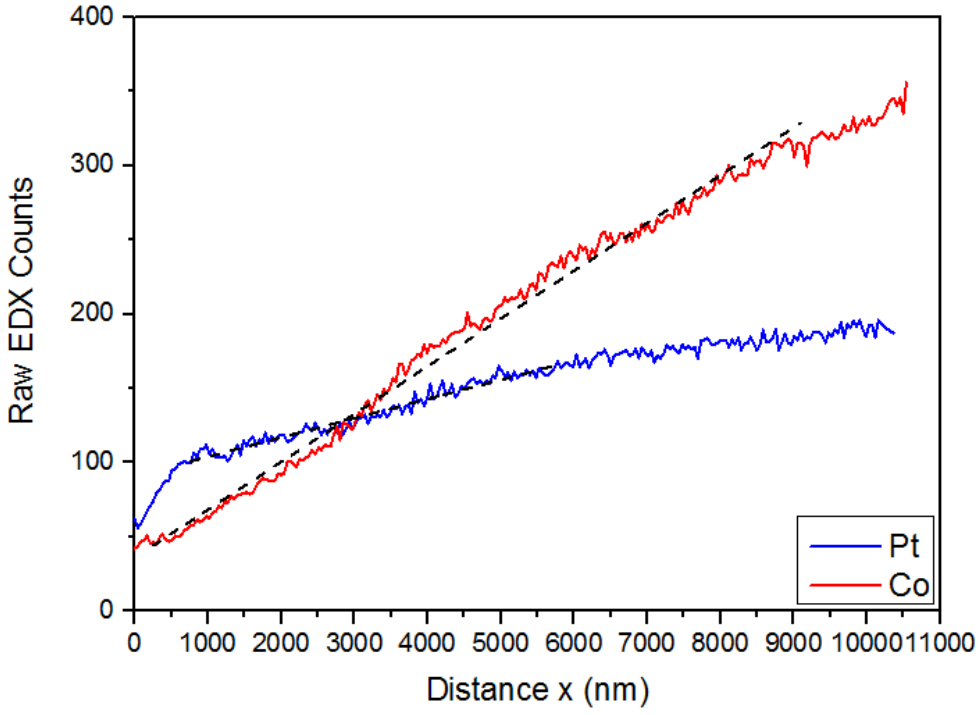


Figure 7.3 – EDX line profiles for the Pt and Co wedges standards taken on the Oxford ARM. The dashed black lines demonstrate linear fitted gradients used for the quantification.

Metal	EDX σ (b)		ADF σ (Mb)	
	ARM	Titan	ARM	Titan
Pt	6.15	5.42	1.77	1.12
Co	3.93	2.89	0.352	0.204

Table 7.2 – Table summarising the ADF and EDX cross sections for 1 Pt or Co atom as calculated for the Oxford ARM (with an ADF inner detector angle of 53.2mrad) and the Manchester Titan (with an ADF inner detector angle of 75mrad).

7.3. Background Subtraction

The background subtraction method used for EDX analysis is a simple linear interpolation from the three window approach (two windows to define the background and one to define the integration bounds for the signal). A linear background subtraction is a reasonable estimate provided the amount of Bremsstrahlung is small and there is no overlap with neighbouring peaks.

Region	Selection Window (keV)
Background 1	4.16-5.98
Background 2	13.68-15.26
Co K_1	6.66-7.08
Co K_2	7.4-7.82
Pt L_1	9.2-9.62
Pt L_2	10.66-11.64

Table 7.3 – Summary of the windows used to carry out the background subtraction and integrations from the EDX spectrum.

7.4. Converting to Atom Counts

With knowledge of the partial scattering cross section of each element for a particular microscope it is then possible to calibrate EDX maps into atom counts, N_x, per pixel of the spectrum image using equation 7.7 and resulting in Figure 7.4(a).

$$N_x = n_x tA = \frac{eI_x A}{i\tau\sigma_x} \qquad 7.7.$$

EDX mapping is often carried out at the same pixel sampling as the ADF reference image, resulting in the raw data cubes being sampled spatially much more finely than the spacing of atomic columns. Binning of the spectrum image is therefore required to improve signal-to-noise ratio (SNR) and to get an estimate of the number of atoms per column, giving us a more physical presentation of the sample structure. If an atomic resolution ADF image is achieved in tandem with the spectrum image then a more intelligent Voronoi cell type integration could be applied similar to those applied in ADF STEM quantification.[155] However, often probe sizes larger than the atomic spacing are

used to improve the X-ray counts making this not possible. An estimate of atomic column density must necessarily be used.

When viewing down the Pt <110> crystallographic zone-axis the size of the Voronoi cell to integrate over one atomic column is 0.054nm^2, assuming the nanoparticle is pure Pt and ignoring any strain effects. This means that for a typical pixel width of 0.024nm an integration of 92 pixels is needed to result in realistic atom counts per atomic column. In Figure 7.4 the benefit of such integration on the SNR of the EDX map and being able to determine the particle shape is shown.

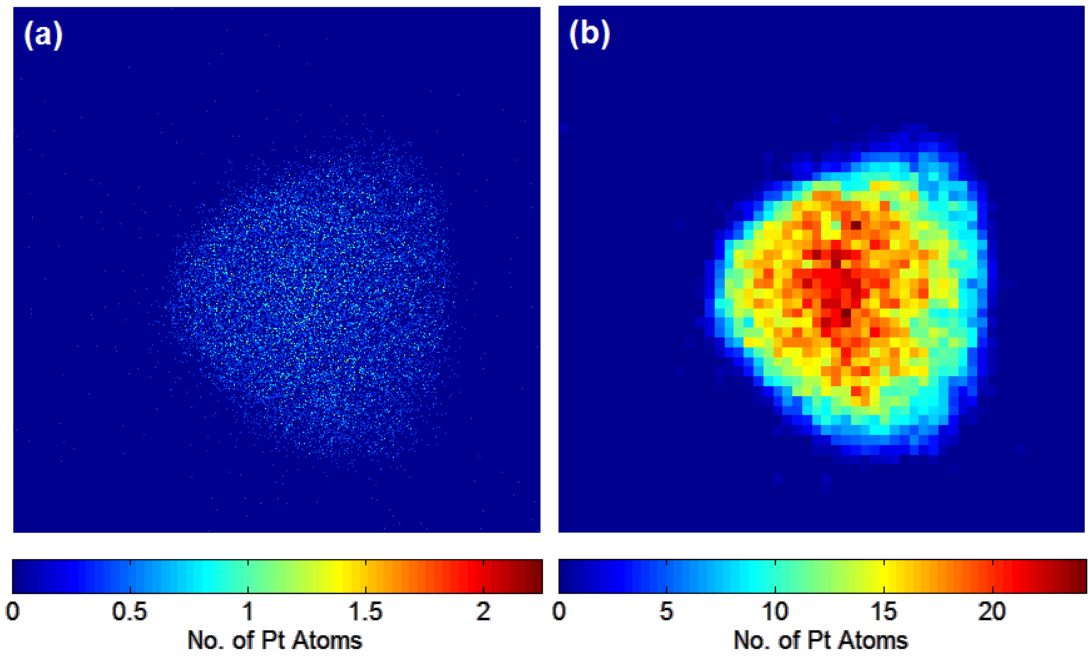


Figure 7.4 –EDX maps of the Pt-L peak from a PtCo nanoparticle converted to atom counts per pixel using the cross section quantification, at the original pixel sampling (a) and binned to a sampling of roughly 1 pixel per atomic column (b) with pixel width of 0.23nm.

Once we have elemental maps for each constituent atom it is possible to create composite (Figure 7.5) and fractional maps (see Figure 7.6) which clearly demonstrate the Pt enrichment at the particle surface, with less Pt at the apexes. The enrichment (defined here as greater than 85at% Pt) is patchy but penetrates up to 5 atomic layers into the particle. The overall composition of the particle is 71at% Pt. In order to make the fractional maps more easily interpretable the noise surrounding the particle was removed. This was done by setting any pixel where the total atom counts are less than 0.35 to zero using a mask (see Figure 7.7). This method maintains the surface structure of the nanoparticles, which is what we care about, whilst removing most of the noise surrounding the particle.

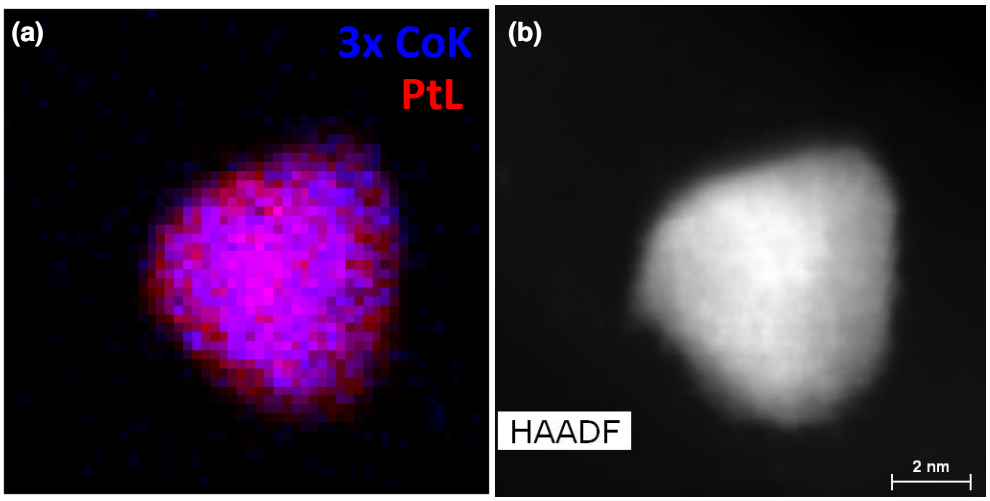


Figure 7.5 – Composite elemental image of a PtCo nanoparticle, with Co in blue and Pt in red (a) and the original ADF image (b). The Co signal has been increased by three times to make its location more visible relative to the Pt. Signals were extracted from EDX spectrum imaging of the particle using the Co-K and Pt-L characteristic X-ray peaks, combining α and β peaks.

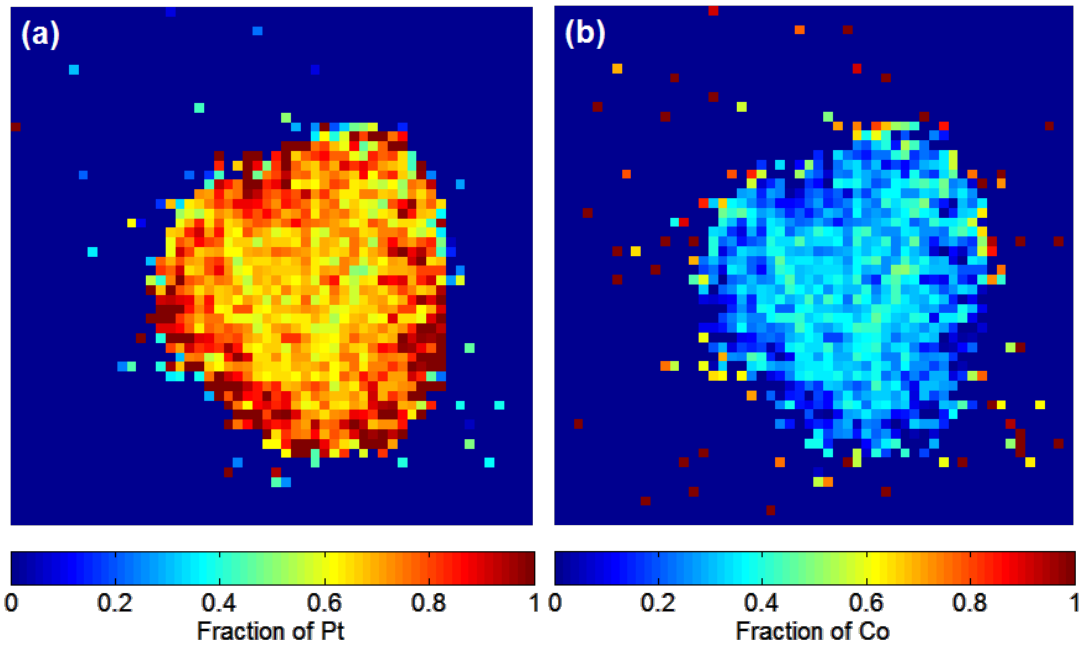


Figure 7.6 – Fractional maps of Pt (a) and Co (b) assuming a two element system, demonstrating Pt enrichment at the particle surface.

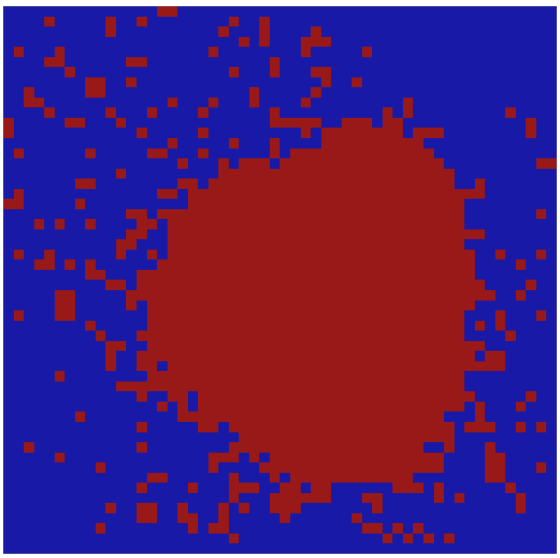


Figure 7.7 – Mask used for cropping the noise out of the fractional elemental maps where the total number of atoms is greater than 0.35.

Cliff-Lorimer quantification (carried out by T. J. A. Slater), using calculated k-factors predetermined in Bruker's Esprit software package, gives an overall

composition of 79at% Pt (compared to an average composition for all the leached PtCo nanoparticles of 83at% Pt). The visible variations in Pt composition from the middle to exterior of 8x8 binned maps produced by the Cliff-Lorimer technique (Figure 7.8) are much smaller than those produced with the cross section method (80at% - 100at% compared to 60at% - 100at%).

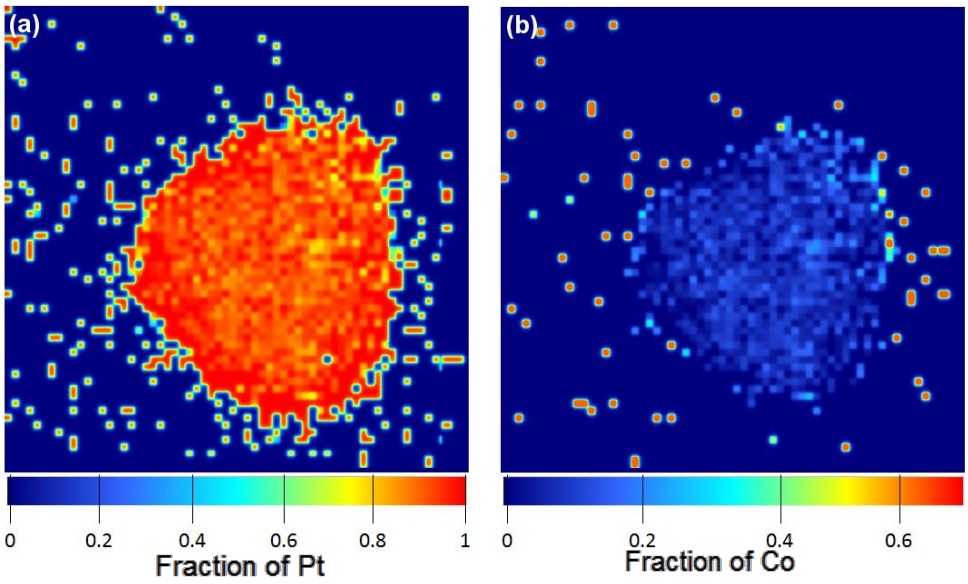


Figure 7.8 – Fractional elemental maps of Pt (a) and Co (b) using the Cliff-Lorimer method it giving an overall composition of 79at% Pt. The Pt surface enrichment is much less clear. Figure courtesy of Thomas Slater.

7.5. Error Analysis

One important aspect of quantification is to evaluate the sources of error in order to understand the accuracy of the data obtained. A summary of the main error sources is laid out in Table 7.4, resulting in a total relative error for Pt of 20% or ±4 atoms for an average atomic column and for Co an error of 37% or ±5 atoms for an average atomic column.

Source of Error	Magnitude (Pt)	Magnitude (Co)
$\sqrt{N}$ Counting statistics	16%	35%
Magnification	4%	
Gradient	2%	0.7%
Wedge Angle	10%*	
Probe current	0.5%	
Pixel dwell time	negligible	

Table 7.4 – Summary of the main sources of error and their estimated magnitude for Pt, Co and Pd calculated cross sections (as relative errors).*The wedge angle error comes primarily from the cautious assumed error in the theoretical determination of the inelastic mean free-path.

7.5.1. Counting Statistics

The main limiting source of error for quantifying nanoparticles is the poor SNR resulting from a low number of characteristic X-ray counts for a particular element, even after integrating over the whole atomic column. Assuming each ionization event can be treated as occurring independently at a constant rate during the pixel dwell time, τ, i.e. following a Poisson distribution, the noise simply follows the square root of the total X-ray counts. Therefore the absolute error in I, is simply $\sqrt{I}$. We have considered the error in background subtraction negligible. From the particle in Figure 7.4b the raw counts for a midrange thickness of Co counts (around 13 atoms) is 8.22, resulting in a relative error of 35% or ±4.5 atoms. For the Pt counts, due to the larger number Pt atoms in the particle the raw counts for a midrange thickness of 20 atoms (37.2 counts) results in a relative error of 16%, or ±3 atoms. Increasing the total number of X-rays collected can provide significant reduction in the statistical error on the measurement. A great deal of improvement has been seen with the new SDDs but there is still further to go until counts are no longer the limiting factor for nanoscale objects. Unfortunately for beam sensitive samples like these catalysts

longer acquisition times or larger probe currents could cause larger errors from the amount of resulting damage in the particles. The next generation of microscopes are likely to have detectors with double the solid angle which would reduce the statistics error by $\sqrt{2}$, taking the Pt error down to ±2.3 atoms.

7.5.2. Probe Interaction Volume

The key parameter needed to quantify EDX counts is the volume of sample being excited by the electron probe. This can be determined by the probe diameter and some knowledge of the thickness or areal density.

Probe size is often confused with the pixel size in EDX analysis; in actuality these two are rarely the same. If the probe is sufficiently smaller than the pixel area and sub-pixel scanning is carried out then the excitation area can be approximated to the pixel area. However, in the cases where sub-pixel scanning is not incorporated, or with some software not available, some time needs to be spent understanding which interaction volume estimate to apply.

7.5.2.1. Nanoparticles

The catalyst nanoparticles are sufficiently thin such that beam spreading effects can be ignored. In the limit of the thin sample the interaction area can be described by the equation for estimating the probe diameter.

7.5.2.2. Calibration Samples

The wedge calibration samples are considerably thicker than the catalyst particles, such that beam broadening should be taken into account. This results in a larger apparent probe area for the same size. The line scans will most likely be carried out at a much lower magnification than the catalyst maps. This means that without sub-pixel scanning the excited volume of sample is likely to be notably smaller than the image pixel size. Not incorporating this could result in an under/over estimate of the final calculated cross section.

7.5.2.3. Magnification Calibration

As with all the ADF STEM images the magnification calibration is critical. Although the EDX cross section is area independent I still need to be able to know the area of sample being excited in order to estimate the number of atoms being excited. The easiest method of ensuring accuracy of the magnification calibration is to calibrate off the ADF STEM image and then carry out the spectrum image with either the same pixel width or an integer multiple of it. This makes the error in magnification the same as for the ADF image used to determine it.

7.5.3. Wedge Geometry

The cross section calibrations are dependent on the known geometry of the pure element wedge samples. The wedge samples were prepared from polycrystalline wires in the FIB. Due to the rate of damage depending on grain orientation, the wedge thicknesses can vary across their width, causing a degree

of uncertainty in the absolute thickness, although this was not observed while preparing the samples. Towards the wedge tip, the thin region is considerably less stable under the ion beam. It is therefore rare that the calibration specimen drops off linearly to a fine point; more likely is a blunt round end with an amorphous region at the very tip. These variations in the sample geometry are overcome by using equation 7.6 to calculate the cross section, where only the change in thickness or the gradient of the line profile is required rather than the absolute thickness of the wedge. The random error from uncertainties of sample thickness and those introduced due to channelling of the different grain orientations causing fluctuations in the line scans can be seen in Figure 7.1. They result in an error in the gradient measurement of 2% for the Pt wedge and 0.7% for the Co wedge.

The wedge angle can be changed as long as there is a large enough region within the thickness ranges where absorption and fluorescence can be neglected (or where the X-rays detected change linearly with thickness). Too large an angle and too few data points will be collected in this linear regime, especially taking into account the blunt nature of the wedge tip; too small an angle and the sample might buckle or the point of absorption might not fit into the experimental field of view. A gradient approach is still dependent on accurate knowledge of the angle, θ, of the wedge which may vary considerably from that set by the FIB operator. If the wedge angle of the pure element calibration samples is determined via the t/λ method, it will carry a relative error of 10% for both elements. This error would be negligible if one assumes that the nominal angle set up in the FIB is correct. Assuming a 10% relative error in the theoretical determination of the inelastic mean free-path, the wedge angles were

determined using two t/λ EELS methods. For the Co sample, a wedge angle of 1.41±0.14° is obtained with the Malis method[215] and 1.9±0.2° with Iakoubovskii's.[216] Similarly, for the Pt sample, a wedge angle of 0.53±0.06° is obtained with the Malis method and 0.79±0.08° with Iakoubovskii's. It should be noted that the error is mostly coming from the assumed 10% uncertainty in the mean free path calculation. The linearity of the t/λ curve was preserved for t/λ<2 for both samples and the slope determination had a relative error below 4% in both samples. The uncertainty in the calculated inelastic partial cross-section, which is a consequence of the uncertainty in the exact wedge angle value, could be reduced via improved sample preparation routes, which are currently being explored. It is worth mentioning that the use of needle-shaped samples in a high-tilt tomography TEM holder would allow for a more accurate experimental determination of the inelastic mean free-path and, therefore, the sample thickness at any point, although with the drawbacks previously discussed.

The effect that this wedge angle variation has on the partial scattering cross sections calculated is summarised in Table 7.5. An increase in the wedge angle results in a smaller cross section and so larger number of atom counts is determined from the X-ray map. Figure 7.9 shows that the wedge angle determination has only a small effect on atomic fraction maps if the method produces a change in the ratio between the cross sections.

Source of θ	Set at FIB	t/λ - Malis	t/λ - Iakoubovskii
θ Pt (deg)	0.5	0.53	0.79
θ Co (deg)	1.5	1.41	1.90
σ Pt (b)	8.56	8.07	5.42
σ Co (b)	3.67	3.90	2.89

Table 7.5 – Summary of the resulting cross sections depending on the method used to determine the angle of the wedge standard samples.

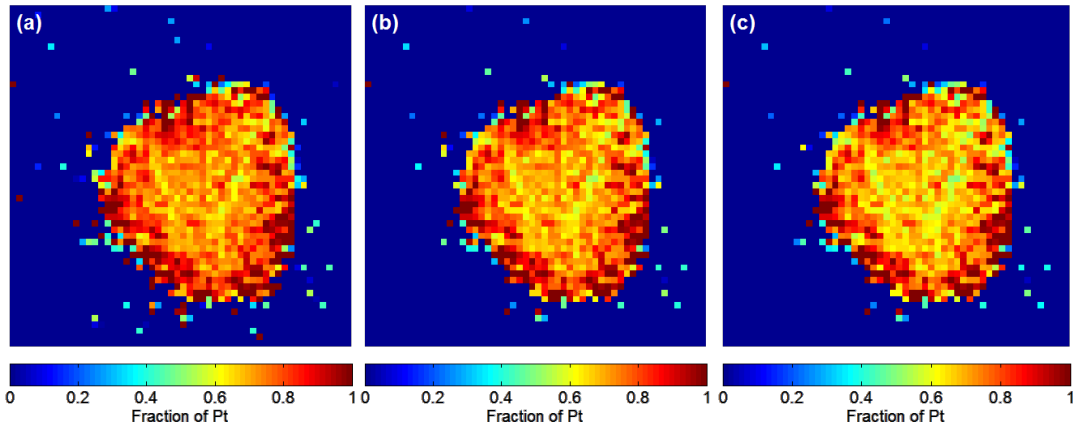


Figure 7.9 – Atomic ratio maps for Pt for the different methods of θ determination for the wedge standard samples, Iakoubovskii (a), Malis (b) and the angle selected in the FIB (c).

7.5.4. Probe Current

The probe current measurement can provide a systematic source of error if the calibration of the ammeter is inaccurate. This can be the case in electron microscopes where the probe current is being read off from the phosphor screen rather than a dedicated pico-ammeter. A systematic error in the probe current reading will not affect the accuracy of the quantification results as this error will be incorrect by the same amount for both the standards and the experimental images causing them to cancel out. However, it does produce limitations on using the cross sections to draw comparisons between different machines and detector settings. The random error from the probe current can be estimated

from fluctuations witnessed in the current reading over time, which provides a relative error of 0.5%.

7.5.5. Integration Window and Background Subtraction

Integration window and background subtraction have a considerable effect on the resulting extracted counts. The background subtraction method should remain consistent between the wedge standards and the nanoparticles. Here a three window method was applied where the selection of the background subtraction windows in particular needs to be carefully chosen in order to suit both types of spectra; the bulk wedge samples and the bimetallic nanoparticles. The spectra from the wedge samples could contain potential artefacts such as escape peaks which need to be avoided in the background selection windows. The background windows for the nanoparticle spectra also need to avoid any peaks from the other elements within the system.

7.5.6. Channelling

The final source of error to discuss is the effect of channelling on ionisation events and X-ray generation occurring. In the same way that the ADF scattering cross section demonstrates a 60% increase for an on-axis column due to channelling of the electron probe, an increase in the amount of X-ray generation is also seen for on-axis crystals.[217] Traditional EDX analysis worked around this issue by deliberately tilting away from a channelling case; unfortunately such a tilt severely limits the image resolution in the tilt direction.[217]

During EDX mapping of nanoparticles, the map is a cumulative image over several scans. Under such a beam dose the particles often reconstruct and rotate during the course of the acquisition. With this in mind the resulting maps are therefore an average over several different channelling and non-channelling conditions. This means that the average profile taken through the channelling variation witnessed in the wedge line profiles is not as unrealistic an estimate of the conditions for the particle maps.

7.5.7. Error Variation with Thickness

Unlike the critical sources of error for ADF cross sections, the limiting errors in EDX quantification are dependent on thickness. The error due to poor counting statistics will reduce with increasing number of counts and therefore an increasing number of atoms in the column also. Using equation 7.7 it is possible to calculate the number of X-ray counts produced by each given number of atoms and therefore quantify the reduction in relative error variation with increasing sample thickness (see Figure 7.10a), although this reduction is not sufficient to diminish the absolute error in terms of atom counts with thickness (see Figure 7.10b).

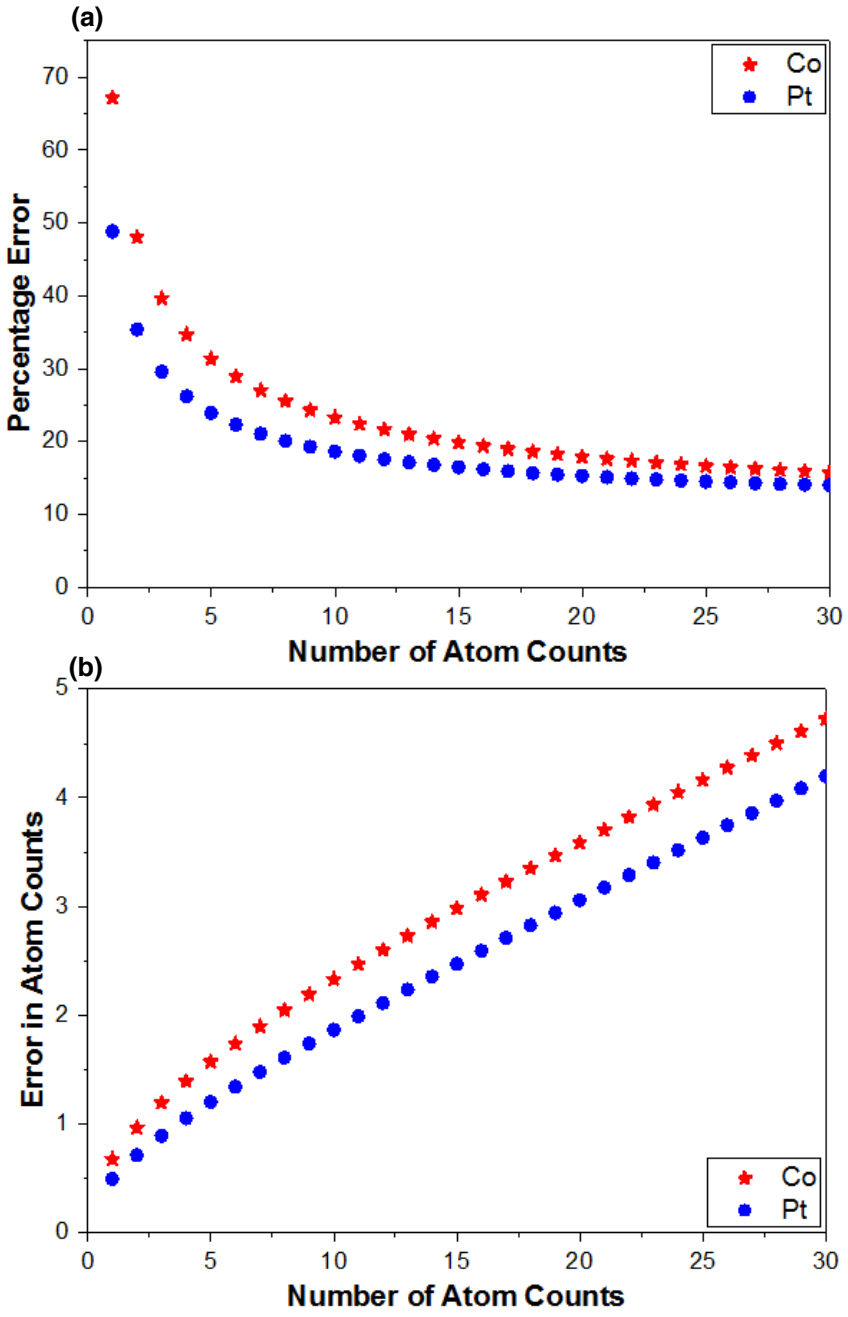


Figure 7.10 – How the percentage error (a) in the EDX cross section and the error in terms of atom counts (b) change with increasing sample thickness. The percentage error decreases with thickness due to the increase in the number of X-ray counts and so the improvement in the counting statistics error.

7.6. Pt-Pd Nanoparticles

Pt(Pd) core-shell nanoparticles are manufactured by depositing Pd nanoparticles on the carbon support; their surface is functionalised with hydrogen to

encourage the Pt to attach to the functionalised sites. As such the particles are expected to demonstrate a well-defined core-shell interface. The sample investigated here is referred to as having 2-monolayer coverage. This means that the amount of Pt deposited is enough to create a uniform 2-monolayer thick coverage over the average particle size, assuming the particles are spherical. In reality (Figure 7.11), because the Pd core is deposited on the carbon before the Pt shell is applied, the Pt forms more of a cap structure over the Pd core as it is unable to coat where the particles are sitting on the support. The well-defined asymmetry of the core-shell geometry gives a clear estimate of the where the carbon-support in located in our compositional maps. Only one incidence was found of more uniform looking core-shell coverage where the particle-support interface is likely to be perpendicular to the viewing direction (see Figure 7.12).

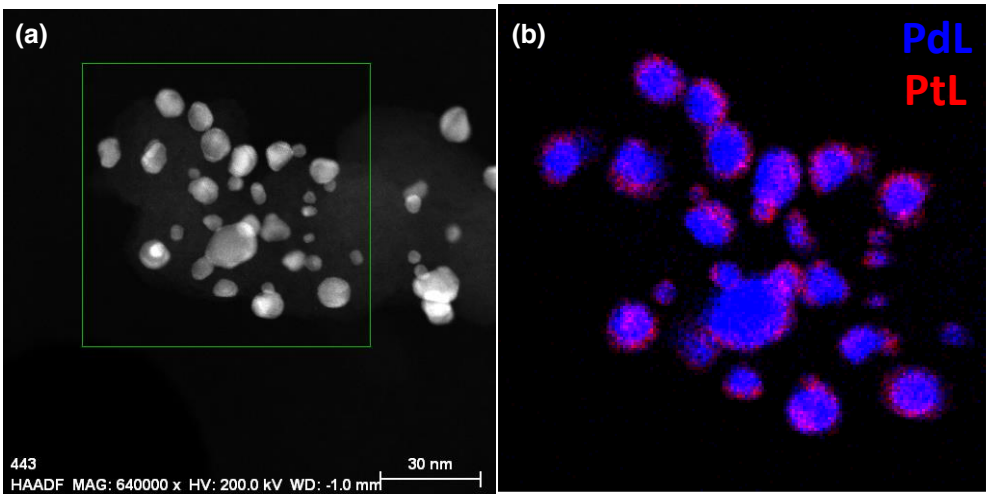


Figure 7.11 – Low magnification ADF image (a), and the corresponding composite EDX map (b); Pt is red and Pd is blue demonstrating the non-uniform coverage of the Pt shell due to where they sit on the carbon support.

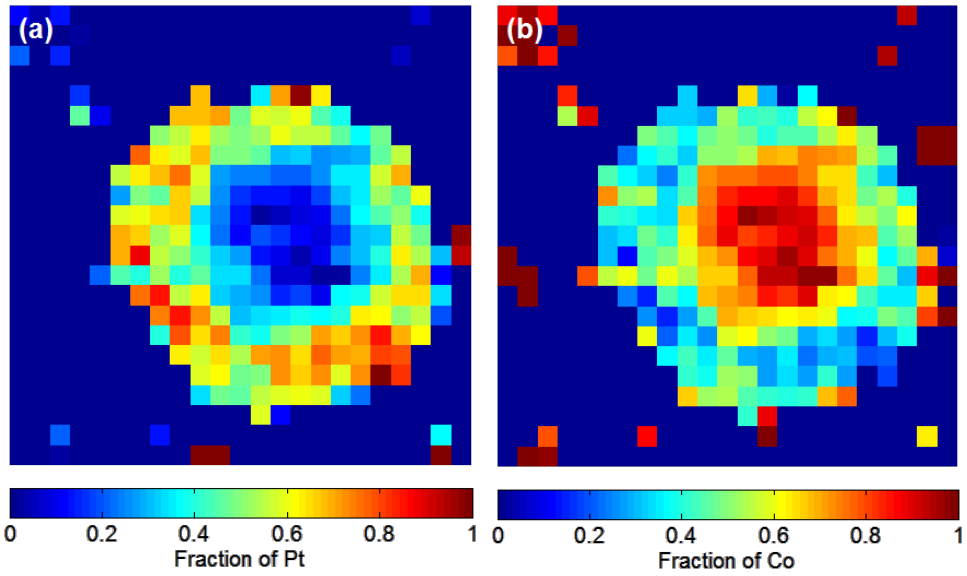


Figure 7.12 – The fractional Pt (a) and Pd (b) maps of a particle demonstrating a more uniform Pt coverage which implies that the particle is laying on top of the carbon support, therefore the interface cannot be seen in the image.

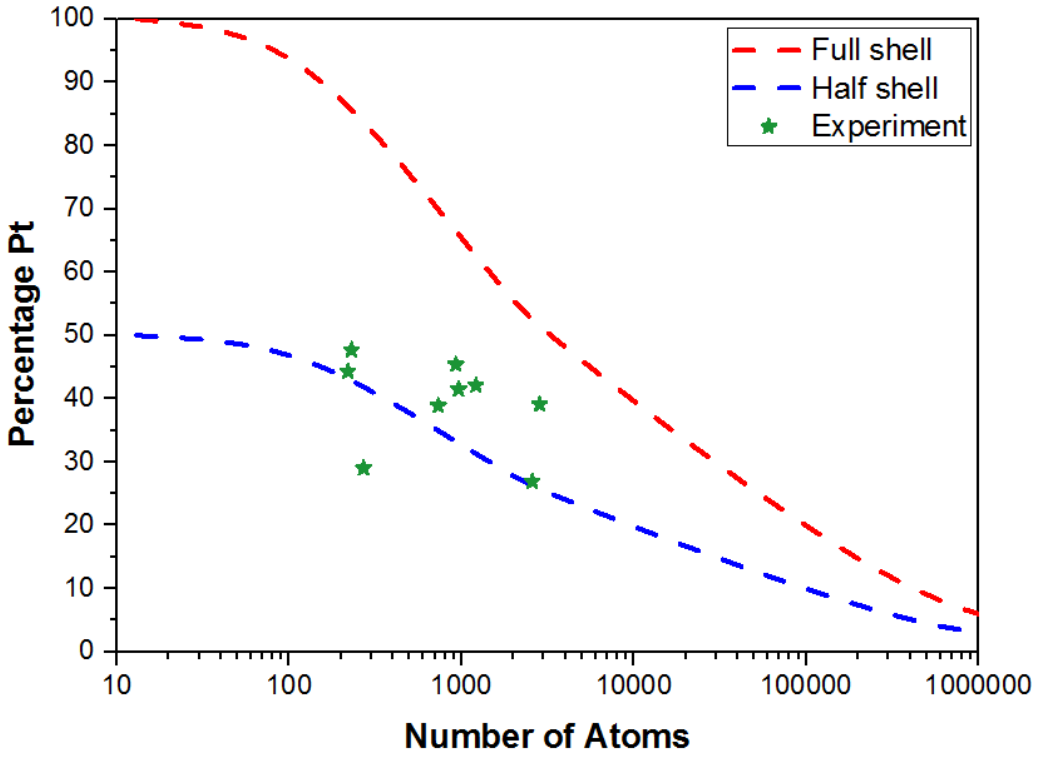


Figure 7.13 – Comparison between the experimental compositions and those predicted by a uniform 2-monolayer coverage of magic number cuboctohedral nanoparticles. A complete 2-monolayer coverage is shown by the red line and a half shell of 2-monolayer coverage is shown by a blue line.

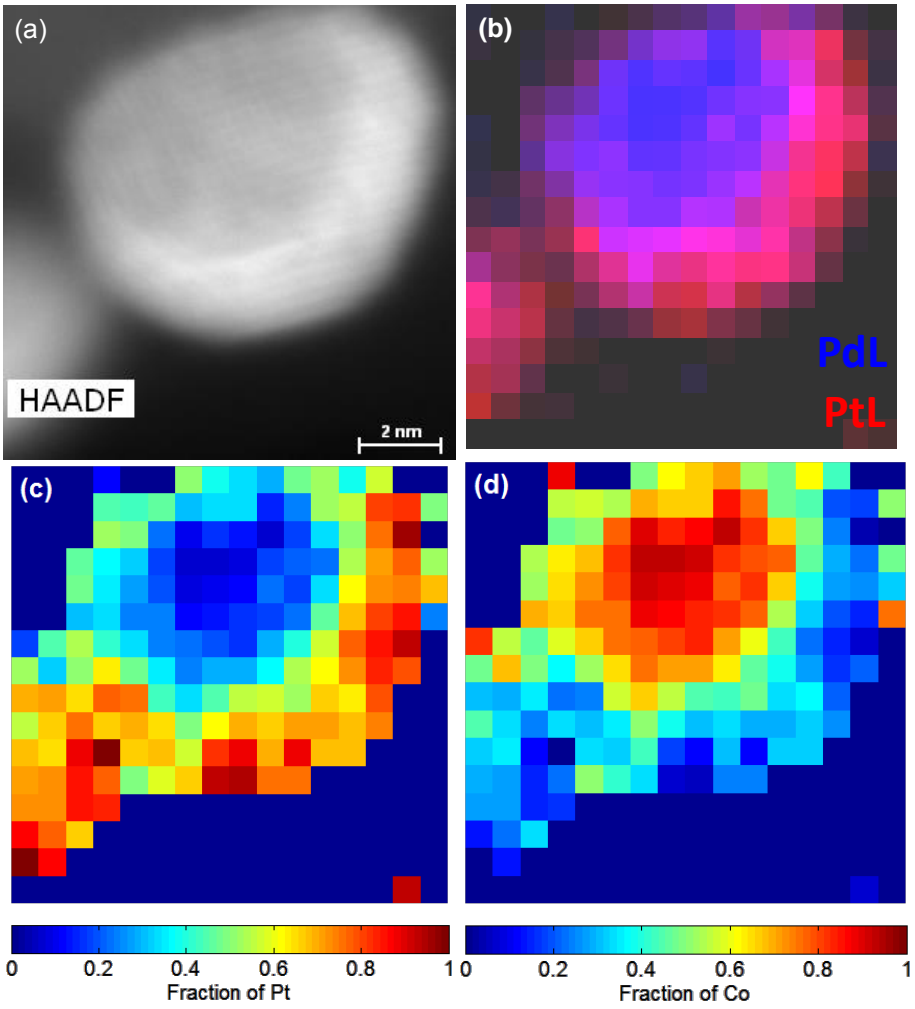


Figure 7.14 – A 6-7nm particle demonstrating the more usual Pt capping of the particles, with overall composition of 45.4% Pt. The cumulative STEM image (a) shows a clear step contrast variation towards the particle surface. The composite image (b) and the fractional Pt (c) and Pd (d) maps show distinct Pd core with a Pt rich cap covering two thirds of the particle edge. The Pt shell cannot cover where the particle is sitting on the carbon black support.

From the high resolution maps (see Figures 7.12, 7.14 and 7.15) it is possible to quantify the Pt coverage and compare this with the composition expected for a uniform 2-monolayer shell. In, the experimentally determined whole particle compositions are plotted alongside the theoretical compositions expected for a perfect cuboctohedral nanoparticle, with either half or full coverage of two monolayers of Pt. The real particle compositions primarily lie in the region

between these two curves, demonstrating higher than 2-monolayer coverage on the exposed surfaces of the particle. This either suggests a coverage of more than 50% of the particle surface as demonstrated in Figure 7.15 or a thicker than 2-monolayer coverage.

Some of the smaller particles demonstrate evidence of alloying (see Figure 7.15); whilst only one example was found here there is evidence for this in the literature.[51] Energetically Pt and Pd are entirely miscible over all compositions so it is likely for the two species to want to intermix. The majority of the particles investigated demonstrated the core-shell step composition (see Figure 7.14). There is no clear dependence of composition on particle size suggesting the synthesis route produces a size dependent Pt shell i.e. larger particles have a larger shell to maintain the same composition. Not all the nanoparticles investigated demonstrate an entirely uniform Pt coverage. In Figure 7.16, facet decoration is visible as much higher intensity lattice fringes in the ADF image which directly relates to higher counts in the Pt elemental map. This sort of Pt decoration is evidence for non-uniform coverage which we want to understand, particularly what effect this has on the catalytic activity.

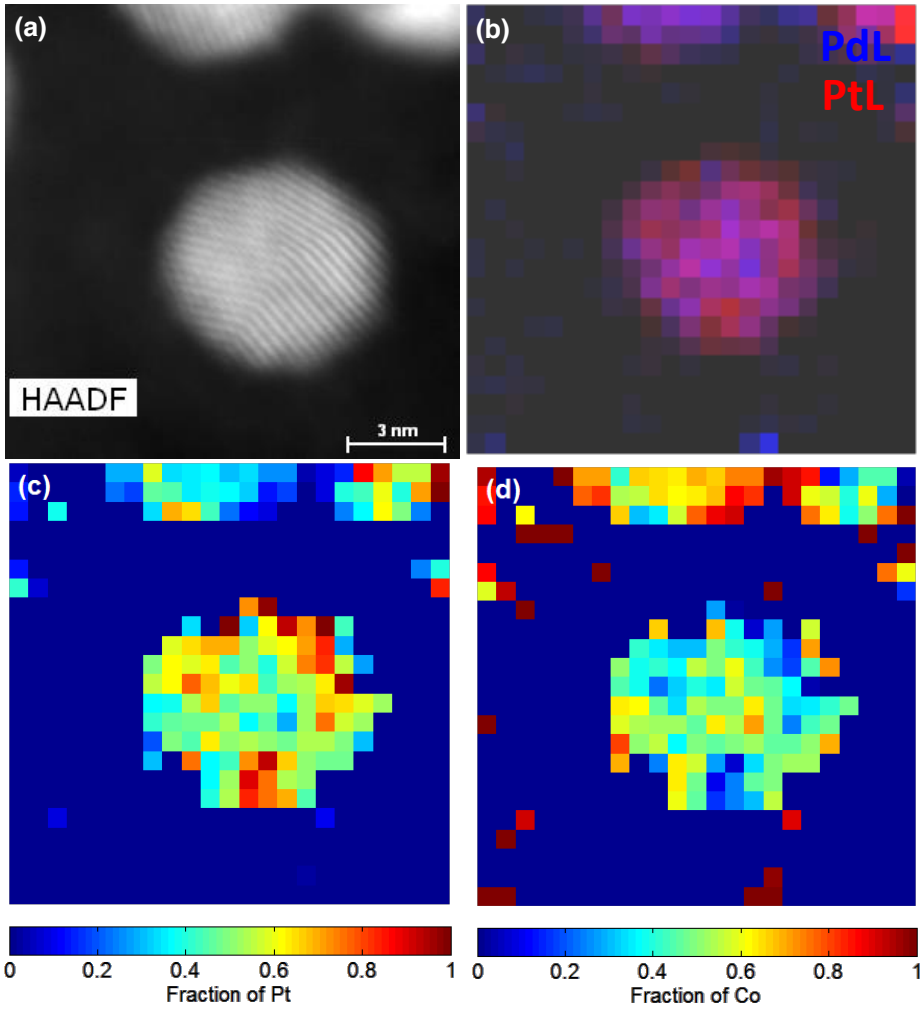


Figure 7.15 – Small ~5nm particle showing evidence of alloying rather than the expected core-shell structure with an overall composition of 48.5% Pt. The cumulative STEM image (a) shows patchy contrast variation and a decahedral structure. The composite image (b) and the fractional Pt (c) and Pd (d) maps show a rather uniform elemental distribution with some Pt surface enrichment still present.

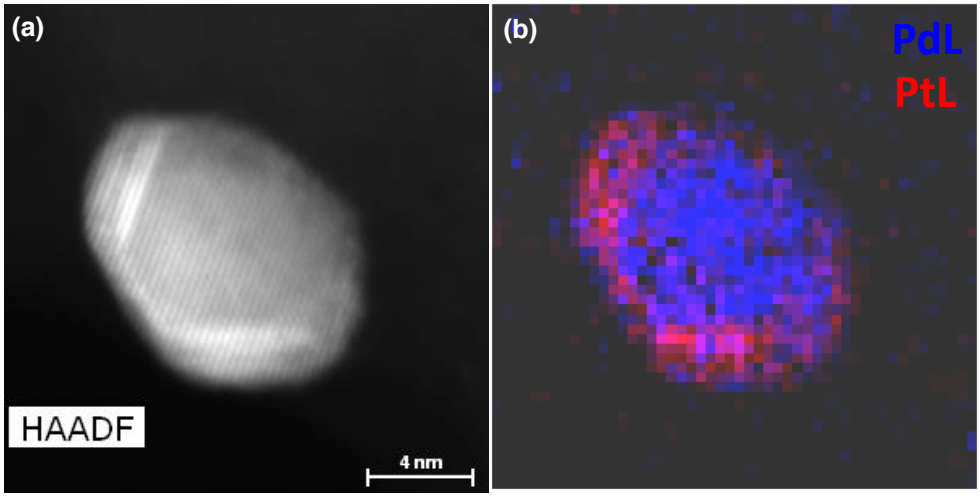


Figure 7.16 – ADF image (a) and composite map (b) of an ~8nm particle with 27.3%Pt overall composition. This particle shows evidence of non-uniform facet decoration by the higher intensity in the ADF and the corresponding higher counts in the Pt map.

7.7. Pt-Co Nanoparticles

A selection of both the acid leached and the un-leached nanoparticles were mapped and quantified at high resolution to investigate the Pt enrichment which the leaching process introduces. The particles begin with a nominal composition of 75% Pt from deposition of both species onto the carbon support and subsequently treated such that they coalesce into alloy particles. During acid leaching the Co reacts preferentially and is removed from the particle surfaces leaving behind the less reactive Pt metal. Comparison of the overall Pt composition with particle size demonstrates very little change in the average composition due to leaching (see Figure 7.17).

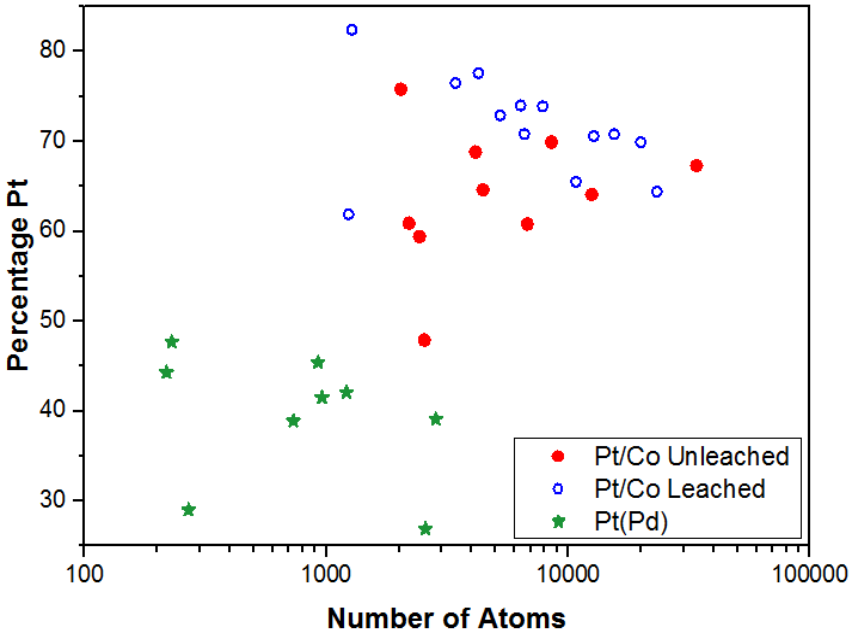


Figure 7.17 – Comparison of the total Pt content of a particle against the number of atoms it contains for both the leached and un-leached Pt/Co samples and the Pt(Pd) core-shell particles. Overall the leached particles only demonstrate a slightly higher Pt content.

Considering the primary aim of the acid leaching process is to remove Co a difference in composition is expected. However this difference in composition seems to be largely focused on the particles surfaces. Only a small amount of Co is seen in the first few outer layers of the leached particles in comparison to the much more uniform composition seen throughout the un-leached particles (see Figure 7.18). The percentage Pt increases with decreasing particle size (Figure 7.17), which is in agreement with this being a surface depletion of Co; smaller particles have a larger surface area to volume ration so will be affected more by the leaching. As in the Pt(Pd) system, there is evidence of a non-uniform shell because Co depletion cannot occur for the region of particles in contact with the support. In Figure 7.18c and d the Co depletion is less apparent towards the bottom of the particle which may indicate where it is attached to the carbon.

The surface segregation becomes more apparent when the fractional Pt maps are plotted as binary images highlighting the pixels ≥85%Pt (see Figure 7.19). Pt enrichment is patchy with no enrichment at the vertices of the more angular particles, penetrating up to 5-6 atomic layers into the particles.

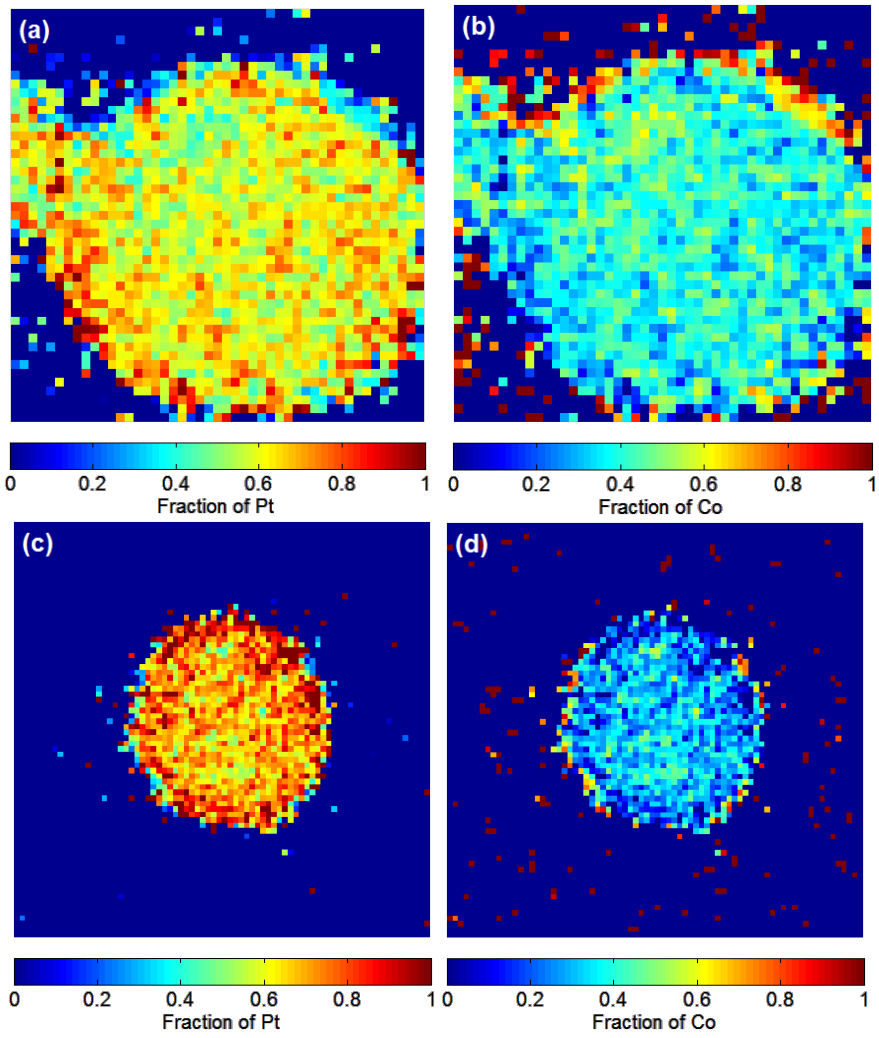


Figure 7.18 – Example fractional Pt and Co maps for an un-leached sample (a) and (b) and for an acid leached particle (c) and (d).

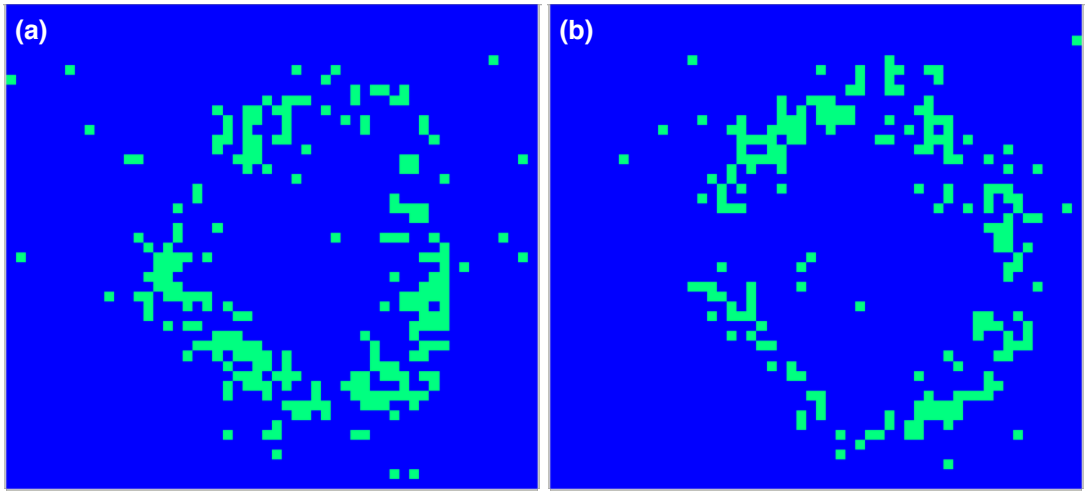


Figure 7.19 – Two example maps for the acid leached PtCo nanoparticles. Binary maps showing the pixels where the percentage of Pt is greater than or equal to 85% Pt. Pt enrichment is visible around the particle edges.

7.8. Conclusions

Here I have demonstrated a new direct method for quantifying EDX analysis using partial scattering cross sections. It is simple to implement using single element calibration samples and also allows ease of comparison with both ADF and EELS quantification results. Partial scattering cross sections are robust to a range of acquisition parameters including magnification, dose, and sample thickness, making them a measure for accurate comparison of EDX detection efficiency between different microscopes. The main sources of error in this approach originate from determining the wedge angle for the pure element standards and the poor counting statistics, particularly for low mass samples.

The Pt(Pd) nanoparticles show a clearly defined core and shell where the core is more of a cap than a complete shell due to the obstruction of the carbon support. This is beneficial as it means a further reduction of the Pt content where it is not needed. Large variations are seen in the core thickness between

particles and occasionally facet decoration rather than complete coverage. Some smaller particles have also been seen to demonstrate alloying. The Pt(Pd) nanoparticles demonstrate much lower Pt content than the Pt/Co. However the Pd metal is of a much higher cost than Co so the saving is not as large as might be expected.

I have also quantified the Pt surface enrichment or rather the Co depletion at the surface of Pt/Co acid leached particles. This depletion penetrates up to 5/6 atomic layers into the particles and seems to be rather absent at the apexes of the more facetted nanoparticles. The leaching process demonstrates very little change in Co composition when investigating the whole particle but produces a localised surface depletion which is demonstrated by the high resolution maps. As for the Pt(Pd) system there is also evidence of the Co depletion only occurring on the exposed particle surfaces, although unlike with the Pt(Pd) particles the higher surface Pt content is not apparent from the ADF STEM images alone. EDX analysis is therefore essential to quantifying and understanding them.

8. COMBINING ADF AND EDX SCATTERING CROSS SECTIONS

Bimetallic nanoparticles represent a considerable step up in complexity for trying to solve their 3D structure. This is primarily due to the fact that several different thickness and composition combinations for an atomic column will result in the same or a similar ADF scattering cross section. As such a combination approach towards their characterisation is essential. Here I compare both ADF and EDX quantification techniques and outline an iterative method for determining the thickness profile of an acid leached Pt-Co particle, making using of information provided by both.

8.1. Initial Cross Section Analysis

I begin by using a comparison of the ADF cross sections (see Figure 8.1) with the pure Pt library (as outlined in Chapter 6) to provide a first estimate for the thickness profile of the particle (see Figure 8.2). Such an approach results in an estimated total number of 5304 atoms. Co atoms are approximately 1/3 the atomic number of Pt atoms, therefore any increase in Co content from the pure Pt estimate will require a corresponding increase in column thickness to maintain the same total ADF scattering cross section. As such the preliminary map in Figure 8.1 should be used as a lower thickness estimate of the particle.

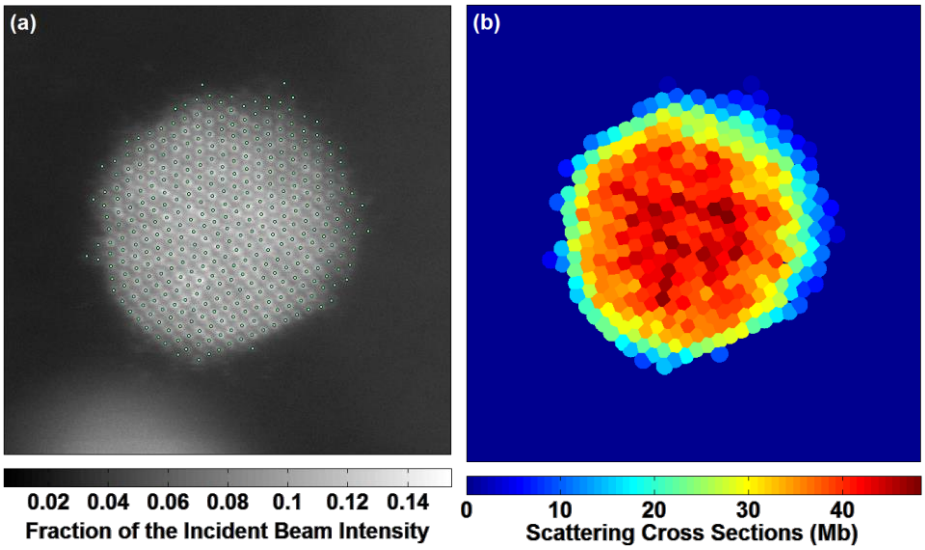


Figure 8.1 – ADF image of the Pt-Co leached particle (a) with the corresponding ADF scattering cross section map (b).

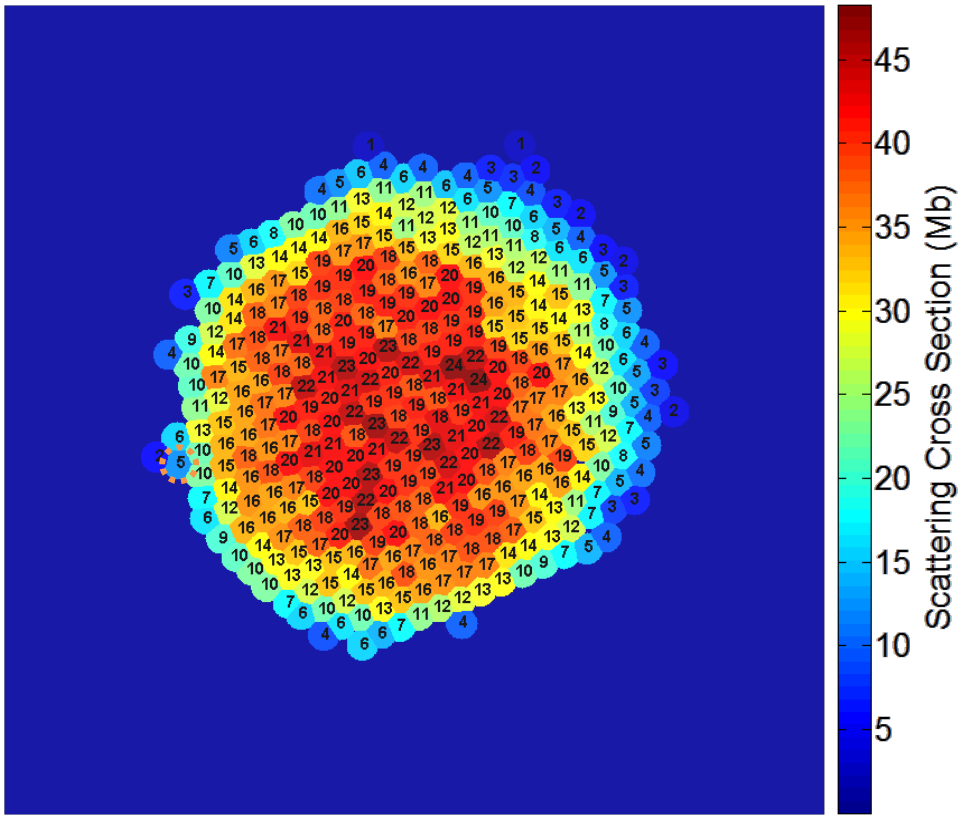


Figure 8.2 – Scattering cross section map showing the atom assignments for the acid leached particle based on comparison with the single element Pt library. All atom counts should therefore be considered as a lower thickness limit as replacing Pt atoms with Co atoms will require an increase in sample thickness in order to maintain the same scattering cross section value. The dotted orange circle highlights the atomic column used to find an iterative solution.

8.2. EDX Composition Analysis

Using the EDX partial scattering cross sections it is possible to evaluate how the composition varies across the nanoparticle diameter (see Figure 8.3). Quantification using the method outlined in Chapter 7 gives us an overall atom count of 4247 atoms at a composition of 73 ±8% Pt, which increases to 75 ±9% Pt when analysing only the first five atomic layers from the particle surface. This is only a very marginal increase in Pt content at the surface (which is smaller than the error boundaries on this measurement) which may be due to asymmetry in the Co depletion. In Figure 8.3b the Co depletion is more prevalent on the left hand side of the particle; such asymmetry is realistic from what I know about the catalyst preparation route and will lower the Pt surface composition estimate.

The surface Co depletion could not be estimated from the original ADF image (see Figure 8.4a) or from the ADF quantification, because there is such a large change in particle thickness towards the particle edges, any increase in atomic number is lost.

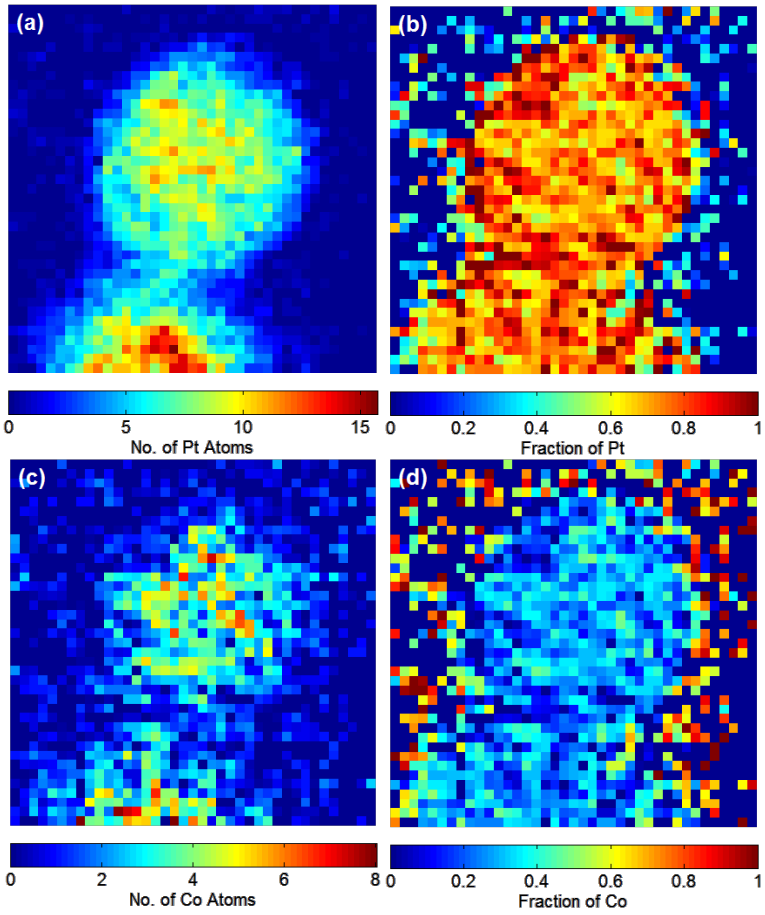


Figure 8.3 – Summary of the EDX cross section analysis. The number of Pt atoms (a), the atomic fraction of Pt (b), the number of Co atoms (c) and the atomic fraction of Co (d). The overall composition of the particle is 73 ±8 atPt%.

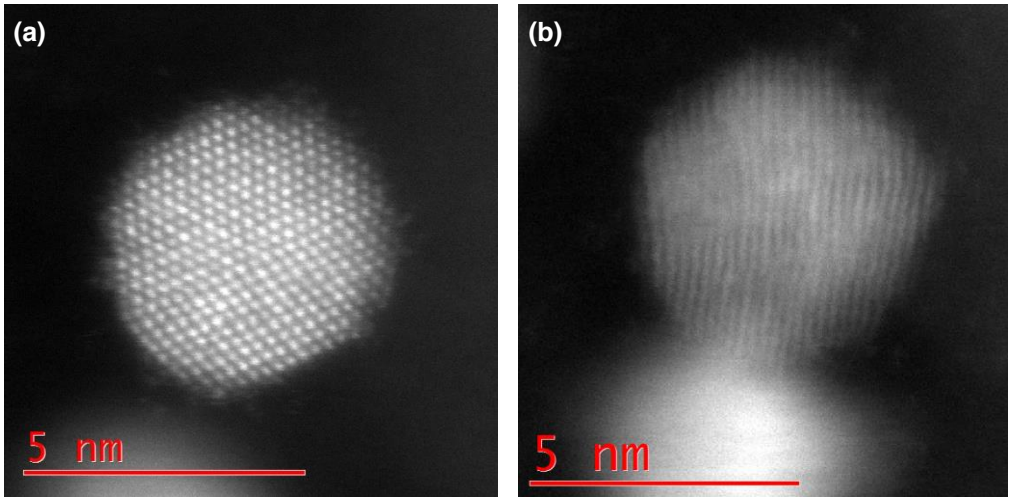


Figure 8.4 – The ADF images of the leached nanoparticle before (a) and after (b) EDX analysis, demonstrating that the particle has rotated during analysis but suffered from low amounts of damage and reconstruction.

8.3. Comparison of ADF and EDX Quantification

The initial ADF quantification on the particle results in an estimate of 5304 atoms in total. However, from the EDX quantification the total number of atom counts is only 4247. The ADF estimate is a lower thickness estimate so the final atom counts of the bimetallic particle are expected to be higher than this making the difference between the two techniques larger. If a measurable amount of sputtering has occurred during the prolonged acquisition time necessary for the EDX analysis one would expect a decrease in the total number of atoms counted from EDX. However, a difference of more than 600 atoms is seems unexpectedly large suggesting that this may not be the sole explanation.

One potential source of discrepancy could be the fact that the EDX cross section calibration using the wedge samples described in Chapter 7 neglects the different amounts of channelling presented by each grain. Replacing the polycrystalline wedge with an on-axis single crystal wedge would result in higher counts and more importantly larger counts with increasing samples thickness and therefore a larger σ, due to channelling. In the cross section quantification on the nanoparticle dividing by this larger σ would reduce the number of atom counts estimated in the nanoparticle by EDX, making the difference between ADF and EDX worse rather than better.

Alternatively grains in the wedge sample could actually be exhibiting some channelling where I have assumed there is no channelling at all. In this case the cross section would be overestimated and an underestimate of the resulting atom counts in the particle would result. There may be an inconsistency between the X-ray counts being detected with the wedge-sample and the Cu-grid with the

particle data acquisition. The geometry effects could be different, affecting the tilt angle or shadowing/absorption effects from the surrounding sample. Each sample was loaded into the sample holder in order to minimise shadowing from the Cu Omniprobe® or mesh grids

Another source of discrepancy could occur if the wedge calibration samples were under-sampled during spectrum imaging, where the pixel width is much larger than the probe diameter. There is a greater danger of under sampling with the wedge samples because of the lower magnification used so the pixel width is larger. The way interaction volume will affect the cross section calculation is through the gradient measurement of EDX counts with samples thickness in equation 7.6 as the cross section is independent to integration area. Although under sampling may produce a smaller volume at each probe point the percentage increase to the next pixel will not change, resulting in a vertical shift in the line profile but no change in the gradient measured.

What will affect the gradient is if there is considerable beam spreading in the thicker regions of the specimen over the thinner regions. Therefore the interaction volume would increase with increasing thickness. Accounting for this would result in a smaller calculated gradient and larger atom counts.

8.4. Combining ADF and EDX Quantification

Despite the discrepancy between the total atom counts evaluated by each method it is still possible to combine both sets of information into our quantification analysis, by using the EDX quantification to provide a composition map rather than atom counts. The approximate lower thickness estimate is taken

from the ADF comparison with the pure Pt library. The Pt/Co ratios can be calculated from the EDX data and used to reduce the number of possible solutions predicted by the ADF data. The approached suggested here for combining the ADF and EDX information on a column by column basis is as follows.

Take the highlighted atomic column in Figure 8.2 as an example column, which has an ADF scattering cross section of 14.6Mb giving an initial atom assignment of 6 atoms thick. The composition from EDX analysis is estimated to be 70at% Pt. These experimentally determined values are plotted as the orange circle in Figure 8.5. There are only 3 possible atomic configurations which lie in close proximity to both the EDX composition and the ADF cross section these are:

- 7 atoms thick with 5 Pt and 2 Co
- 8 atoms thick with 5 Pt and 3 Co
- 9 atoms thick with 6 Pt and 3 Co

Due to channelling, any simulated atomic column with a defined number of both Pt and Co atoms will have a range of ADF scattering cross sections depending on the atom arrangement down the column. This is why they are represented by vertical lines in Figure 8.5. The end points of these vertical lines were determined by carrying out two simulations, one with all the Co at the top of the column and one with all the Co at the bottom of the column.

For the 7 and 9 atom thick columns the experimental ADF scattering cross section value only just lies within the available range predicted by the simulations, therefore the Co atoms would either have to be all at the bottom and top of the column respectively. Using the prior knowledge that the nanoparticles

started out as a mixed alloy before acid leaching it is reasonable to assume a more uniform elemental distribution than this. Therefore the most feasible option is an 8 atom thick column containing 5 Pt atoms and 3 Co atoms. The 8 atom thick column lies further off the experimental composition value in order to match more closely to the ADF cross section. Such a decision is justified as the ADF cross section has smaller errors associated with the measurement than the EDX cross sections and so should be trusted more.

Finally I carry out comparison with yet more simulations for the possible different atomic arrangements which can be seen as the additional blue crosses in Figure 8.5. The arrangement with the closest match to the ADF cross section will provide the most likely solution of atomic ordering. In this case the closest match is Pt-Co-Co-Pt-Pt-Co-Pt-Pt. However, considering the 6% error in our ADF cross section calculation and the close proximity of several similar atomic configurations this cannot be confirmed with a great deal of confidence.

The approach described above to estimate both the particle thickness, atomic ratios, and atomic ordering requires upwards of 10 simulations per atomic column to account for all the different potential ordering arrangements within each column, making it very time intensive. Although the number of simulations will not scale linearly with the number of atomic columns as there will be some overlap of what simulations are needed, it still adds up over the 375 atomic columns in the image. Additionally the accuracy with which atomic order can actually be quantified is questionable due to the range of possible configurations with similar ADF scattering cross sections. Therefore it seems prudent to limit ourselves to only evaluating and separating out composition and thickness information of a particle rather than guessing at the atomic ordering.

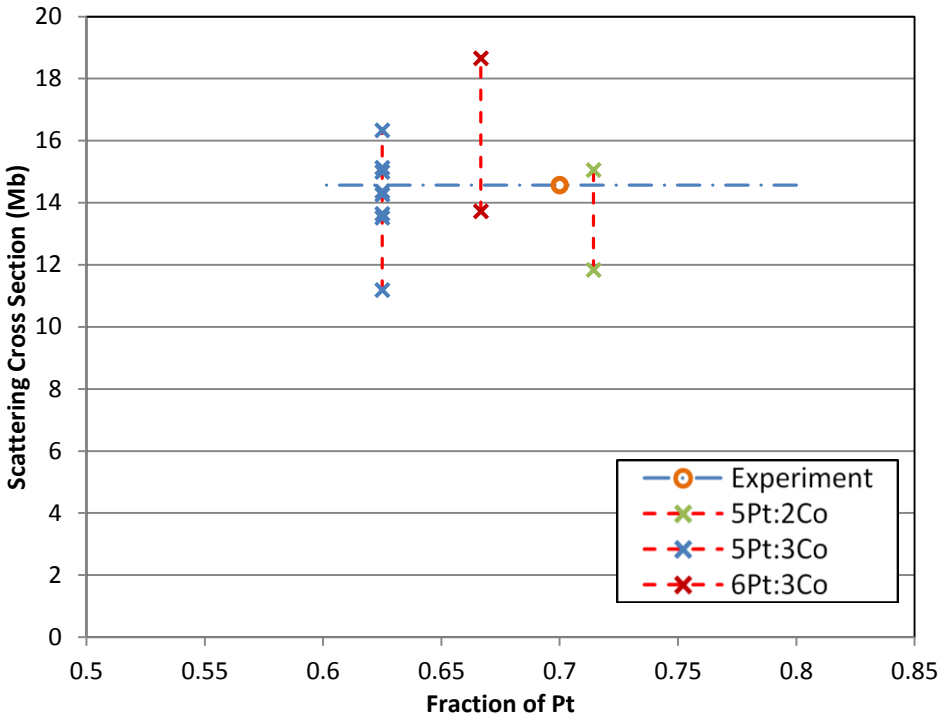


Figure 8.5 – Illustrating the optimisation process from knowing the scattering cross section of an atomic column and the composition. The experimental composition and cross section is represented by the orange circle with the horizontal blue line emphasising the ADF cross section of the column. The vertical dashed red lines represent the ADF scattering cross section range predicted by simulations for a particular combination of atoms depending on the ordering within the atomic column.

8.4.1. Thickness Profile

In order to have confidence in an EDX and ADF combined quantitative analysis on each atomic column I need to trust that both data sets are represented on an atomic column by atomic column basis and can be aligned carefully with respect to one another. Although the square binning used on the EDX data is a reasonable approximation to use when minimal lattice information is available it does make it harder to correlate and compare atomic columns with the ADF analysis. For the comparison investigation both images have therefore been rotated to align the twin boundary parallel to the image axis, which also aligns the square pixels in the EDX data. The fractional Pt EDX map and the ADF

cross section map have been redrawn against each other after rotation (see Figure 8.6).

After rotation, the cross sections of the central twin boundary were compared on a column by column basis, resulting in Figure 8.7. As described above two simulations, one with all the Co at the top of the column and one with all the Co at the bottom yield the upper and lower ADF cross sections for each composition and thickness combination. The total column thickness can be estimated by selecting the simulation line (see Figure 8.5) that is closest to the experimentally determined composition and cross section.

The thickness profile demonstrates the particle to be roughly spherical with the 25 atom thickness corresponding to the 26 atom width. The Co depletion is well defined on the left hand side of the profile as four atomic layers before the number of Co atoms jumps up significantly. Through the remainder of the profile the number of Co atoms remains roughly constant up until the particle edge on the right hand side. As discussed earlier the acid leaching is carried out after deposition onto the carbon black support therefore regions of particle touching the support will not demonstrate Co depletion.

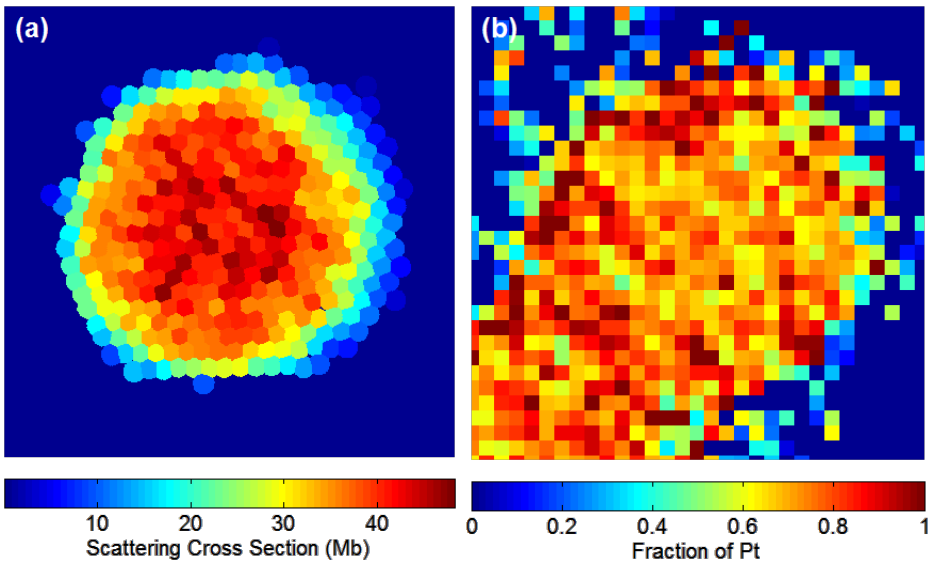


Figure 8.6 – ADF cross section map (a) and fractional Pt EDX map (b) rotated to have the main crystallographic zone-axis parallel to the square pixels edges.

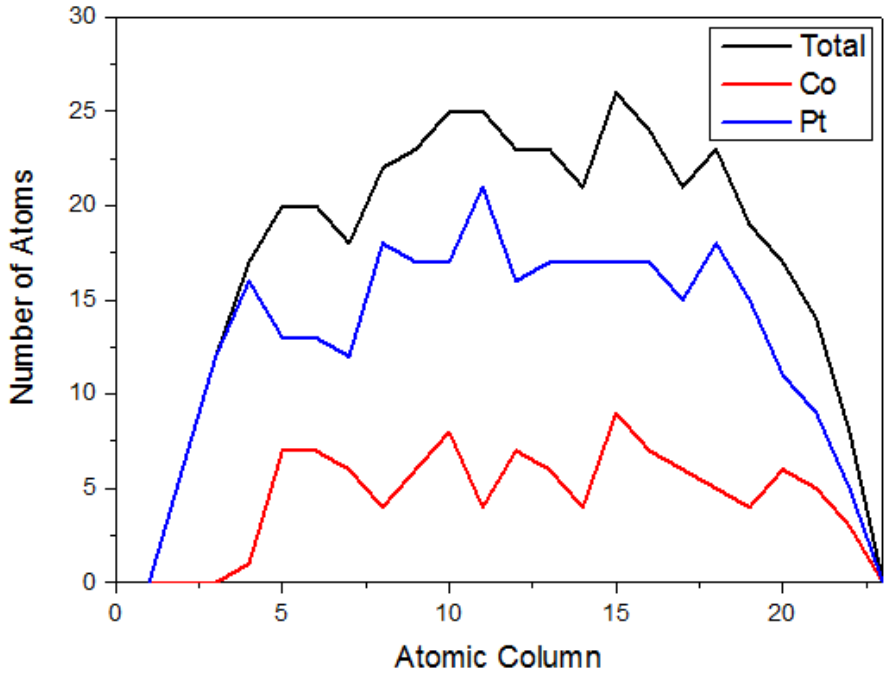


Figure 8.7 – Reconstructed thickness profile resulting from combined EDX and ADF cross section analysis.

8.5. Conclusions

I have presented a methodology for combining EDX and ADF quantification in order to separate out the thickness and composition information. The initial ADF comparison with a simulated pure Pt library provides us with an initial thickness estimate. This is refined by comparing with a range of thickness and composition simulations that have been simulated with all the Co at the top and bottom of the column, to provide the range of scattering cross section values from ordering. Such an approach yields column by column thickness and composition information of the particle.

Extensions of this method to analyse a whole particle hinges on being able to accurately relate the ADF and EDX maps on a column by column basis. This is difficult to achieve with the square pixel binning used here for the EDX analysis so a more intelligent binning process may be necessary. If this method can be expanded over the whole particle, 3D reconstructions could be made also with an understanding of how the composition varies throughout the particle. There are then huge potentials for improving our understanding of catalyst systems. In particular it would allow us to answer one of the fundamental questions about the acid leaching process as to whether or not the surface reconstructs during leaching to produce a more atomically smooth facet again. From a catalytic mechanism point of view we are looking at how flat or rough a surface is left behind from the leaching.

9. CONCLUSIONS AND FUTURE WORK

This thesis has presented advances in quantitative compositional and structural STEM characterisation for investigating catalyst nanoparticles. For the quantification of single element nanoparticles it is now possible to reconstruct their 3D structure from one experimental image, demonstrating single atom sensitivity (less than ± 1 atom) up to 14 atoms thickness. A counting precision of ± 2 atoms begins at 20 atoms and thicker. Such results can lead to information on the degree of coordination at the particle surfaces which provides us with a better understanding of the available electrochemical environments for oxygen adsorption.

The improvements in ADF atom counting have been made possible by using the scattering cross section as the measure for comparison with simulations. I have investigated the robustness of these cross sections to various microscope imaging parameters and the importance of accurate optimised image simulation for comparison with experimental results. The μSTEM simulation code was compared against other available software in order to establish a consistency in the calculated libraries. In Chapter 4, I demonstrated improvements to the detector angle calibration and understanding detector asymmetry and the outer flux cut off, which has improved the experimental accuracy.

The experimental parameters, including a smaller detector collection inner angle and a large convergence angle, have been optimised for maximum robustness to sample mis-tilt. This is an accuracy limiting factor when investigating catalyst

nanoparticles; if one were investigating bulk samples with a large degree of strain a smaller detector angle might not be the most accurate option.

Some of the reconstructed Pt particle structures presented here have been used as the input structures to molecular dynamics (MD) simulations, in order to improve the understanding of gas species interactions with the surface of real experimentally determined particle structures. Previous MD work has focused in the simulation of ideal catalysts of cuboctohedral or truncated octahedral shape with atomically flat facets and no additional steps or ad-atoms. MD work on experimentally determined structures opens up a new area for understanding how reactant species interact with the surface of real particles.

Chapter 7 presented a new direct method for quantifying EDX analysis using partial scattering cross sections. It is simple to implement using single element calibration wedge samples and also allows ease of comparison with both ADF and EELS quantification results. Partial scattering cross sections are robust to a range of acquisition parameters including magnification, dose, and sample thickness making them a measure for accurate comparison of EDX detection efficiency between different microscopes. The main sources of error in this approach originate from determining the wedge angle for the pure element standards and the poor counting statistics, particularly for low mass samples.

EDX cross section quantification has been applied to Pt(Pd) core-shell and de-alloyed PtCo nanoparticles to provide accurate quantification of the Pt surface enrichment or Co depletion present. This information is critical to understanding and subsequently improving the higher catalytic activity demonstrated by these sorts of systems. The core-shell particles demonstrate a well defined core to

shell interface with a step composition change, and provide a much lower Pt content than the PtCo. There is a higher risk of alloying and losing the Pt surface enrichment. This was witnessed particularly in the smaller particles. The Pt deposition can only happen on the regions of the particles not supported by the carbon black, which is the reason for the shells appearing more like caps in the experimental maps. Evidence has been found of facet decoration showing coverage is not always uniform which will affect particle activity, although further investigation is required to establish which the preferential facets for Pt deposition are. The techniques outlined in this thesis could be used to further investigate this phenomenon more closely, in particular the variation across a statistically representational range of nanoparticles.

By comparison the Co depletion in the PtCo particles is a much more gradual gradient towards the particle surface but also shows evidence of non-uniformity, with no enrichment at the apex of the more angular particles and certain facets which are assumed to be in contact with the support. During acid leaching Co atoms are removed from the first few atomic layers of the particle surface resulting in a change in composition which is size dependent. Such composition variation across the particles is not apparent in the ADF STEM images alone where the increase in atomic number is swamped by the large variation in sample thickness towards the particle edge.

Finally, in Chapter 8, I propose a method for combining EDX and ADF analysis of the same PtCo particle, in order to separate out composition and thickness information. With more accurate quantification of the sample thickness and composition it is possible to observe asymmetry in the Pt enrichment where the particles are located on carbon black support. If this method can be expanded

over the whole particle, 3D reconstructions could be made also with an understanding of how the composition varies throughout the particle which has huge implications for our understanding of catalyst systems. In particular it would allow us to answer one of the fundamental questions about the acid leaching process of how smooth or rough the particle surface is after leaching.

As with all electron microscope analysis one should be aware of the damage which the electron beam causes. For the ADF structural quantification I take this into account by determining a 3D structure from a single experimental image, thereby providing a significant reduction in the total dose over tomography techniques. The rough surface of the 3D reconstructions may be in part due to the damage inflicted by electron beam during imaging, but they may also be realistic imperfections for real industrial catalysts. The larger particles seem to demonstrate greater beam stability and smoother facets although the accuracy of atom counting does decrease for thicker samples.

The much higher doses required for EDX analysis does require larger particles due to the beam stability required. During such a long acquisition the particle will necessarily rotate and reconstruct under the beam making the EDX signal inherently more delocalised than that provided from the ADF scattering. Although, with the combined approach we are collecting two signals in parallel in order to achieve as much information as possible per unit dose. This could be further improved by incorporating EELS signal into the analysis as well.

Immediate directions for future work can be divided into four key sections. Firstly, the single element particle reconstruction could be more automated for high throughput analysis in order to gain more statistically representational

particle structure information. Secondly, the option of evaluating a hybrid method with the ICL statistical deconvolution approach. Both the ICL and scattering cross section approaches have different limitations which may be overcome through using a combination of the two. Thirdly, for the EDX quantification the next step is in trying to reduce the size of the primary source of error by improving the number of counts. Finally, an approach to EDX and ADF combination has been proposed here but there is considerable room for development, automation and refinement.

9.1. Towards High Throughput and Statistics

The largest criticism of using high resolution electron microscopy to analyse catalyst nanoparticles is the limitation of statistics. Therefore the next key step in this line of research is to extend the methods described here to cover a much more statistically relevant number of particles. The automated analysis code outlined in Chapter 6 goes a considerable way to achieving this. Although the 3D reconstructions presented here have been carried out by hand, work has already been undertaken to make this process automated with the energy relaxation.

For single element nanoparticles the time consuming factor for high throughput and statistics is the time at the microscope acquiring on-axis nanoparticles images. Moving towards larger numbers of reconstructed nanoparticles one must also begin to take into account the concept of user bias. At the microscope, what criteria are used to select the particles incorporated into the statistics? Does the user inadvertently select only a subset of the range of particles in choosing which particles to image?

In this thesis some attempt has been made to image every available on-axis particle in the field of view at the microscope. The challenge with this is that the height variation means that only those particles specifically in focus will demonstrate any lattice fringes, so focus should be varied continually during searching. Additionally, due to channelling particles which are optimum for atomically resolved imaging (orientated to the low order zone-axis), will appear brighter than those tilted further off. In the search of on-axis particles one may unconsciously begin to focus on the brighter particles resulting in a bias towards particles which are thicker in the beam direction, which will also make them brighter. Particle size distributions have also been used during this thesis to begin to relate the few analysed particles back to the catalyst system as a whole. Comparison with such a distribution gives an idea of how much the individual particles structures can be considered as representative of the remaining particles in the sample.

9.2. Hybrid Method with ICL

The statistical approach or ICL method should not be ignored when it comes to atom counting in quantitative ADF. The major advantage of ICL is that it provides an independent measure of components which can then be related back to atom counts. Therefore it reduces the chance of a systematic error being present in the atom counting which could go unnoticed when using just direct comparison with simulations. Unfortunately, the major limitation for investigation of nanoparticles is the critical number of observations per component necessary to provide enough statistics. In the limitations of small nanoparticles, and indeed

with some of the particles investigated in this thesis, there are likely to be missed components (where no atomic column of that thickness happens to be present in that particular image) or small numbers of two neighbouring components which get mistaken for one. The ideal solution would therefore be to establish a hybrid method for optimum accuracy and confidence in the atom counting results.

A first approach to this has been carried out here. Figure 9.1 shows the atom counting results for a Pt/Ir particle based on the statistical ICL analysis by A. DeBacker. ICL results suggest that the particle contains 10 components making it at least 10 atoms in thickness. In contrast, the scattering cross section approach using direct comparison with simulations suggests a nanoparticle with thickness of only 8 atoms. However the original image (see Figure 9.2) does appear to show some ellipticity and poor resolution, suggesting the particle is rather tilted with respect to the beam direction. From investigations on channelling I know this to have an effect on the quantification results. This becomes apparent when examining the atom assignments based on comparison with the normal on-axis simulated library.

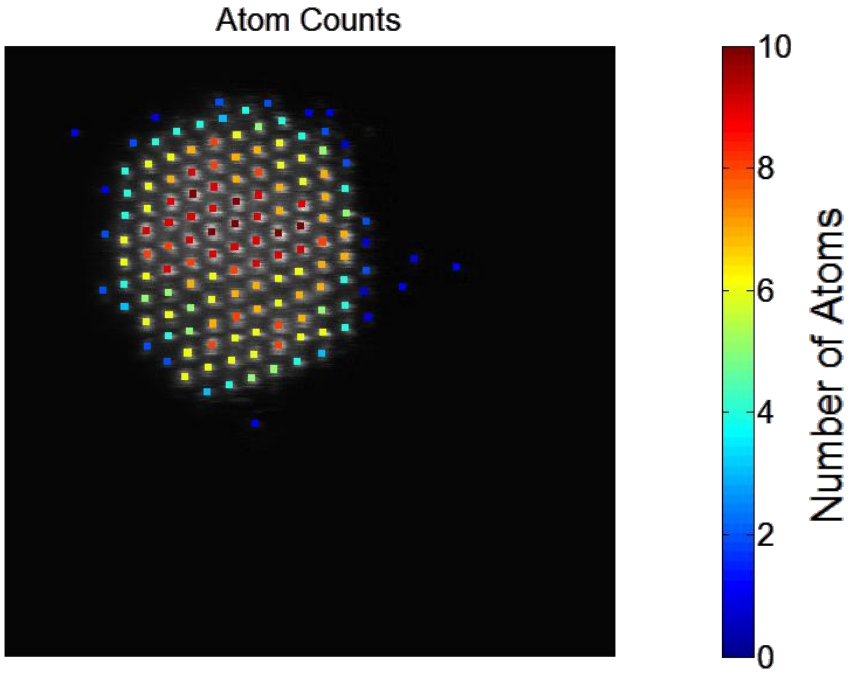


Figure 9.1 – Plot of the atom count assignments from ICL analysis carried out on the tilted Pt/Ir particle image by A. DeBacker.

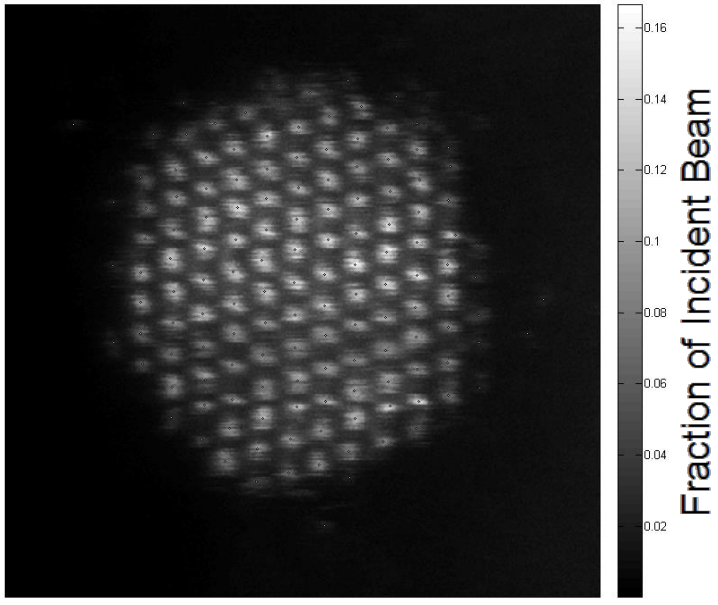


Figure 9.2 – Original experimental image of a Pt/Ir nanoparticle which is clearly tilted with respect to the beam direction.

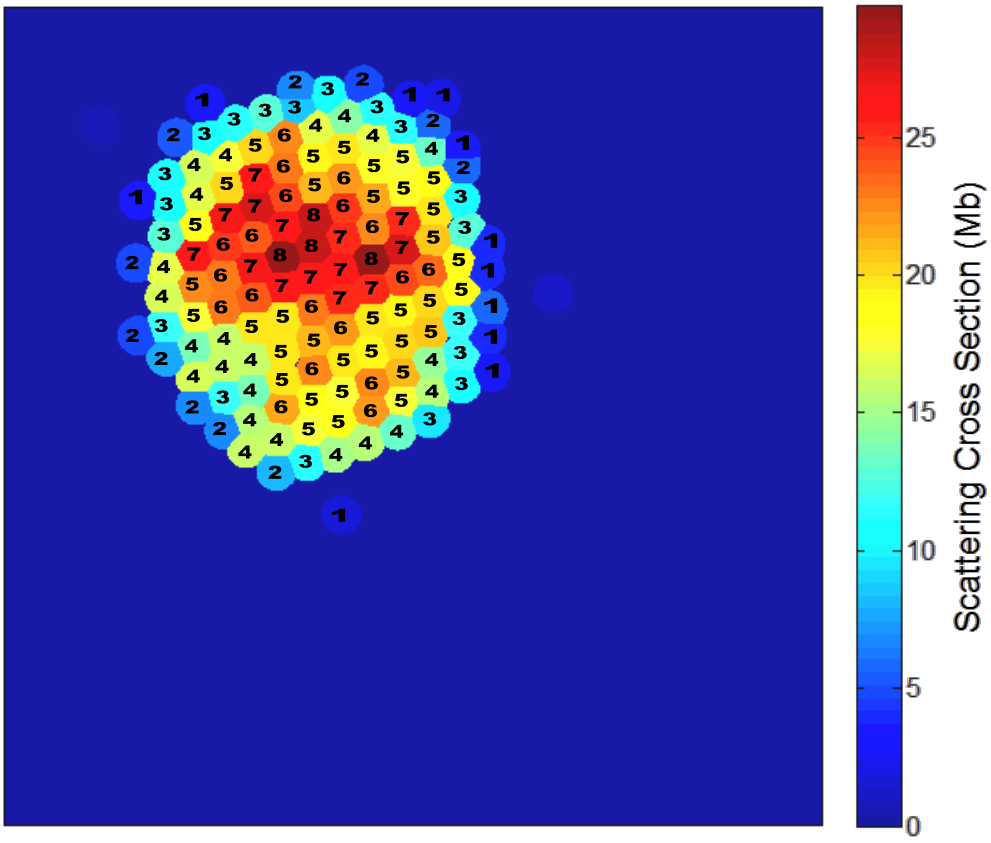


Figure 9.3 – The atom assignments of the Pt/Ir particle based on comparison with an on-axis simulation library.

Using knowledge of the number of components gleaned from the ICL analysis of the image it is possible to select a tilted library where the 10 atoms has a similar scatter cross section to the thickest atomic column in the image. The atom assignments resulting from comparison with such a library for 2.6˚ tilt is shown in Figure 9.4. Purple numbers in this Figure indicate columns which differ by one atomic count from the ICL assignments, and black numbers indicate atom columns where the atom assignments match. The match has clearly improved in comparison to the ICL assignment although the numbers indicated in purple are mostly still on the low side. This suggests that a slightly more tilted library should be used. Iteration of this match with atom assignments for libraries at different

degrees of tilt could provide a combined atom counting solution, providing accurate knowledge of the sample tilt as well.

Being able to accurately quantify even tilted images would also aid with high throughput analysis by giving us a greater field of particles, which are of acceptable standard to quantify.

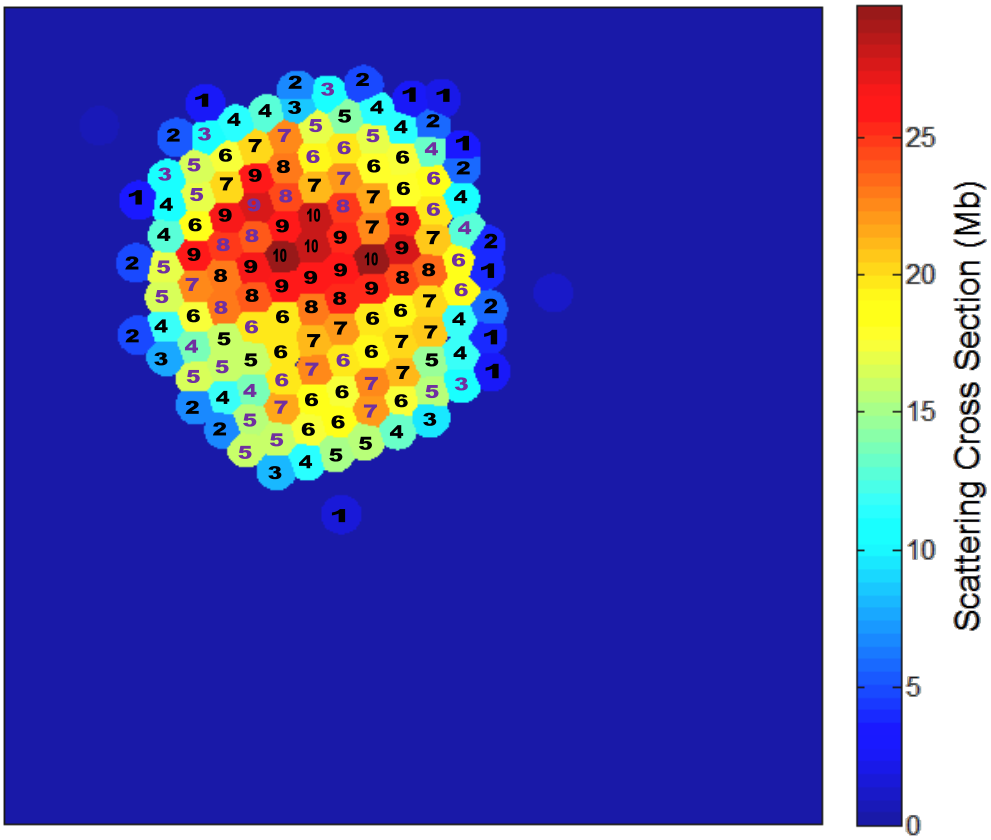


Figure 9.4 – The atom assignments of the Pt/Ir particle based on comparison with a 2.6° tilted library. Those numbers in purple differ from the ICL components in Figure whereas the black numbers match.

9.3. Improving EDX Counts

In the EDX side of the analysis it is very clear that the Poisson noise statistics are the limiting source of error. Increasing the number of counts per pixel in the X-ray maps is critical to improving the accuracy of the quantification analysis.

The simplest method to improve the total number of counts is to acquire the maps for longer. However, a longer collection time increases the problems of sample drift and damage. Some new work has recently been carried by L. Jones looking at saving each individual EDX frame and then more accurately re-registering the frames back together in post processing using the ADF image acquired in parallel. This opens up the opportunities for non-rigid registration instead of the effectively rigid registration which is drift correction. However this does very quickly lead into large cumbersome data sets which may be impractical.

A lower damage is often seen when using faster pixel dwell times (whilst still maintaining the same overall dose). It is unclear why this occurs but during this thesis the dwell times used were as fast as the software would allow. If this is only a software limitation rather than a hardware limitation an improvement could be achieved here. Otherwise an improvement to the scan coils or the speed of the electronics readout will be necessary.

The final method for increased counts would be to increase the solid angle of the detector used. The largest cross section in this thesis was found on the Oxford ARM using the 100mm^2 side entry detector. A new generation of microscopes being manufactured now have the option of two of these detectors which should

significantly improve the solid angle available. If the solid angle is doubled this will decrease the counting error by $\sqrt{2}$.

9.3.1. EDX Analysis at 80kV Accelerating Voltage

During the preliminary ADF quantification studies on single atom species (see Section 5.4) dropping the accelerating voltage of the microscope to lower voltages was shown to reduce their movement during imaging. A reduction in the structural rearrangement and damage was also seen in the nanoparticles themselves. This suggests that the primary damage mechanism is knock-on damage which has been shown to generally decrease when using lower incident energy electrons.

Table 9.1 shows a comparison of how the partial EDX scattering cross section increases when lowering the microscope accelerating voltage. The lower energy, and therefore slower, electrons will spend more time in the close proximity of an atom. It is therefore logical to assume that the longer interaction time will result in a greater probability of an ionisation event occurring. Using 80kV could therefore provide a small but not immeasurable improvement in X-ray counts, from both the increase in scattering cross section but also the reduction in particle damage which will allow for longer dwell times.

Acc. Voltage	200kV	80kV
σ Pt (b)	6.15	7.94
σ Co (b)	3.93	6.22

Table 9.1 – Comparison between the EDX partial scattering cross sections of a single atom for the Oxford ARM at 200kV and 80kV accelerating voltages.

The drawback to using lower accelerating voltages can be a loss in the resolution of the microscope. The aberration tuning becomes much more critical in order to achieve the atom resolution needed for quantification.

9.4. Electron Energy Loss Spectroscopy

The preliminary investigations in Chapter 7 on comparing EDX, ADF and EELS cross sections, showed that EELS counts are likely to be three orders of magnitude larger than the equivalent EDX counts. For compositional analysis, a logical assumption would be to explore the possibilities which EELS could provide. Unfortunately there was no access to an EELS detector during the course of this thesis in order to try any EELS.

The challenge with using EELS for compositional analysis of the catalysts systems investigated in this thesis is the location of the Pt ionization edge. The first major Pt edge is the $M_{4,5}$ at 2100eV with a delayed maxima. At such high energy losses, the number of detected counts becomes very small and it is difficult to collect the spectrum from two edges within the same view with any reasonable dispersion. The new generation of duel-EELS detectors may provide

the potential for collecting two core-loss regions simultaneously, which would allow the collections of Pt and another element for compositional quantification.

In the STEM EELS could be collected simultaneously with both the ADF and EDX signals. This would allow for even more data to be collected on the same particle with no further increase to the amount of electron dose experienced by the sample. Additionally the near fine structure may provide insight into the local bonding of elements within the nanoparticles.

9.5. Combining ADF and EDX Cross Sections

The solution to solving the structure of bimetallic nanoparticles lays in the combination of both ADF and EDX cross sections. Here I have presented an approach which uses the atomic fraction of each column determined by EDX and the cross section in ADF to separate the composition and thickness information. The critical step in accurately combining these two techniques lies in relating the two separate images to each other on a column by column basis. This becomes especially challenging if the particle has reconstructed or rotated during the EDX analysis. Future work should focus on automating this approach, in a similar way to how the ADF integration and quantification has been automated. This would allow faster processing and lead towards the analysis of more particles.

If the method outlined here can be expanded to whole particles this will allow 3D reconstructions combined with knowledge of how the composition varies across the particle. The potential this technique has for improving our knowledge of catalyst systems is exciting.

10. REFERENCES

[1] B.C. Tessier, A.E. Russell, B. Theobald, D. Thompsett, PtML/Pd/C Core-Shell Electrocatalysts for the ORR in PEMFC. *ECS Trans.* **16** (2009) 1–11.

[2] S. Mukerjee, Role of Structural and Electronic Properties of Pt and Pt Alloys on Electrocatalysis of Oxygen Reduction. *J. Electrochem. Soc.* **142** (1995) 1409. doi:10.1149/1.2048590.

[3] Oxford English Dictionary. *Oxford Univ. Press*. (2012). www.oed.com.

[4] H.S. Taylor, A Theory of the Catalytic Surface. *Proc R Soc A.* **108** (1925) 105–111. doi:10.1098/rspa.1925.0061.

[5] A.K. Datye, D.J. Smith, The Study of Heterogeneous Catalysts by High-Resolution Transmission Electron Microscopy. *Catal. Rev.* **34** (1992) 129–178. doi:10.1080/01614949208021920.

[6] A. Kulkarni, M. Chi, V. Ortalan, N.D. Browning, B.C. Gates, Atomic Resolution of the Structure of a Metal-Support Interface: Triosmium Clusters on MgO(110). *Angew. Chem. Int. Ed. Engl.* **49** (2010) 10089–10092. doi:10.1002/anie.201005105.

[7] P.L. Hansen, J.B. Wagner, S. Helveg, J.R. Rostrup-Nielsen, B.S. Clausen, H. Topsøe, Atom-resolved imaging of dynamic shape changes in supported copper nanocrystals. *Science.* **295** (2002) 2053–5. doi:10.1126/science.1069325.

[8] J. Hagen, Industrial Catalysis: A Practical Approach, *Wiley-Vch*, 2006.

[9] R.C. Tiruvalam, J.C. Pritchard, N. Dimitratos, J.A. Lopez-Sanchez, J.K. Edwards, A.F. Carley, et al., Aberration Corrected Analytical Electron Microscopy Studies of Sol-Immobilized Au + Pd, Au{Pd} and Pd{Au} Catalysts Used for Benzyl Alcohol Oxidation and Hydrogen Peroxide Production. *Faraday Discuss.* **152** (2011) 63–86. doi:10.1039/c1fd00020a.

[10] J.L. Elechiguerra, J. Reyes-Gasga, M. José-Yacamán, The Role of Twinning in Shape Evolution of Anisotropic Noble Metal Nanostructures. *J. Mater. Chem.* **16** (2006) 3906–3919. doi:10.1039/b607128g.

[11] K.M. Bratlie, H. Lee, K. Komvopoulos, P. Yang, G.A. Somorjai, Platinum nanoparticle shape effects on benzene hydrogenation selectivity. *Nano Lett.* **7** (2007) 3097–101. doi:10.1021/nl0716000.

[12] W. Zhou, I.E. Wachs, C.J. Kiely, Nanostructural and Chemical Characterization of Supported Metal Oxide Catalysts by Aberration Corrected Analytical Electron Microscopy. *Curr. Opin. Solid State Mater. Sci.* **16** (2012) 10–22. doi:10.1016/j.cossms.2011.06.001.

[13] S.E. Skrabalak, Y. Xia, Pushing Nanocrystal Synthesis Toward Nanomanufacturing. *ACS Nano*. **3** (2009) 10–15. doi:10.1021/nn800875p.

[14] L.C. Gontard, L.-Y. Chang, C.J.D. Hetherington, A.I. Kirkland, D. Ozkaya, R.E. Dunin-Borkowski, Aberration-Corrected Imaging of Active Sites on Industrial Catalyst Nanoparticles. *Angew. Chem. Int. Ed. Engl.* **46** (2007) 3683–3685. doi:10.1002/anie.200604811.

[15] Platinum Group Metals. *Platin. Gr. Met. Ltd*. (2009). http://www.platinumgroupmetals.net/about_platinum/.

[16] M. Frenkel, Deodorisation of the Exhaust Gases in Motor Vehicles. *J. Soc. Chem. Ind., London*. **28** (1910) 692–693.

[17] P. Millington, A. York, Opportunities for Platinum Group Metals in Future Emissions Control Technology. *Platin. Met. Rev.* (2012) 58–60.

[18] A.J. Appleby, From Sir William Grove to today: fuel cells and the future. *J. Power Sources*. **29** (1990) 3–11. doi:10.1016/0378-7753(90)80002-U.

[19] T. Ralph, M. Hogarth, Catalysis for Low Temperature Fuel Cells. *Platin. Met. Rev.* (2002) 117–135.

[20] J. Rosenthal, D.G. Nocera, Role of Proton-Coupled Electron Transfer in O-O Bond Activation. *Acc. Chem. Res.* **40** (2007) 543–553. doi:10.1021/ar7000638.

[21] Fuel Cell Technologies Program. *U.S. Dep. Energy*. (2011). http://www1.eere.energy.gov/hydrogenandfuelcells/fc_animation_components.html.

[22] P.L. Gai, E.D. Boyes, Advances in Atomic Resolution In Situ Environmental Transmission Electron Microscopy and 1Å Aberration Corrected In Situ Electron Microscopy. *Microsc. Res. Tech.* **72** (2009) 153–164. doi:10.1002/jemt.20668.

[23] J.T. Yates Jr., Surface Chemistry at Metallic Step Defect Sites. *J. Vac. Sci. Technol. A Vacuum, Surfaces, Film.* **13** (1995) 1359–1367. doi:10.1116/1.579564.

[24] M. José-Yacamán, J.A. Ascencio, H.B. Liu, J. Gardea-Torresdey, Structure shape and stability of nanometric sized particles. *J. Vac. Sci. Technol. B Microelectron. Nanom. Struct.* **19** (2001) 1091. doi:10.1116/1.1387089.

[25] J.K. Nørskov, T. Bligaard, A. Logadottir, S. Bahn, L.B. Hansen, M. Bollinger, et al., Universality in Heterogeneous Catalysis. *J. Catal.* **209** (2002) 275–278. doi:10.1006/jcat.2002.3615.

[26] B. Lang, R.W. Joyner, G.A. Somorjai, Low Energy Electron Diffraction Studies of High Index Crystal Surfaces of Platinum. *Surf. Sci.* **30** (1972) 440–453.

[27] P. Gambardella, Ž. Šljivančanin, B. Hammer, M. Blanc, K. Kuhnke, K. Kern, Oxygen Dissociation at Pt Steps. *Phys. Rev. Lett.* **87** (2001) 1–4. doi:10.1103/PhysRevLett.87.056103.

[28] P.J. Feibelman, B. Hammer, J.K. Nørskov, F.T. Wagner, M. Scheffler, R. Stumpf, et al., The CO/Pt(111) Puzzle. *J. Phys. Chem. B*. **105** (2001) 4018–4025. doi:10.1021/jp002302t.

[29] Z.-P. Liu, S.J. Jenkins, D.A. King, Step-Enhanced Selectivity of NO Reduction on Platinum-Group Metals. *J. Am. Chem. Soc.* **125** (2003) 14660–1. doi:10.1021/ja0372208.

[30] A. Amali, P. Rez, Theory of Lattice Resolution in High-angle Annular Dark-Field Images. *Microsc. Microanal.* **3** (1997) 28–46.

[31] E.M. Crabb, R. Marshall, D. Thompsett, Carbon Monoxide Electro-Oxidation Properties of Carbon-Supported PtSn Catalysts Prepared Using Surface Organometallic Chemistry. *J. Electrochem. Soc.* **147** (2000) 4440–44447. doi:10.1149/1.1394083.

[32] P. Liu, A. Logadottir, J.K. Nørskov, Modeling the electro-oxidation of CO and H2/CO on Pt, Ru, PtRu and Pt3Sn. *Electrochim. Acta*. **48** (2003) 3731–3742. doi:10.1016/S0013-4686(03)00538-3.

[33] C.E. Lyman, H.G. Stenger Jr., Analytical Electron Microscopy of a Sulfur-Poisoned Palladium Catalyst with a Dedicated STEM. *Ultramicroscopy*. **22** (1987) 129–133.

[34] J.A. Lopez-Sanchez, N. Dimitratos, C. Hammond, G.L. Brett, L. Kesavan, S. White, et al., Facile Removal of Stabilizer-Ligands From

Supported Gold Nanoparticles. *Nat. Chem.* **3** (2011) 551–556. doi:10.1038/nchem.1066.

[35] C. Solliard, M. Flueli, Surface Stress and Size Effect on the Lattice Parameter in Small Particles of Gold and Platinum. *Surf. Sci.* **156** (1985) 487–494.

[36] J.A. Ascencio, M. Peréz, M. José-Yacamán, A Truncated Icosahedral Structure Observed in Gold Nanoparticles. *Surf. Sci.* **447** (2000) 73–80. doi:10.1016/S0039-6028(99)01112-7.

[37] K.E. MacArthur, N.P. Young, J.W. Critchell, A.I. Kirkland, “Ex-Situ” Annealing and Structural Transformations in Gold Nanoparticles. *J. Phys. Conf. Ser.* **371** (2012) 12068–12072.

[38] H. Shi, C. Stampfl, Shape and surface structure of gold nanoparticles under oxidizing conditions. *Phys. Rev. B*. **77** (2008) 094127. doi:10.1103/PhysRevB.77.094127.

[39] H. Skriver, N. Rosengaard, Surface Energy and Work Function of Elemental Metals. *Phys. Rev. B. Condens. Matter*. **46** (1992) 7157–7168. http://www.ncbi.nlm.nih.gov/pubmed/10002423.

[40] P. Buffat, J.-P. Borel, Size Effect on the Melting Temperature of Gold Particles. *Phys. Rev. A*. **13** (1976) 2287–2298.

[41] L.D. Marks, D.J. Smith, Direct Atomic Imaging of Solid Surfaces II. Gold (111) Surfaces During and After in Situ Carbon Etching. *Surf. Sci. Lett.* **143** (1984) 495–508. doi:10.1016/0167-2584(84)90649-2.

[42] L.R. Wallenberg, J.-O. Bovin, A.K. Petford-Long, D.J. Smith, Atomic-Resolution Study of Structural Rearrangements in Small Platinum Crystals. *Ultramicroscopy*. **20** (1986) 71–76.

[43] N.J. Long, R.F. Marzke, M. Mckelvy, W.S. Glaunsinger, Characterization of Pt Microcrystals Using High Resolution Electron Microscopy. *Ultramicroscopy*. **20** (1986) 15–20.

[44] R. Narayanan, M.A. El-Sayed, Shape-Dependent Catalytic Activity of Platinum Nanoparticles in Colloidal Solution. *Nano Lett.* **4** (2004) 1343–1348. doi:10.1021/nl0495256.

[45] C.J. Zhong, M.M. Maye, Core-Shell Assembled Nanoparticles as Catalysts. *Adv. Mater.* **13** (2001) 1507–1511. doi:10.1002/1521-4095(200110)13:19<1507::AID-ADMA1507>3.0.CO;2-#.

[46] J.M. Thomas, O. Terasaki, P.L. Gai, W. Zhou, Structural Elucidation of Microporous and Mesoporous Catalysts and Molecular Sieves by High-Resolution Electron Microscopy. *Acc. Chem. Res.* **34** (2001) 583–594.

[47] S. Alayoglu, A.U. Nilekar, M. Mavrikakis, B. Eichhorn, Ru-Pt Core-Shell Nanoparticles for Preferential Oxidation of Carbon Monoxide in Hydrogen. *Nat. Mater.* **7** (2008) 333–338. doi:10.1038/nmat2156.

[48] J. Zhang, M.B. Vukmirovic, K. Sasaki, A.U. Nilekar, M. Mavrikakis, R.R. Adzic, Mixed-Metal Pt Monolayer Electrocatalysts for Enhanced Oxygen Reduction Kinetics. *J. Am. Chem. Soc.* **127** (2005) 12480–12481. doi:10.1021/ja053695i.

[49] J. Zhang, Y. Mo, M.B. Vukmirovic, R.F. Klie, K. Sasaki, R.R. Adzic, Platinum Monolayer Electrocatalysts for O2 Reduction: Pt Monolayer on Pd(111) and on Carbon-Supported Pd Nanoparticles. *J. Phys. Chem. B*. **108** (2004) 10955–10964. doi:10.1021/jp0379953.

[50] N. Shibata, A. Goto, S.-Y. Choi, T. Mizoguchi, S.D. Findlay, T. Yamamoto, et al., Direct imaging of reconstructed atoms on TiO2 (110) surfaces. *Science.* **322** (2008) 570–3. doi:10.1126/science.1165044.

[51] T. Shibata, B.A. Bunker, Z. Zhang, D. Meisel, C.F. Vardeman, J.D. Gezelter, Size-Dependent Spontaneous Alloying of Au−Ag Nanoparticles. *J. Am. Chem. Soc.* **124** (2002) 11989–11996. doi:10.1021/ja026764r.

[52] V. Jalan, E.J. Taylor, Importance of interatomic spacing in catalytic reduction of oxygen in phosphoric acid. *J. Electrochem. Soc.* **12** (1983) 2299–2302. doi:10.1149/1.2119574.

[53] H.A. Gasteiger, S.S. Kocha, B. Sompalli, F.T. Wagner, Activity Benchmarks and Requirements for Pt, Pt-Alloy, and Non-Pt Oxygen Reduction Catalysts for PEMFCs. *Appl. Catal. B Environ.* **56** (2005) 9–35. doi:10.1016/j.apcatb.2004.06.021.

[54] P. Strasser, S. Koh, T. Anniyev, J. Greeley, K. More, C. Yu, et al., Lattice-strain control of the activity in dealloyed core-shell fuel cell catalysts. *Nat. Chem.* **2** (2010) 454–60. doi:10.1038/nchem.623.

[55] L. Gan, R. Yu, J. Luo, Z. Cheng, J. Zhu, Lattice Strain Distributions in Individual Dealloyed Pt–Fe Catalyst Nanoparticles. *J. Phys. Chem. Lett.* **3** (2012) 934–938. doi:10.1021/jz300192b.

[56] L. Gan, M. Heggen, S. Rudi, P. Strasser, Core − Shell Compositional Fine Structures of Dealloyed Pt. *Nanoletters*. **12** (2012) 5423–5430.

[57] J. Greeley, M. Mavrikakis, Alloy catalysts designed from first principles. *Nat. Mater.* **3** (2004) 810–5. doi:10.1038/nmat1223.

[58] D. Wang, H.L. Xin, R. Hovden, H. Wang, Y. Yu, D.A. Muller, et al., Structurally ordered intermetallic platinum-cobalt core-shell nanoparticles with enhanced activity and stability as oxygen reduction electrocatalysts. *Nat. Mater.* **12** (2012) 81–87. doi:10.1038/nmat3458.

[59] S. Prabhudev, M. Bugnet, C. Bock, G.A. Botton, Strained Lattice with Persistent Atomic Order in Pt 3 Fe 2 Intermetallic. *ACS Nano*. **7** (2013) 6103–6110.

[60] S. Koh, P. Strasser, Electrocatalysis on bimetallic surfaces: modifying catalytic reactivity for oxygen reduction by voltammetric surface dealloying. *J. Am. Chem. Soc.* **129** (2007) 12624–5. doi:10.1021/ja0742784.

[61] L. Gan, C. Cui, S. Rudi, P. Strasser, Core–Shell and Nanoporous Particle Architectures and Their Effect on the Activity and Stability of Pt ORR Electrocatalysts. *Top. Catal.* **57** (2013) 236–244. doi:10.1007/s11244-013-0178-z.

[62] A.S.A. Khan, R. Ahmed, M.L. Mirza, Evaluation of Catalytic Activity of Pt and Pt-Ru Catalysts for Electro-oxidation of Methanol in Acid Medium by Cyclic Voltammetry. *Port. Electrochim. Acta*. **27** (2009) 429–442. doi:10.4152/pea.200904429.

[63] F. Krumeich, S. Marx, A. Baiker, R. Nesper, Characterization of AuPd Nanoparticles by Probe-Corrected Scanning Transmission Electron Microscopy and X-ray Absorption Spectroscopy. *Zeitschrift Für Anorg. Und Allg. Chemie*. **637** (2011) 875–881. doi:10.1002/zaac.201100038.

[64] R.F. Egerton, Electron Energy-Loss Spectroscopy in the TEM. *Reports Prog. Phys.* **72** (2009) 1–25. doi:10.1088/0034-4885/72/1/016502.

[65] J. Liu, High-Resolution and Low-Voltage FE-SEM Imaging and Microanalysis in Materials Characterization. *Mater. Charact.* **44** (2000) 353–363. doi:10.1016/S1044-5803(99)00076-5.

[66] J. Liu, J.M. Cowley, High-Angle ADF and High-Resolution SE Imaging of Supported Catalyst Clusters. *Ultramicroscopy*. **34** (1990) 119–128. doi:10.1016/0304-3991(90)90066-U.

[67] A.K. Datye, Electron Microscopy of Catalysts: Recent Achievements and Future Prospects. *J. Catal.* **216** (2003) 144–154.

[68] F. Haguenau, P.W. Hawkes, J.L. Hutchison, B. Satiat-Jeunemaître, G.T. Simon, D.B. Williams, Key Events in the History of Electron

Microscopy. *Microsc. Microanal.* **9** (2003) 96–138. doi:10.1017/S1431927603030113.

[69] N.R. Avery, J. V Sanders, The structure of metallic particles in dispersed catalysts. *J. Catal.* **18** (1970) 129–132.

[70] M. José-Yacamán, J. Manuel Dominguez, Characterization of Small Platinum Particles Supported on Graphite by Electron Microscopy. *J. Catal.* **64** (1980) 213–222.

[71] M. José-Yacamán, T. Ocaña Z., High-Resolution Topographical Images of Small Metal Particles. *Appl. Phys. Lett.* **30** (1977) 359–360. doi:10.1063/1.89400.

[72] L.C. Gontard, R.E. Dunin-Borkowski, M.J. Hÿtch, D. Ozkaya, Delocalisation in Images of Pt Nanoparticles. *J. Phys. Conf. Ser.* **26** (2006) 292–295. doi:10.1088/1742-6596/26/1/070.

[73] K. Ishizuka, N. Uyeda, A New Theoretical and Practical Approach to the Multislice Method. *Acta Crystallogr. Sect. A*. **33** (1977) 740–749. doi:10.1107/S0567739477001879.

[74] A.K. Datye, A. Logan, K. Blankenburg, D.J. Smith, Characterization of Surface Structure in Heterogeneous Catalysts by High-Resolution Transmission Electron Microscopy. *Ultramicroscopy*. **34** (1990) 47–53. doi:10.1016/0304-3991(90)90056-R.

[75] L.D. Marks, Experimental Studies of Small Particle Structures. *Reports Prog. Phys.* **57** (1994) 603–649.

[76] B.R. Cuenya, Synthesis and catalytic properties of metal nanoparticles: Size, shape, support, composition, and oxidation state effects. *Thin Solid Films*. **518** (2010) 3127–3150. doi:10.1016/j.tsf.2010.01.018.

[77] L.C. Gontard, L.-Y. Chang, R.E. Dunin-Borkowski, A.I. Kirkland, C.J.D. Hetherington, D. Ozkaya, The Application of Spherical Aberration Correction and Focal Series Restoration to High-Resolution Images of Platinum Nanocatalyst Particles. *J. Phys. Conf. Ser.* **26** (2006) 25–28. doi:10.1088/1742-6596/26/1/006.

[78] L.C. Gontard, R.E. Dunin-Borkowski, D. Ozkaya, Three-Dimensional Shapes and Spatial Distributions of Pt and PtCr Catalyst Nanoparticles on Carbon Black. *J. Microsc.* **232** (2008) 248–259. doi:10.1111/j.1365-2818.2008.02096.x.

[79] R.R. Meyer, J. Sloan, R.E. Dunin-Borkowski, A.I. Kirkland, M.C. Novotny, S.R. Bailey, et al., Discrete Atom Imaging of One-

Dimensional Crystals Formed Within Single-Walled Carbon Nanotubes. *Science.* **289** (2000) 1324–1326. doi:10.1126/science.289.5483.1324.

[80] A.T. DeLaRiva, T.W. Hansen, S.R. Challa, A.K. Datye, In situ Transmission Electron Microscopy of catalyst sintering. *J. Catal.* **308** (2013) 291–305. doi:10.1016/j.jcat.2013.08.018.

[81] A.A. V Crewe, J. Wall, J.P. Langmore, Visibility of Single Atoms. *Am. Assoc. Adv. Sci.* **168** (1970) 1338–1340. http://www.jstor.org/stable/1730030.

[82] P.D. Nellist, S.J. Pennycook, Direct Imaging of the Atomic Configuration of Ultradispersed Catalysts. *Science.* **274** (1996) 413–415. doi:10.1126/science.274.5286.413.

[83] S.J. Pennycook, D.E. Jesson, High-Resolution Incoherent Imaging of Crystals. *Phys. Rev. Lett.* **64** (1990) 938–942.

[84] D.O. Klenov, S. Stemmer, Contributions to the Contrast in Experimental High-Angle Annular Dark-Field Images. *Ultramicroscopy*. **106** (2006) 889–901. doi:10.1016/j.ultramic.2006.03.007.

[85] P.D. Nellist, J.M. Rodenburg, Beyond the Conventional Information Limit : The Relevant Coherence Function. *Ultramicroscopy*. **54** (1994) 61–74.

[86] D.B. Williams, B. Carter, Transmission Electron Microscopy, Second Edi, *Springer, New York*, 2009.

[87] S. Lee, Y. Oshima, H. Sawada, F. Hosokawa, E. Okunishi, T. Kaneyama, et al., Counting lithium ions in the diffusion channel of an LiV2O4 crystal. *J. Appl. Phys.* **109** (2011) 113530. doi:10.1063/1.3592239.

[88] S.D. Findlay, S. Azuma, N. Shibata, E. Okunishi, Y. Ikuhara, Direct oxygen imaging within a ceramic interface, with some observations upon the dark contrast at the grain boundary. *Ultramicroscopy*. **111** (2011) 285–289. doi:10.1016/j.ultramic.2010.12.022.

[89] E. Okunishi, H. Sawada, Y. Kondo, Experimental study of annular bright field (ABF) imaging using aberration-corrected scanning transmission electron microscopy (STEM). *Micron*. **43** (2012) 538–544. doi:10.1016/j.micron.2011.10.007.

[90] A. Howie, Image-Contrast and Localized Signal Selection Techniques. *J. Microsc. Oxford*. **117** (1979) 11–23.

[91] D.E. Jesson, S.J. Pennycook, Incoherent Imaging of Crystals Using Thermally Scattered Electrons. *Proceeding R. Soc. London*. **449** (1995) 273–293.

[92] Z.W. Wang, Z.Y. Li, S.J. Park, a. Abdela, D. Tang, R. Palmer, Quantitative Z-contrast imaging in the scanning transmission electron microscope with size-selected clusters. *Phys. Rev. B*. **84** (2011) 073408. doi:10.1103/PhysRevB.84.073408.

[93] K. Nanda, A. Maisels, F. Kruis, H. Fissan, S. Stappert, Higher Surface Energy of Free Nanoparticles. *Phys. Rev. Lett.* **91** (2003) 1–4. doi:10.1103/PhysRevLett.91.106102.

[94] F. Baletto, R. Ferrando, Structural Properties of Nanoclusters: Energetic, Thermodynamic, and Kinetic Effects. *Rev. Mod. Phys.* **77** (2005) 371–423.

[95] R.F. Egerton, Choice of operating voltage for a transmission electron microscope. *Ultramicroscopy*. **145** (2014) 85–93. doi:10.1016/j.ultramic.2013.10.019.

[96] C.M. McGilvery, A.E. Goode, M.S.P. Shaffer, D.W. McComb, Contamination of holey/lacey carbon films in STEM. *Micron*. **43** (2012) 450–5. doi:10.1016/j.micron.2011.10.026.

[97] T.F. Budinger, R.M. Glaeser, Measurement of Focus and Spherical Abberation of an Electron Microscope Objective Lens. *Ultramicroscopy*. **2** (1976) 31–41.

[98] O. Scherzer, Über einige Fehler von Elektronenlinsen. *Zeitschrift Für Phys.* **101** (1936) 593–603.

[99] P. Xu, E.J. Kirkland, J. Silcox, R. Keyse, High Resolution Imaging of Silicon (111) Using a 100keV STEM. *Ultramicroscopy*. **32** (1990) 93–102.

[100] M. Watanabe, D.W. Ackland, C.J. Kiely, D.B. Williams, M. Kanno, R. Hynes, et al., The Aberration Corrected JEOL JEM-2200FS FEG-STEM/TEM Fitted with an Ω Electron Energy-Filter: Performance Characterization and Selected Applications. *JEOL News*. **41** (2006) 2–7.

[101] O.L. Krivanek, N. Dellby, A.J. Spence, R.A. Camps, L.M. Brown, Aberration Correction in the STEM. *Electron Microsc. Anal.* (1997) 35–40.

[102] P.D. Nellist, M.F. Chisholm, N. Dellby, O.L. Krivanek, M.F. Murfitt, Z.S. Szilagyi, et al., Direct Sub-Angstrom Imaging of a Crystal Lattice. *Science.* **305** (2004) 1741. doi:10.1126/science.1100965.

[103] H. Müller, S. Uhlemann, P. Hartel, M. Haider, Advancing the Hexapole Cs-Corrector for the Scanning Transmission Electron Microscope. *Microsc. Microanal.* **12** (2006) 442–455. doi:10.1017/S1431927606060600.

[104] P.E. Batson, N. Dellby, O.L. Krivanek, Sub-Ångstrom Resolution Using Aberration Corrected Electron Optics. *Nature*. **418** (2002) 617–20. doi:10.1038/nature00972.

[105] D.J. DeRosier, A. Klug, Reconstruction of Three Dimensional Structures from Electron Micrographs. *Nature*. **217** (1968) 130–134.

[106] B.P. Flannery, H.W. Deckman, W.G. Roberge, K.L.D. Amico, Three-Dimensional X-ray Microtomography. *Adv. Sci.* **237** (1987) 1439–1444.

[107] M. Weyland, P.A. Midgley, J.M. Thomas, Electron Tomography of Nanoparticle Catalysts on Porous Supports: A New Technique Based on Rutherford Scattering. *J. Phys. Chem. B*. **105** (2001) 7882–7886. doi:10.1021/jp011566s.

[108] M. Weyland, Electron Tomography of Catalysts. *Top. Catal.* **21** (2002) 175–183.

[109] R.A. Crowther, D.J. DeRosier, A. Klug, The Reconstruction of a Three-Dimensional Structure from Projections and its Application to Electron Microscopy. *Proc. R. Soc. A Math. Phys. Eng. Sci.* **317** (1970) 319–340.

[110] A.J. Koster, U. Ziese, A.J. Verkleij, A.H. Janssen, K.P. De Jong, Three-Dimensional Transmission Electron Microscopy : A Novel Imaging and Characterization Technique with Nanometer Scale Resolution for Materials Science. *J. Phys. Chem. B*. **104** (2000) 9368–9370.

[111] J.R. Jinschek, K.J. Batenburg, H.A. Calderon, R. Kilaas, V. Radmilovic, C. Kisielowski, 3D Reconstruction of the Atomic Positions in a Simulated Gold Nanocrystal Based on Discrete Tomography: Prospects of Atomic Resolution Electron Tomography. *Ultramicroscopy*. **108** (2008) 589–604.

[112] L.C. Gontard, R.E. Dunin-Borkowski, R.K.K. Chong, D. Ozkaya, P.A. Midgley, Electron Tomography of Pt Nanocatalyst Particles and Their Carbon Support. *J. Phys. Conf. Ser.* **26** (2006) 203–206. doi:10.1088/1742-6596/26/1/048.

[113] G. Möbus, B.J. Inkson, Three-Dimensional Reconstruction of Buried Nanoparticles by Element-Sensitive Tomography Based on Inelastically Scattered Electrons. *Appl. Phys. Lett.* **79** (2001) 1369. doi:10.1063/1.1400080.

[114] R. Grothausmann, S. Fiechter, R. Beare, G. Lehmann, H. Kropf, G.S. Vinod Kumar, et al., Automated quantitative 3D analysis of faceting of particles in tomographic datasets. *Ultramicroscopy*. **122** (2012) 65–75. doi:10.1016/j.ultramic.2012.07.024.

[115] H. Friedrich, S. Guo, P.E. de Jongh, X. Pan, X. Bao, K.P. de Jong, A Quantitative Electron Tomography Study of Ruthenium Particles on the Interior and Exterior Surfaces of Carbon Nanotubes. *ChemSusChem*. **4** (2011) 957–963. doi:10.1002/cssc.201000325.

[116] S. Sueda, K. Yoshida, N. Tanaka, Quantification of Metallic Nanoparticle Morphology on TiO2 Using HAADF-STEM Tomography. *Ultramicroscopy*. **110** (2010) 1120–1127. doi:10.1016/j.ultramic.2010.04.003.

[117] J.J. Fernández, J.I. Agulleiro, A. Martínez, I. García, F.J. Chichón, Image processing in electron tomography. *Microsc. Sci. Technol. Appl. Educ.* (2010) 19–28.

[118] Z. Saghi, D.J. Holland, R. Leary, A. Falqui, G. Bertoni, A.J. Sederman, et al., Three-Dimensional Morphology of Iron Oxide Nanoparticles with Reactive Concave Surfaces. A Compressed Sensing-Electron Tomography (CS-ET) Approach. *Nano Lett.* **11** (2011) 4666–4673. doi:10.1021/nl202253a.

[119] K.J. Batenburg, J. Sijbers, DART: A Practical Reconstruction Algorithm for Discrete Tomography. *IEEE Trans. Image Process.* **20** (2011) 2542–2553. doi:10.1109/TIP.2011.2131661.

[120] K.J. Batenburg, S. Bals, J. Sijbers, C. Kübel, P.A. Midgley, J.C. Hernandez, et al., 3D Imaging of Nanomaterials by Discrete Tomography. *Ultramicroscopy*. **109** (2009) 730–740. doi:10.1016/j.ultramic.2009.01.009.

[121] S. Van Aert, K.J. Batenburg, M.D. Rossell, R. Erni, G. Van Tendeloo, Three-Dimensional Atomic Imaging of Crystalline Nanoparticles. *Nature*. **470** (2011) 374–377. doi:10.1038/nature09741.

[122] S. Bals, M. Casavola, M.A. van Huis, S. Van Aert, K.J. Batenburg, G. Van Tendeloo, et al., Three-Dimensional Atomic Imaging of Colloidal Core-Shell Nanocrystals. *Nano Lett.* **11** (2011) 3420–3424. doi:10.1021/nl201826e.

[123] S. Van Aert, J. Verbeeck, R. Erni, S. Bals, M. Luysberg, D. Van Dyck, et al., Quantitative atomic resolution mapping using high-angle annular dark field scanning transmission electron microscopy. *Ultramicroscopy*. **109** (2009) 1236–44. doi:10.1016/j.ultramic.2009.05.010.

[124] M.C. Scott, C. Chen, M. Mecklenburg, C. Zhu, R. Xu, P. Ercius, et al., Electron tomography at 2.4-ångström resolution. *Nature*. **483** (2012) 444–447. doi:10.1038/nature10934.

[125] C.E. Lyman, Microanalysis of Catalysts by Analytical Electron Microscopy. *J. Mol. Catal.* **20** (1983) 357 – 368.

[126] J.J. Friel, C.E. Lyman, X-ray Mapping in Electron-Beam Instruments. *Microsc. Microanal.* **12** (2006) 2–25. doi:10.1017/S1431927606060211.

[127] H. Meltzman, Y. Kauffmann, P. Thangadurai, M. Drozdov, M. Baram, D. Brandon, et al., An experimental method for calibration of the plasmon mean free path. *J. Microsc.* **236** (2009) 165–173. doi:10.1111/j.1365-2818.2009.03214.x.

[128] J. Park, S. Heo, J.G. Chung, H. Kim, H. Lee, K. Kim, et al., Bandgap measurement of thin dielectric films using monochromated STEM-EELS. *Ultramicroscopy*. **109** (2009) 1183–1188. doi:10.1016/j.ultramic.2009.04.005.

[129] R.J. Nicholls, A.T. Murdock, J. Tsang, J. Britton, T.J. Pennycook, A. Koós, et al., Probing the bonding in nitrogen-doped graphene using electron energy loss spectroscopy. *ACS Nano*. **7** (2013) 7145–50. doi:10.1021/nn402489v.

[130] N.D. Browning, M.F. Chisholm, S.J. Pennycook, Atomic-Resolution Chemical Analysis at 100kV in the Scanning Transmission Electron Microscope. *Mater. Res.* **332** (1994) 297–302.

[131] E.C. Cosgriff, M.P. Oxley, L.J. Allen, S.J. Pennycook, The spatial resolution of imaging using core-loss spectroscopy in the scanning transmission electron microscope. *Ultramicroscopy*. **102** (2005) 317–326. doi:10.1016/j.ultramic.2004.11.001.

[132] F.L. Deepak, G. Casillas-Garcia, R. Esparza, H. Barron, M. José-Yacamán, New Insights into the Structure of Pd-Au Nanoparticles as Revealed by Aberration-Corrected STEM. *J. Cryst. Growth*. **325** (2011) 60–67. doi:10.1016/j.jcrysgro.2011.04.026.

[133] R. Darji, A. Howie, Scattering Corrections in Small Particle Imaging. *Micron*. **28** (1997) 95–100. doi:10.1016/S0968-4328(96)00053-4.

[134] R. Prestvik, B. Tøtdal, C.E. Lyman, A. Holmen, Bimetallic Particle Formation in Pt–Re/Al2O3 Reforming Catalysts Revealed by Energy-Dispersive X-Ray Spectrometry in the Analytical Electron Microscope. *J. Catal.* **176** (1998) 246–252. doi:10.1006/jcat.1998.2025.

[135] J. Titchmarsh, EDX Spectrum Modelling and Multivariate Analysis of Sub-Nanometer Segregation. *Micron*. **30** (1999) 159–171. doi:10.1016/S0968-4328(99)00020-7.

[136] L.J. Allen, A.J. D'Alfonso, B. Freitag, D.O. Klenov, Chemical Mapping at Atomic Resolution Using Energy-Dispersive X-Ray Spectroscopy. *MRS Bull.* **37** (2012) 47–52. doi:10.1557/mrs.2011.331.

[137] D.T. Tran, I.P. Jones, J.A. Preece, R.L. Johnston, C.R. Brom, C.R. van den Brom, TEM Characterization of Chemically Synthesized Copper–Gold Nanoparticles. *J. Nanoparticle Res.* **13** (2011) 4229–4237. doi:10.1007/s11051-011-0367-2.

[138] M. Retsky, Observed single atom elastic cross sections in a scanning electron microscope. *Optik.* **41** (1974) 127–142.

[139] M.S. Isaacson, D. Kopf, M. Ohtsuki, M. Utlaut, Atomic Imaging Using the Dark-Field Annular Detector in the STEM. *Ultramicroscopy*. **4** (1979) 101–104. doi:10.1016/0304-3991(79)90013-5.

[140] N.P. Young, Z.Y. Li, Y. Chen, S. Palomba, M. Di Vece, R. Palmer, Weighing Supported Nanoparticles: Size-Selected Clusters as Mass Standards in Nanometrology. *Phys. Rev. Lett.* **101** (2008) 246103. doi:10.1103/PhysRevLett.101.246103.

[141] A. Singhal, J.C. Yang, J.M. Gibson, STEM-based mass spectroscopy of supported Re clusters. *Ultramicroscopy*. **67** (1997) 191–206. doi:10.1016/S0304-3991(96)00094-0.

[142] S.C. Anderson, C.R. Birkeland, G.R. Anstis, D.J.H. Cockayne, An Approach to Quantitative Compositional Profiling at Near-Atomic Resolution Using High-Angle Annular Dark Field Imaging. *Ultramicroscopy*. **69** (1997) 83–103. doi:10.1016/S0304-3991(97)00041-7.

[143] V. Ortalan, A. Uzun, B.C. Gates, N.D. Browning, Towards Full-Structure Determination of Bimetallic Nanoparticles With an Aberration-Corrected Electron Microscope. *Nat. Nanotechnol.* **5** (2010) 843–7. doi:10.1038/nnano.2010.234.

[144] J.M. LeBeau, S. Stemmer, Experimental Quantification of Annular Dark-Field Images in Scanning Transmission Electron Microscopy.

Ultramicroscopy. **108** (2008) 1653–1658. doi:10.1016/j.ultramic.2008.07.001.

[145] J.M. LeBeau, S.D. Findlay, X. Wang, A. Jacobson, L.J. Allen, S. Stemmer, High-Angle Scattering of Fast Electrons From Crystals Containing Heavy Elements: Simulation and Experiment. *Phys. Rev. B*. **79** (2009) 214110. doi:10.1103/PhysRevB.79.214110.

[146] J.M. LeBeau, S.D. Findlay, L.J. Allen, S. Stemmer, Standardless atom counting in scanning transmission electron microscopy. *Nano Lett.* **10** (2010) 4405–8. doi:10.1021/nl102025s.

[147] A.J. den Dekker, S. Van Aert, A. van den Bos, D. Van Dyck, Maximum likelihood estimation of structure parameters from high resolution electron microscopy images. Part I: a theoretical framework. *Ultramicroscopy*. **104** (2005) 83–106. doi:10.1016/j.ultramic.2005.03.001.

[148] B. Goris, A. De Backer, S. Van Aert, S. Gómez-Graña, L.M. Liz-Marzán, G. Van Tendeloo, et al., Three-dimensional elemental mapping at the atomic scale in bimetallic nanocrystals. *Nano Lett.* **13** (2013) 4236–41. doi:10.1021/nl401945b.

[149] S. Van Aert, A. De Backer, G.T. Martinez, B. Goris, S. Bals, G. Van Tendeloo, et al., Procedure to count atoms with trustworthy single-atom sensitivity. *Phys. Rev. B*. **87** (2013) 064107. doi:10.1103/PhysRevB.87.064107.

[150] A. De Backer, G.T. Martinez, A. Rosenauer, S. Van Aert, Atom counting in HAADF STEM using a statistical model-based approach: methodology, possibilities, and inherent limitations. *Ultramicroscopy*. **134** (2013) 23–33. doi:10.1016/j.ultramic.2013.05.003.

[151] A. De Backer, G.T. Martinez, K.E. MacArthur, L. Jones, A. Béché, P.D. Nellist, et al., Dose limited reliability of quantitative annular dark field scanning transmission electron microscopy for nano-particle atom-counting. *Ultramicroscopy*. **151** (2015) 56–61. doi:10.1016/j.ultramic.2014.11.028.

[152] H. Katz-Boon, C.J. Rossouw, C. Dwyer, J. Etheridge, Rapid measurement of nanoparticle thickness profiles. *Ultramicroscopy*. **124** (2013) 61–70. doi:10.1016/j.ultramic.2012.08.009.

[153] D. Hernández-Maldonado, M. Herrera, P. Alonso-González, Y. González, L. González, J. Gazquez, et al., Compositional Analysis With Atomic Column Spatial Resolution by 5th-Order Aberration-Corrected Scanning Transmission Electron Microscopy. *Microsc. Microanal.* **17** (2011) 578–581. doi:10.1017/S1431927611000213.

[154] A. Rosenauer, K. Gries, K. Müller, M. Schowalter, A. Pretorius, A. Avramescu, et al., Measurement of composition profiles in III-nitrides by quantitative scanning transmission electron microscopy. *J. Phys. Conf. Ser.* **209** (2010) 012009. doi:10.1088/1742-6596/209/1/012009.

[155] A. Rosenauer, T. Mehrtens, K. Müller, K. Gries, M. Schowalter, P.V. Satyam, et al., Composition mapping in InGaN by scanning transmission electron microscopy. *Ultramicroscopy*. **111** (2011) 1316–27. doi:10.1016/j.ultramic.2011.04.009.

[156] A. Rosenauer, K. Gries, K. Müller, A. Pretorius, M. Schowalter, A. Avramescu, et al., Measurement of specimen thickness and composition in Al(x)Ga(1-x)N/GaN using high-angle annular dark field images. *Ultramicroscopy*. **109** (2009) 1171–82. doi:10.1016/j.ultramic.2009.05.003.

[157] H. E, Quantitative Analysis of Core-Shell Nanoparticle Catalysts by Scanning Transmission Electron Microscopy. *D.Phil Thesis* (2013).University of Oxford

[158] S.D. Findlay, J.M. LeBeau, Detector Non-Uniformity in Scanning Transmission Electron Microscopy. *Ultramicroscopy*. **124** (2013) 52–60. doi:10.1016/j.ultramic.2012.09.001.

[159] K.E. MacArthur, L. Jones, P.D. Nellist, How flat is your detector? Non-uniform annular detector sensitivity in STEM quantification. *J. Phys. Conf. Ser.* **522** (2014) 012018. doi:10.1088/1742-6596/522/1/012018.

[160] G.T. Martinez, L. Jones, A. De Backer, Quantitative STEM normalisation : the importance of the electron flux. *Ultramicroscopy*. Submitted.

[161] J.M. LeBeau, S.D. Findlay, L.J. Allen, S. Stemmer, Position averaged convergent beam electron diffraction: Theory and applications. *Ultramicroscopy*. **110** (2010) 118–125. doi:10.1016/j.ultramic.2009.10.001.

[162] J. Hwang, J.Y. Zhang, A.J. D'Alfonso, L.J. Allen, S. Stemmer, Three-Dimensional Imaging of Individual Dopant Atoms in SrTiO3. *Phys. Rev. Lett.* **111** (2013) 266101. doi:10.1103/PhysRevLett.111.266101.

[163] S. Maccagnano-Zacher, K.A. Mkhoyan, E.J. Kirkland, J. Silcox, Effects of tilt on high-resolution ADF-STEM imaging. *Ultramicroscopy*. **108** (2008) 718–26. doi:10.1016/j.ultramic.2007.11.003.

[164] D. Van Dyck, M. Op de Beeck, A simple intuitive theory for electron diffraction. *Ultramicroscopy*. **64** (1996) 99–107. doi:10.1016/0304-3991(96)00008-3.

[165] E. Rotunno, M. Albrecht, T. Markurt, T. Remmele, V. Grillo, Three dimensional analysis of the composition in solid alloys by variable probe in scanning transmission electron microscopy. *Ultramicroscopy*. **146** (2014) 62–70. doi:10.1016/j.ultramic.2014.07.003.

[166] R.F. Loane, E.J. Kirkland, J. Silcox, Visibility of single heavy atoms on thin crystalline silicon in simulated annular dark-field STEM images. *Acta Crystallogr. Sect. A Found. Crystallogr.* **44** (1988) 912–927. doi:10.1107/S0108767388006403.

[167] P.M. Voyles, D.A. Muller, E.J. Kirkland, Depth-dependent imaging of individual dopant atoms in silicon. *Microsc. Microanal.* **10** (2004) 291–300. doi:10.1017/S1431927604040012.

[168] P.M. Voyles, J.L. Grazul, D.A. Muller, Imaging individual atoms inside crystals with ADF-STEM. *Ultramicroscopy*. **96** (2003) 251–73. doi:10.1016/S0304-3991(03)00092-5.

[169] R. Ishikawa, A.R. Lupini, S.D. Findlay, T. Taniguchi, S.J. Pennycook, Three-dimensional location of a single dopant with atomic precision by aberration-corrected scanning transmission electron microscopy. *Nano Lett.* **14** (2014) 1903–8. doi:10.1021/nl500564b.

[170] L.J. Allen, S.D. Findlay, M.P. Oxley, C.J. Rossouw, Lattice-Resolution Contrast From a Focused Coherent Electron Probe. Part II. *Ultramicroscopy*. **96** (2003) 65–81. doi:10.1016/S0304-3991(02)00381-9.

[171] T. Yamazaki, K. Watanabe, K. Kuramochi, I. Hashimoto, Extended Dynamical HAADF STEM Image Simulation Using the Bloch-Wave Method. *Acta Crystallogr. A.* **62** (2006) 233–236. doi:10.1107/S0108767306011974.

[172] Y. Peng, P.D. Nellist, S.J. Pennycook, HAADF-STEM Imaging with Sub-Angstrom Probes: a Full Bloch Wave Analysis. *J. Electron Microsc. (Tokyo).* **53** (2004) 257–266. http://www.ncbi.nlm.nih.gov/pubmed/15332652.

[173] K. Watanabe, T. Yamazaki, I. Hashimoto, M. Shiojiri, Atomic-Resolution Annular Dark-Field STEM Image Calculations. *Phys. Rev. B.* **64** (2001) 1–5. doi:10.1103/PhysRevB.64.115432.

[174] J. Cowley, A. Moodie, The scattering of electrons by atoms and crystals. I. A new theoretical approach. *Acta Crystallogr.* (1957). doi:10.1107/S0365110X57002194.

[175] R.F. Loane, P. Xu, J. Silcox, Thermal Vibrations in Convergent-Beam Electron Diffraction. *Acta Crystallogr. Sect. A*. **47** (1991) 267–278. doi:10.1107/S0108767391000375.

[176] C.R. Hall, P.B. Hirsch, Effect of Thermal Diffuse Scattering on Propagation of High Energy Electrons Through Crystals. *Proc. R. Soc. A Math. Phys. Eng. Sci.* **286** (1965) 158–177. doi:10.1098/rspa.1965.0136.

[177] E.J. Kirkland, R.F. Loane, J. Silcox, Simulation of Annular Dark Field STEM Images Using a Modified Multislice Method. *Ultramicroscopy*. **23** (1987) 77–96. doi:10.1016/0304-3991(87)90229-4.

[178] B.D. Forbes, A. V. Martin, S.D. Findlay, A.J. D'Alfonso, L.J. Allen, Quantum mechanical model for phonon excitation in electron diffraction and imaging using a Born-Oppenheimer approximation. *Phys. Rev. B*. **82** (2010) 104103. doi:10.1103/PhysRevB.82.104103.

[179] P. Lechner, C. Fiorini, R. Hartmann, J. Kemmer, N. Krause, P. Leutenegger, et al., Silicon Drift Detectors for High Count Rate X-ray Spectroscopy at Room Temperature. *Nucl. Instruments Methods Phys. Res. A*. **458** (2001) 281–287.

[180] P.J. Phillips, T. Paulauskas, N. Rowlands, A.W. Nicholls, K.-B. Low, S. Bhadare, et al., A new silicon drift detector for high spatial resolution STEM-XEDS: performance and applications. *Microsc. Microanal.* **20** (2014) 1046–1052. doi:10.1017/S1431927614001639.

[181] M. Itakura, N. Watanabe, M. Nishida, T. Daio, S. Matsumura, Atomic-Resolution X-ray Energy-Dispersive Spectroscopy Chemical Mapping of Substitutional Dy Atoms in a High-Coercivity Neodymium Magnet. *Jpn. J. Appl. Phys.* **52** (2013) 050201. doi:10.7567/JJAP.52.050201.

[182] G. Kothleitner, M.J. Neish, N.R. Lugg, S.D. Findlay, W. Grogger, F. Hofer, et al., Quantitative Elemental Mapping at Atomic Resolution Using X-Ray Spectroscopy. *Phys. Rev. Lett.* **112** (2014) 085501. doi:10.1103/PhysRevLett.112.085501.

[183] P.G. Kotula, D.O. Klenov, H.S. Von Harrach, Challenges to quantitative multivariate statistical analysis of atomic-resolution X-ray spectral. *Microsc. Microanal.* **18** (2012) 691–698.

[184] T.J.A. Slater, P.H.C. Camargo, M.G. Burke, N.J. Zaluzec, S.J. Haigh, Understanding the limitations of the Super-X energy dispersive x-ray spectrometer as a function of specimen tilt angle for tomographic data acquisition in the S/TEM. *J. Phys. Conf. Ser.* **522** (2014) 012025. doi:10.1088/1742-6596/522/1/012025.

[185] G. Cliff, G.W. Lorimer, The quantitative analysis of thin specimens. *J. Microsc.* **103** (1975) 203–207.

[186] M. Watanabe, D.B. Williams, Y. Tomokiyo, Comparison of Detectability Limits for Elemental Mapping by EF-TEM and STEM-XEDS. *Micron*. **34** (2003) 173–183. doi:10.1016/S0968-4328(03)00028-3.

[187] M. Watanabe, D.B. Williams, The quantitative analysis of thin specimens: a review of progress from the Cliff-Lorimer to the new zeta-factor methods. *J. Microsc.* **221** (2006) 89–109. doi:10.1111/j.1365-2818.2006.01549.x.

[188] M. Watanabe, Z. Horita, M. Nemoto, Absorption correction and thickness determination using the zeta factor in quantitative X-ray microanalysis. *Ultramicroscopy*. **65** (1996) 187–198.

[189] D.B. Williams, A.J. Papworth, M. Watanabe, High Resolution X-Ray Mapping in the STEM. **51** (2002) 113–126.

[190] A.A. Herzing, M. Watanabe, J.K. Edwards, M. Conte, Z.-R. Tang, G.J. Hutchings, et al., Energy Dispersive X-ray Spectroscopy of Bimetallic Nanoparticles in an Aberration Corrected Scanning Transmission Electron Microscope. *Faraday Discuss.* **138** (2007) 337–351. doi:10.1039/b706293c.

[191] J. Liu, Scanning Transmission Electron Microscopy and Its Application to the Study of Nanoparticles and Nanoparticle Systems. *J. Electron Microsc.* **54** (2005) 251–278. doi:10.1093/jmicro/dfi034.

[192] H. E, P.D. Nellist, S. Lozano-Perez, D. Ozkaya, Towards quantitative analysis of core-shell catalyst nano-particles by aberration corrected high angle annular dark field STEM and EDX. *J. Phys. Conf. Ser.* **241** (2010) 012067. doi:10.1088/1742-6596/241/1/012067.

[193] H.X. Gao, L.-M. Peng, Parameterization of the Temperature Dependence of the Debye–Waller Factors. *Acta Crystallogr. Sect. A Found. Crystallogr.* **55** (1999) 926–932. doi:10.1107/S0108767399005176.

[194] R.G. Newton, Scattering Theory of Waves and Particles, *Courier Dover Publications*, 1982.

[195] R.F. Egerton, M. Malac, EELS in the TEM. *J. Electron Spectros. Relat. Phenomena*. **143** (2005) 43–50.

[196] C. Dwyer, R. Erni, J. Etheridge, Measurement of effective source distribution and its importance for quantitative interpretation of STEM

images. *Ultramicroscopy*. **110** (2010) 952–957. doi:10.1016/j.ultramic.2010.01.007.

[197] H. E, K.E. MacArthur, T.J. Pennycook, E. Okunishi, A.J. D'Alfonso, N.R. Lugg, et al., Probe integrated scattering cross sections in the analysis of atomic resolution HAADF STEM images. *Ultramicroscopy*. **133** (2013) 109–19. doi:10.1016/j.ultramic.2013.07.002.

[198] D.O. Klenov, S.D. Findlay, L.J. Allen, S. Stemmer, Influence of orientation on the contrast of high-angle annular dark-field images of silicon. *Phys. Rev. B*. **76** (2007) 014111. doi:10.1103/PhysRevB.76.014111.

[199] G.T. Martinez, A. De Backer, A. Rosenauer, J. Verbeeck, S. Van Aert, The effect of probe inaccuracies on the quantitative model-based analysis of high angle annular dark field scanning transmission electron microscopy images. *Micron*. **63** (2014) 57–63. doi:10.1016/j.micron.2013.12.009.

[200] J.M. LeBeau, S.D. Findlay, L.J. Allen, S. Stemmer, Quantitative atomic resolution scanning transmission electron microscopy. *Phys. Rev. Lett.* **100** (2008) 206101. doi:10.1103/PhysRevLett.100.206101.

[201] E.C. Cosgriff, V. Nicolosi, J.N. Coleman, P.D. Nellist, Quantification of ADF STEM images of molybdenum chalcogenide nanowires. *J. Phys. Conf. Ser.* **26** (2006) 280–283. doi:10.1088/1742-6596/26/1/067.

[202] R. Aveyard, R. Ferrando, R.L. Johnston, J. Yuan, Modeling Nanoscale Inhomogeneities for Quantitative HAADF STEM Imaging. *Phys. Rev. Lett.* **113** (2014) 075501. doi:10.1103/PhysRevLett.113.075501.

[203] A. De Backer, A. De wael, J. Gonnissen, S. Van Aert, Optimal experimental design for nano-particle atom-counting from high-resolution STEM images. *Ultramicroscopy*. **151** (2015) 46–55. doi:10.1016/j.ultramic.2014.10.015.

[204] Z. Yu, D.A. Muller, J. Silcox, Study of strain fields at a-Si/c-Si interface. *J. Appl. Phys.* **95** (2004) 3362. doi:10.1063/1.1649463.

[205] L. Jones, K.E. MacArthur, V.T. Fauske, A.T.J. van Helvoort, P.D. Nellist, Rapid estimation of catalyst nanoparticle morphology and atomic-coordination by high-resolution z-contrast electron microscopy. *Nano Lett.* **14** (2014) 6336–6341. doi:10.1021/nl502762m.

[206] W. Lee, The equilibrium shape and surface energy anisotropy of clean platinum. *J. Catal.* **126** (1990) 658–670. doi:10.1016/0021-9517(90)90028-I.

[207] L. Jones, H. Yang, T.J. Pennycook, M.S.J. Marshall, S. Van Aert, N.D. Browning, et al., Smart Align—a new tool for robust non-rigid registration of scanning microscope data. *Adv. Struct. Chem. Imaging*. **1** (2015) 8. doi:10.1186/s40679-015-0008-4.

[208] A.B. Yankovich, B. Berkels, W. Dahmen, P. Binev, S.I. Sanchez, S. a Bradley, et al., Picometre-precision analysis of scanning transmission electron microscopy images of platinum nanocatalysts. *Nat. Commun.* **5** (2014) 4155. doi:10.1038/ncomms5155.

[209] N. Lopez, T.V.W. Janssens, B.S. Clausen, Y. Xu, M. Mavrikakis, T. Bligaard, et al., On the origin of the catalytic activity of gold nanoparticles for low-temperature CO oxidation. *J. Catal.* **223** (2004) 232–235. doi:10.1016/j.jcat.2004.01.001.

[210] A.R. Roosen, R.P. McCormack, W.C. Carter, Wulffman: A tool for the calculation and display of crystal shapes. *Comput. Mater. Sci.* **11** (1998) 16–26. doi:10.1016/S0927-0256(97)00167-5.

[211] B.D. Todd, R.M. Lynden-Bell, Surface and bulk properties of metals modelled with Sutton-Chen potentials. *Surf. Sci.* **281** (1993) 191–206.

[212] W.M. Skiff, R.W. Carpenter, S.H. Lin, A. Higgs, K, L, M, N, O and P ionziation cross-sections for electron energy loss spectroscopy. *Ultramicroscopy*. **25** (1988) 47–60.

[213] F. Hofer, Determination of inner-shell cross-sections for EELS-quantification. *Microsc. Microanal. Microstruct.* **2** (1991) 215–230. doi:10.1051/mmm:0199100202-3021500.

[214] N. Ni, S. Lozano-Perez, J. Sykes, C. Grovenor, Quantitative EELS analysis of zirconium alloy metal/oxide interfaces. *Ultramicroscopy*. **111** (2011) 123–130. doi:10.1016/j.ultramic.2010.10.020.

[215] T. Malis, S.C. Cheng, R.F. Egerton, EELS log-ratio technique for specimen-thickness measurement in the TEM. *J. Electron Microsc. Tech.* **8** (1988) 193–200. doi:10.1002/jemt.1060080206.

[216] K. Iakoubovskii, K. Mitsuishi, Y. Nakayama, K. Furuya, Thickness measurements with electron energy loss spectroscopy. *Microsc. Res. Tech.* **71** (2008) 626–631. doi:10.1002/jemt.20597.

[217] N.R. Lugg, G. Kothleitner, N. Shibata, Y. Ikuhara, On the quantitativeness of EDS STEM. *Ultramicroscopy*. **151** (2014) 150–159. doi:10.1016/j.ultramic.2014.11.029.

[218] R.F. Egerton, Electron Energy Loss Spectroscopy in the Electron Microscope, 3rd ed., *Springer New York*, 2011.

11. APPENDICES

11.1. Appendix A – Microscope Imaging Parameters

During the course of this thesis a great range of microscopes have been used to acquire data; it is therefore beneficial to summarise the main microscope imaging parameters used in the table below.

The probe convergence angle (CA) and detector angles were only calibrated personally for the Oxford ARM. Other angles have been taken from tabulated lists produced by someone else.

Microscope	Location	Description	Acc. Volt. (kV)	Wave Length (pm)	CA Imaging (mrad)	Detector Angles (mrad)
Jeol 2200MCO	Oxford University	Double corrected (S)TEM with Omega filter	200	2	25	90-180
FEI Titan^3 80-300	EMAT Antwerp	Double corrected (S)TEM	300	2.5	20.2	35-190
FEI Titan G2 80-200	Manchester University	Probe corrected (S)TEM	200	2.5	26.2	75-300*
UltraSTEM 100	SuperSTEM National Lab	Probe corrected dedicated STEM	100	3.7	31.4	74-195
			60	4	30.0	79-196
Jeol ARM 200F	Oxford University	Probe corrected (S)TEM	200	2	22.48	53.2-132.2

*The outer cut-off for this microscope is unknown; the value quoted here is that predicted by the inner to outer angle ratio. However this machine was only used for quantitative EDX not ADF, so the exact detector angles were not needed.

11.2. Appendix B – Parameters for Simulation Code Comparison

For the comparison between different simulation codes the following parameters were used.

- Voltage: 300kv
- Zero aberrations (including zero defocus)
- Convergence Angle: 20.2mrad
- Detector Angles: 35-190mrad

  90-190mrad
- Real space sample: 6 pixels/Å
- DWF: 0.02938 (0K)

  0.14224(100K)

  0.38401 (300K)
- These DWFs correspond to a mean square displacement value of:

  0.00372nm^2 (0K)

  0.001801nm^2 (100K)

  0.004864nm^2 (300K)

- Each set of simulations is carried out for both a single Pt atom in 0.5 x 0.5 x 0.5nm box and on a <110> projected crystal of 10 unit cells thickness.
- Reciprocal space sampling should be sufficiently large such that sampling is out to twice the detector out angle – for μSTEM, for the single unit cell I use 8X8 tiling with 2048x2048 reciprocal space sampling.

11.3. Appendix C – Calibrating Images from Fourier Transforms

An image of dimensions $a_0 \times b_0$ in real space, with $N_x \times N_y$ pixels has pixels of the sizes $\Delta x = \frac{a_0}{N_x}$ and $\Delta y = \frac{b_0}{N_y}$. The Fourier transform (FT) of the image will also have $N_x \times N_y$ pixels, however the dimension of the image in reciprocal space is $\frac{N_x}{a_o} \times \frac{N_y}{b_0}$. This makes each pixel in reciprocal space:

$$\Delta k_x = \frac{1}{a_0} \text{ and } \Delta k_y = \frac{1}{b_0} \qquad 11.1.$$

The distance of a spot from the origin in the FT for a given cubic crystal diffraction pattern is:

$$|g_{hkl}| = \frac{1}{d_{hkl}} \qquad 11.2.$$

Where:

$$d_{hkl} = \frac{a}{\sqrt{h^2 + k^2 + l^2}} \qquad 11.3.$$

Where a is the lattice parameter of for the crystal and h, k and l are the miller indices of the diffraction spot selected, which for a typical <110> direction is normally (111) planes. The distance of the 111 spot from the origin is:

$$|g_{111}| = \frac{\sqrt{3}}{a} \qquad 11.4.$$

At this stage it is important to note that the maths can be simplified by assuming square pixels and calibrating using purely the modulus diffraction spot distance from the origin. However, in real experimental images, if there is any sample drift during the image acquisition this will distort the magnification in the image

making the pixels not completely square. Therefore we take the vectors of both the selected spots:

$$|g_{\bar{1}11}|^2 = {x_1}^2 {\Delta k_x}^2 + {y_1}^2 {\Delta k_y}^2 = \frac{3}{a^2} \qquad 11.5.$$

$$|g_{1\bar{1}1}|^2 = {x_2}^2 {\Delta k_x}^2 + {y_2}^2 {\Delta k_y}^2 = \frac{3}{a^2} \qquad 11.6.$$

These can then be solved as simultaneous equations where x_1, y_1, x_2 and y_2 are simply the pixel lengths of each vector in the x and y directions of the FT.

11.4. Appendix D – Background Subtracted Images for Pt Particles

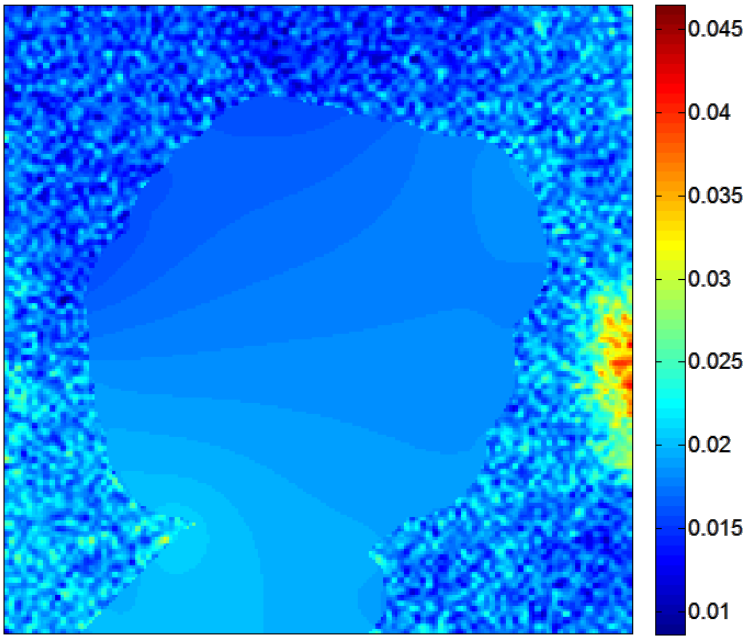


Figure 11.1 – Subtracted background image for pure Pt Particle 1.

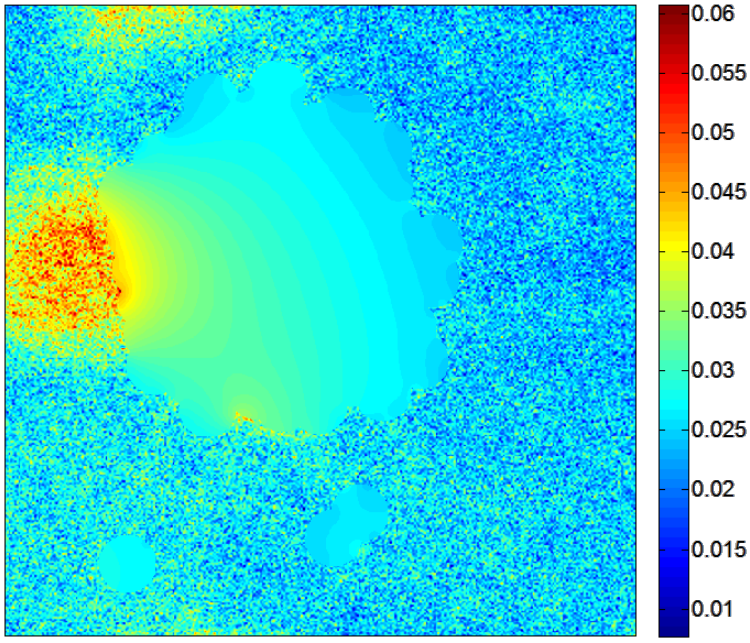


Figure 11.2 – Subtracted background image for pure Pt Particle 2.

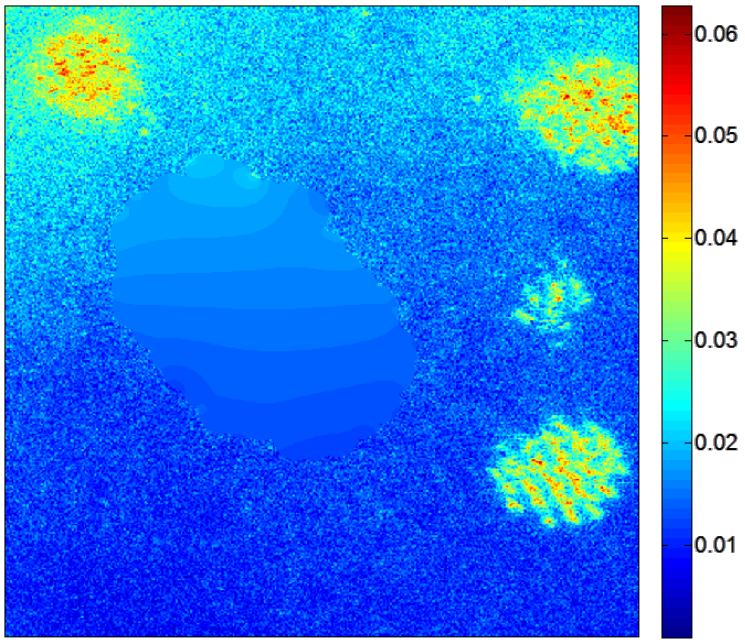


Figure 11.3 – Subtracted background image for pure Pt Particle 3.

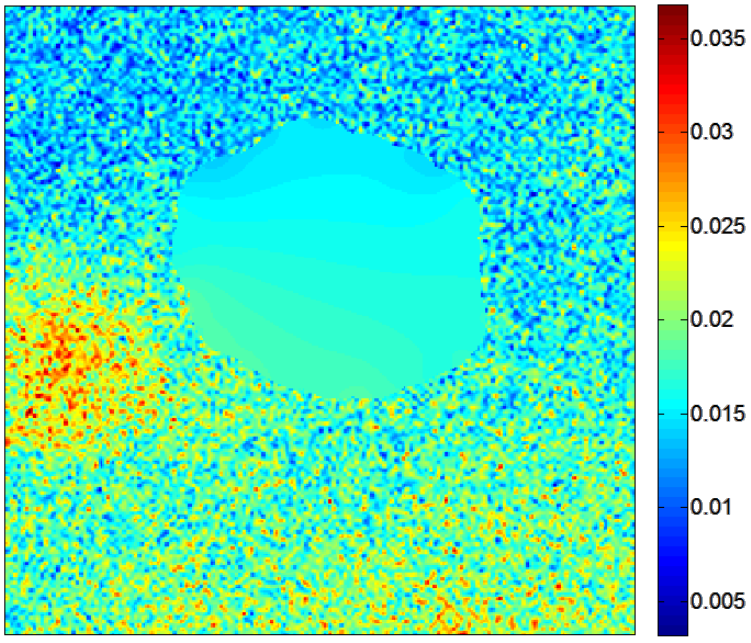


Figure 11.4 – Subtracted background image for pure Pt Particle 4.

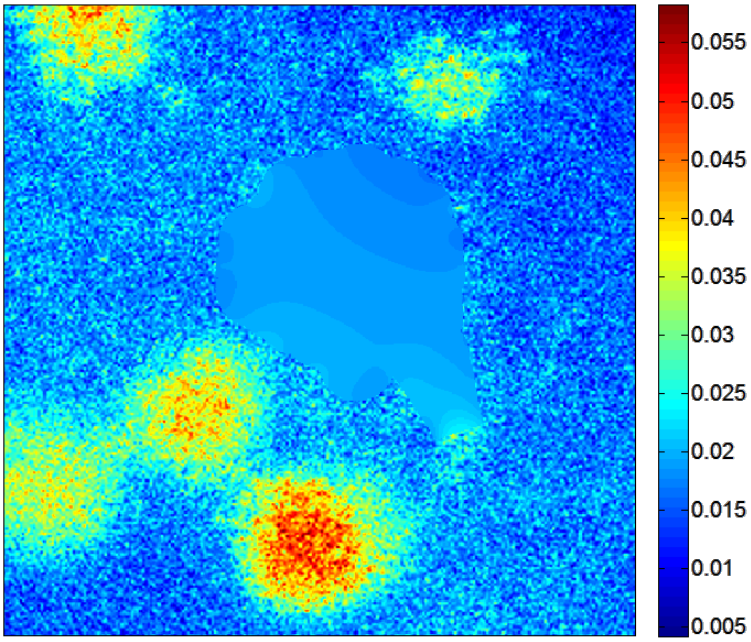


Figure 11.5 – Subtracted background image for pure Pt Particle 5.

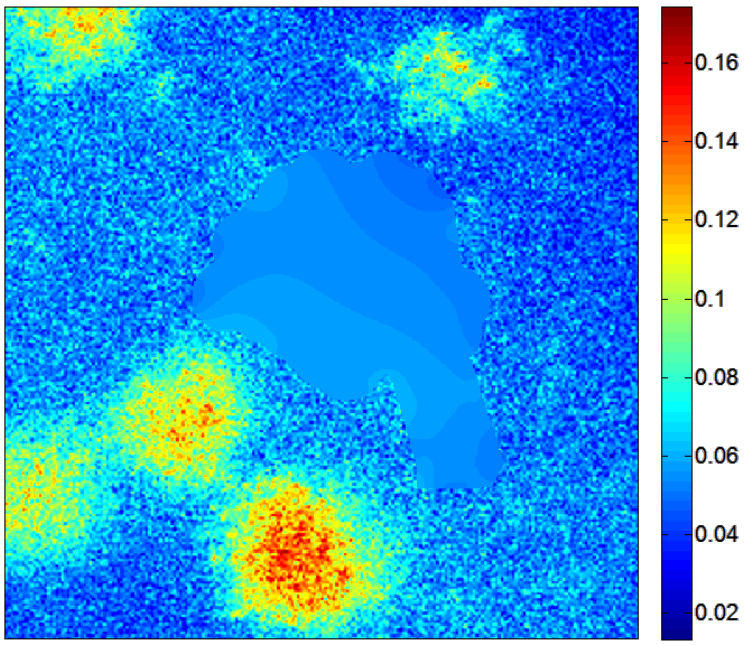


Figure 11.6 – Subtracted background image for pure Pt Particle 5b.